DOT/FAA/AR-08/37,P1

Air Traffic Organization
Operations Planning
Office of Aviation Research
and Development
Washington, DC 20591

Explicit Finite Element Modeling of Multilayer Composite Fabric for Gas Turbine Engine Containment Systems, Phase II

Part 1: Fabric Material Tests and Modeling

February 2009

Final Report

This document is available to the U.S. public through the National Technical Information Service (NTIS), Springfield, Virginia 22161.

U.S. Department of Transportation
Federal Aviation Administration

NOTICE

This document is disseminated under the sponsorship of the U.S. Department of Transportation in the interest of information exchange. The United States Government assumes no liability for the contents or use thereof. The United States Government does not endorse products or manufacturers. Trade or manufacturer's names appear herein solely because they are considered essential to the objective of this report. This document does not constitute FAA certification policy. Consult your local FAA aircraft certification office as to its use.

This report is available at the Federal Aviation Administration William J. Hughes Technical Center's Full-Text Technical Reports page: actlibrary.tc.faa.gov in Adobe Acrobat portable document format (PDF).

Technical Report Documentation Page

1. Report No.	2. Government Accession No.	3. Recipient's Catalog No.
DOT/FAA/AR-08/37,P1		

4. Title and Subtitle	5. Report Date
EXPLICIT FINITE ELEMENT MODELING OF MULTILAYER COMPOSITE FABRIC FOR GAS TURBINE ENGINE CONTAINMENT SYSTEMS, PHASE II PART 1: FABRIC MATERIAL TESTS AND MODELING	February 2009
	6. Performing Organization Code
7. Author(s) S.D. Rajan, B. Mobasher, S. Sankaran, D. Naik, and Z. Stahlecker	8. Performing Organization Report No.
9. Performing Organization Name and Address Department of Civil & Environmental Engineering Arizona State University Tempe, AZ 85287-5306	10. Work Unit No. (TRAIS)
	11. Contract or Grant No.
12. Sponsoring Agency Name and Address U.S. Department of Transportation Federal Aviation Administration Air Traffic Organization Operations Planning Office of Aviation Research and Development Washington, DC 20591	13. Type of Report and Period Covered Final Report
	14. Sponsoring Agency Code ANM-100/AME-100

15. Supplementary Notes

The Federal Aviation Administration Airport and Aircraft Safety R&D Division COTR was Donald Altobelli.

16. Abstract

Under the Federal Aviation Administration Airworthiness Assurance Center of Excellence, sponsored by the Aircraft Catastrophic Failure Prevention Program, a research team consisting of members from Arizona State University (ASU), Honeywell Engines, Systems & Services (Honeywell), National Aeronautics and Space Administration Glenn Research Center (NASA-GRC), and SRI International (SRI) collaborated to develop test procedures and computational models for designing and evaluating ballistic fabric containment structures. This report contains the details of additional tensile tests, friction tests, and static ring tests and their finite element simulations conducted at ASU. It also contains a comparison of the Honeywell and SRI finite element models of the NASA-GRC ballistic impact tests.

17. Key Words	18. Distribution Statement
Aircraft engine fragments, Containment, Zylon, Kevlar, Finite element analysis, Ballistic testing, Static testing	This document is available to the U.S. public through the National Technical Information Service (NTIS), Springfield, Virginia 22161.

19. Security Classif. (of this report)	20. Security Classif. (of this page)	21. No. of Pages	22. Price
Unclassified	Unclassified	189	

Form DOT F 1700.7 (8-72) Reproduction of completed page authorized

ACKNOWLEDGEMENTS

The investigators wish to thank Mr. William Emmerling, Mr. Donald Altobelli, Mr. Chip Queitzsch, and Mr. Jim White of the Federal Aviation Administration for their technical and financial support. To meet the objectives of this project, the technical collaborations with several other organizations, including Honeywell Engines, Systems & Services (Honeywell), SRI International (SRI), and the National Aeronautics and Space Administration Glenn Research Center (NASA-GRC), were invaluable. Some of the individuals who contributed immensely to this project include Mr. Ion Vintilescu, Mr. Reha Gomuc, and Mr. Wil Baker of Honeywell, Dr. Don Shockey, Dr. Jeff Simons, and Mr. Dave Erlich of SRI, and Mr. J. M. Pereira and Mr. Duane Revilock of NASA-GRC. Their support and cooperation in meeting the research objectives is greatly appreciated.

TABLE OF CONTENTS

			Page
EXECUTIVE SUMMARY			xxv
1.	INTRODUCTION		1
2.	TENSION TESTS		3
	2.1	Overview	3
	2.2	Test Setup and Procedure	3
	2.3	Test Results	5
		2.3.1 Kevlar 49 Tension Tests	5
		2.3.2 Zylon AS-500 Tension Tests	11
		2.3.3 Zylon AS-1500 Tension Tests	17
		2.3.4 Comparison of Fabrics	23
3.	FRICTION TESTS		23
	3.1	Overview	23
	3.2	Test Setup and Procedure	24
	3.3	Test Results	26
		3.3.1 Kevlar Friction Tests	26
		3.3.2 Zylon AS-500 Friction Tests	29
		3.3.3 Zylon AS-1500 Friction Tests	32
4.	STATIC RING TESTS		36
	4.1	Overview	36
	4.2	Test Setup and Procedure	36
		4.2.1 Specimen Preparation Procedure	36
		4.2.2 Test Setup	36
		4.2.3 Test Procedure	37
	4.3	Test Results	38
		4.3.1 Kevlar Results	38
		4.3.2 Zylon Results	49
5.	COMPARISON OF STATIC RING TESTS TO FE SIMULATIONS		59
	5.1	Overview	59

5.2 The FE Model Description 59
5.3 Results 65

5.3.1 Kevlar Results 65
5.3.2 Zylon AS-500 Results 113

6. CONCLUDING REMARKS 156

7. REFERENCES 157

APPENDIX A—DIFFERENCES BETWEEN HONEYWELL AND SRI LS-DYNA MODELS

LIST OF FIGURES

Figure		Page
1	Test Setup With Specimen	3
2	Grip Assembly	4
3	Experimental Test Setup for Poisson's Ratio	5
4	Button Apparatus	5
5	Stress-Strain Curves for the Kevlar Samples for E_{11}	6
6	Comparison of Stress-Strain Curves for Kevlar Phases I and II	7
7	Axial Stress Versus Lateral Strain for Kevlar Samples for ν_{12}	8
8	Axial Stress Versus Axial and Lateral Strains for Sample 4 for ν_{12}	8
9	Stress-Strain Curves for the Kevlar 49 Samples for E_{22}	9
10	Axial Stress Versus Lateral Strain for Kevlar 49 Samples for ν_{21}	10
11	Axial Stress Versus Axial and Lateral Strains for Sample 5 for ν_{21}	11
12	Stress-Strain Curves for the Zylon AS-500 Samples for E_{11}	12
13	Comparison of Stress-Strain Curves for Zylon AS-500 From Phases I and II	13
14	Axial Stress Versus Lateral Strains for Zylon AS-500 Samples for ν_{12}	14
15	Axial Stress Versus Axial and Lateral Strains for Sample 2 for ν_{12}	14
16	Stress-Strain Curves for Zylon AS-500 Samples for E_{22}	15
17	Axial Stress Versus Lateral Strain for Zylon AS-500 Samples for ν_{21}	16
18	Axial Stress Versus Axial and Lateral Strains for Sample 2 for ν_{21}	17
19	Stress-Strain Curves for the Zylon AS-1500 Samples for E_{11}	18
20	Axial Stress Versus Lateral Strain for Zylon AS-1500 Samples for ν_{12}	19
21	Axial Stress Versus Axial and Lateral Strains for Sample 2 for ν_{12}	20

22	Stress-Strain Curves for Zylon AS-1500 Samples for E_{22}	21
23	Axial Stress Versus Lateral Strain for Zylon AS-1500 Samples for ν_{21}	22
24	Axial Stress Versus Axial and Lateral Strains for Sample 1 for ν_{21}	22
25	Stress-Strain Curves for all Three Fabrics	23
26	Schematic Setup for Friction Test	24
27	Testing Apparatus	25
28	Typical Friction Test Output	25
29	Kevlar Friction Tests for Loading Rate of 2.0 in/min	26
30	Coefficient of Friction for Kevlar for Loading Rate of 2.0 in/min	26
31	Kevlar Friction Tests for Loading Rate of 6.0 in/min	27
32	Coefficient of Friction for Kevlar for Loading Rate of 6.0 in/min	27
33	Coefficient of Static Friction for Kevlar	28
34	Coefficient of Dynamic Friction for Kevlar	28
35	Zylon AS-500 Friction Tests for Loading Rate of 2.0 in/min	29
36	Coefficient of Friction for Zylon AS-500 for Loading Rate of 2.0 in/min	30
37	Zylon AS-500 Friction Tests for Loading Rate of 6.0 in/min	30
38	Coefficient of Friction for Zylon AS-500 for Loading Rate of 6.0 in/min	31
39	Coefficient of Static Friction for Zylon AS-500	31
40	Coefficient of Dynamic Friction for Zylon AS-500	32
41	Zylon AS-1500 Friction Tests for Loading Rate of 2.0 in/min	33
42	Coefficient of Friction for Zylon AS-1500 for Loading Rate of 2.0 in/min	33
43	Zylon AS-1500 Friction Tests for Loading Rate of 6.0 in/min	34
44	Coefficient for Zylon AS-1500 for Loading Rate of 6.0 in/min	34

45 Coefficient for Static Friction for Zylon AS-1500 35

46 Coefficient for Dynamic Friction for Zylon AS-1500 35

47 Load-Deformation Response of Four-Layer Kevlar Specimen With and Without Slack Adjustment Using Penetrator A 38

48 Load-Deformation Response of Four-Layer Kevlar Specimen With and Without Slack Adjustment Using Penetrator B 39

49 Load-Deflection Response of Kevlar for Same Orientation of Thicker Blunt Nose for Multilayer Specimens 40

50 Load-Deflection Response of Kevlar for Same Orientation of Thinner Blunt Nose for Multilayer Specimens 40

51 Load Deflection for Various Orientations of Thicker Blunt Nose With One-Layer Kevlar 41

52 Various Orientations of Thicker Blunt Nose—Four-Layer Kevlar Fabric 42

53 Various Orientations of Thicker Blunt Nose—Eight-Layer Kevlar Fabric 43

54 Load Deflection for Various Orientations of Thinner Blunt Nose With One-Layer Kevlar 43

55 Various Orientations of Thinner Blunt Nose—Four-Layer Kevlar Fabric 45

56 Various Orientations of Thinner Blunt Nose—Eight-Layer Kevlar Fabric 45

57 One-Layer Kevlar—45-Degree Orientation—Both Penetrators 46

58 Four-Layer Kevlar—0-Degree Orientation—Both Penetrators 46

59 Eight-Layer Kevlar—Off-Center Orientation—Both Penetrators 47

60 Eight-Layer Kevlar—90-Degree Orientation—Both Penetrators 47

61 Load-Deformation Response of Eight-Layer Zylon Specimen With and Without Slack Adjustment Using the Thicker Penetrator 49

62 Load-Deformation Response of Four-Layer Zylon Specimen With and Without Slack Adjustment Using the Penetrator 50

63 Load-Deflection Response of Zylon for Same Orientation of Thicker Blunt Nose for Multilayer Specimens 50

64 Load-Deflection Response of Zylon for Same Orientation of Thinner Blunt Nose for Multilayer Specimens 51

65 Load-Deflection Response for Various Orientations of Thicker Blunt Nose With One-Layer Zylon 51

66 Various Orientations of Thicker Blunt Nose—Four-Layer Zylon Fabric 52

67 Various Orientations of Thicker Blunt Nose—Eight-Layer Zylon Fabric 53

68 Load Deflection for Various Orientations of the Thinner Blunt Nose With One-Layer Zylon 53

69 Various Orientations of the Thinner Blunt Nose—Four-Layer Zylon Fabric 54

70 Various Orientations of the Thinner Blunt Nose—Eight-Layer Zylon Fabric 55

71 One-Layer Zylon—Off-Center Orientation—Both Penetrators 55

72 One-Layer Zylon—45-Degree Orientation—Both Penetrators 56

73 Four-Layer Zylon—0-Degree Orientation—Both Penetrators 56

74 Eight-Layer Zylon—90-Degree Orientation—Both Penetrators 57

75 The FE Mesh for the 0-Degree Orientation Models 60

76 The FE Mesh for 45-Degree Orientation Models Showing the Outer Surface of the Ring 61

77 The FE Mesh for 45-Degree Orientation Models Showing the Inner Surface of the Ring 62

78 The FE Mesh for 90-Degree Orientation Models 63

79 The FE Mesh for Off-Center Orientation Models 64

80a Comparison of the Load-Displacement Graphs for the One-Layer Kevlar, 0-Degree Orientation, Thinner Blunt-Nose Test 65

80b One-Layer Kevlar—0-Degree Orientation (Thinner Blunt Nose)—Plot of In-Plane Strain ε_1 Superimposed on Deformation at the End of the Last Load Step 66

80c One-Layer Kevlar—0-Degree Orientation (Thinner Blunt Nose)—Plot of In-Plane Strain ε_2 Superimposed on Deformation at the End of the Last Load Step 66

81a Comparison of the Load-Displacement Graphs for the One-Layer Kevlar, 45-Degree Orientation, Thinner Blunt-Nose Test 67

81b One-Layer Kevlar—45-Degree Orientation (Thinner Blunt Nose)—Plot of In-Plane Strain ε_1 Superimposed on Deformation at the End of the Last Load Step 68

81c One-Layer Kevlar—45-Degree Orientation (Thinner Blunt Nose)—Plot of In-Plane Strain ε_2 Superimposed on Deformation at the End of the Last Load Step 69

82a Comparison of the Load-Displacement Graphs for the One-Layer Kevlar, 90-Degree Orientation, Thinner Blunt-Nose Test 70

82b One-Layer Kevlar—90-Degree Orientation (Thinner Blunt Nose)—Plot of In-Plane Strain ε_1 Superimposed on Deformation at the End of the Last Load Step 71

82c One-Layer Kevlar—90-Degree Orientation (Thinner Blunt Nose)—Plot of In-Plane Strain ε_2 Superimposed on Deformation at the End of the Last Load Step 71

83a Comparison of the Load-Displacement Graphs for the One-Layer Kevlar, Off-Center Orientation, Thinner Blunt-Nose Test 72

83b One-Layer Kevlar—Off-Center Orientation (Thinner Blunt Nose)—Plot of In-Plane Strain ε_1 Superimposed on Deformation at the End of the Last Load Step 73

83c One-Layer Kevlar—Off-Center Orientation (Thinner Blunt Nose)—Plot of In-Plane Strain ε_2 Superimposed on Deformation at the End of the Last Load Step 73

84a Comparison of the Load-Displacement Graphs for the One-Layer Kevlar, 45-Degree Orientation, Thicker Blunt-Nose Test 74

84b One-Layer Kevlar—45-Degree Orientation (Thicker Blunt Nose)—Plot of In-Plane Strain ε_1 Superimposed on Deformation at the End of the Last Load Step 75

84c One-Layer Kevlar—45-Degree Orientation (Thicker Blunt Nose)—Plot of In-Plane Strain ε_2 Superimposed on Deformation at the End of the Last Load Step 76

85a Comparison of the Load-Displacement Graphs for the One-Layer Kevlar, 90-Degree Orientation, Thicker Blunt-Nose Test 77

85b One-Layer Kevlar—90-Degree Orientation (Thicker Blunt Nose)—Plot of In-Plane Strain ε_1 Superimposed on Deformation at the End of the Last Load Step 78

85c One-Layer Kevlar—90-Degree Orientation (Thicker Blunt Nose)—Plot of In-Plane Strain ε_2 Superimposed on Deformation at the End of the Last Load Step 78

86a Comparison of the Load-Displacement Graphs for the One-Layer Kevlar, Off-Center Orientation, Thicker Blunt-Nose Test 79

86b One-Layer Kevlar—Off-Center Orientation (Thicker Blunt Nose)—Plot of In-Plane Strain ε_1 Superimposed on Deformation at the End of the Last Load Step 80

86c One-Layer Kevlar—Off-Center Orientation (Thicker Blunt Nose)—Plot of In-Plane Strain ε_2 Superimposed on Deformation at the End of the Last Load Step 80

87a Comparison of the Load-Displacement Graphs for the Four-Layer Kevlar, 0-Degree Orientation, Thinner Blunt-Nose Test 81

87b Four-Layer Kevlar—0-Degree Orientation (Thinner Blunt Nose)—Plot of In-Plane Strain ε_1 Superimposed on Deformation at the End of the Last Load Step 82

87c Four-Layer Kevlar—0-Degree Orientation (Thinner Blunt Nose)—Plot of In-Plane Strain ε_2 Superimposed on Deformation at the End of the Last Load Step 82

88a Comparison of the Load-Displacement Graphs for the Four-Layer Kevlar, 45-Degree Orientation, Thinner Blunt-Nose Test 83

88b Four-Layer Kevlar—45-Degree Orientation (Thinner Blunt Nose)—Plot of In-Plane Strain ε_1 Superimposed on Deformation at the End of the Last Load Step 84

88c Four-Layer Kevlar—45-Degree Orientation (Thinner Blunt Nose)—Plot of In-Plane Strain ε_2 Superimposed on Deformation at the End of the Last Load Step 85

89a Comparison of the Load-Displacement Graphs for the Four-Layer Kevlar, 90-Degree Orientation, Thinner Blunt-Nose Test 86

89b Four-Layer Kevlar—90-Degree Orientation (Thinner Blunt Nose)—Plot of In-Plane Strain ε_1 Superimposed on Deformation at the End of the Last Load Step 87

89c Four-Layer Kevlar—90-Degree Orientation (Thinner Blunt Nose)—Plot of In-Plane Strain ε_2 Superimposed on Deformation at the End of the Last Load Step 87

90a Comparison of the Load-Displacement Graphs for the Four-Layer Kevlar, Off-Center Orientation, Thinner Blunt-Nose Test 88

90b Four-Layer Kevlar—Off-Center Orientation (Thinner Blunt Nose)—Plot of In-Plane Strain ε_1 Superimposed on Deformation at the End of the Last Load Step 89

90c Four-Layer Kevlar—Off-Center Orientation (Thinner Blunt Nose)—Plot of In-Plane Strain ε_2 Superimposed on Deformation at the End of the Last Load Step 89

91a Comparison of the Load-Displacement Graphs for the Four-Layer Kevlar, 45-Degree Orientation, Thicker Blunt-Nose Test 90

91b Four-Layer Kevlar—45-Degree Orientation (Thicker Blunt Nose)—Plot of In-Plane Strain ε_1 Superimposed on Deformation at the End of the Last Load Step 91

91c Four-Layer Kevlar—45-Degree Orientation (Thicker Blunt Nose)—Plot of In-Plane Strain ε_2 Superimposed on Deformation at the End of the Last Load Step 92

92a Comparison of the Load-Displacement Graphs for the Four-Layer Kevlar, 90-Degree Orientation, Thicker Blunt-Nose Test 93

92b Four-Layer Kevlar—90-Degree Orientation (Thicker Blunt Nose)—Plot of In-Plane Strain ε_1 Superimposed on Deformation at the End of the Last Load Step 94

92c Four-Layer Kevlar—90-Degree Orientation (Thicker Blunt Nose)—Plot of In-Plane Strain ε_2 Superimposed on Deformation at the End of the Last Load Step 94

93a Comparison of the Load-Displacement Graphs for the Four-Layer Kevlar, Off-Center Orientation, Thicker Blunt-Nose Test 95

93b Four-Layer Kevlar—Off-Center Orientation (Thicker Blunt Nose)—Plot of In-Plane Strain ε_1 Superimposed on Deformation at the End of the Last Load Step 96

93c Four-Layer Kevlar—Off-Center Orientation (Thicker Blunt Nose)—Plot of In-Plane Strain ε_2 Superimposed on Deformation at the End of the Last Load Step 96

94a Comparison of the Load-Displacement Graphs for the Eight-Layer Kevlar, 0-Degree Orientation, Thinner Blunt-Nose Test 97

94b Eight-Layer Kevlar—0-Degree Orientation (Thinner Blunt Nose)—Plot of In-Plane Strain ε_1 Superimposed on Deformation at the End of the Last Load Step 98

94c Eight-Layer Kevlar—0-Degree Orientation (Thinner Blunt Nose)—Plot of In-Plane Strain ε_2 Superimposed on Deformation at the End of the Last Load Step 98

95a Comparison of the Load-Displacement Graphs for the Eight-Layer Kevlar, 45-Degree Orientation, Thinner Blunt-Nose Test 99

95b Eight-Layer Kevlar—45-Degree Orientation (Thinner Blunt Nose)—Plot of In-Plane Strain ε_1 Superimposed on Deformation at the End of the Last Load Step 100

95c Eight-Layer Kevlar—45-Degree Orientation (Thinner Blunt Nose)—Plot of In-Plane Strain ε_2 Superimposed on Deformation at the End of the Last Load Step 101

96a Comparison of the Load-Displacement Graphs for the Eight-Layer Kevlar, 90-Degree Orientation, Thinner Blunt-Nose Test 102

96b Eight-Layer Kevlar—90-Degree Orientation (Thinner Blunt Nose)—Plot of In-Plane Strain ε_1 Superimposed on Deformation at the End of the Last Load Step 103

96c Eight-Layer Kevlar—90-Degree Orientation (Thinner Blunt Nose)—Plot of In-Plane Strain ε_2 Superimposed on Deformation at the End of the Last Load Step 103

97a Comparison of the Load-Displacement Graphs for the Eight-Layer Kevlar, Off-Center Orientation, Thinner Blunt-Nose Test 104

97b Eight-Layer Kevlar—Off-Center Orientation (Thinner Blunt Nose)—Plot of In-Plane Strain ε_1 Superimposed on Deformation at the End of the Last Load Step 105

97c Eight-Layer Kevlar—Off-Center Orientation (Thinner Blunt Nose)—Plot of In-Plane Strain ε_2 Superimposed on Deformation at the End of the Last Load Step 105

98a Comparison of the Load-Displacement Graphs for the Eight-Layer Kevlar, 45-Degree Orientation, Thicker Blunt-Nose Test 106

98b Eight-Layer Kevlar—45-Degree Orientation (Thicker Blunt Nose)—Plot of In-Plane Strain ε_1 Superimposed on Deformation at the End of the Last Load Step 107

98c Eight-Layer Kevlar—45-Degree Orientation (Thicker Blunt Nose)—Plot of In-Plane Strain ε_2 Superimposed on Deformation at the End of the Last Load Step 108

99a Comparison of the Load-Displacement Graphs for the Eight-Layer Kevlar, 90-Degree Orientation, Thicker Blunt-Nose Test 109

99b Eight-Layer Kevlar—90-Degree Orientation (Thicker Blunt Nose)—Plot of In-Plane Strain ε_1 Superimposed on Deformation at the End of the Last Load Step 110

99c Eight-Layer Kevlar—90-Degree Orientation (Thicker Blunt Nose)—Plot of In-Plane Strain ε_2 Superimposed on Deformation at the End of the Last Load Step 110

100a Comparison of the Load-Displacement Graphs for the Eight-Layer Kevlar, Off-Center Orientation, Thicker Blunt-Nose Test 111

100b Eight-Layer Kevlar—Off-Center Orientation (Thicker Blunt Nose)—Plot of In-Plane Strain ε_1 Superimposed on Deformation at the End of the Last Load Step 112

100c Eight-Layer Kevlar—Off-Center Orientation (Thicker Blunt Nose)—Plot of In-Plane Strain ε_2 Superimposed on Deformation at the End of the Last Load Step 112

101 Comparison of the Load-Displacement Graphs for the One-Layer Zylon, 0-Degree Orientation, Thinner Blunt-Nose Test 113

102a Comparison of the Load-Displacement Graphs for the One-Layer Zylon, 90-Degree Orientation, Thinner Blunt-Nose Test 114

102b One-Layer Zylon—90-Degree Orientation (Thinner Blunt Nose)—Plot of In-Plane Strain ε_1 Superimposed on Deformation at the End of the Last Load Step 115

102c One-Layer Zylon—90-Degree Orientation (Thinner Blunt Nose)—Plot of In-Plane Strain ε_2 Superimposed on Deformation at the End of the Last Load Step 115

103a Comparison of the Load-Displacement Graphs for the One-Layer Zylon, Off-Center Orientation, Thinner Blunt-Nose Test 116

103b One-Layer Zylon—Off-Center Orientation (Thinner Blunt Nose)—Plot of In-Plane Strain ε_1 Superimposed on Deformation at the End of the Last Load Step 117

103c One-Layer Zylon—Off-Center Orientation (Thinner Blunt Nose)—Plot of In-Plane Strain ε_2 Superimposed on Deformation at the End of the Last Load Step 117

104a Comparison of the Load-Displacement Graphs for the One-Layer Zylon, 45-Degree Orientation, Thicker Blunt-Nose Test 118

104b One-Layer Zylon—45-Degree Orientation (Thicker Blunt Nose)—Plot of In-Plane Strain ε_1 Superimposed on Deformation at the End of the Last Load Step 119

104c One-Layer Zylon—45-Degree Orientation (Thicker Blunt Nose)—Plot of In-Plane Strain ε_2 Superimposed on Deformation at the End of the Last Load Step 120

105a Comparison of the Load-Displacement Graphs for the One-Layer Zylon, 90-Degree Orientation, Thicker Blunt-Nose Test 121

105b One-Layer Zylon—90-Degree Orientation (Thicker Blunt Nose)—Plot of In-Plane Strain ε_1 Superimposed on Deformation at the End of the Last Load Step 122

105c One-Layer Zylon—90-Degree Orientation (Thicker Blunt Nose)—Plot of In-Plane Strain ε_2 Superimposed on Deformation at the End of the Last Load Step 122

106a Comparison of the Load-Displacement Graphs for the One-Layer Zylon, Off-Center Orientation, Thicker Blunt-Nose Test 123

106b One-Layer Zylon—Off-Center Orientation (Thicker Blunt Nose)—Plot of In-Plane Strain ε_1 Superimposed on Deformation at the End of the Last Load Step 124

106c One-Layer Zylon—Off-Center Orientation (Thicker Blunt Nose)—Plot of In-Plane Strain ε_2 Superimposed on Deformation at the End of the Last Load Step 124

107a Comparison of the Load-Displacement Graphs for the Four-Layer Zylon, 0-Degree Orientation, Thinner Blunt-Nose Test 125

107b Four-Layer Zylon—0-Degree Orientation (Thinner Blunt Nose)—Plot of In-Plane Strain ε_1 Superimposed on Deformation at the End of the Last Load Step 126

107c Four-Layer Zylon—0-Degree Orientation (Thinner Blunt Nose)—Plot of In-Plane Strain ε_2 Superimposed on Deformation at the End of the Last Load Step 126

108a Comparison of the Load-Displacement Graphs for the Four-Layer Zylon, 45-Degree Orientation, Thinner Blunt-Nose Test 127

108b Four-Layer Zylon—45-Degree Orientation (Thinner Blunt Nose)—Plot of In-Plane Strain ε_1 Superimposed on Deformation at the End of the Last Load Step 128

108c Four-Layer Zylon—45-Degree Orientation (Thinner Blunt Nose)—Plot of In-Plane Strain ε_2 Superimposed on Deformation at the End of the Last Load Step 129

109a Comparison of the Load-Displacement Graphs for the Four-Layer Zylon, 90-Degree Orientation, Thinner Blunt-Nose Test 130

109b Four-Layer Zylon—90-Degree Orientation (Thinner Blunt Nose)—Plot of In-Plane Strain ε_1 Superimposed on Deformation at the End of the Last Load Step 131

109c Four-Layer Zylon—90-Degree Orientation (Thinner Blunt Nose)—Plot of In-Plane Strain ε_2 Superimposed on Deformation at the End of the Last Load Step 131

110a Comparison of the Load-Displacement Graphs for the Four-Layer Zylon, Off-Center Orientation, Thinner Blunt-Nose Test 132

110b Four-Layer Zylon—Off-Center Orientation (Thinner Blunt Nose)—Plot of In-Plane Strain ε_1 Superimposed on Deformation at the End of the Last Load Step 133

110c Four-Layer Zylon—Off-Center Orientation (Thinner Blunt Nose)—Plot of In-Plane Strain ε_2 Superimposed on Deformation at the End of the Last Load Step 133

111a Comparison of the Load-Displacement Graphs for the Four-Layer Zylon, 45-Degree Orientation, Thicker Blunt-Nose Test 134

111b Four-Layer Zylon—45-Degree Orientation (Thicker Blunt Nose)—Plot of In-Plane Strain ε_1 Superimposed on Deformation at the End of the Last Load Step 135

111c Four-Layer Zylon—45-Degree Orientation (Thicker Blunt Nose)—Plot of In-Plane Strain ε_2 Superimposed on Deformation at the End of the Last Load Step 136

112a Comparison of the Load-Displacement Graphs for the Four-Layer Zylon, 90-Degree Orientation, Thicker Blunt-Nose Test 137

112b Four-Layer Zylon—90-Degree Orientation (Thicker Blunt Nose)—Plot of In-Plane Strain ε_1 Superimposed on Deformation at the End of the Last Load Step 138

112c Four-Layer Zylon—90-Degree Orientation (Thicker Blunt Nose)—Plot of In-Plane Strain ε_2 Superimposed on Deformation at the End of the Last Load Step 138

113a Comparison of the Load-Displacement Graphs for the Four-Layer Zylon, Off-Center Orientation, Thicker Blunt-Nose Test 139

113b Four-Layer Zylon—Off-Center Orientation (Thicker Blunt Nose)—Plot of In-Plane Strain ε_1 Superimposed on Deformation at the End of the Last Load Step 140

113c Four-Layer Zylon—Off-Center Orientation (Thicker Blunt Nose)—Plot of In-Plane Strain ε_2 Superimposed on Deformation at the End of the Last Load Step 140

114a Comparison of the Load-Displacement Graphs for the Eight-Layer Zylon, 0-Degree Orientation, Thinner Blunt-Nose Test 141

114b Eight-Layer Zylon—0-Degree Orientation (Thinner Blunt Nose)—Plot of In-Plane Strain ε_1 Superimposed on Deformation at the End of the Last Load Step 142

114c Eight-Layer Zylon—0-Degree Orientation (Thinner Blunt Nose)—Plot of In-Plane Strain ε_2 Superimposed on Deformation at the End of the Last Load Step 142

115a Comparison of the Load-Displacement Graphs for the Eight-Layer Zylon, 45-Degree Orientation, Thinner Blunt-Nose Test 143

115b Eight-Layer Zylon—45-Degree Orientation (Thinner Blunt Nose)—Plot of In-Plane Strain ε_1 Superimposed on Deformation at the End of the Last Load Step 144

115c Eight-Layer Zylon—45-Degree Orientation (Thinner Blunt Nose)—Plot of In-Plane Strain ε_2 Superimposed on Deformation at the End of the Last Load Step 145

116a Comparison of the Load-Displacement Graphs for the Eight-Layer Zylon, 90-Degree Orientation, Thinner Blunt-Nose Test 146

116b Eight-Layer Zylon—90-Degree Orientation (Thinner Blunt Nose)—Plot of In-Plane Strain ε_1 Superimposed on Deformation at the End of the Last Load Step 147

116c Eight-Layer Zylon—90-Degree Orientation (Thinner Blunt Nose)—Plot of In-Plane Strain ε_2 Superimposed on Deformation at the End of the Last Load Step 147

117a Comparison of the Load-Displacement Graphs for the Eight-Layer Zylon, 45-Degree Orientation, Thicker Blunt-Nose Test 148

117b Eight-Layer Zylon—45-Degree Orientation (Thicker Blunt Nose)—Plot of In-Plane Strain ε_1 Superimposed on Deformation at the End of the Last Load Step 149

117c Eight-Layer Zylon—45-Degree Orientation (Thicker Blunt Nose)—Plot of In-Plane Strain ε_2 Superimposed on Deformation at the End of the Last Load Step 150

118a Comparison of the Load-Displacement Graphs for the Eight-Layer Zylon, 90-Degree Orientation, Thicker Blunt-Nose Test 151

118b Eight-Layer Zylon—90-Degree Orientation (Thicker Blunt Nose)—Plot of In-Plane Strain ε_1 Superimposed on Deformation at the End of the Last Load Step 152

118c Eight-Layer Zylon—90-Degree Orientation (Thicker Blunt Nose)—Plot of In-Plane Strain ε_2 Superimposed on Deformation at the End of the Last Load Step 152

119a Comparison of the Load-Displacement Graphs for the Eight-Layer Zylon, Off-Center Orientation, Thicker Blunt-Nose Test 153

119b Eight-Layer Zylon—Off-Center Orientation (Thicker Blunt Nose)—Plot of In-Plane Strain ε_1 Superimposed on Deformation at the End of the Last Load Step 154

119c Eight-Layer Zylon—Off-Center Orientation (Thicker Blunt Nose)—Plot of In-Plane Strain ε_2 Superimposed on Deformation at the End of the Last Load Step 154

LIST OF TABLES

Table		Page
1	Tension Test Results for the Kevlar Samples for E_{11}	6
2	Comparison of Kevlar Tension Test Results From Phases I and II	7
3	Poisson's Ratio ν_{12} for the Kevlar Samples	9
4	Tension Test Results From Kevlar Samples for E_{22}	10
5	Poisson's Ratio ν_{21} for the Kevlar 49 Samples	11
6	Tension Test Results for Zylon AS-500 Samples for E_{11}	12
7	Comparison of the Zylon AS-500 Tension Test Results From Phases I and II	13
8	Poisson's Ratio ν_{12} for the Zylon AS-500 Samples	15
9	Tension Test Results for Zylon AS-500 Samples for E_{22}	16
10	Poisson's Ratio ν_{21} for the Zylon AS-500 Samples	17
11	Specimen Properties for Zylon AS-1500	18
12	Tension Test Results for Zylon AS-1500 Samples for E_{11}	19
13	Poisson's Ratio ν_{12} for the Zylon AS-1500 Samples	20
14	Tension Test Results for the Zylon AS-1500 Samples for E_{22}	21
15	Poisson's Ratio ν_{21} for the Zylon AS-1500 Samples	23
16	Comparison of Friction Coefficients for Kevlar	29
17	Comparison of Friction Coefficients for Zylon AS-500	32
18	Comparison of Friction Coefficients for Zylon AS-1500	36
19	Dimensions of the Various Blunt Noses	37
20	Values of Maximum Load and Stiffness for Kevlar Using the Thicker Penetrator	42
21	Values of Maximum Load and Stiffness for Kevlar Using the Thinner Penetrator	44

22	Summary of Kevlar Static Test Results	48
23	Values of Maximum Load and Stiffness for Zylon Using the Thicker Penetrator	52
24	Values of Maximum Load and Stiffness for Zylon Using the Thinner Penetrator	54
25	Summary of Zylon Static Test Results	58
26	Model Type and Typical Element Length	59
27	Static Test—FEA Comparison for the One-Layer Kevlar, 0-Degree Orientation, Thinner Blunt-Nose Test	65
28	Static Test—FEA Comparison for the One-Layer Kevlar, 45-Degree Orientation, Thinner Blunt-Nose Test	67
29	Static Test—FEA Comparison for the One-Layer Kevlar, 90-Degree Orientation, Thinner Blunt-Nose Test	70
30	Static Test—FEA Comparison for the One-Layer Kevlar, Off-Center Orientation, Thinner Blunt-Nose Test	72
31	Static Test—FEA Comparison for the One-Layer Kevlar, 45-Degree Orientation, Thicker Blunt-Nose Test	74
32	Static Test—FEA Comparison for the One-Layer Kevlar, 90-Degree Orientation, Thicker Blunt-Nose Test	77
33	Static Test—FEA Comparison for the One-Layer Kevlar, Off-Center Orientation, Thicker Blunt-Nose Test	79
34	Static Test—FEA Comparison for the Four-Layer Kevlar, 0-Degree Orientation, Thinner Blunt-Nose Test	81
35	Static Test—FEA Comparison for the Four-Layer Kevlar, 45-Degree Orientation, Thinner Blunt-Nose Test	83
36	Static Test—FEA Comparison for the Four-Layer Kevlar, 90-Degree Orientation, Thinner Blunt-Nose Test	86
37	Static Test—FEA Comparison for the Four-Layer Kevlar, Off-Center Orientation, Thinner Blunt-Nose Test	88
38	Static Test—FEA Comparison for the Four-Layer Kevlar, 45-Degree Orientation, Thicker Blunt-Nose Test	90

39 Static Test—FEA Comparison for the Four-Layer Kevlar, 90-Degree Orientation, Thicker Blunt-Nose Test 93

40 Static Test—FEA Comparison for the Four-Layer Kevlar, Off-Center Orientation, Thicker Blunt-Nose Test 95

41 Static Test—FEA Comparison for the Eight-Layer Kevlar, 0-Degree Orientation, Thinner Blunt-Nose Test 97

42 Static Test—FEA Comparison for the Eight-Layer Kevlar, 45-Degree Orientation, Thinner Blunt-Nose Test 99

43 Static Test—FEA Comparison for the Eight-Layer Kevlar, 90-Degree Orientation, Thinner Blunt-Nose Test 102

44 Static Test—FEA Comparison for the Eight-Layer Kevlar, Off-Center Orientation, Thinner Blunt-Nose Test 104

45 Static Test—FEA Comparison for the Eight-Layer Kevlar, 45-Degree Orientation, Thicker Blunt-Nose Test 106

46 Static Test—FEA Comparison for the Eight-Layer Kevlar, 90-Degree Orientation, Thicker Blunt-Nose Test 109

47 Static Test—FEA Comparison for the Eight-Layer Kevlar, Off-Center Orientation, Thicker Blunt-Nose Test 111

48 Static Test—FEA Comparison for the One-Layer Zylon, 0-Degree Orientation, Thinner Blunt-Nose Test 113

49 Static Test—FEA Comparison for the One-Layer Zylon, 90-Degree Orientation, Thinner Blunt-Nose Test 114

50 Static Test—FEA Comparison for the One-Layer Zylon, Off-Center Orientation, Thinner Blunt-Nose Test 116

51 Static Test—FEA Comparison for the One-Layer Zylon, 45-Degree Orientation, Thicker Blunt-Nose Test 118

52 Static Test—FEA Comparison for the One-Layer Zylon, 90-Degree Orientation, Thicker Blunt-Nose Test 121

53 Static Test—FEA Comparison for the One-Layer Zylon, Off-Center Orientation, Thicker Blunt-Nose Test 123

54 Static Test—FEA Comparison for the Four-Layer Zylon, 0-Degree Orientation, Thinner Blunt-Nose Test 125

55 Static Test—FEA Comparison for the Four-Layer Zylon, 45-Degree Orientation, Thinner Blunt-Nose Test 127

56 Static Test—FEA Comparison for the Four-Layer Zylon, 90-Degree Orientation, Thinner Blunt-Nose Test 130

57 Static Test—FEA Comparison for the Four-Layer Zylon, Off-Center Orientation, Thinner Blunt-Nose Test 132

58 Static Test—FEA Comparison for the Four-Layer Zylon, 45-Degree Orientation, Thicker Blunt-Nose Test 134

59 Static Test—FEA Comparison for the Four-Layer Zylon, 90-Degree Orientation, Thicker Blunt-Nose Test 137

60 Static Test—FEA Comparison for the Four-Layer Zylon, Off-Center Orientation, Thicker Blunt-Nose Test 139

61 Static Test—FEA Comparison for the Eight-Layer Zylon, 0-Degree Orientation, Thinner Blunt-Nose Test 141

62 Static Test—FEA Comparison for the Eight-Layer Zylon, 45-Degree Orientation, Thinner Blunt-Nose Test 143

63 Static Test—FEA Comparison for the Eight-Layer Zylon, 90-Degree Orientation, Thinner Blunt-Nose Test 146

64 Static Test—FEA Comparison for the Eight-Layer Zylon, 45-Degree Orientation, Thicker Blunt-Nose Test 148

65 Static Test—FEA Comparison for the Eight-Layer Zylon, 90-Degree Orientation, Thicker Blunt-Nose Test 151

66 Static Test—FEA Comparison for the Eight-Layer Zylon, Off-Center Orientation, Thicker Blunt-Nose Test 153

LIST OF ACRONYMS

ASTM	American Society for Testing Materials
AS	As spun
ASU	Arizona State University
D	Denier
FE	Finite element
FEA	Finite element analysis
ID	Inner diameter
NASA-GRC	National Aeronautics and Space Administration Glenn Research Center
OD	Outer diameter
SRI	SRI International

EXECUTIVE SUMMARY

A team consisting of Arizona State University (ASU), Honeywell Engines, Systems & Services (Honeywell), National Aeronautics and Space Administration Glenn Research Center (NASA-GRC), and SRI International (SRI) collaborated to develop computational models and verification tests for designing and evaluating turbine engine fan blade fabric containment structures. This research was conducted under the Federal Aviation Administration Airworthiness Assurance Center of Excellence and was sponsored by the Aircraft Catastrophic Failure Prevention Program. The research was directed toward improving the modeling of a turbine engine fabric containment structure for an engine blade-out containment demonstration test required for certification of aircraft engines.

In Phase I, progress was made in testing and computational analysis. A material model was developed for Kevlar® and Zylon® fabrics. Static testing of containment wraps subjected to loads through a blunt-nose impactor was performed at ASU. Ballistic testing of containment wraps subjected to a high-velocity blunt projectile was performed at NASA-GRC. These tests provided test cases (benchmark results) to validate the developed finite element (FE) methodology. While the work performed in Phase I met the stated objectives, improvements in robustness and confidence of the finite element simulations and predictions were desired.

The research conducted in Phase II brought a new level of capability to design and develop fan blade containment systems for turbine engines. To achieve the program objectives, a program plan consisting of the following four technical tasks was developed and implemented:

- Task 1: Robust FE Model Development. The objective of this task was to increase confidence and robustness in the material models for the Kevlar and Zylon material models developed in Phase I.

- Task 2: Improve FE Modeling Capability for Multiple Layers of Fabric. In Phase I, most of the LS-DYNA® models used a single-element through the thickness to model the fabric, ranging from 1 to 24 layers.

- Task 3: 1500 denier (D) Zylon Material Model Development. In Phase I, limited ballistic and static tests of 1500 D Zylon indicated this configuration of Zylon might have the potential to offer a 60-percent weight advantage over a similar configuration of Kevlar 49 fabric for the same fragment energy. The objective of this task was to develop and validate a material model for 1500 D Zylon. It should be noted that during this research, it was discovered that Zylon was found to have excessive deterioration due to heat and humidity. As a result, it was decided that the remainder of this research would focus only on Kevlar fabrics.

- Task 4: Engine Simulations. As in Phase I, the objective of this task was to validate improvements to the material models and FE methods developed under Phase II as they relate to propulsion engine fan blade containment. Existing fabric material models

and modeling methods and their improvements will be validated using fan containment test data.

Each member of the team developed a comprehensive report describing the details of the research task and the findings. The comprehensive report consists of the following four parts:

1. Arizona State University Department of Civil & Environmental Engineering, Part 1: Fabric Material Tests

2. NASA-Glenn Research Center, Part 2: Ballistic Impact Testing

3. SRI International, Part 3: Material Model Development and Simulation of Experiments

4. Honeywell Engines, Systems & Services, Part 4: Model Simulation for Ballistic Tests, Engine Fan Blade-Out and Generic Engine

This report (Part 1) contains the details of the fabric material tests and their finite element simulations as well as additional tensile tests, friction tests, and static ring tests and their finite element simulations carried out at ASU. It also contains a comparison of the Honeywell and SRI ring model from the NASA-GRC ballistic impact tests.

1. INTRODUCTION.

Composite fiber fabric wraps are widely used in the containment systems of aircraft gas turbine engines. These systems are found to be especially cost-effective for mitigating engine debris during a fan blade-out event because fabrics have a high strength per unit weight. Moreover, it is inexpensive to manufacture this containment system compared to the traditional metallic systems. To use this advantage properly, it is necessary to have a robust finite element analysis (FEA) modeling methodology for daily design tasks. Modeling a multilayer fabric composite for engine containment systems during a fan blade-out event has been a difficult task, partially due to a lack of accurate numerical modeling techniques, including material formulation. Numerical instability is frequently encountered during an analysis by finite element (FE) analysis programs. This is believed to be due to the complicated interaction between the different components in a model and the high velocity of the projectile. Modeling the damaged material behavior has also been a challenge. In Phase I of this research, progress was made in addressing the above-mentioned issues. The combined efforts of Honeywell Engines, Systems & Services (Honeywell), SRI International (SRI), National Aeronautics and Space Administration Glenn Research Center (NASA-GRC), and Arizona State University (ASU) resulted in the following major accomplishments:

- A material model was developed for Kevlar® and Zylon® fabrics. Independent laboratory tests conducted at ASU and SRI form the basis of this model. These material models are general enough to be used as the constitutive model for both static and dynamic/explicit FEAs.

- Static testing of containment wraps subjected to loads through a blunt-nose impactor was carried out at ASU. Ballistic tests of containment wraps subjected to a high-velocity projectile were carried out at NASA-GRC. These tests have provided test cases (benchmark results) to validate the developed FE methodology.

- The material models developed in Phase I Task 1 were used by the research team in the FE simulation of static and ballistic tests. The static test results were validated by ASU using the ABAQUS FE program. The ballistic test results were validated by Honeywell and SRI using the LS-DYNA® FE program.

- The knowledge gained from Phase I Tasks 1-3 was used by Honeywell for the numerical simulation of engine fan blade-out events involving existing production engine models and compared against test results (employing Kevlar containment).

- An understanding was reached of the relative comparison between Kevlar and Zylon materials in turbine engine blade-out containment systems.

It is clear from Phase I that the developed FEA procedure provides a reliable simulation of the various tests, including actual engine fan blade-out events. However, it is desirable to increase the confidence of the FE simulations and predictions. Phase II brings a new level of capability to design and develop fan containment systems for turbine engines, thereby leading to more

economical and safer containment system designs. To achieve the program objectives, a program plan consisting of the following four technical tasks was developed and implemented:

(1) Task 1: Robust FE Model Development. The objective of this task was to increase confidence in the material models for 1420 denier (D) Kevlar 49 17x17 (Kevlar) and 500 D Zylon as-spun (AS) 35x35 (Zylon) and to increase confidence that these previously developed models and methodologies could accurately predict design conditions.

(2) Task 2: FE Modeling Capability for Multiple Layers of Fabric Improvement. In Phase I, most of the LS-DYNA models used a single-element through the thickness to model the fabric, which ranged from 1 to 24 layers. Although this technique is simple, it does not provide the predictive capability of computing the number of fabric layers that are penetrated during a containment event. Therefore, the containment margin cannot be accurately predicted in terms of the number of unpenetrated layers versus the total number of layers. The objective of this task was to improve the modeling capability for multiple layers of fabric using multiple layers of shell elements.

(3) Task 3: 1500 D Zylon Material Model Development. In Phase I, limited ballistic and static tests of 1500 D Zylon (17x17 weave) indicated that 1500 D Zylon has the potential to offer a 60-percent weight advantage over Kevlar for the same fragment energy. Apparently, 1500 D Zylon enables either a dramatic increase in fan containment safety margin, a decrease in engine weight, or a combination of both. The objective of this task was to conduct further testing to develop and validate a material model for 1500 D Zylon. It should be noted that during this research, it was discovered that Zylon was found to have excessive deterioration due to heat and humidity. As a result, it was decided that the remainder of this research would focus only on Kevlar fabrics.

(4) Task 4: Engine Simulations. As in Phase I, the objective of this task is to validate improvements to the material models and FE methods developed under this phase as they relate to propulsion engine fan blade containment. Existing fabric material models and modeling methods and their improvements will be validated using fan containment test data.

This report discusses the details of various experimental tests and FE simulations conducted at ASU. Tasks 1.2.1, 1.3.1, and 3.1 discuss tension tests conducted to develop the basic material properties. The details and results are discussed in section 2.

Section 3 discusses the friction tests (Task 1.2.3) conducted to determine the coefficient of friction between fabric layers.

Section 4 discusses the details and results of the static ring tests (Task 1.5) and section 5 discusses the comparison between the static ring tests (Task 1.6) and the FE simulations (Task 1.4). Section 6 presents final thoughts and suggestions for improvements.

Appendix A contains a modeling study that compares the Honeywell and SRI FE models for the NASA ballistic impact tests conducted in this phase of the program.

2. TENSION TESTS.

2.1 OVERVIEW.

A series of uniaxial tension tests were conducted on fabrics specifically obtained for this phase of the research so the test results could be compared to the earlier test results. These tests were conducted in a 22-kips servo-hydraulic test frame operated under closed-loop conditions and were used to calculate the uniaxial stress-strain response of Kevlar 49, Zylon AS-500, and Zylon AS-1500 fabrics and to evaluate their material constants.

2.2 TEST SETUP AND PROCEDURE.

The tests were performed according to the standard American Society for Testing Materials (ASTM) procedure, Tensile Testing of Polymer Matrix Composites–ASTM D 3039, "Standard Test Method for Tensile Properties of Fiber-Resin Composites." Tests were conducted in a 22-kips servo-hydraulic test frame operated under closed-loop control.

The test used a displacement control procedure with the rate of displacement of the actuator (stroke) set at 0.1 in/min. Digital data acquisition was used to collect data every 0.5 second. The test was continued until complete failure of the specimen was achieved. The load-deformation results were used to calculate the stress-strain response. The overall specimen deformation was measured by the stroke movement of the actuator. Figure 1 shows a typical test setup with a fabric sample.

Figure 1. Test Setup With Specimen

The gripping fixture (denoted as Grip T2 developed during Phase I of the research) was used to ensure that specimens slipping from the grips did not influence the deflection values as shown in figure 2(a)-(c). Flat steel plates (2.5″ wide by 2″ long by 0.25″ thick) were used to grip the specimen at both ends. One plate had a curved groove at the center throughout its width, which was half the thickness of the plate. A V-notch was cut in the other plate in the same position, also about half the thickness of the plate. A round aluminum rod was cut lengthwise to the shape of the existing grooves in the steel plate. Two shoulder pins at the top of the plates kept the assembly intact and prevented the plates from wobbling around the aluminum piece. The fabric was held between the V-notch and the aluminum rod so that the notch pinched against the fabric and prevented slipping. The two plates were pressed with hydraulic grips, thereby ensuring uniform pressure application to minimize or prevent any fabric slippage.

(a) End Plates for Gripping

(b) Side View

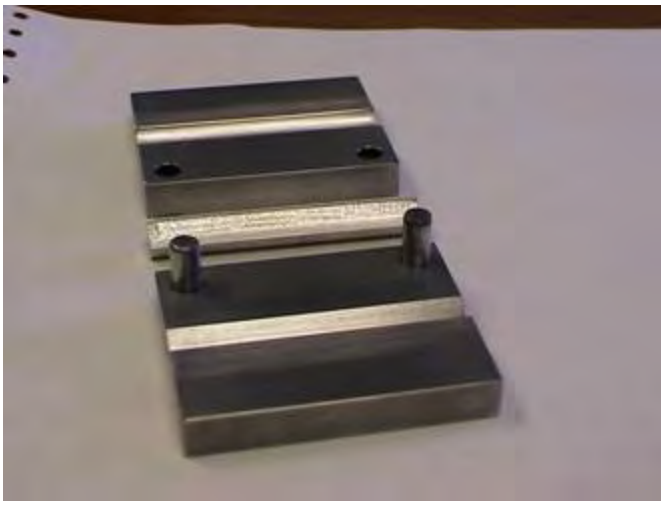

(c) Inner View

Figure 2. Grip Assembly

A clip gage system was used to calculate the Poisson's ratio for the Kevlar fabric. The experimental setup for the Poisson's ratio is shown in figure 3. The primary part of the clip gage system consists of two rectangular wood buttons that are woven onto the fabric. A button stitched onto the fabric is shown in figure 4. A calibrated extensometer fitted on the button measures the strain of the fabric. The extensometer can be used for different gage lengths and is mounted in a direction perpendicular to the fabric length to obtain lateral strain response from the deformed fabric.

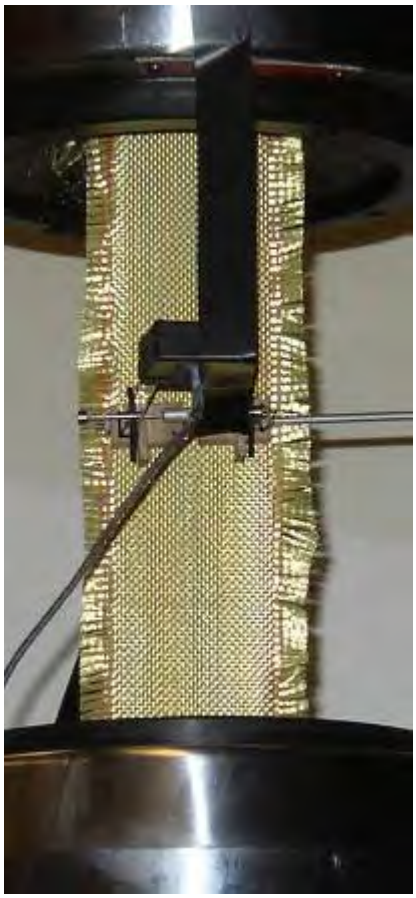

Figure 3. Experimental Test Setup for Poisson's Ratio

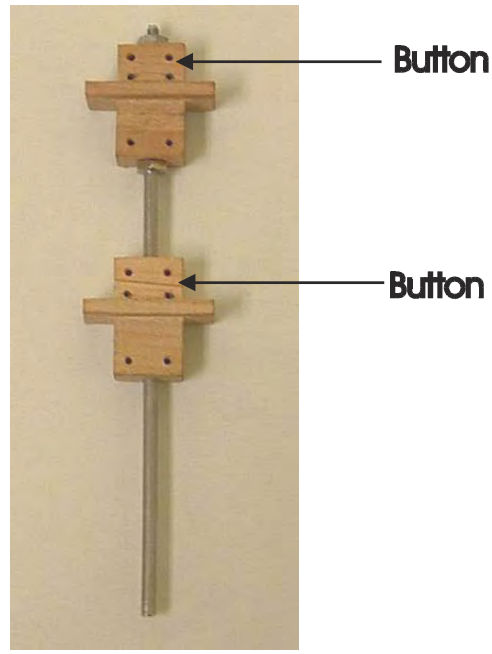

Figure 4. Button Apparatus

2.3 TEST RESULTS.

2.3.1 Kevlar 49 Tension Tests.

This section presents the results of the tension tests performed on Kevlar samples to determine Young's Modulus E_{11}. Figure 5 shows the stress-strain response of five Kevlar samples. Table 1 summarizes the results.

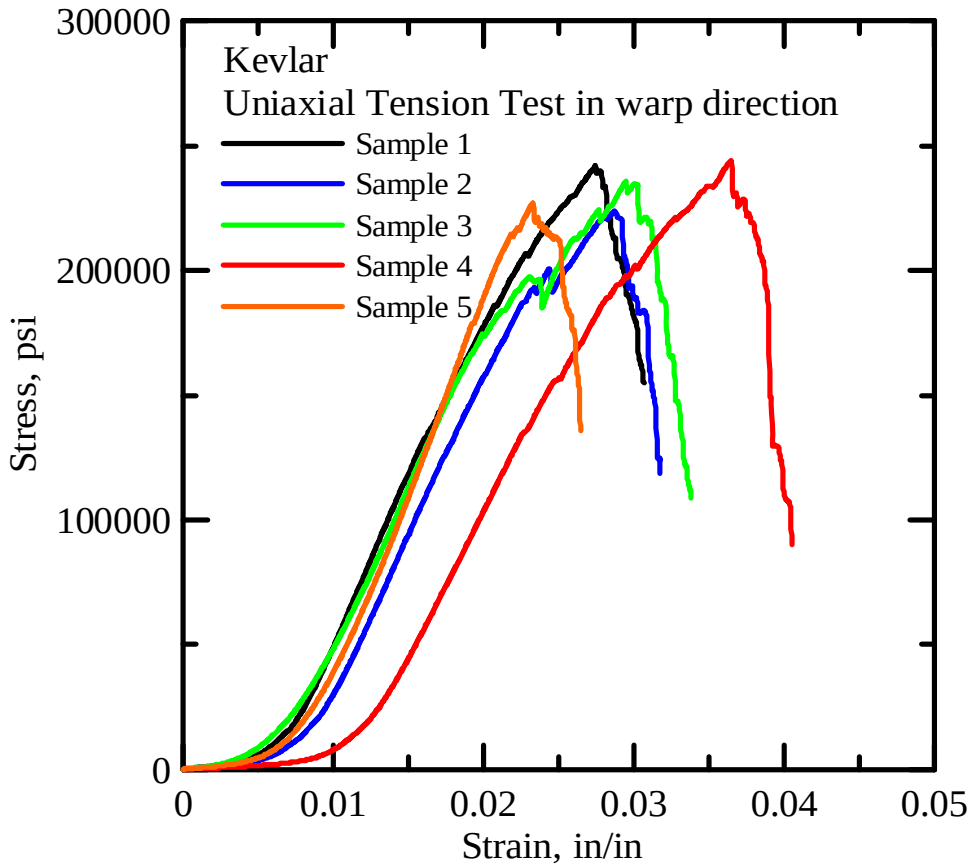

Figure 5. Stress-Strain Curves for the Kevlar Samples for E_{11}

Table 1. Tension Test Results for the Kevlar Samples for E_{11}

	Sample Replicate No.	Maximum Stress (psi)	Ultimate Strain (in/in)	Toughness (psi)	Stiffness, E (psi)
	1	241933	0.0274	3523.5	13605045.5
	2	223866	0.0287	3262.5	13184531.0
	3	235901	0.0295	4002	13521931.5
	4	244267	0.0365	4248.5	13150586.5
	5	226882	0.0233	2537.5	13862768.5
Average		234567	0.03	3509	13464975.5
Std. Dev.		8990	0.00	667	299410.5

Std. Dev. = Standard deviation

Figure 6 and table 2 show the comparison of the samples tested in Phase I (Ktest2, Ktest3, KSwath1, KSwath2) and Phase II (Samples 1 through 5).

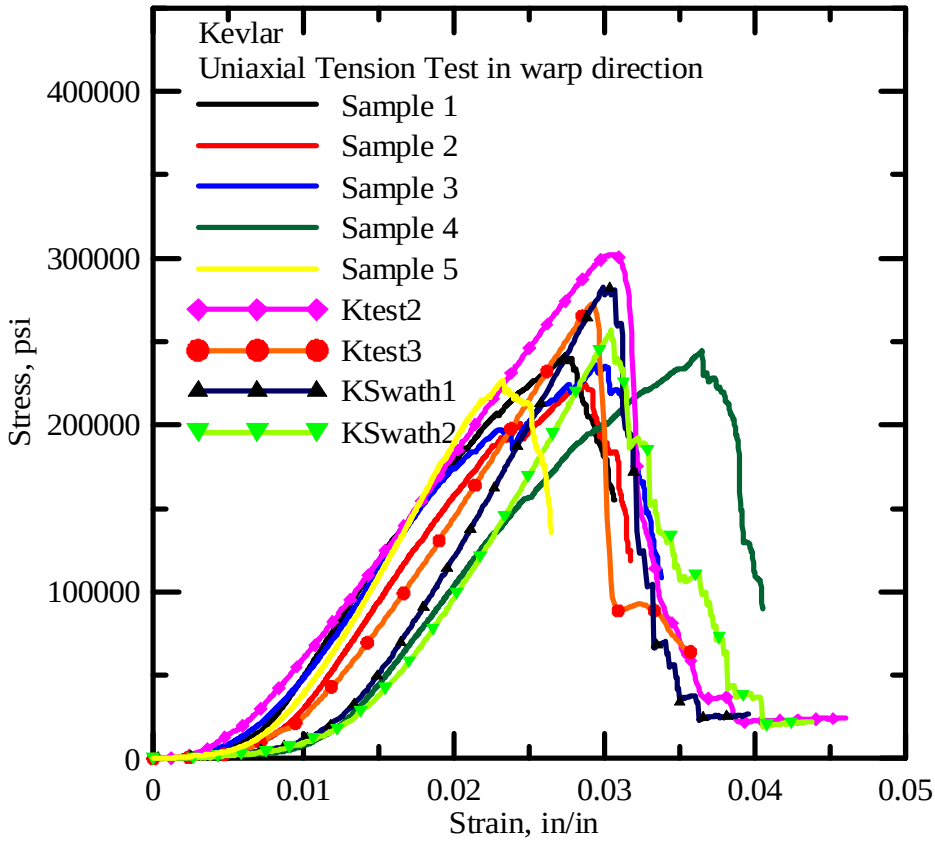

Figure 6. Comparison of Stress-Strain Curves for Kevlar Phases I and II

Table 2. Comparison of Kevlar Tension Test Results From Phases I and II

Source	Average Value of Stiffness (psi)
Phase I results (all 4 samples)	16837835
Phase II results (all 5 samples)	13464990

The Poisson's ratio ν_{12} for Kevlar fabric was obtained from the tension tests using the clip gauge system. Figures 7 and 8 show the axial stress versus lateral strain for these samples.

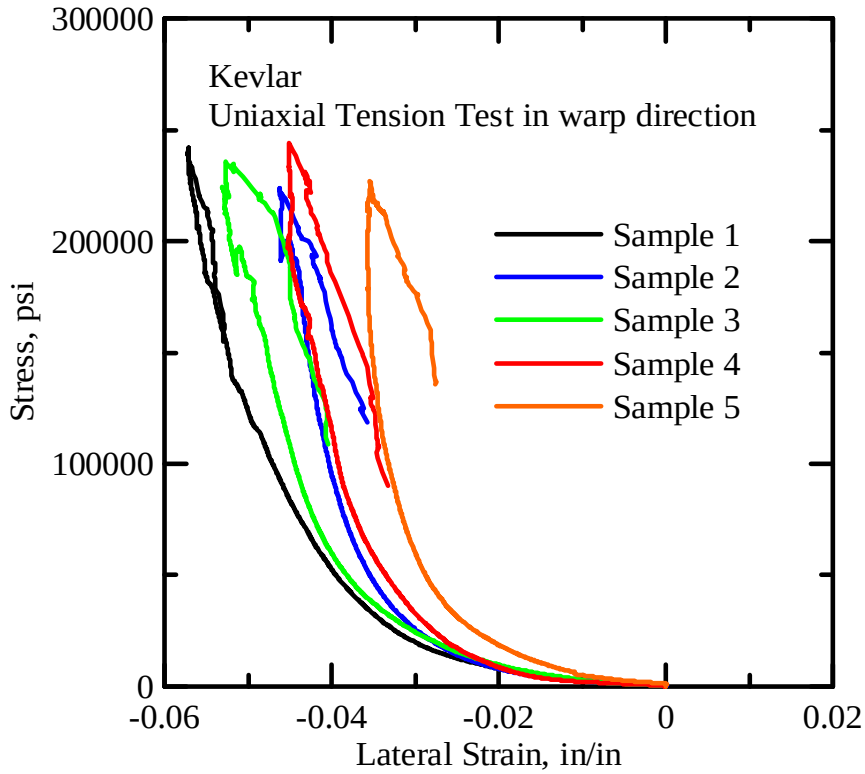

Figure 7. Axial Stress Versus Lateral Strain for Kevlar Samples for ν_{12}

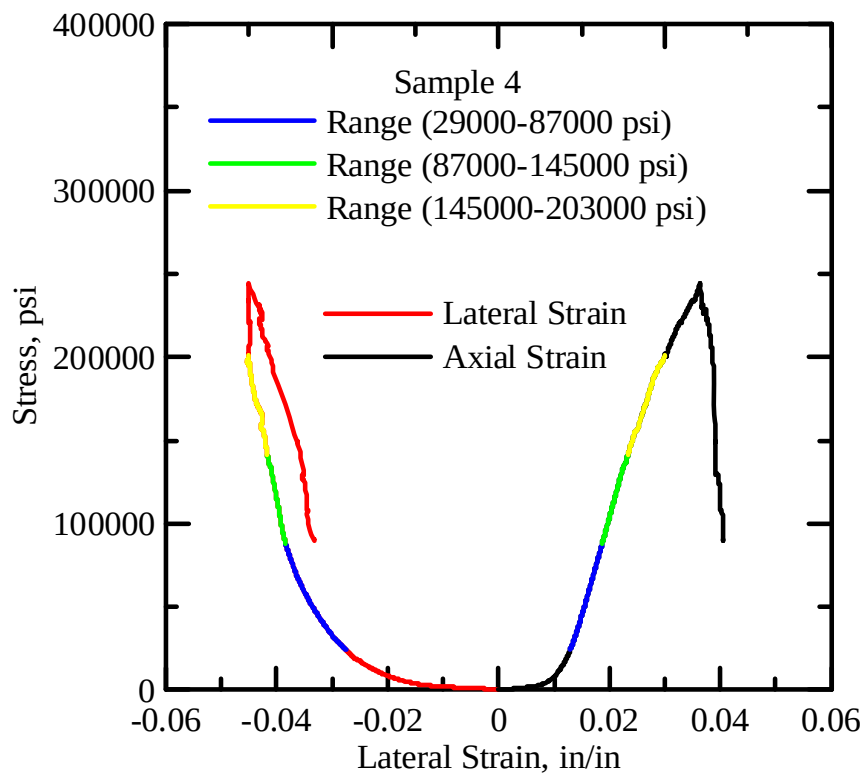

Figure 8. Axial Stress Versus Axial and Lateral Strains for Sample 4 for ν_{12}

The Poisson's ratio ν_{12} was calculated for three different ranges of stresses and the results are summarized in table 3.

Table 3. Poisson's Ratio ν_{12} for the Kevlar Samples

Stress Range (psi)	Poisson's Ratio						
	Sample 1	Sample 2	Sample 3	Sample 4	Sample 5	Average	Std. Dev.
29000 -87000	1.945	1.746	1.921	1.842	1.764	1.844	0.090
87000-145000	0.797	0.680	0.746	0.685	0.615	0.705	0.069
145000-203000	0.738	0.524	0.618	0.578	0.631	0.618	0.079

Std. Dev. = Standard deviation

The results obtained from five tension tests run on Kevlar 49 for Young's Modulus E_{22} are shown in figure 9 and table 4.

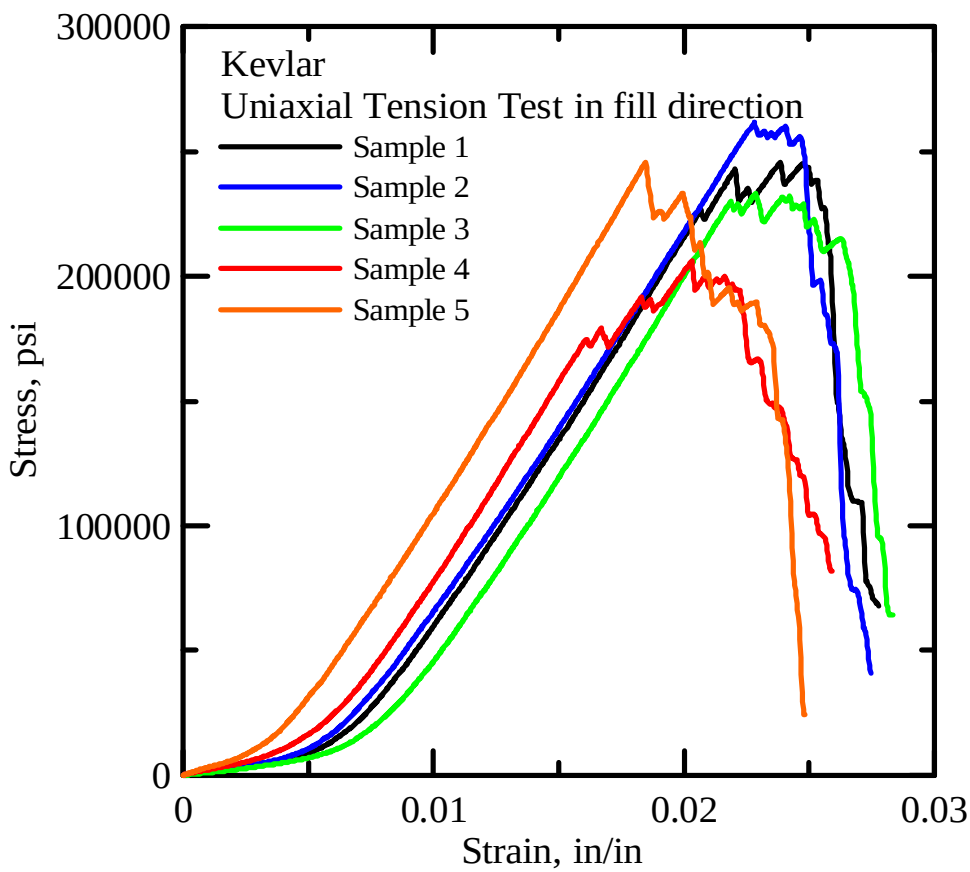

Figure 9. Stress-Strain Curves for the Kevlar 49 Samples for E_{22}

Table 4. Tension Test Results From Kevlar Samples for E_{22}

	Sample Replicate No.	Maximum Stress (psi)	Ultimate Strain (in/in)	Toughness (psi)	Stiffness, E (psi)
	1	245760.5	0.0238	3103.0	15132751.0
	2	261667.0	0.0228	3146.5	15009776.5
	3	233319.5	0.0228	3001.5	15374248.5
	4	206291.5	0.0203	2682.5	15150223.5
	5	245876.5	0.0185	3045.0	15732674.0
Average		238583.0	0.02	3001.5	15279940.5
Std. Dev.		20662.5	0.00	188.5	285186.0

Std. Dev. = Standard deviation

The Poisson's ratio ν_{21} for Kevlar fabric was obtained from the tension tests using the clip gauge system. Figures 10 and 11 show the axial stress versus lateral strain for these samples.

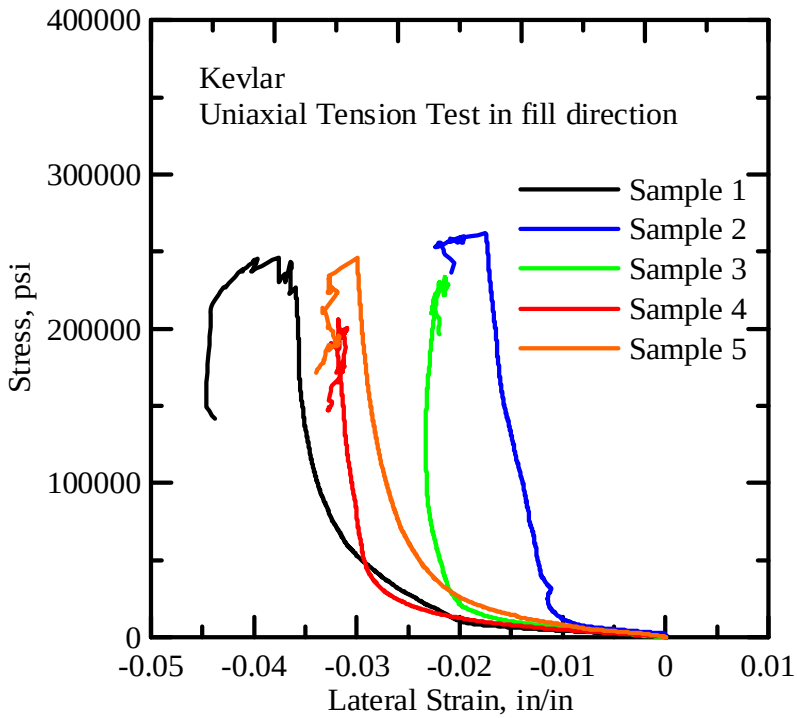

Figure 10. Axial Stress Versus Lateral Strain for Kevlar 49 Samples for ν_{21}

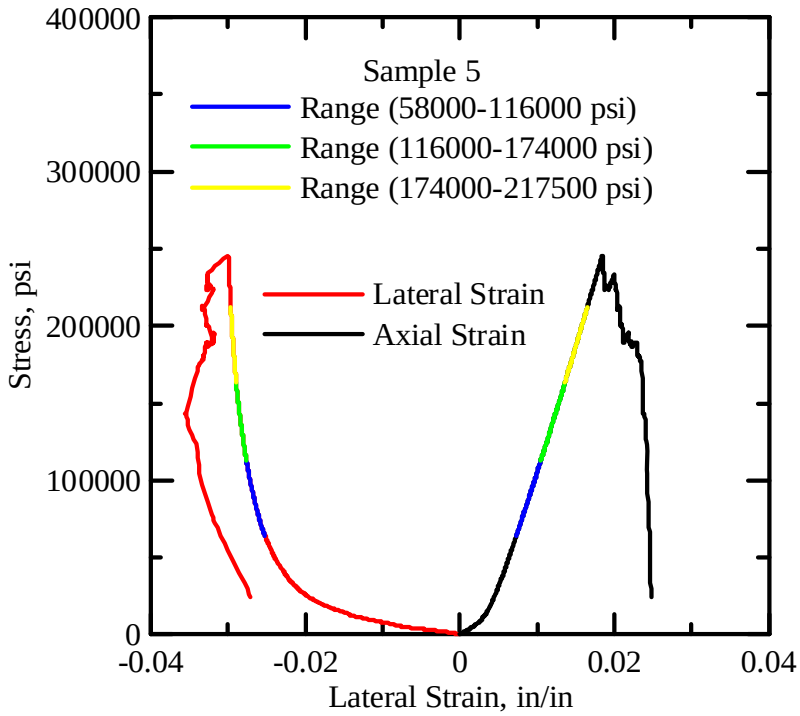

Figure 11. Axial Stress Versus Axial and Lateral Strains for Sample 5 for ν_{21}

The Poisson's ratio ν_{21} was calculated for three different ranges of stresses and the results are summarized in table 5.

Table 5. Poisson's Ratio ν_{21} for the Kevlar 49 Samples

Stress Range (psi)	Poisson's Ratio						
	Sample 1	Sample 2	Sample 3	Sample 4	Sample 5	Average	Std. Dev.
58000-116000	0.828	0.802	0.290	0.350	0.786	0.611	0.267
116000-174000	0.302	0.345	-0.110	0.182	0.391	0.222	0.201
174000-217500	0.211	0.256	-0.261	0.000	0.231	0.087	0.220

Std. Dev. = Standard deviation

2.3.2 Zylon AS-500 Tension Tests.

The results obtained from five tension tests run on Zylon AS-500 for Young's Modulus E_{11} are shown in figure 12 and table 6.

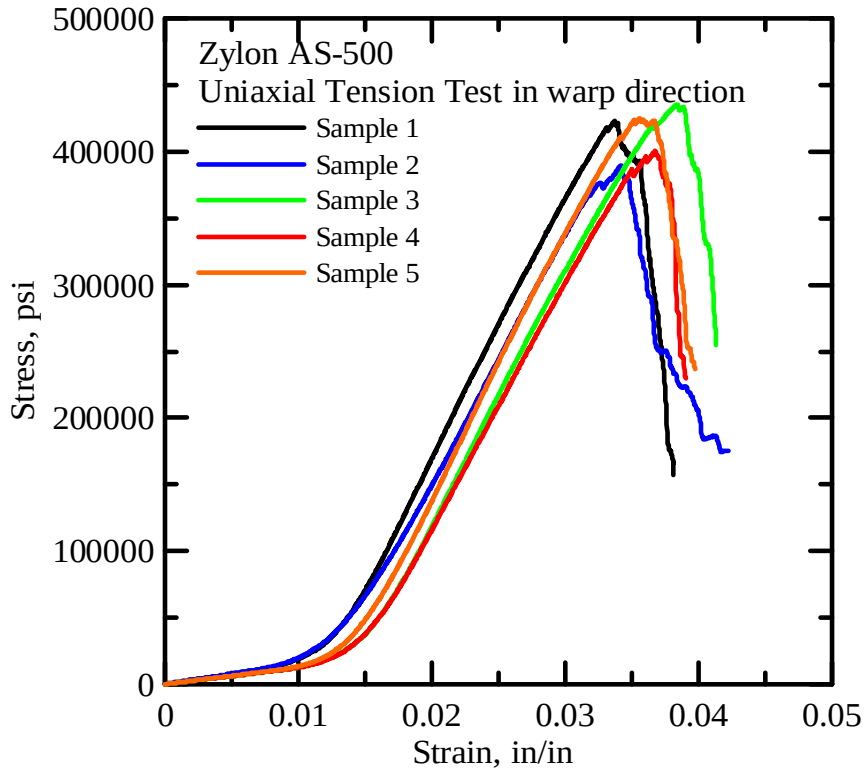

Figure 12. Stress-Strain Curves for the Zylon AS-500 Samples for E_{11}

Table 6. Tension Test Results for Zylon AS-500 Samples for E_{11}

	Sample Replicate No.	Maximum Stress (psi)	Ultimate Strain (in/in)	Toughness (psi)	Stiffness, E (psi)
	1	423095.5	0.0337	6481.5	19667814.5
	2	445701.0	0.0365	6916.5	19924812.5
	3	400591.5	0.0368	5800.0	18608183.5
	4	425256.0	0.0356	6699.0	19212050.5
	5	435261.0	0.0384	6989.0	19110550.5
Average		425981.0	0.04	6583.0	19304676.5
Std. Dev.		16791.0	0.00	478.5	511806.5

Std. Dev. = Standard deviation

The stress-strain response and the stiffness values for Zylon AS-500 (Phase II—Samples 1 through 5) are compared with the results from Phase I (Ztest1, Ztest4, ZSwath1, and ZSwath2) in figure 13 and table 7, respectively.

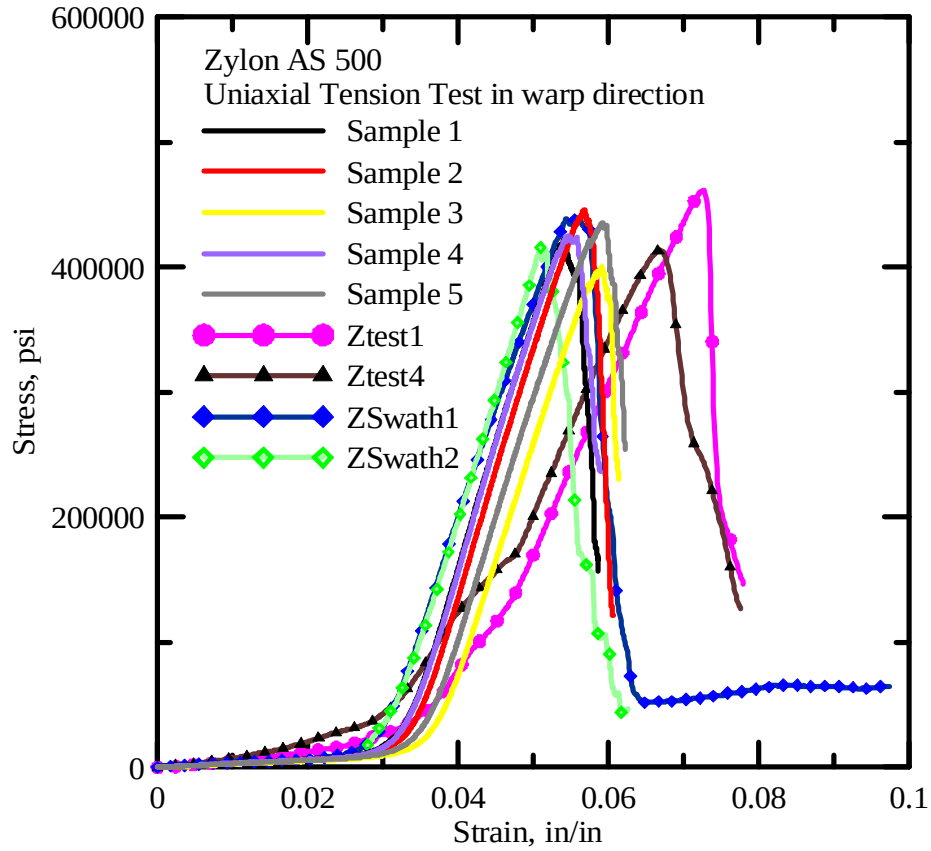

Figure 13. Comparison of Stress-Strain Curves for Zylon AS-500 From Phases I and II

Table 7. Comparison of the Zylon AS-500 Tension Test Results From Phases I and II

Source	Average Value of Stiffness (psi)
Phase I results (all 4 samples)	18552170
Phase II results (all 5 samples)	19304720

The Poisson's ratio ν_{12} for Zylon AS-500 was obtained from the tension tests using the clip gauge system. Figures 14 and 15 show the axial stress versus lateral strain for these samples.

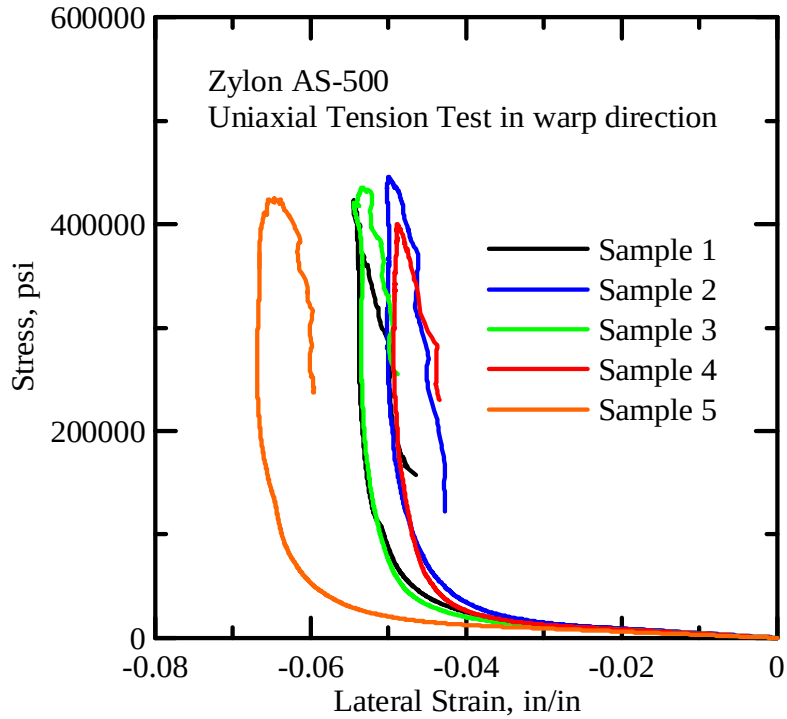

Figure 14. Axial Stress Versus Lateral Strains for Zylon AS-500 Samples for ν_{12}

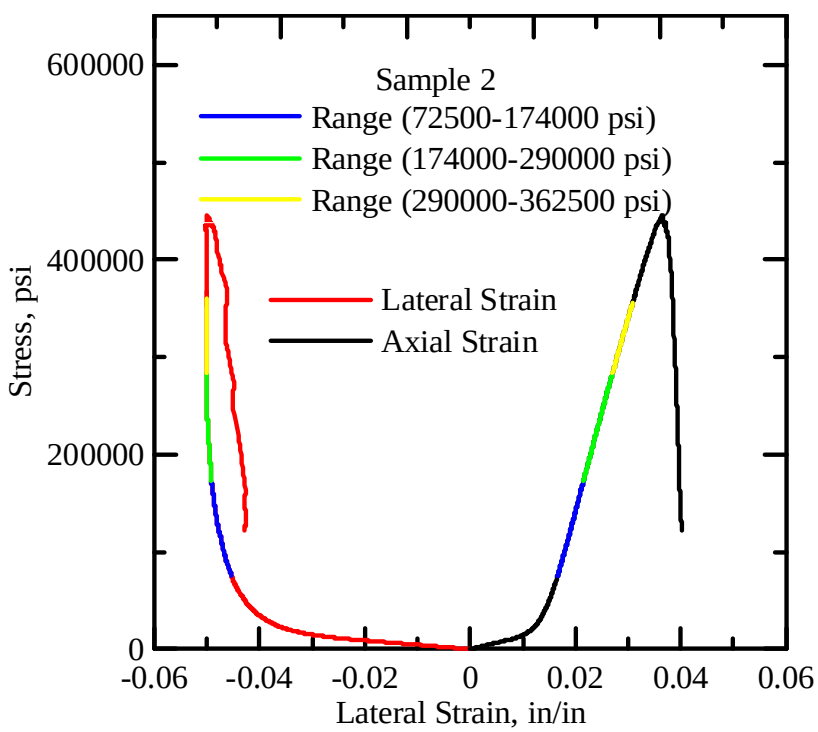

Figure 15. Axial Stress Versus Axial and Lateral Strains for Sample 2 for ν_{12}

The Poisson's ratio ν_{12} was calculated for three different ranges of stresses and the results are summarized in table 8.

Table 8. Poisson's Ratio ν_{12} for the Zylon AS-500 Samples

Stress Range (psi)	Poisson's Ratio						
	Sample 1	Sample 2	Sample 3	Sample 4	Sample 5	Average	Std. Dev.
72500-174000	0.822	0.793	0.486	0.718	0.560	0.676	0.147
174000-290000	0.147	0.186	0.130	0.173	0.122	0.152	0.027
290000-362500	0.033	0.044	0.056	0.070	0.056	0.052	0.014

Std. Dev. = Standard deviation

The results obtained from five tension tests run on Zylon AS-500 for Young's Modulus E_{22} are shown in figure 16 and table 9.

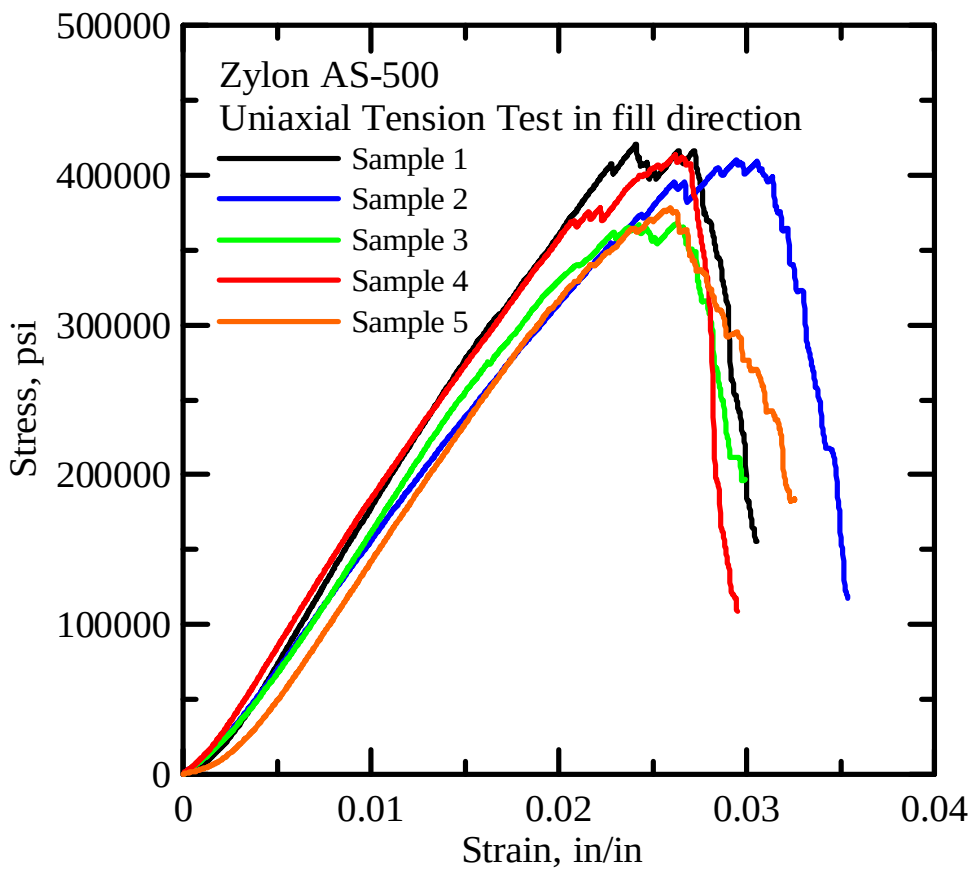

Figure 16. Stress-Strain Curves for Zylon AS-500 Samples for E_{22}

Table 9. Tension Test Results for Zylon AS-500 Samples for E_{22}

	Sample Replicate No.	Maximum Stress (psi)	Maximum Ultimate Strain (in/in)	Toughness (psi)	Stiffness, E (psi)
	1	420587.0	0.0241	7366.0	19725698.5
	2	410205.0	0.0294	8468.0	18906057.0
	3	368300.0	0.0263	6496.0	19169029.0
	4	413801.0	0.0262	6931.0	19712344.0
	5	378044.0	0.0260	6902.0	19269659.0
Average		398184.5	0.0264	7235.5	19356557.5
Std. Dev.		23388.5	0.0019	754.0	356555.0

Std. Dev. = Standard deviation

The Poisson's ratio ν_{21} for Zylon AS-500 was obtained from the tension tests using the clip gauge system. Figures 17 and 18 show the axial stress versus lateral strain for these samples.

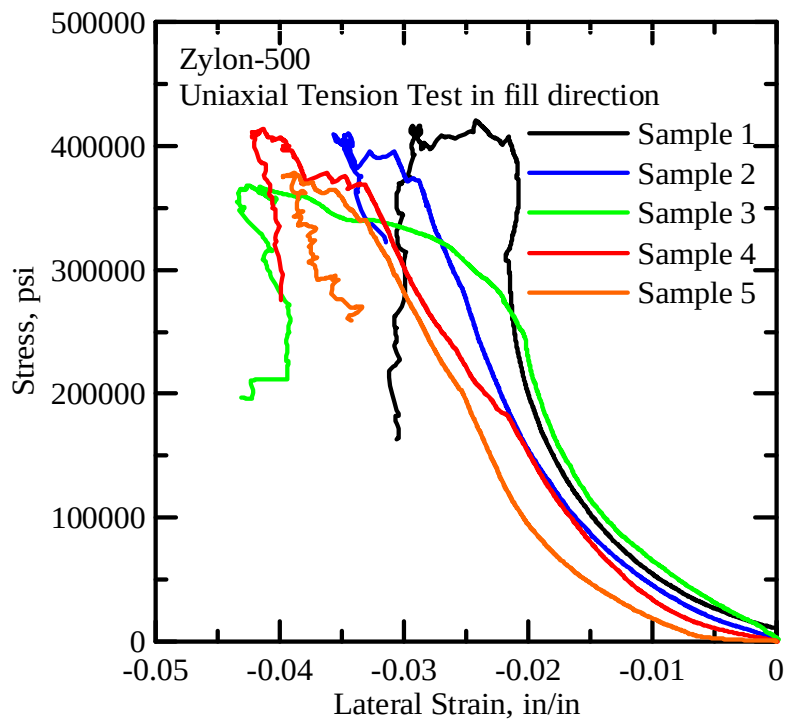

Figure 17. Axial Stress Versus Lateral Strain for Zylon AS-500 Samples for ν_{21}

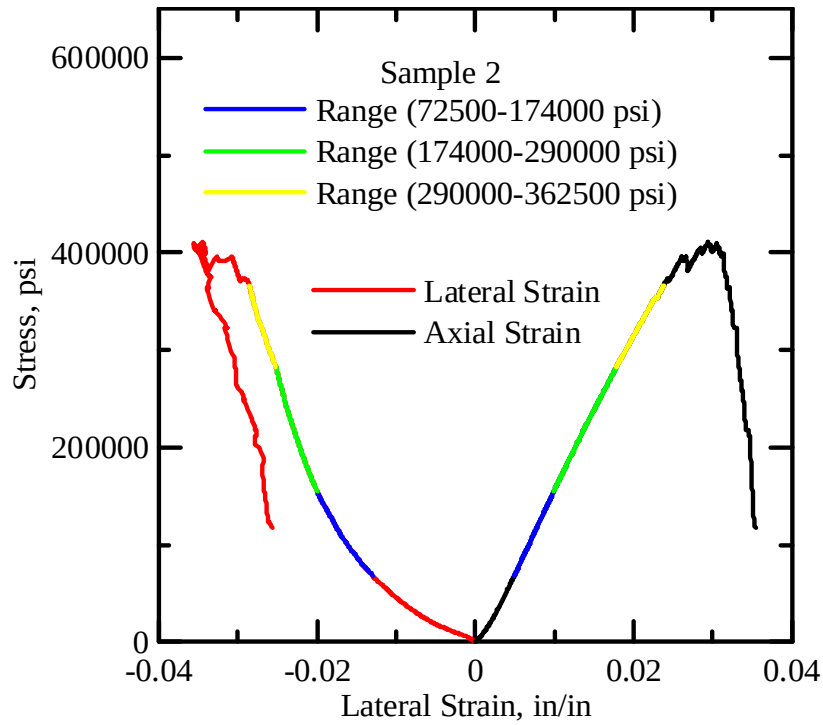

Figure 18. Axial Stress Versus Axial and Lateral Strains for Sample 2 for ν_{21}

The Poisson's ratio ν_{21} was calculated for three different ranges of stresses and the results are summarized in table 10.

Table 10. Poisson's Ratio ν_{21} for the Zylon AS-500 Samples

Stress Range (psi)	Sample 1	Sample 2	Sample 3	Sample 4	Sample 5	Average	Std. Dev.
72500-174000	1.434	1.280	1.295	1.357	1.101	1.293	0.124
174000-290000	0.724	0.613	0.711	0.961	0.801	0.762	0.130
290000-362500	0.482	0.564	1.583	0.785	0.671	0.817	0.443

Std. Dev. = Standard deviation

2.3.3 Zylon AS-1500 Tension Tests.

For Zylon AS-1500, the total cross-sectional area was calculated using the values of the linear and bulk densities of the material. Initially, the cross-sectional area of each yarn was calculated by taking into account the linear density of the yarn (material) and dividing it by its bulk density. The total cross-section of the specimen was defined as the cross-sectional area per yarn multiplied by the number of yarns per inch of fabric, multiplied by the total fabric width. Details are presented in table 11.

Table 11. Specimen Properties for Zylon AS-1500

Material	Yarn Count	Bulk Density (lb/in^3)	Linear Density (lb/in)	Cross-Sectional Area per Yarn (in^2)	Specimen Size (in.)
Zylon AS-1500	17 x 17	0.00567358	$9.13395(10^{-7})$	$1.61(10^{-4})$	2.5 x 10.25

Figure 19 shows the stress-strain response of five Zylon AS-1500 samples for a loading rate of 0.2 inch per minute. Table 12 summarizes the results.

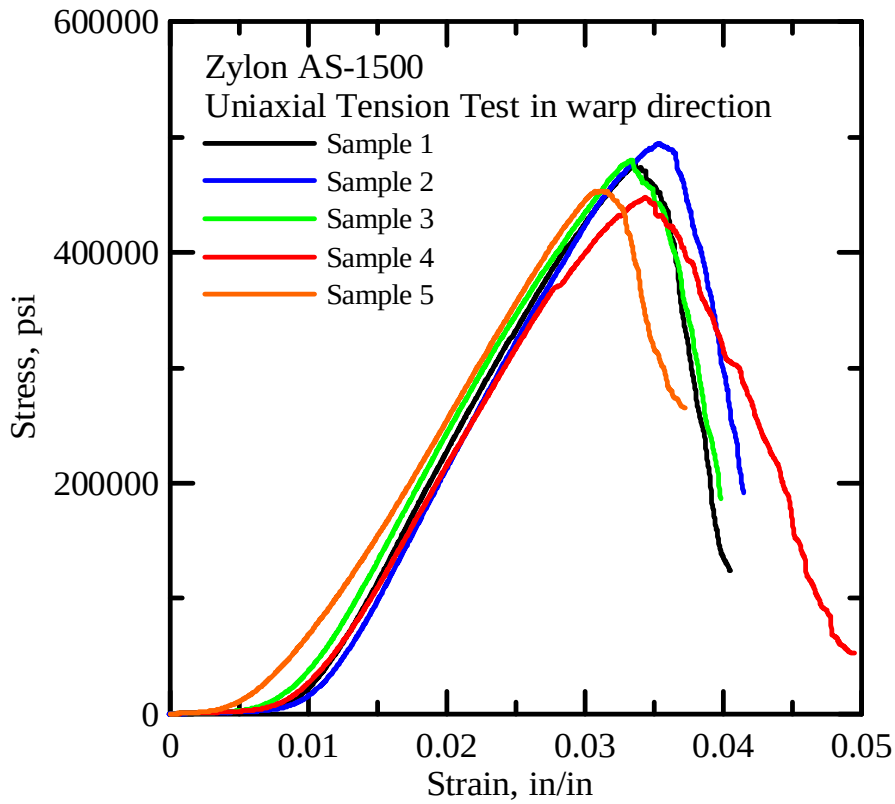

Figure 19. Stress-Strain Curves for the Zylon AS-1500 Samples for E_{11}

Table 12. Tension Test Results for Zylon AS-1500 Samples for E_{11}

	Sample Replicate No.	Maximum Stress (psi)	Ultimate Strain (in/in)	Toughness (psi)	Stiffness, E (psi)
	1	476368.5	0.0336	8453.5	21471962.5
	2	494667.5	0.0354	9091.5	22057110.0
	3	477079.0	0.0334	8801.5	21890128.0
	4	447745.5	0.0343	10106.5	21105968.0
	5	453386.0	0.0312	8018.5	21528889.5
Average		469843.5	0.03	8888.5	21610814.5
Std. Dev.		19169.0	0.00	783.0	373520.0

Std. Dev. = Standard deviation

The Poisson's ratio ν_{21} for Zylon AS-1500 was obtained from the tension tests using the clip gauge system. Figures 20 and 21 show the axial stress versus lateral strain for these samples.

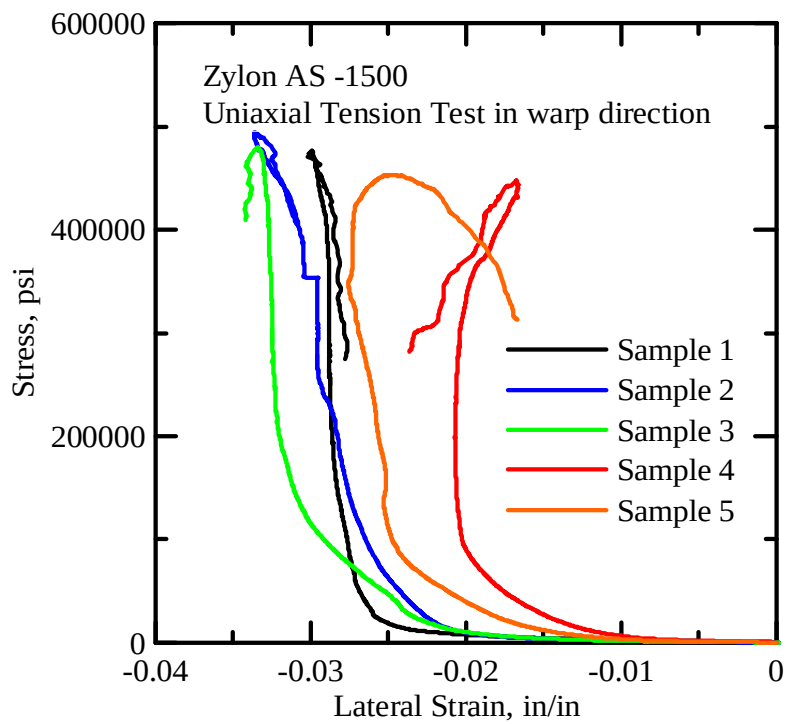

Figure 20. Axial Stress Versus Lateral Strain for Zylon AS-1500 Samples for ν_{12}

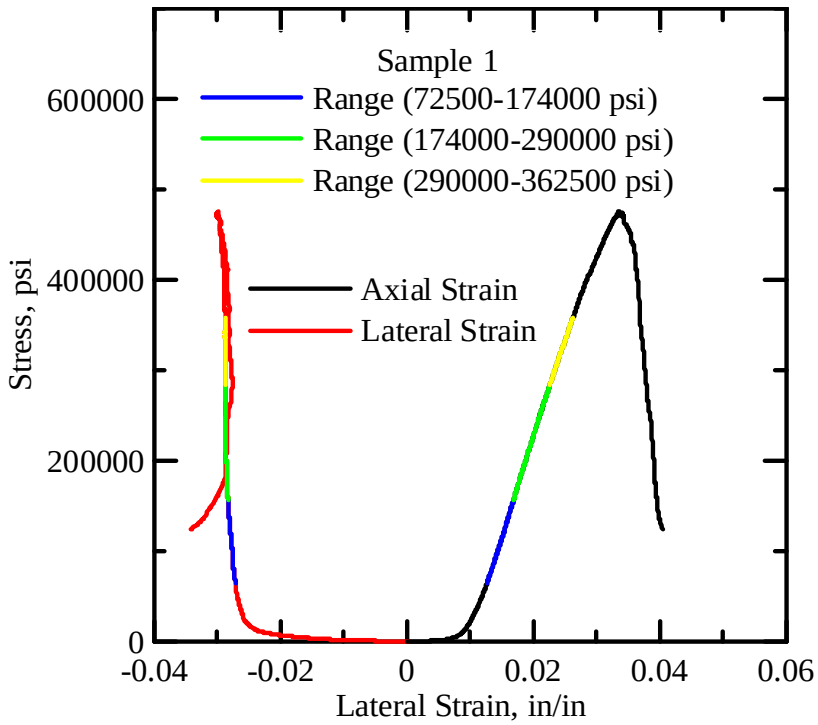

Figure 21. Axial Stress Versus Axial and Lateral Strains for Sample 2 for ν_{12}

The Poisson's ratio ν_{12} was calculated for three different ranges of stresses and the results are summarized in table 13.

Table 13. Poisson's Ratio ν_{12} for the Zylon AS-1500 Samples

Stress Range (psi)	Sample 1	Sample 2	Sample 3	Sample 4	Sample 5	Average	Std. Dev.
72500-174000	0.467	0.552	0.720	0.309	0.469	0.503	0.150
174000-290000	0.261	0.466	0.159	-0.053	0.244	0.215	0.188
290000-362500	0.014	0.384	0.041	-0.280	0.260	0.084	0.255

Std. Dev. = Standard deviation

The results obtained from five tension tests run on Zylon AS-1500 for Young's Modulus E_{22} are shown in the figure 22 and table 14.

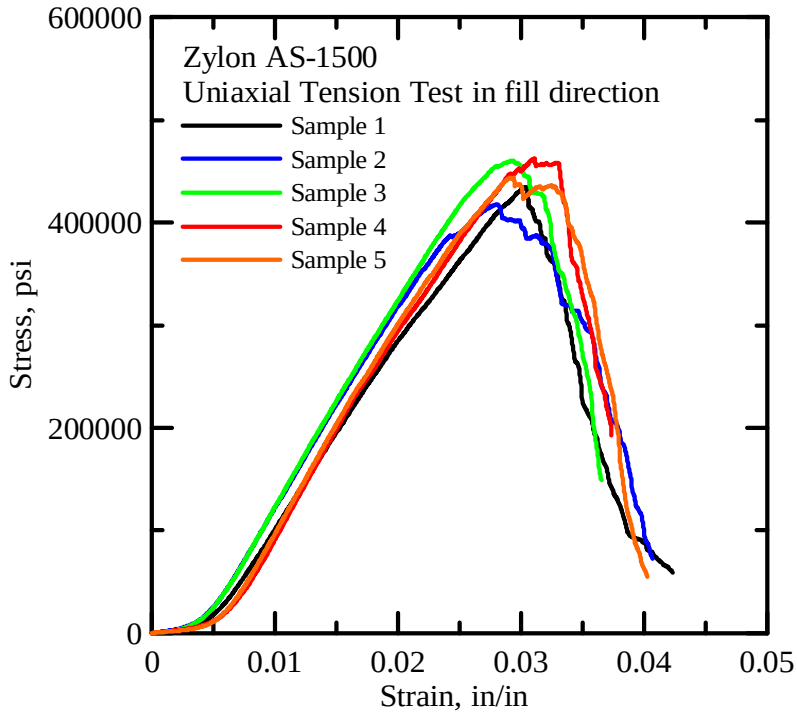

Figure 22. Stress-Strain Curves for Zylon AS-1500 Samples for E_{22}

Table 14. Tension Test Results for the Zylon AS-1500 Samples for E_{22}

	Sample Replicate No.	Maximum Stress (psi)	Ultimate Strain (in/in)	Toughness (psi)	Stiffness, E (psi)
	1	434536.0	0.0303	8526.0	20938797.5
	2	418078.5	0.0281	9309.0	21131053.0
	3	460201.0	0.0293	8961.0	21445500.0
	4	462506.5	0.0311	8772.5	21589412.5
	5	443801.5	0.0291	9280.0	21397534.0
Average		443830.5	0.0296	8975.5	21300456.5
Std. Dev.		18487.5	0.0012	333.5	261464.0

Std. Dev. = Standard deviation

The Poisson's ratio ν_{21} for Zylon AS-1500 was obtained from the tension tests using the clip gauge system. Figures 23 and 24 show the axial stress versus lateral strain for these samples.

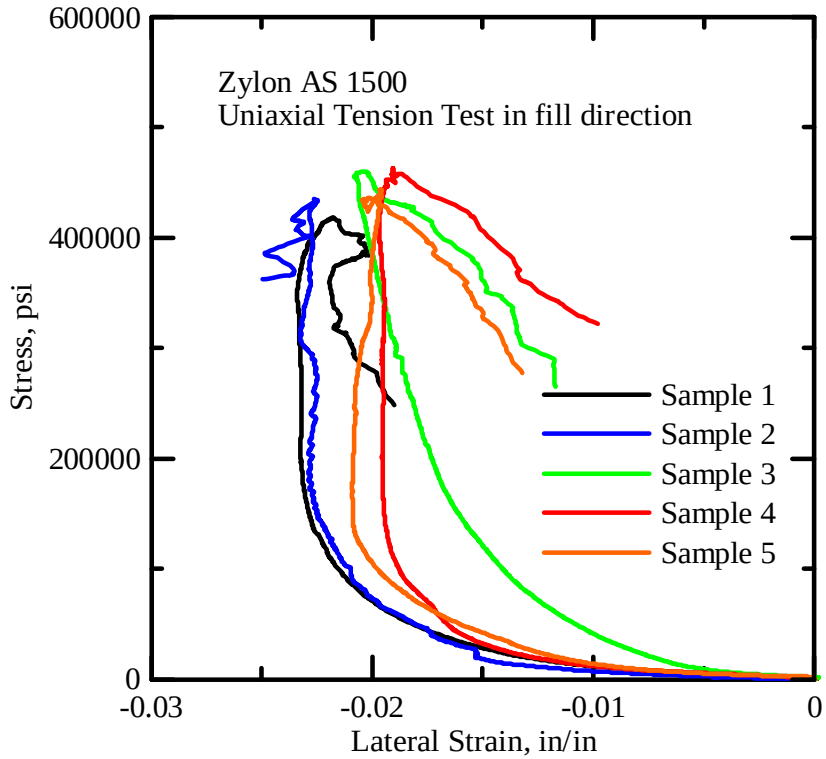

Figure 23. Axial Stress Versus Lateral Strain for Zylon AS-1500 Samples for ν_{21}

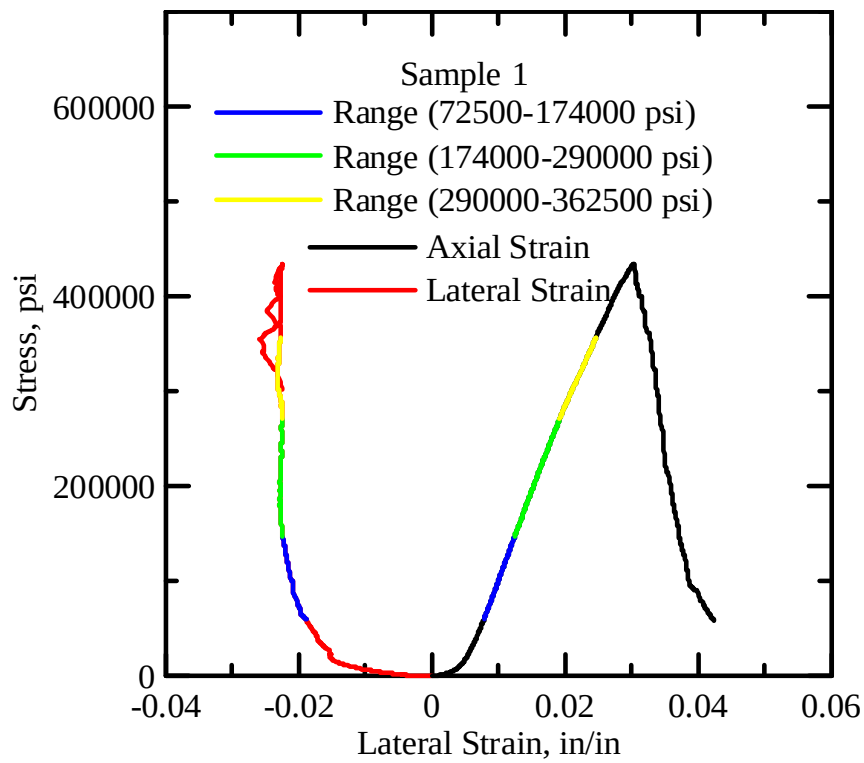

Figure 24. Axial Stress Versus Axial and Lateral Strains for Sample 1 for ν_{21}

The Poisson's ratio ν_{21} was calculated for three different ranges of stresses and the results are summarized in table 15.

Table 15. Poisson's Ratio ν_{21} for the Zylon AS-1500 Samples

Stress Range (psi)	Sample 1	Sample 2	Sample 3	Sample 4	Sample 5	Average	Std. Dev.
72500-174000	0.526	0.539	0.700	0.356	0.501	0.525	0.122
174000-290000	0.095	0.079	0.315	0.090	0.156	0.147	0.098
290000-362500	0.076	0.035	0.231	0.057	0.064	0.093	0.079

Std. Dev. = Standard deviation

2.3.4 Comparison of Fabrics.

A comprehensive graph showing the stress-strain curves for all the fabrics tested in this phase of the research is presented in figure 25.

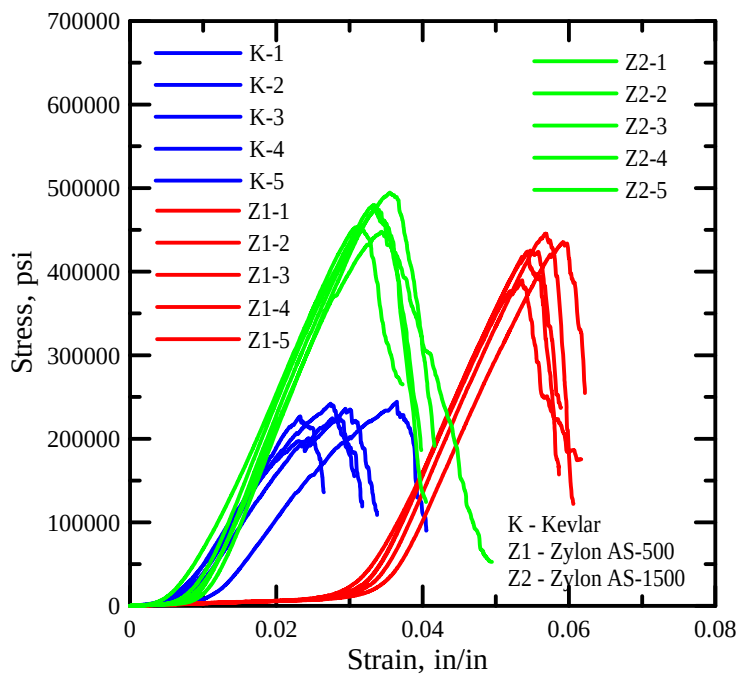

Figure 25. Stress-Strain Curves for all Three Fabrics

3. FRICTION TESTS.

3.1 OVERVIEW.

A series of friction tests were conducted to calculate the coefficients of static and dynamic friction for Kevlar 49, Zylon AS-500, and Zylon AS-1500 fabrics. These tests were conducted on a 55-kips horizontal test frame.

3.2 TEST SETUP AND PROCEDURE.

The test setup is shown in figure 26. For the experiment, a layer of fabric was pulled using a 55-kip horizontal actuator. This fabric layer was sandwiched between another layer of the same fabric that is folded in half around a bolt.

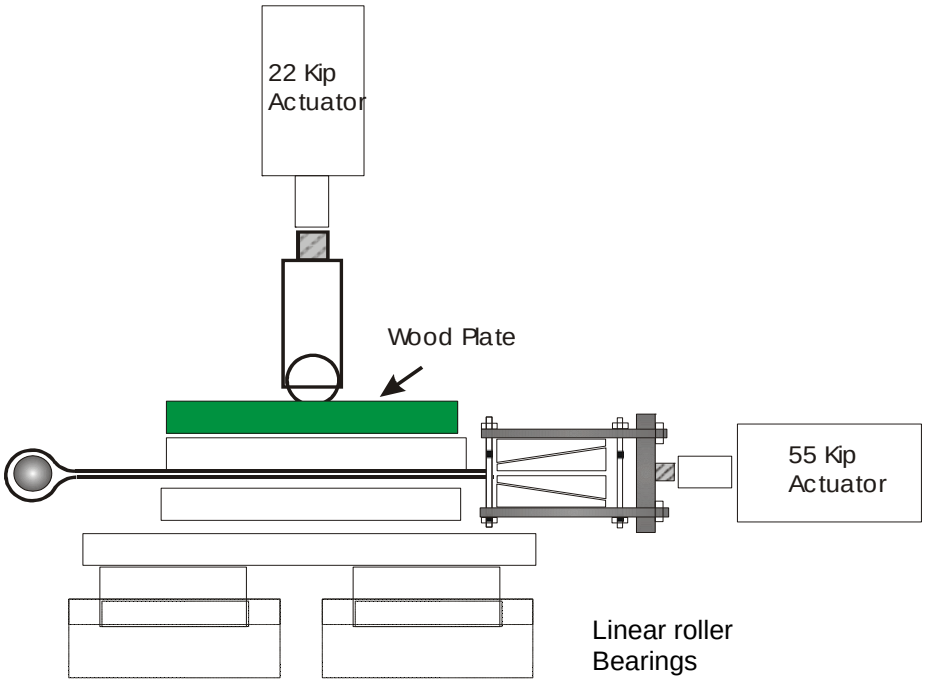

Figure 26. Schematic Setup for Friction Tests

Normal loads were applied on the fabrics so the maximum normal load was 800 pounds for a contact area of 13.75 in^2 (60 psi pressure applied). These normal loads were applied through another vertically mounted actuator on an I-beam resting on two channel sections connected to the four columns, as shown in figure 27. The second layer of fabric was allowed to move using zinc ball-joint rod ends that were fixed to an I-beam. This beam was attached to two column sections, also shown in figure 27.

The coefficient of friction was computed by applying normal loads at loading rates of 2.0 in/min and 6.0 in/min. The coefficient of static friction was computed by plotting the maximum pull for each normal load against the respective normal loads. The coefficient of dynamic friction was computed by plotting the average pull for each normal load against the respective normal loads. A typical output from a friction test is shown in figure 28.

Figure 27. Testing Apparatus

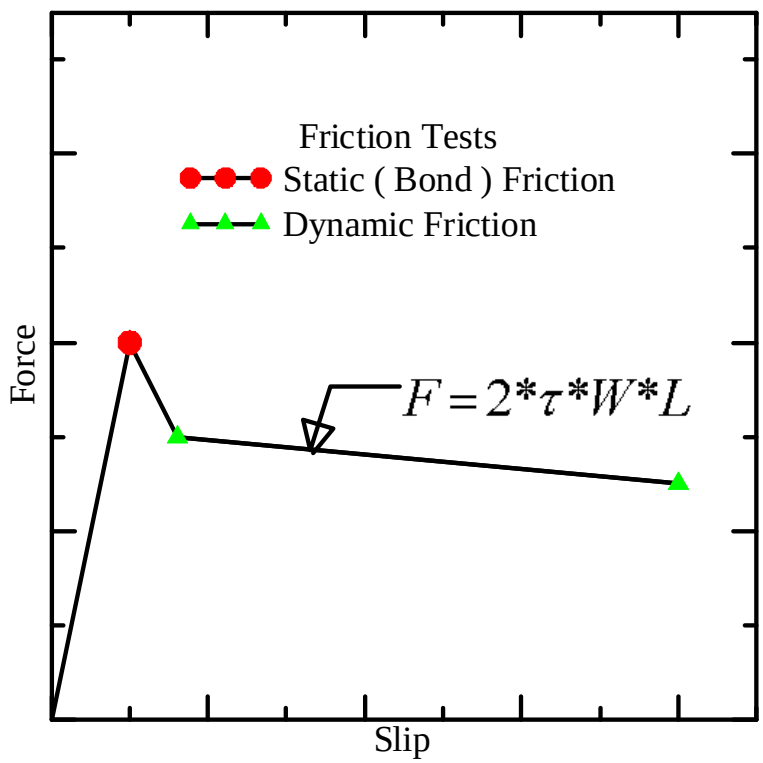

Figure 28. Typical Friction Test Output

3.3 TEST RESULTS.

3.3.1 Kevlar Friction Tests.

The following are the results of the friction tests carried out on Kevlar. Figure 29 shows the force displacement response of ten Kevlar samples.

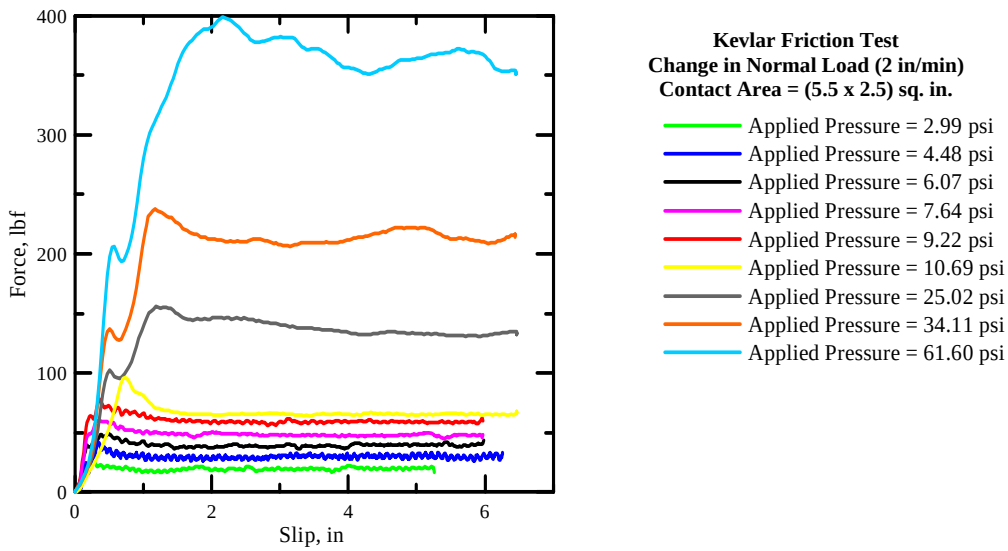

Figure 29. Kevlar Friction Tests for Loading Rate of 2.0 in/min

Figure 30 shows the coefficient of the friction for samples tested with a loading rate of 2.0 in/min.

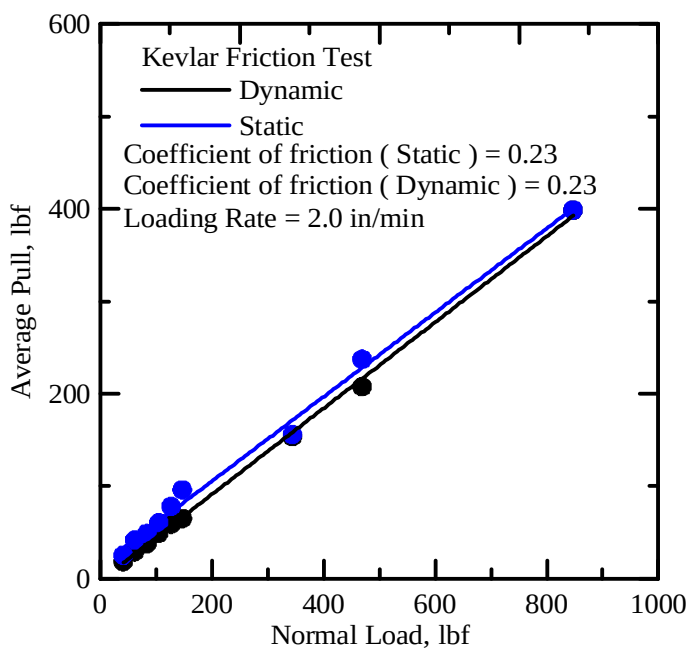

Figure 30. Coefficient of Friction for Kevlar for Loading Rate of 2.0 in/min

Figure 31 shows the results for Kevlar friction test for a loading rate of 6.0 in/min.

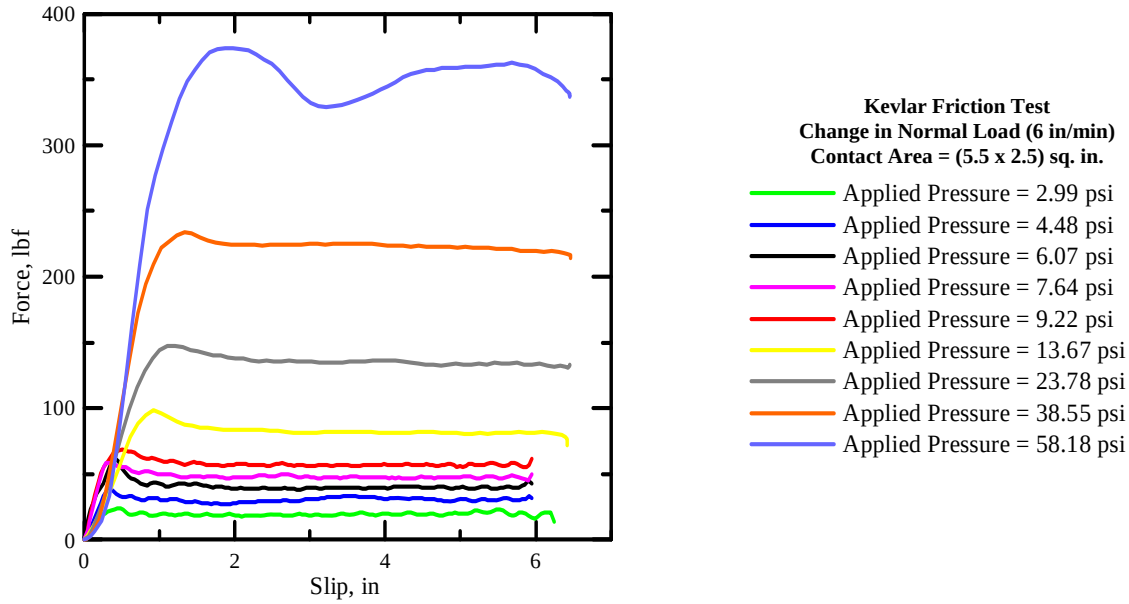

Figure 31. Kevlar Friction Tests for Loading Rate of 6.0 in/min

The coefficients of friction for a loading rate of 6.0 in/min are plotted in figure 32.

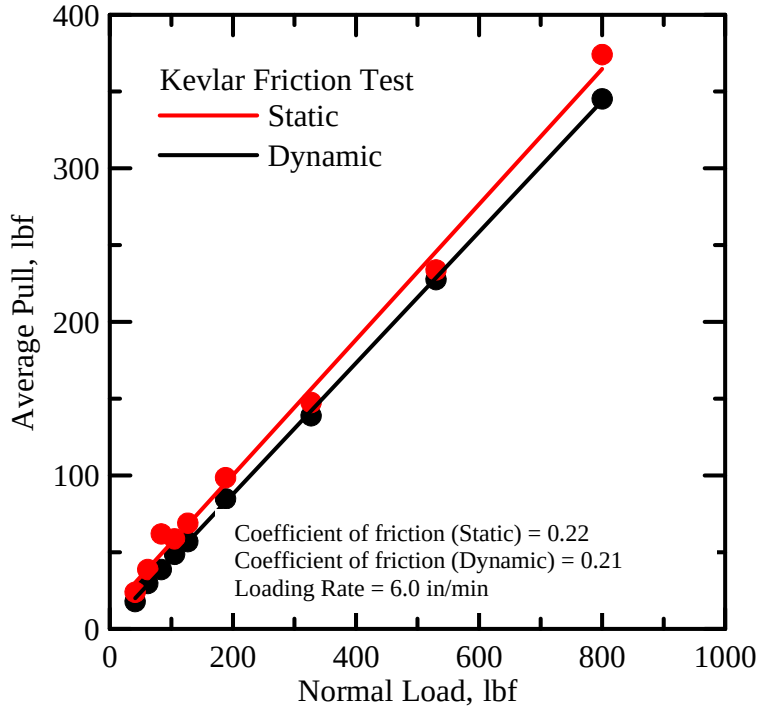

Figure 32. Coefficient of Friction for Kevlar for Loading Rate of 6.0 in/min

Figures 33 and 34 show the comparison of the static and dynamic coefficients of friction obtained through the Kevlar friction tests for the two different loading rates.

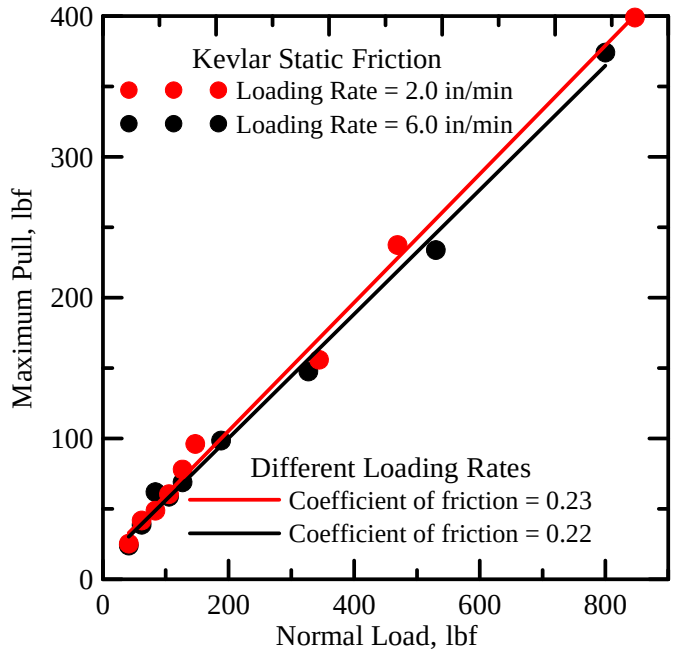

Figure 33. Coefficient of Static Friction for Kevlar

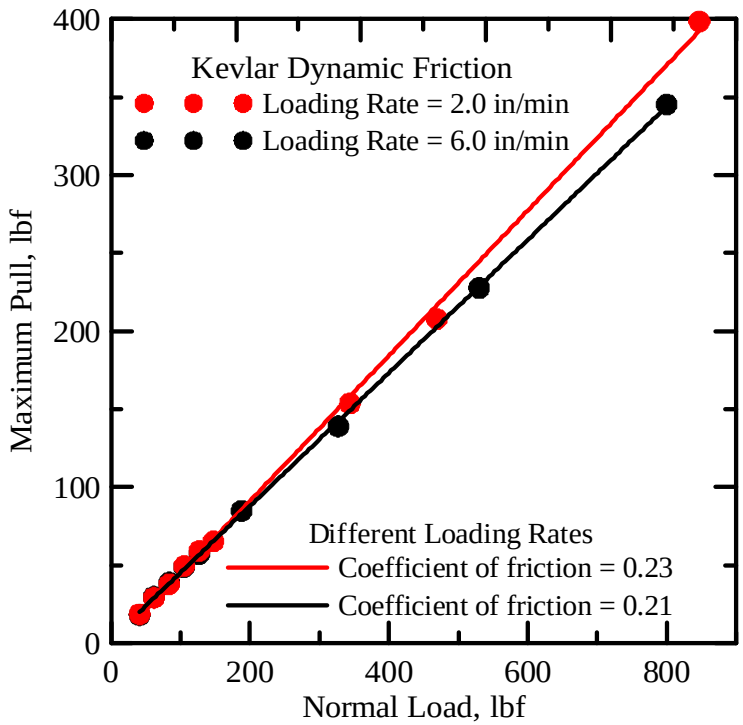

Figure 34. Coefficient of Dynamic Friction for Kevlar

Table 16 shows the coefficients of friction for the different loading rates.

Table 16. Comparison of Friction Coefficients for Kevlar

Loading Rate (in/min)	Coefficient of Static Friction	Coefficient of Dynamic Friction
2.0	0.233	0.228
6.0	0.221	0.213

3.3.2 Zylon AS-500 Friction Tests.

The following are the results of the friction tests carried out on Zylon AS-500. Figure 35 shows the force displacement response of ten Zylon samples.

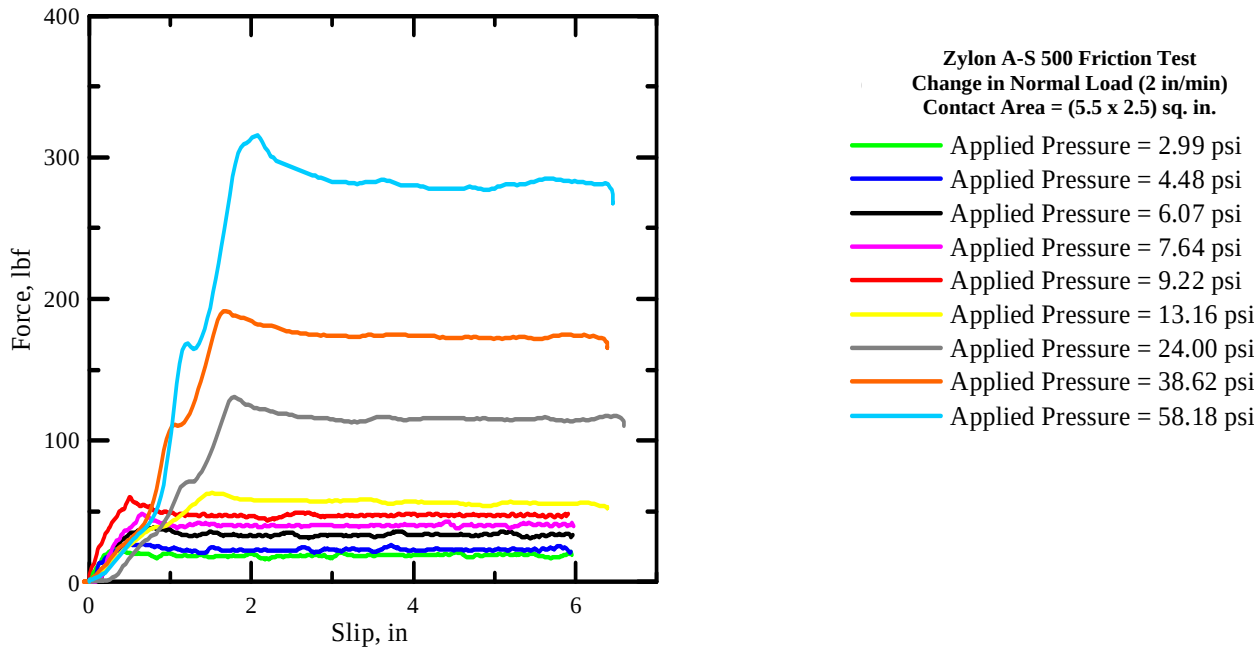

Figure 35. Zylon AS-500 Friction Tests for Loading Rate of 2.0 in/min

Figure 36 shows the coefficient of the friction for Zylon tested with a loading rate of 2.0 in/min.

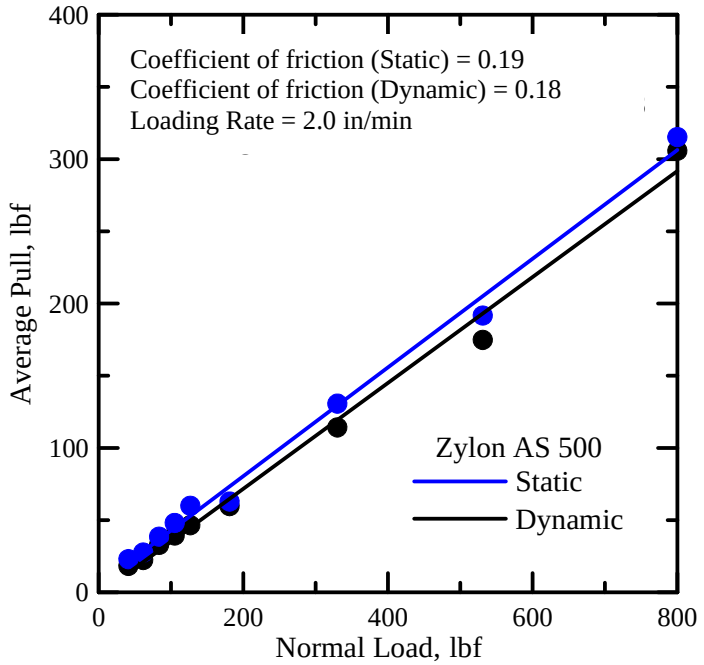

Figure 36. Coefficient of Friction for Zylon AS-500 for Loading Rate of 2.0 in/min

Figure 37 shows the results for Zylon friction test for a loading rate of 6.0 in/min.

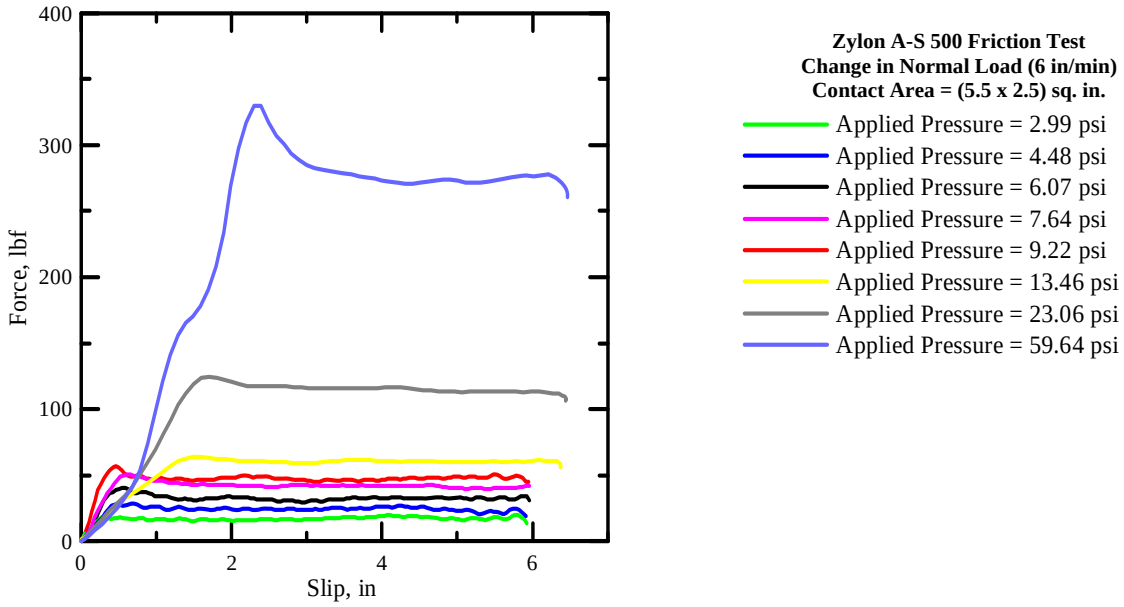

Figure 37. Zylon AS-500 Friction Tests for Loading Rate of 6.0 in/min

The coefficients of friction for a loading rate of 6.0 in/min are plotted in figure 38.

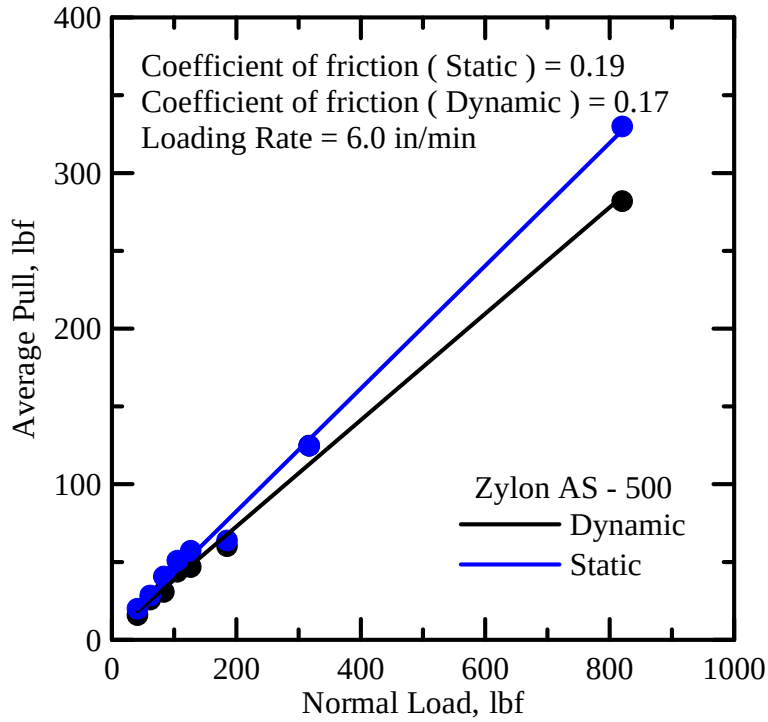

Figure 38. Coefficient of Friction for Zylon AS-500 for Loading Rate of 6.0 in/min

Figures 39 and 40 show the comparison of the static and dynamic coefficient of friction obtained through the Zylon friction tests for the two different loading rates.

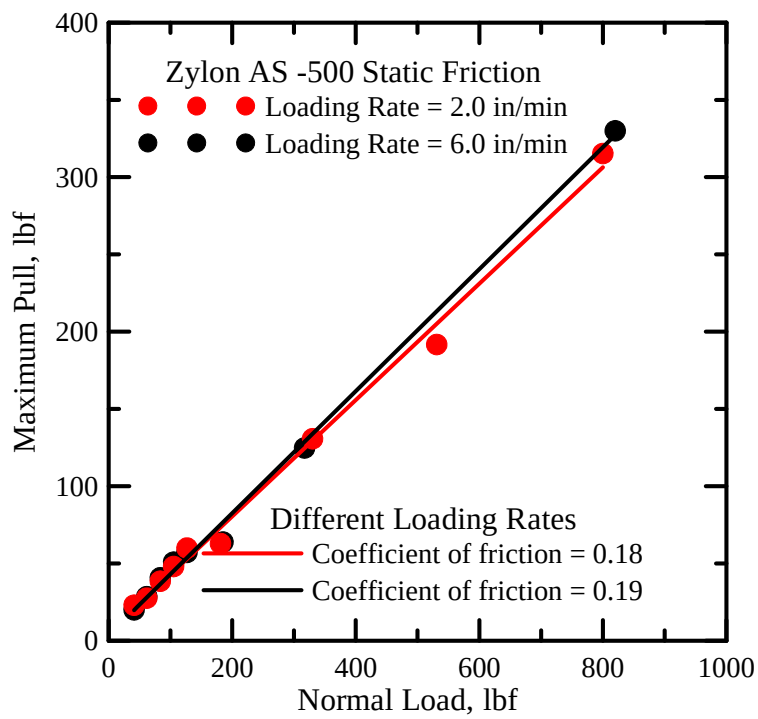

Figure 39. Coefficient of Static Friction for Zylon AS-500

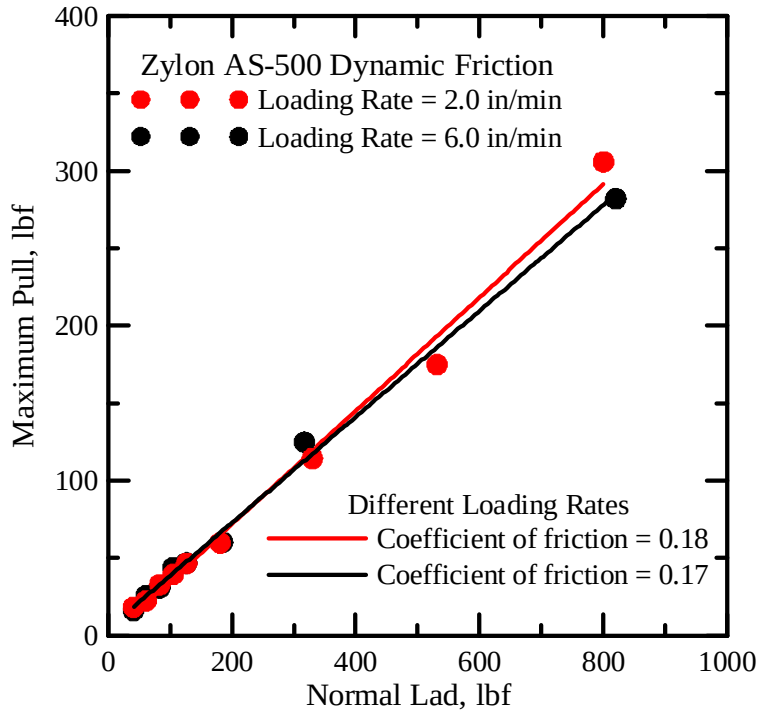

Figure 40. Coefficient of Dynamic Friction for Zylon AS-500

Table 17 shows the coefficients of friction for the different loading rates.

Table 17. Comparison of Friction Coefficients for Zylon AS-500

Loading Rate (in/min)	Coefficient of Static Friction	Coefficient of Dynamic Friction
2.0	0.188	0.183
6.0	0.194	0.171

3.3.3 Zylon AS-1500 Friction Tests.

The following are the results of the friction tests carried out on Zylon AS-1500. Figure 41 shows the force displacement response of five Zylon samples.

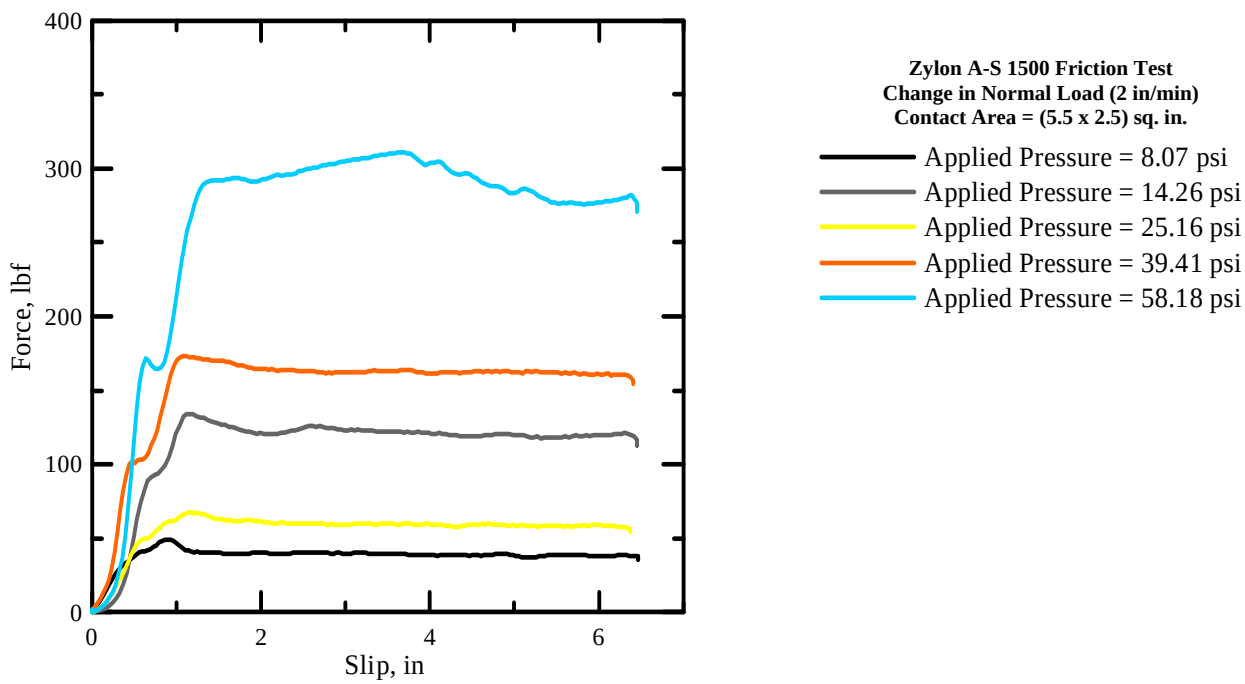

Figure 41. Zylon AS-1500 Friction Tests for Loading Rate of 2.0 in/min

Figure 42 shows the coefficient of the friction for Zylon tested with a loading rate of 2.0 in/min.

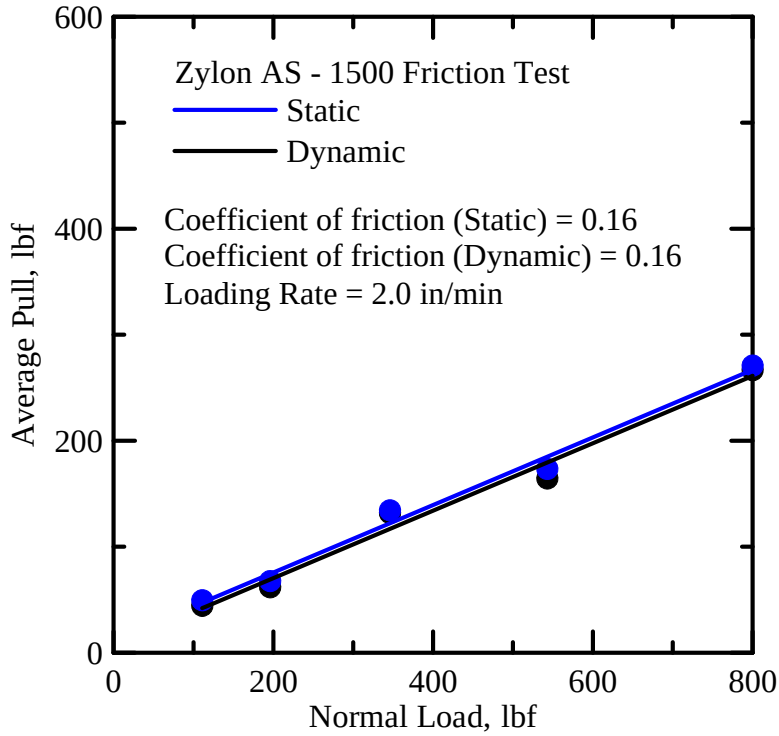

Figure 42. Coefficient of Friction for Zylon AS-1500 for Loading Rate of 2.0 in/min

Figure 43 shows the results for Zylon Friction Test for a loading rate of 6.0 in/min.

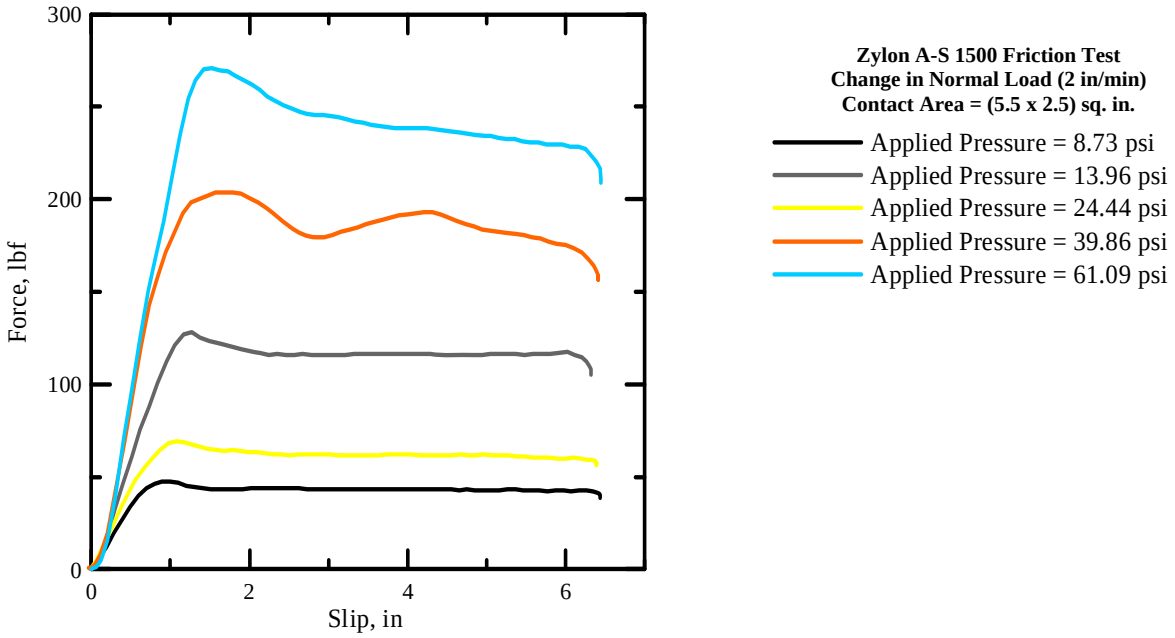

Figure 43. Zylon AS-1500 Friction Tests for Loading Rate of 6.0 in/min

The coefficients of friction for a loading rate of 6.0 in/min are plotted in figure 44.

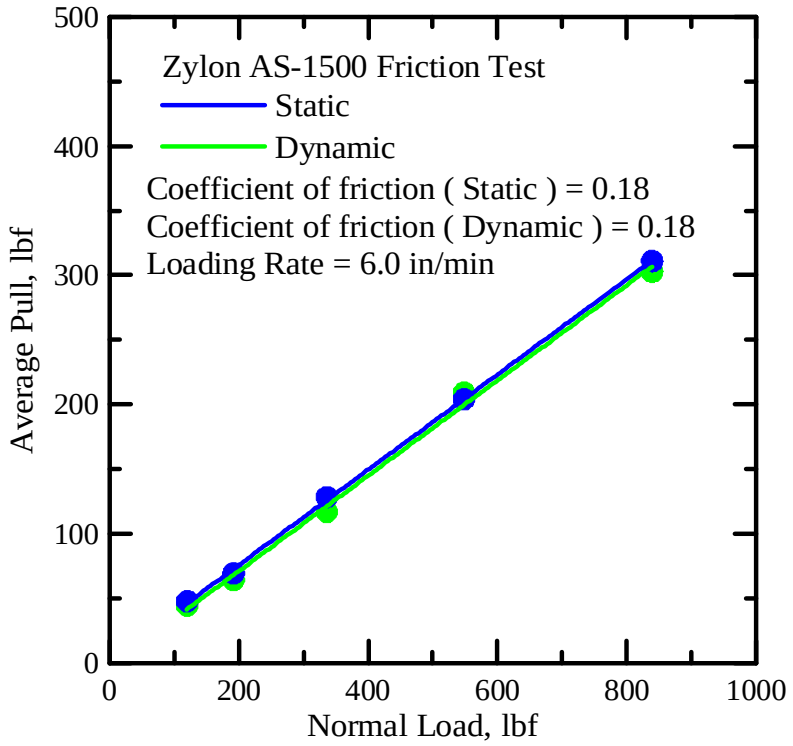

Figure 44. Coefficient for Zylon AS-1500 for Loading Rate of 6.0 in/min

Figures 45 and 46 show the comparison of the static and dynamic coefficient of friction obtained through the Zylon friction tests for the two different loading rates.

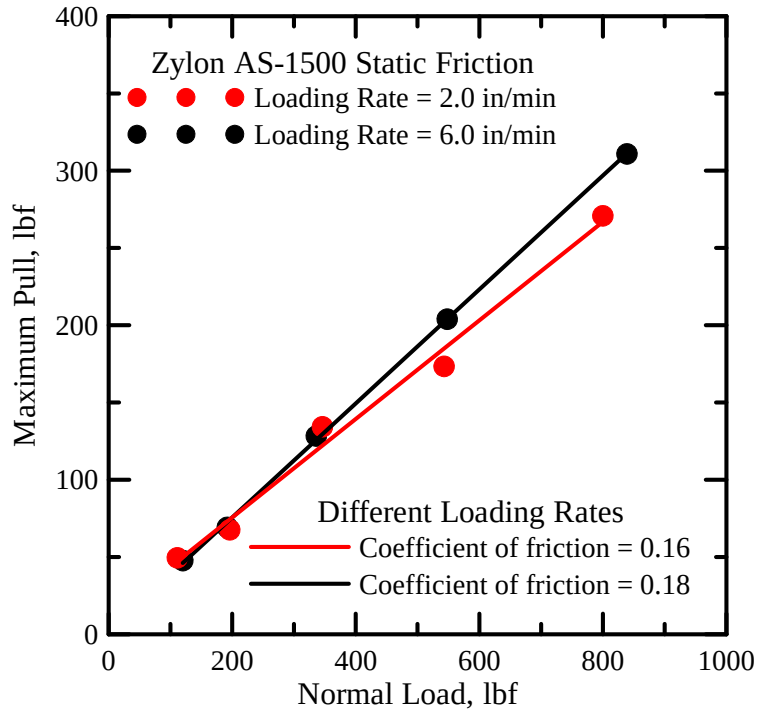

Figure 45. Coefficient for Static Friction for Zylon AS-1500

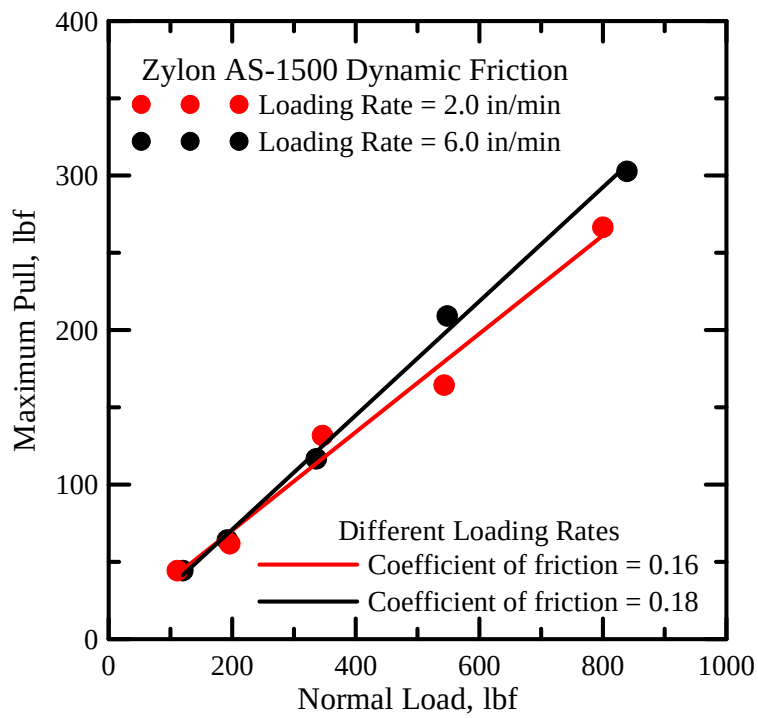

Figure 46. Coefficient for Dynamic Friction for Zylon AS-1500

Table 18 shows the coefficients of friction for the different loading rates.

Table 18. Comparison of Friction Coefficients for Zylon AS-1500

Loading Rate (in/min)	Coefficient of Static Friction	Coefficient of Dynamic Friction
2.0	0.159	0.159
6.0	0.184	0.184

4. STATIC RING TESTS.

4.1 OVERVIEW.

A series of quasi-static ring tests were conducted on fabric obtained for this phase of the research. These tests were conducted in a 55-kips servo-hydraulic test frame operated under closed-loop conditions. The primary objective of the static tests was to simulate penetration of the blunt object through the engine containment system assembly. A steel cylinder was used to simulate the engine housing, and the composite fabric was wrapped around this cylinder. The tests were conducted by applying the load in a quasi-static manner until failure, defined as full penetration of the blunt nose through the single or multilayer fabric. The load and deformation history were collected throughout the test and energy absorption capacity of the structure was calculated from this response. This test may ultimately be used as one of the key parameters in the determination of properties and the containment chamber design. A total of 21 tests were conducted during this period on both Kevlar 49 and Zylon AS-500.

4.2 TEST SETUP AND PROCEDURE.

4.2.1 Specimen Preparation Procedure.

The proposed test plan required the determination of the load-deformation response of single and multilayer specimens for both Kevlar and Zylon wraps. The specimens were subjected to outward penetration motion of a blunt-nose assembly at various orientations and positions of the two different blunt noses. The blunt-nose assembly was initially set up inside the steel ring. The specimens were 32″ in diameter and 4″ wide and consisted of one, four, and eight layers wrapped around the outside of the steel cylinder. A small window was machined in the ring to allow for the penetration of the blunt nose.

For the single-layer specimens, a 6″ length of fabric overlap was used to glue the fabric onto itself. For multilayer fabrics, the first layer was mounted directly onto the ring and temporarily fixed by means of a standard cello tape. The last layer was glued to the previous layer using 5-minute® epoxy. Overlap length for all specimens was 6″. The specimens were covered with opaque plastic sheeting to minimize the degrading effects of moisture and ultraviolet light.

4.2.2 Test Setup.

A test fixture was manufactured by rolling a section of A36 mild steel to the inner diameter of the test setup. The ring dimensions are outer diameter (OD) of 32″, inner diameter (ID) of 30″,

width of 6″, and a thickness of 1″. This ring was the main component of the loading fixture and was fabricated at Karlson Machine Works, Inc., Phoenix, AZ. The complete loading fixture was made up of four major parts. The ring was assembled in two parts—as one large and one small arc. The other components include the two side support plates and an end plate to connect the two ring components. The small arc that was cut from the ring was connected to the bottom of the ring assembly and did not alter the geometry of the test setup. The size of the small arc corresponded to a 38° angle. Use of the ring as two parts allowed for easy installation of the specimen in the loading fixture. The cylinder was attached to two side plates using fifteen 3/4″ diameter high-strength bolts connected along the ring's perimeter. These side plates were connected to the base plate; hence, the ring had a clearance of 3″ from the base plate.

Two different blunt noses were used as the penetrators for the tests in this phase. The dimensions of steel noses are shown in table 19. The terms thicker penetrator and penetrator A, and thinner penetrator and penetrator B are used interchangeably. Also, the terms blunt nose and penetrator are used interchangeably. The static test penetrators corresponded to the same impact cross-sections as the penetrators used in the NASA ballistic impact tests. Part 2 of this report contains photos of the penetrators used in the NASA tests.

Table 19. Dimensions of the Various Blunt Noses

Type of Blunt Nose	Width (in.)	Thickness (in.)	Radius (in.)
Thicker Penetrator (Penetrator A)	2	5/16	5/32
Thinner Penetrator (Penetrator B)	1.5	0.2370	0.1185

To avoid transferring the entire load to the end joint, C-clamps were used at points remote from the blunt head contact. The tests were conducted with the clamps in place for both Kevlar and Zylon specimens. These clamps were placed at the same height on both sides of the ring to maintain symmetry and uniformity—clamps were placed at the height of 13.75″ from the top of the base plate or at the height of 10.75″ from the bottom of the cylinder OD. For testing the fabrics for the off-center orientation, a new set of base blocks was designed. These base blocks, when fixed onto the base plate, align the edge of the penetrator at a distance of 0.15" from the edge of the machined window.

To avoid side loads, which cause tilting of the blunt nose, the fixed-fixed condition for the blunt-nose assembly used in Phase I was used for all eight tests conducted.

4.2.3 Test Procedure.

Each sample was directly mounted onto the test rig and the side plates were attached. An MTS servo-hydraulic test machine with Digital Teststar2 controller software was used for all specimens. All tests were conducted under actuator control using a constant rate of travel of 0.4 in/min. All tests were conducted such that the load cell housing the penetrator remained stationary throughout the test, while the actuator and ring moved downward, thus, loading the

fabric against a stationary penetrator. The data were collected using a digital data acquisition system at a rate of 2 samples per second. For certain specimens, the test was run in a single step and continued until failure occurred. For Zylon, specimens tests were performed in two steps. Since the maximum actuator travel length was limited to 4″, a readjustment of the position of the sample was necessary to extend the total displacement beyond the 4″ expected in the multilayer and Zylon tests. During the first stage, the sample was loaded to 250 lb and the test was placed on hold. At this point the actuator was brought back to the zero position, while the crosshead was moved up to maintain the preload of the sample at the 250 lb. At this point, the test was resumed, and displacement was imposed until specimen failure. The adjustment of the crosshead was necessary to ensure enough travel was available for the sample to fail without causing any impact on the quality of the data obtained.

4.3 TEST RESULTS.

The data obtained from the test machine were used to generate the load-deflection curve for the various specimens tested on the static ring apparatus.

4.3.1 Kevlar Results.

Figures 47 and 48 show the typical load-defection curve obtained for a Kevlar sample tested at a 45-degree orientation using both the thicker and thinner penetrators.

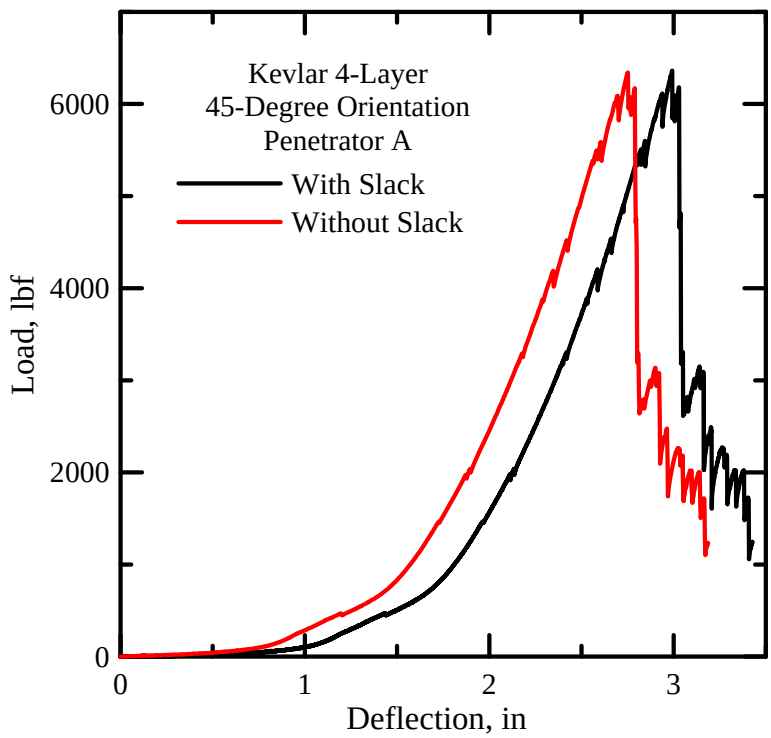

Figure 47. Load-Deformation Response of Four-Layer Kevlar Specimen With and Without Slack Adjustment Using Penetrator A

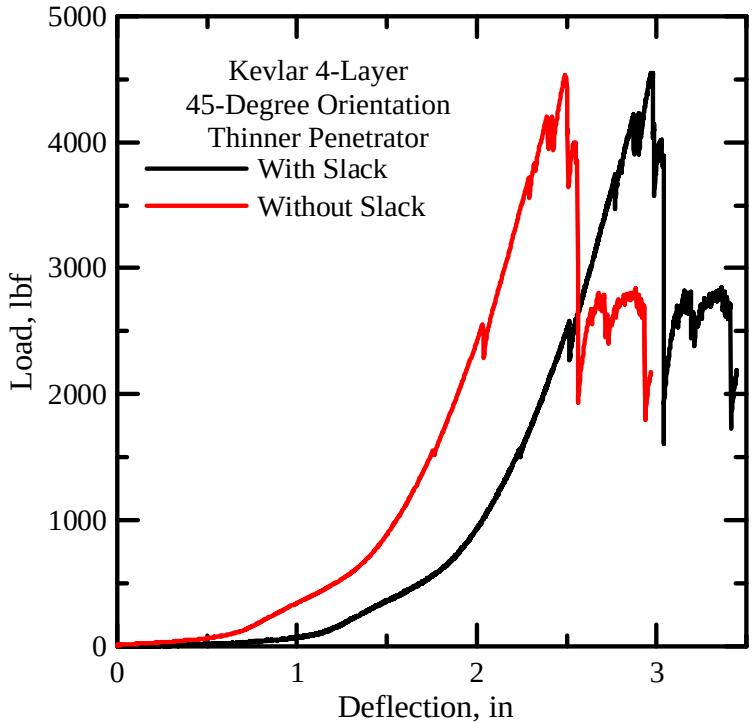

Figure 48. Load-Deformation Response of Four-Layer Kevlar Specimen With and Without Slack Adjustment Using Penetrator B

The slack removal in the figures was achieved by shifting the raw data load-deflection curves along the x-axis so that the curve obtained would coincide with initial portion of the load-deflection curve. The load-deflection curves were obtained from FEA models prepared for various orientations of the blunt nose. For the particular specimens shown in figures 47 and 48, the slack adjustment was 0.239″ and 0.479″, respectively.

Figures 49 and 50 show the load-deflection curves for one-, four-, and eight-layer Kevlar specimens with 45° orientation for both types of penetrators.

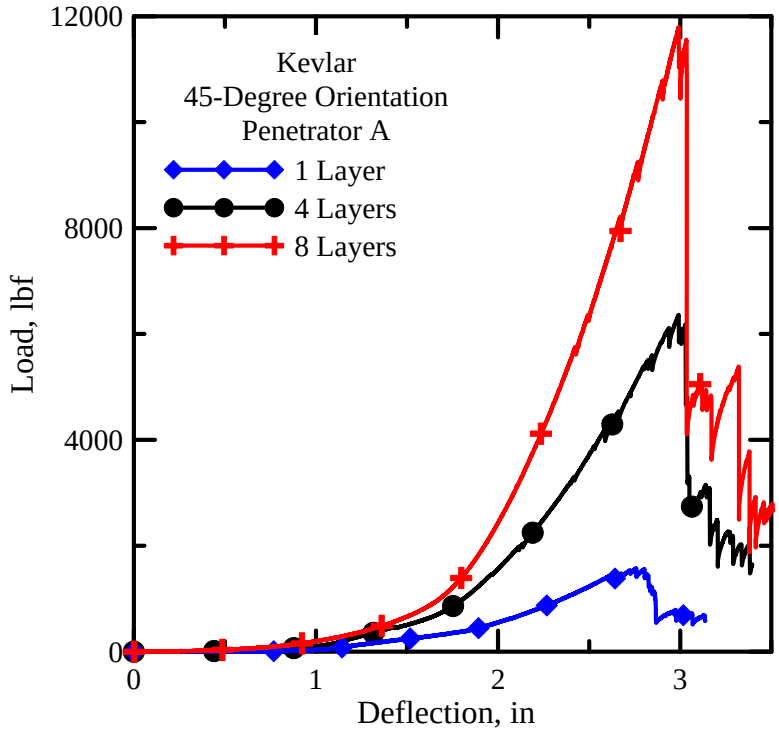

Figure 49. Load-Deflection Response of Kevlar for Same Orientation of Thicker Blunt Nose for Multilayer Specimens

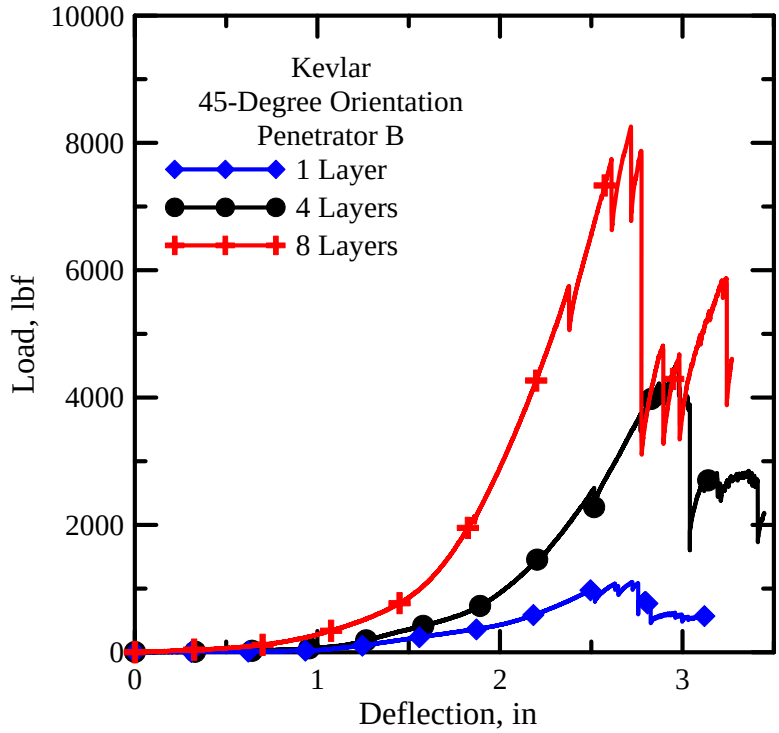

Figure 50. Load-Deflection Response of Kevlar for Same Orientation of Thinner Blunt Nose for Multilayer Specimens

The peak loads with 45-degree orientation and the thicker blunt nose were 1573, 6363, and 11796 lb for the one-, four-, and eight-layer Kevlar tests, respectively. The peak loads with the thinner penetrator were 1104, 4552, and 8257 lb for the one-, four-, and eight-layer Kevlar tests, respectively. These peak loads seem to scale proportionally, according to the number of layers of the Kevlar fabric tested.

Figure 51 shows the load-deflection response of one-layer Kevlar fabric for different orientations of the thicker blunt nose.

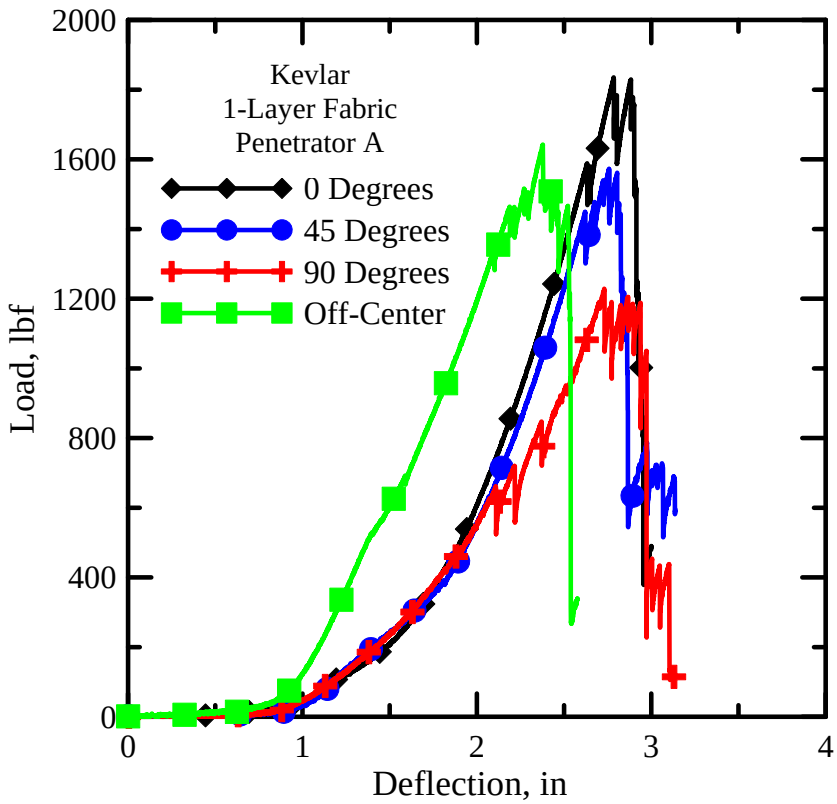

Figure 51. Load Deflection for Various Orientations of Thicker Blunt Nose With One-Layer Kevlar

Examination of figure 51 indicates that maximum loads at failure differed for various orientations of the blunt-nose penetrator for the same number of layers. The maximum load occurred with the 0-degree orientation of the blunt nose and the minimum load occurred with the 90-degree orientation of the blunt nose. The figure also shows that the stiffness of Kevlar (lb/in) remained fairly constant until the fracture of the first yarn. There was a drop in stiffness from the 0-degree to the 45-degree orientation of the blunt nose. The 90-degree orientation had the least stiffness. Similar responses were obtained for four- and eight-layer fabric samples for Kevlar. Table 20 shows the stiffness values for multilayered Kevlar specimens for various orientations of the thicker penetrator. The maximum load for the off-center orientation of the blunt nose was closer to the maximum load of the 45-degree orientation test with deviations of 69, 161, and 829 lb for one-, four-, and eight-layers, respectively. The stiffness for the off-center orientation was between the 45-degree and the 90-degree orientation stiffness.

Table 20. Values of Maximum Load and Stiffness for Kevlar Using the Thicker Penetrator

Layers	Orientation	Maximum Load (lb)	Stiffness (lb/in)
1	0	1858	1715
1	45	1573	1418
1	90	1228	1080
1	Off	1642	1307
4	0	6625	5909
4	45	6363	5271
4	90	4925	4790
4	Off	6202	5079
8	0	13231	11025
8	45	11796	10618
8	90	9110	8340
8	Off	10967	9770

The response for the four- and eight-layer Kevlar tests using the thicker penetrator are plotted in figures 52 and 53, respectively.

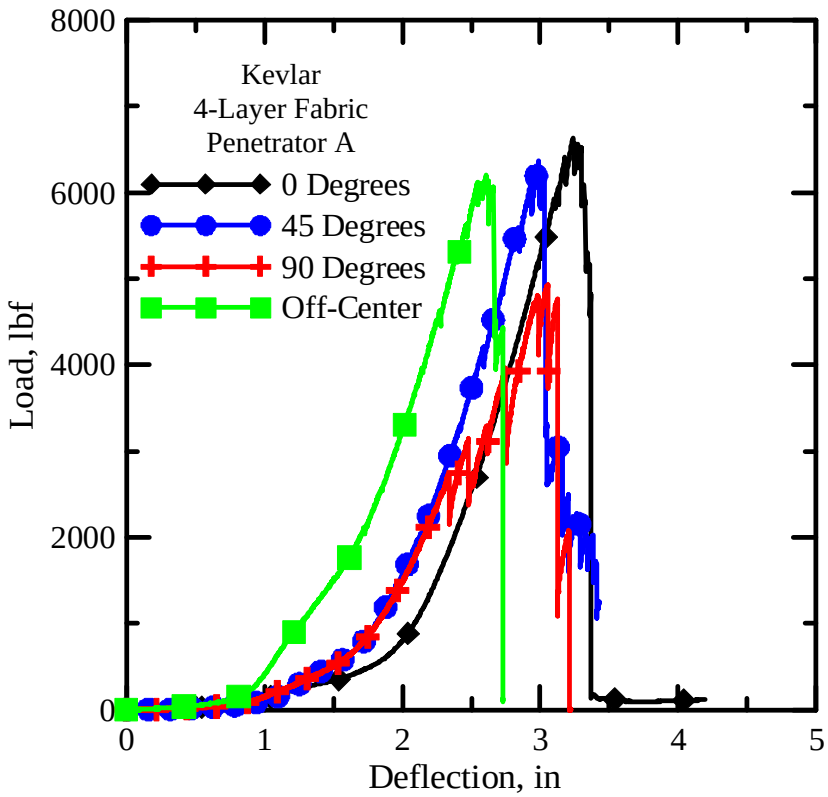

Figure 52. Various Orientations of Thicker Blunt Nose—Four-Layer Kevlar Fabric

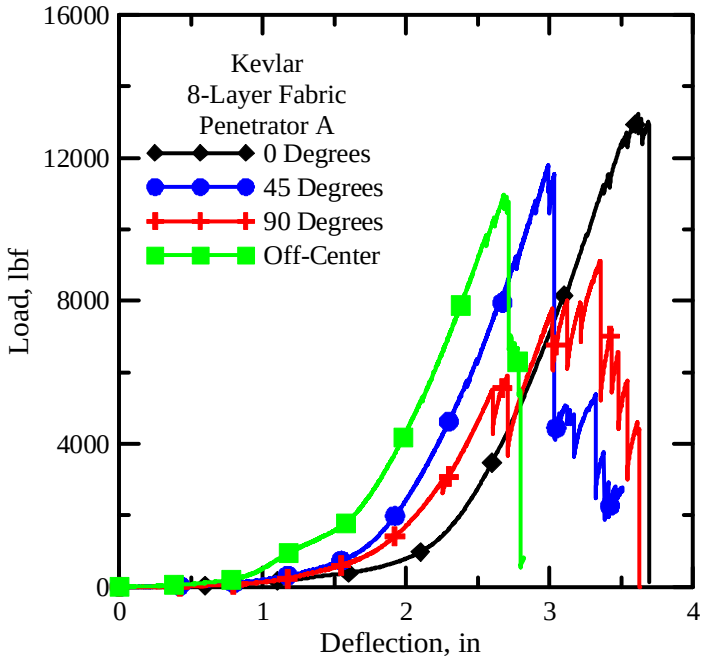

Figure 53. Various Orientations of Thicker Blunt Nose—Eight-Layer Kevlar Fabric

The following plots show the response of multilayered Kevlar fabric with the thinner penetrator. Figure 54 shows the load-deflection plot for various orientations of the thinner blunt nose with one layer of Kevlar.

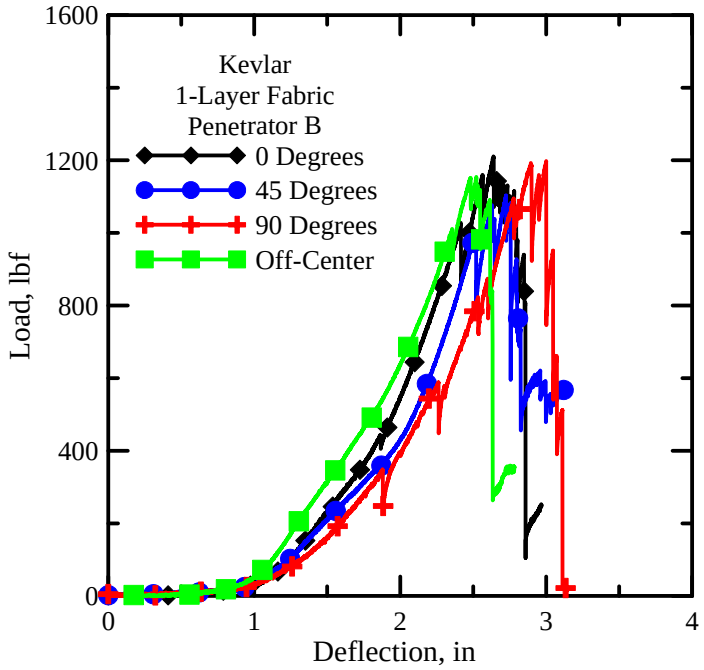

Figure 54. Load Deflection for Various Orientations of Thinner Blunt Nose With One-Layer Kevlar

Figure 54 shows that when using the thinner penetrator, the maximum loads at failure for various orientations of the thinner blunt-nose penetrator with one-layer Kevlar varied marginally compared to the thicker blunt nose for the same number of layers. The stiffness (lb/in) was maximum for the 0-degree orientation of the blunt nose and minimum for the 90-degree orientation of the blunt nose. The 45-degree orientation gave the second-highest value of the stiffness. Similar results for the stiffness were obtained for multilayered Kevlar fabrics using the thinner penetrator. Table 21 shows the values of the maximum loads and stiffness using the thinner penetrator.

Table 21. Values of Maximum Load and Stiffness for Kevlar Using the Thinner Penetrator

Layers	Orientation	Maximum Load (lb)	Stiffness (lb/in)
1	0	1211	1037
1	45	1104	1031
1	90	1198	951
1	Off	1154	980
4	0	5169	4605
4	45	4552	4468
4	90	4511	4093
4	Off	5181	4285
8	0	9095	8391
8	45	8257	8266
8	90	9575	7671
8	Off	8796	8154

The plots for the multilayered Kevlar fabric for different orientations are shown in figures 55 and 56.

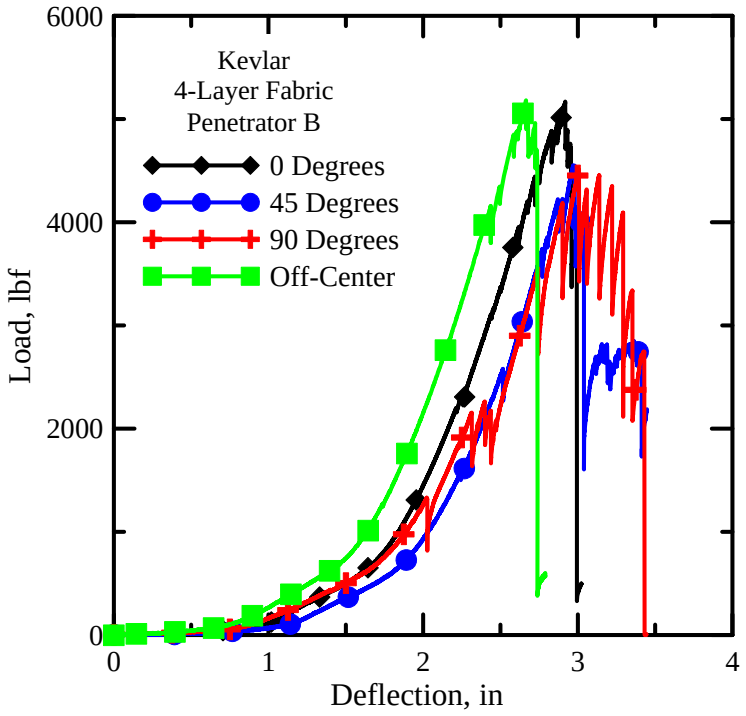

Figure 55. Various Orientations of Thinner Blunt Nose—Four-Layer Kevlar Fabric

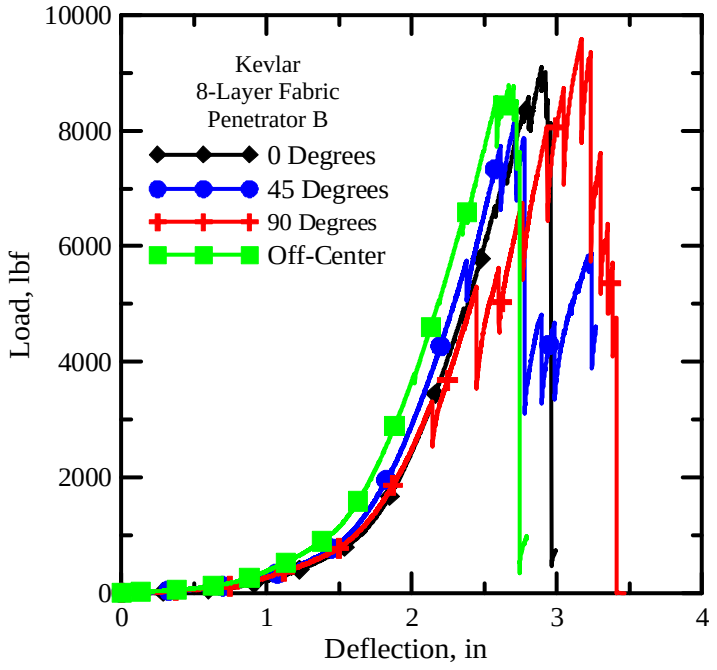

Figure 56. Various Orientations of Thinner Blunt Nose—Eight-Layer Kevlar Fabric

Figures 57, 58, 59, and 60 show the comparison of the results for the equal number of layers with the same orientation using the two different penetrators.

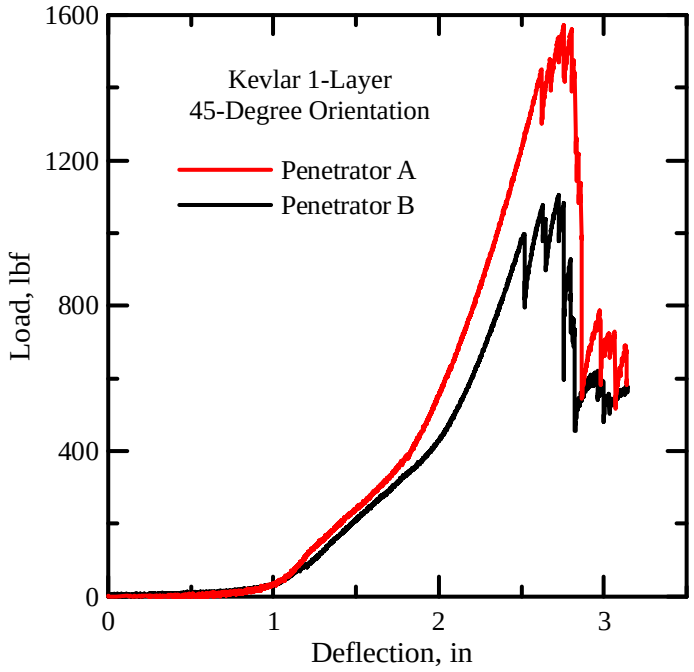

Figure 57. One-Layer Kevlar—45-Degree Orientation—Both Penetrators

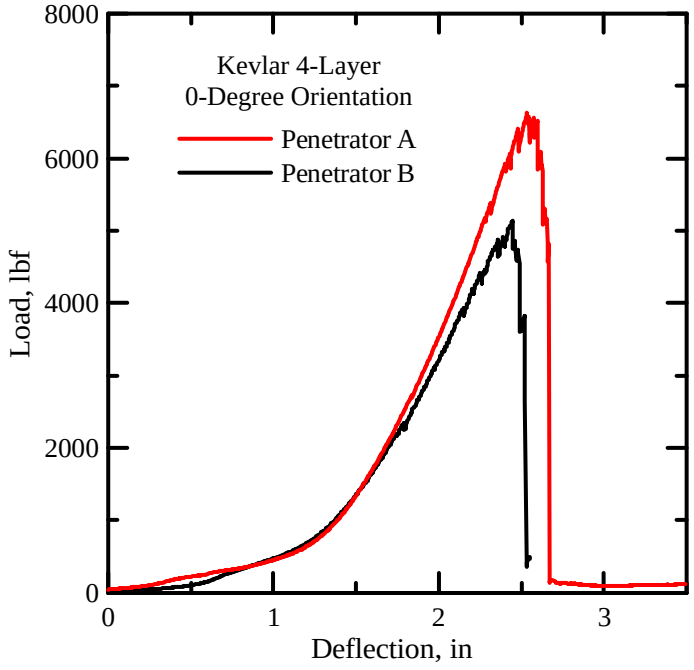

Figure 58. Four-Layer Kevlar—0-Degree Orientation—Both Penetrators

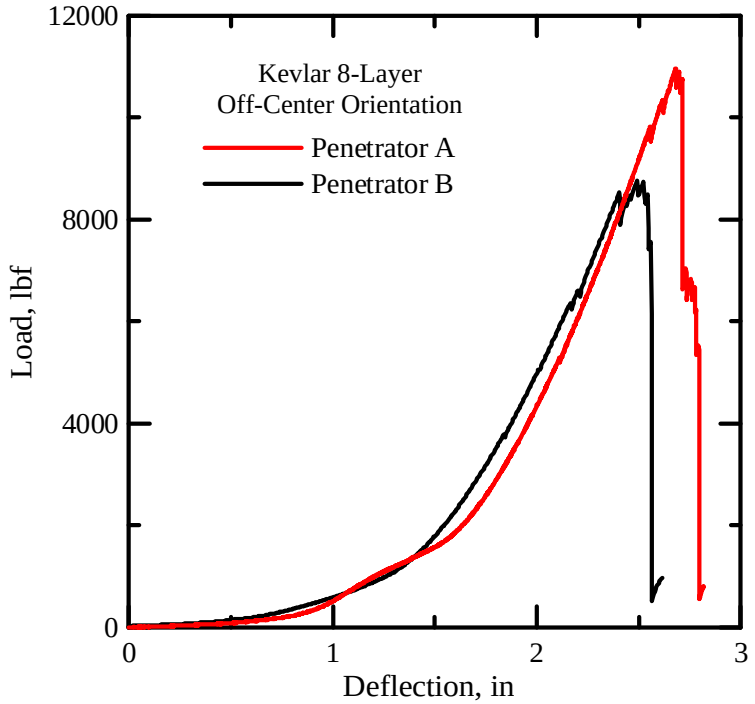

Figure 59. Eight-Layer Kevlar—Off-Center Orientation—Both Penetrators

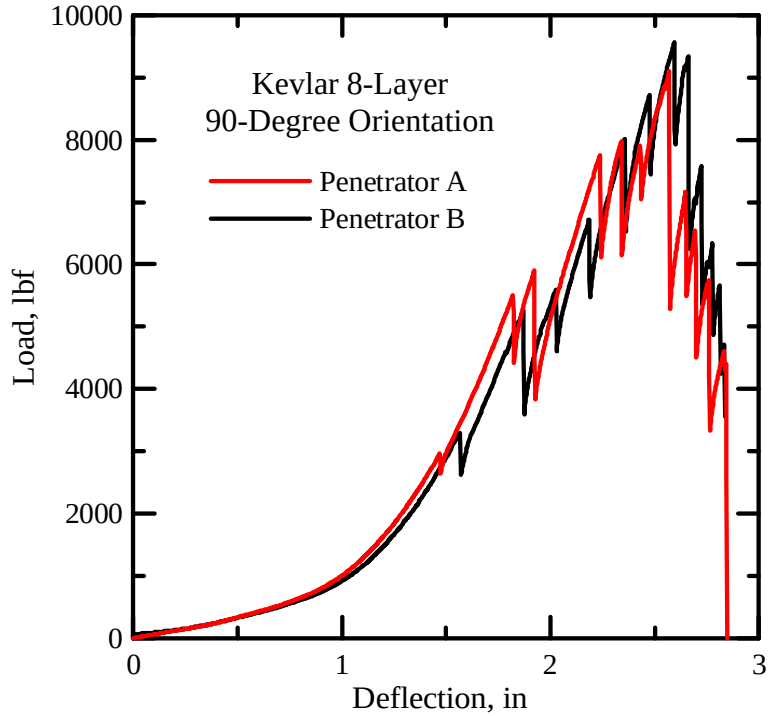

Figure 60. Eight-Layer Kevlar—90-Degree Orientation—Both Penetrators

Table 22 shows all of the Kevlar static ring test results.

Table 22. Summary of Kevlar Static Test Results

Test ID		No. of Layers	Load at First Failure (lb)	Stroke at First Failure (in.)	Peak Load (lb)	Stroke at Peak Load (in.)	Stiffness (lb/in)	Area Under the Curve (lb-in)	
P	Or							Pre-peak	Post-peak
Thick	0	1	1755	2.786	1858	2.900	1715	1293	219
Thick	0	4	6333	3.178	6625	3.230	5909	4503	889
Thick	0	8	8269	3.111	13231	3.620	11025	9907	1036
Thick	45	1	1439	2.610	1573	2.758	1418	1056	334
Thick	45	4	4181	2.583	6363	2.990	5271	4363	1156
Thick	45	8	5271	2.781	11796	2.990	10618	7461	2398
Thick	90	1	663	2.122	1228	2.730	1080	880	328
Thick	90	4	2693	2.325	4925	3.050	4790	3867	479
Thick	90	8	2895	2.244	9110	3.350	8340	7657	1484
Thick	Off	1	1335	2.108	1642	2.379	1307	1171	244
Thick	Off	4	4532	2.270	6202	2.611	5079	4587	622
Thick	Off	8	9810	2.560	10967	2.681	9770	7093	940
Thin	0	1	425	1.859	1211	2.638	1037	814	252
Thin	0	4	2285	2.251	5169	2.919	4605	3567	346
Thin	0	8	4789	2.359	9095	2.893	8391	5987	604
Thin	45	1	993	2.518	1104	2.720	1031	772	265
Thin	45	4	2553	2.509	4552	2.970	4468	2844	1329
Thin	45	8	5697	2.380	8257	2.720	8266	5091	2708
Thin	90	1	351	1.881	1198	3.000	951	956	79
Thin	90	4	1325	2.039	4511	3.010	4093	3170	1495
Thin	90	8	3281	2.131	9575	3.170	7671	7506	1649
Thin	Off	1	1006	2.354	1154	2.353	980	750	211
Thin	Off	4	4148	2.440	5181	2.664	4285	3373	407
Thin	Off	8	6354	2.350	8796	2.671	8154	5759	643

Notes:
1. The blunt-nose end conditions were fixed-fixed and clamps were used.
2. ID denotes the inner diameter, P denotes the type of penetratorm, and Or denotes the orientation of the blunt nose.

Figures 57, 58, and 59 show that the maximum load obtained using the thinner penetrator was less than the maximum load obtained using the thicker penetrator. Similarly, the stiffness of Kevlar with the thicker penetrator was higher than the stiffness with the thinner penetrator. Figure 60 shows that for the 90-degree orientation the maximum loads obtained using either penetrator differed marginally. This may be attributed to the shear loading of the Kevlar specimens in the 90-degree orientation. However, the stiffness obtained gave similar results as compared to the other orientations.

4.3.2 Zylon Results.

The load-deflection curves of two Zylon AS-500 specimens are shown in figures 61 and 62. Both curves were slack-shifted by 1.1397 and 0.1276 inches, respectively, to match the displacements obtained through the FE model.

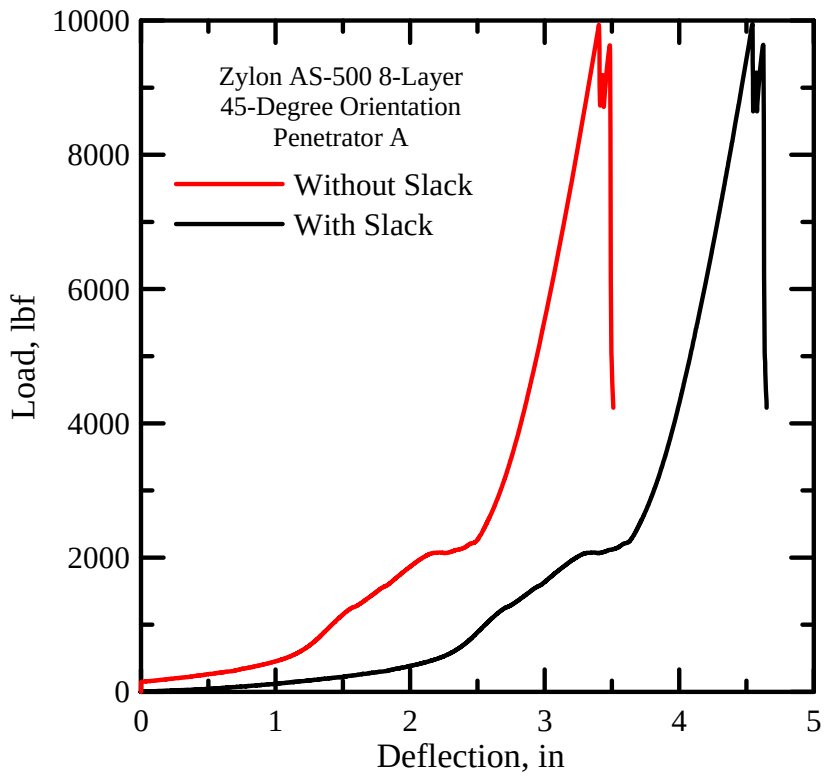

Figure 61. Load-Deformation Response of Eight-Layer Zylon Specimen With and Without Slack Adjustment Using the Thicker Penetrator

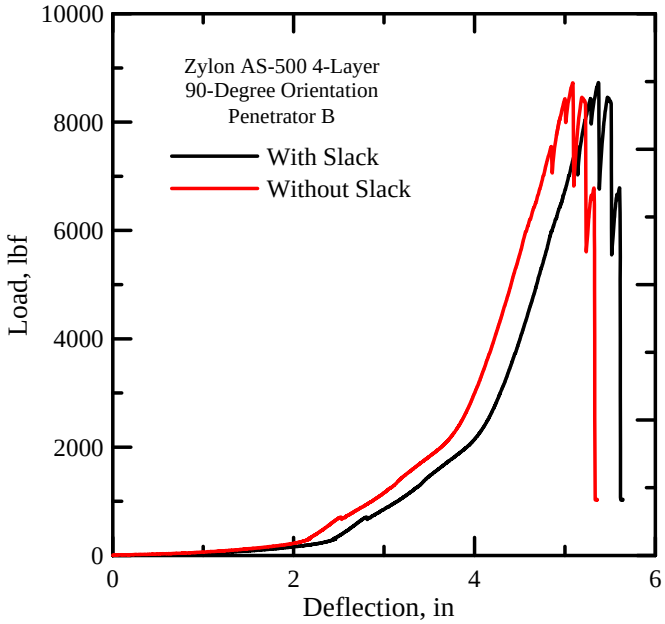

Figure 62. Load-Deformation Response of Four-Layer Zylon Specimen With and Without Slack Adjustment Using the Penetrator

It was found that most of the Zylon fabric specimens exhibited a delayed response in the early stage of loading. This response can be attributed to sliding and loss of grip around the clamps.

Figures 63 and 64 compare the response of the one-, four-, and eight-layer Zylon fabric for the off-center orientation using both penetrators.

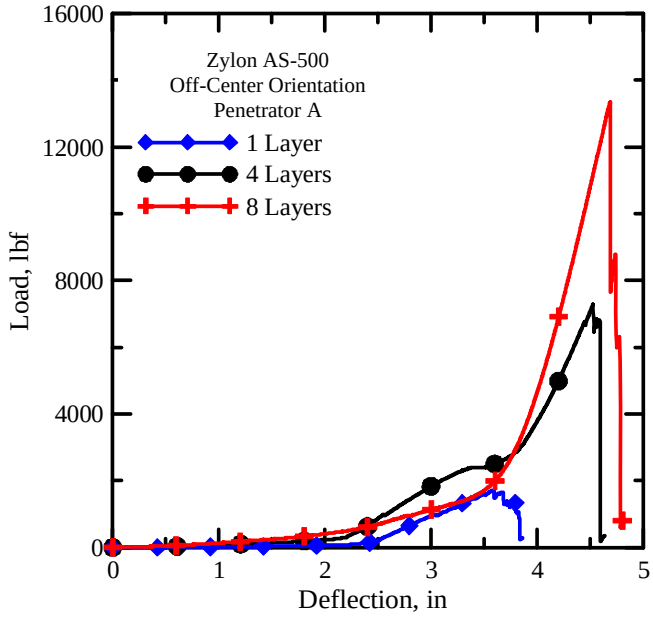

Figure 63. Load-Deflection Response of Zylon for Same Orientation of Thicker Blunt Nose for Multilayer Specimens

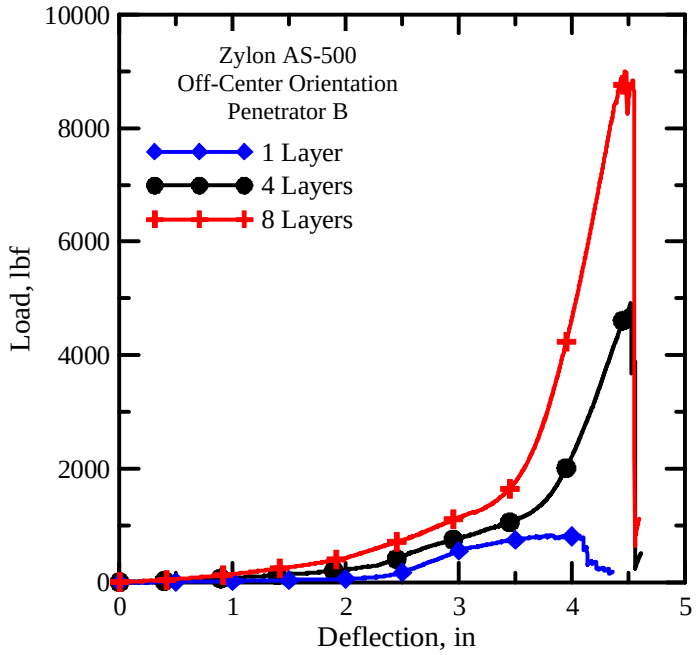

Figure 64. Load-Deflection Response of Zylon for Same Orientation of Thinner Blunt Nose for Multilayer Specimens

Figure 65 shows the load-deflection response of one-layer Zylon fabric for different orientations of the thicker blunt nose.

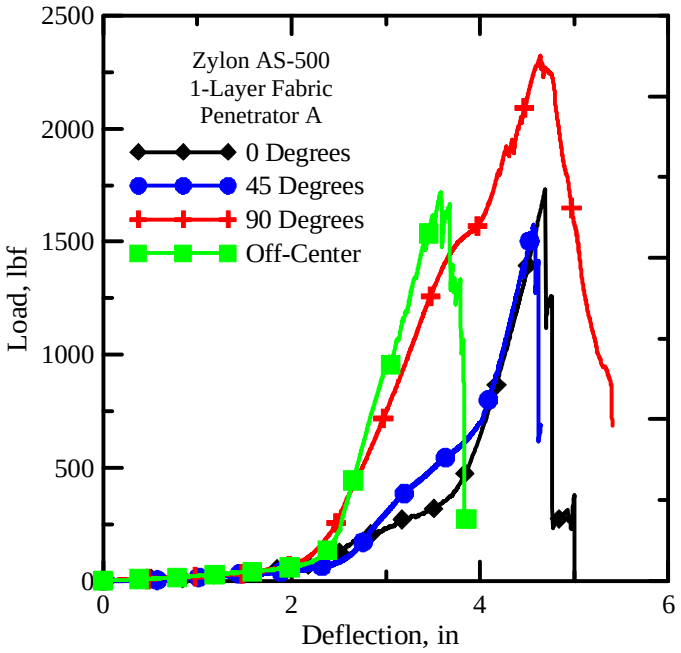

Figure 65. Load-Deflection Response for Various Orientations of Thicker Blunt Nose With One-Layer Zylon

The results show that the 90-degree orientation had the maximum peak load. However, the 90-degree orientation had the least stiffness value, while the 45-degree orientation had the maximum stiffness value. Table 23 shows the maximum loads and stiffness values for the various orientations that were tested using the thicker penetrator. Figures 66 and 67 show the load-deflection response of Zylon for various thicker blunt-nose orientations of the four- and eight-layer Zylon specimens, respectively.

Table 23. Values of Maximum Load and Stiffness for Zylon Using the Thicker Penetrator

Layers	Orientation	Maximum Load (lb)	Stiffness (lb/in)
1	0	1730	1609
1	45	1577	1740
1	90	2324	975
1	Off	1716	1459
4	0	7363	5692
4	45	6279	7349
4	90	8957	5669
4	Off	7276	6647
8	0	13290	11382
8	45	9952	12436
8	90	15669	10025
8	Off	13349	11645

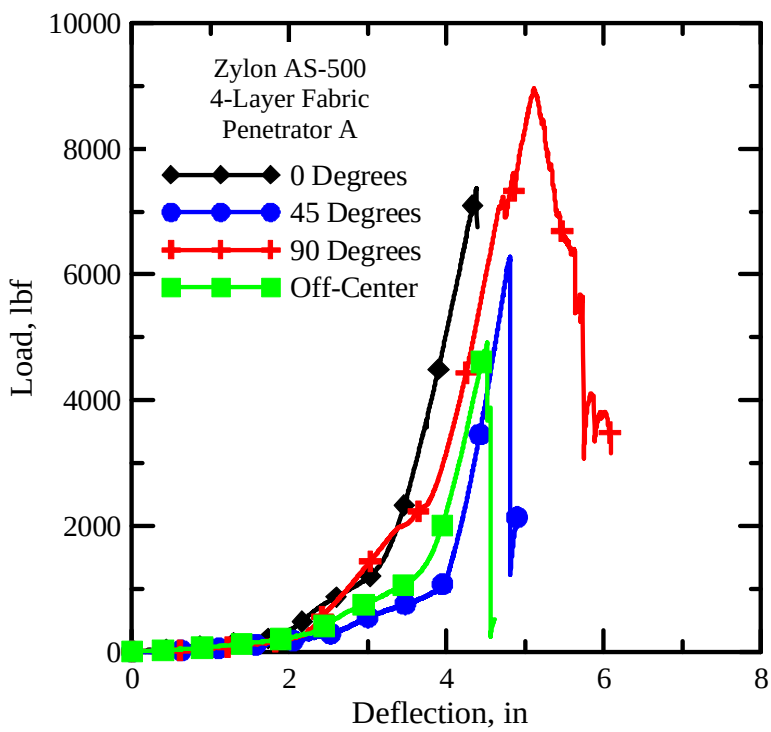

Figure 66. Various Orientations of Thicker Blunt Nose—Four-Layer Zylon Fabric

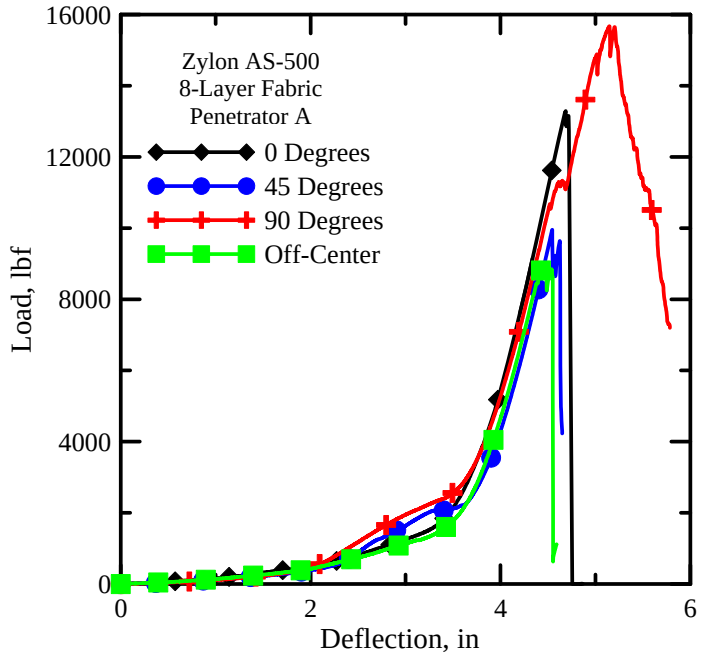

Figure 67. Various Orientations of Thicker Blunt Nose—Eight-Layer Zylon Fabric

Figure 68 shows the load-deflection plot for various orientations of the thinner blunt nose with one layer of Zylon.

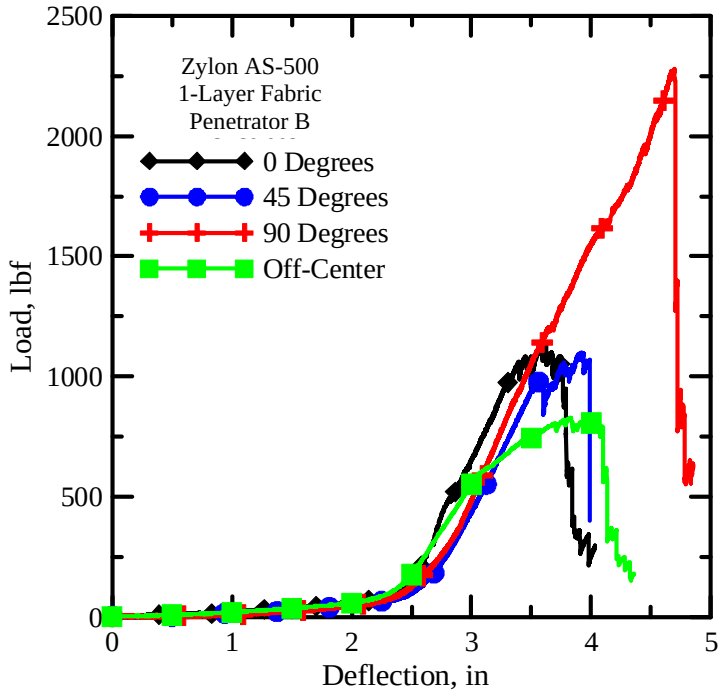

Figure 68. Load Deflection for Various Orientations of the Thinner Blunt Nose With One-Layer Zylon

The results show that the 90-degree orientation had the maximum peak load. The 90-degree orientation also had the maximum stiffness value, while the off-center orientation had the minimum stiffness value. The maximum loads and stiffness values are shown in table 24.

Table 24. Values of Maximum Load and Stiffness for Zylon Using the Thinner Penetrator

Layers	Orientation	Maximum Load (lb)	Stiffness (lb/in)
1	0	1138	1013
1	45	1100	1034
1	90	2278	1148
1	Off	837	755
4	0	5173	5096
4	45	7380	5151
4	90	8729	5499
4	Off	4916	4658
8	0	9446	10149
8	45	12948	8820
8	90	16649	13525
8	Off	9000	8394

Figures 69 and 70 show the load-deflection response of Zylon for various thinner blunt-nose orientations for the four- and eight-layer Zylon specimens, respectively.

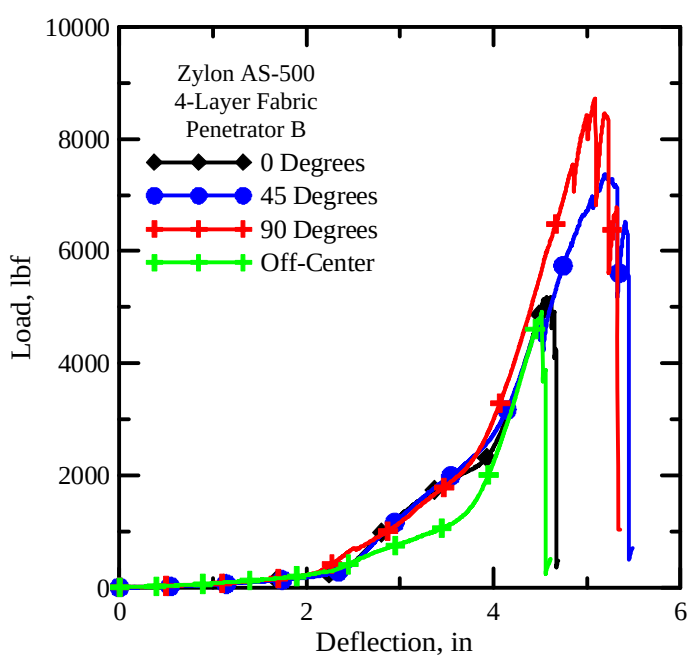

Figure 69. Various Orientations of the Thinner Blunt Nose—Four-Layer Zylon Fabric

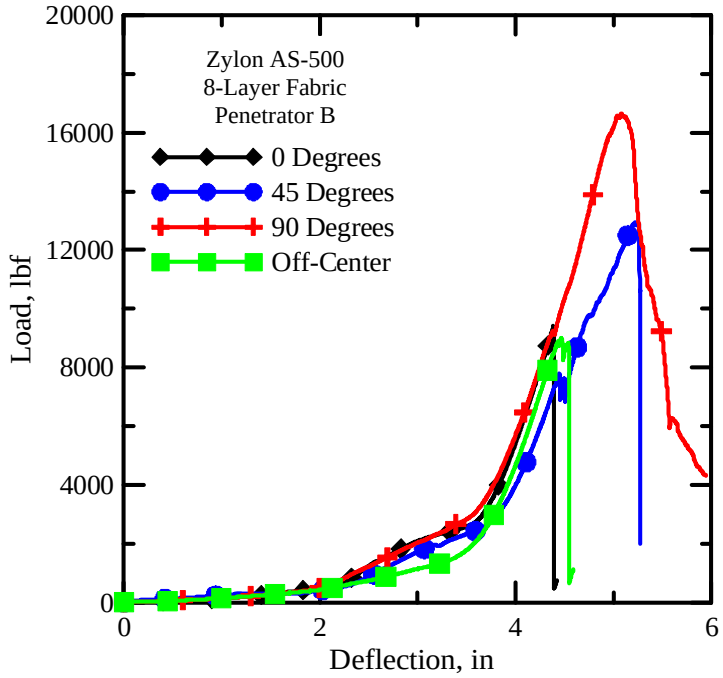

Figure 70. Various Orientations of the Thinner Blunt Nose—Eight-Layer Zylon Fabric

Figures 71, 72, 73, and 74 show the comparative load-deflection responses for Zylon AS-500 fabric with the same number of layers and the same orientation using the two different penetrators.

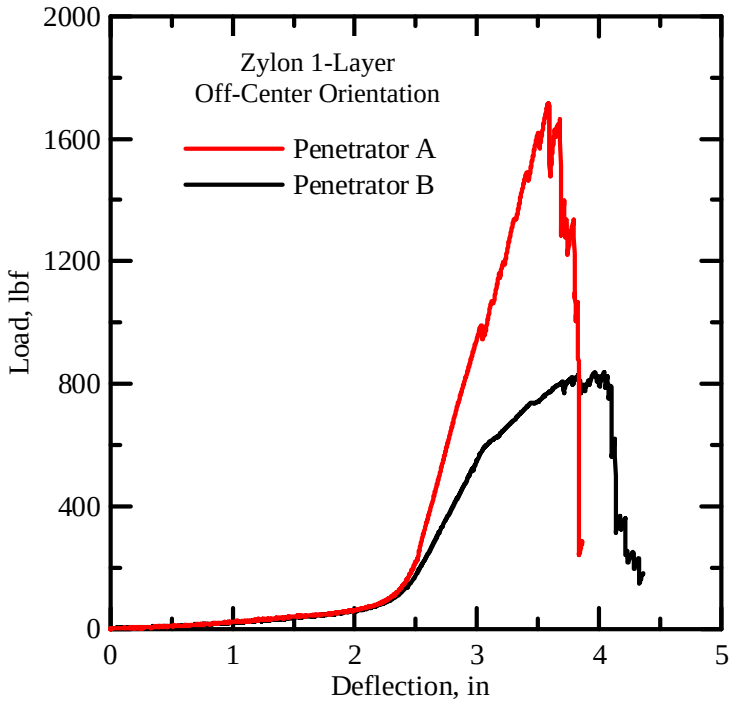

Figure 71. One-Layer Zylon—Off-Center Orientation—Both Penetrators

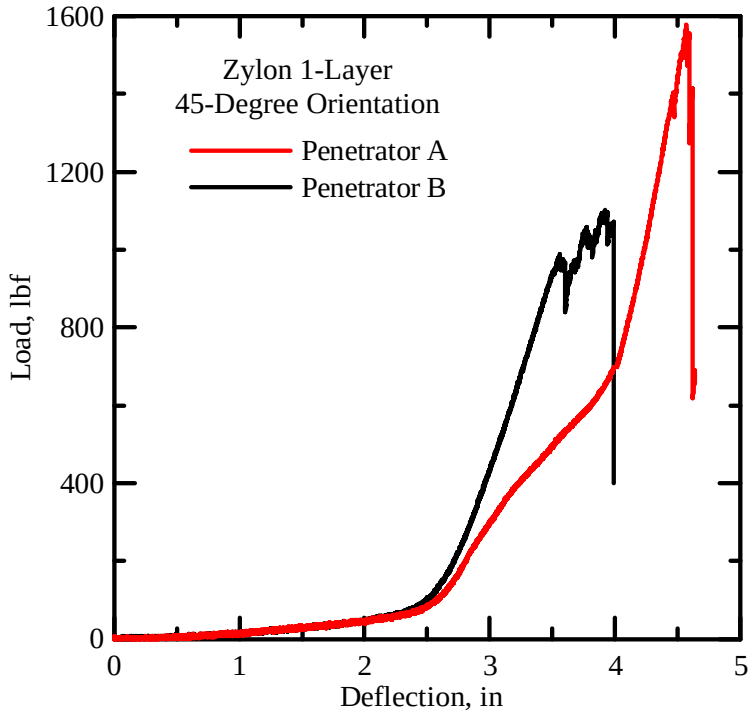

Figure 72. One-Layer Zylon—45-Degree Orientation—Both Penetrators

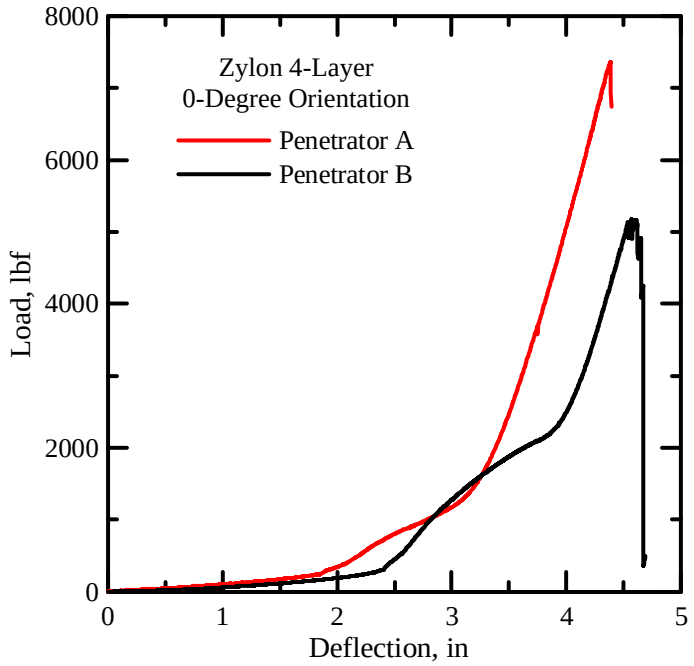

Figure 73. Four-Layer Zylon—0-Degree Orientation—Both Penetrators

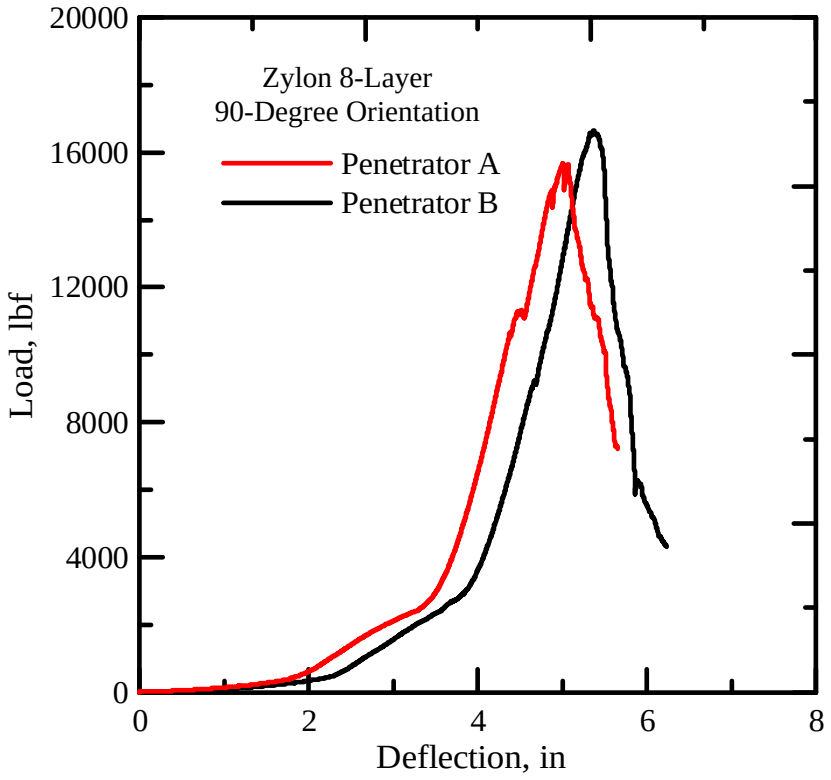

Figure 74. Eight-Layer Zylon—90-Degree Orientation—Both Penetrators

Figures 71, 72, and 73 show that the maximum load obtained with the thinner penetrator was less than the maximum load obtained with the thicker penetrator. Similarly, the stiffness of the Zylon using the thicker penetrator was higher than the stiffness using the thinner penetrator. Figure 74 shows that for the 90-degree orientation the maximum loads obtained using either penetrator differed marginally. This may be attributed to the shear loading of the Zylon specimens in the 90-degree orientation. The stiffness values obtained were higher using the thinner penetrator with the 90-degree orientation.

Table 25 shows a summary of the Zylon static ring test results. All specimens were preloaded with 250 lb load.

Table 25. Summary of Zylon Static Test Results

Test ID		No. of Layers	Load at First Failure (lb)	Stroke at First Failure (in.)	Peak Load (lb)	Stroke at Peak Load (in.)	Stiffness (lb/in)	Area Under the Curve (lb-in)	
P	Or							Pre-peak	Post-peak
Zylon Specimens									
Thick	0	1	1730	4.691	1730	4.691	1609	1323	162
Thick	0	4	7363	4.386	7363	4.386	5692	6105	56
Thick	0	8	13290	4.687	13290	4.687	11382	9499	410
Thick	45	1	1397	4.468	1577	4.570	1740	1274	86
Thick	45	4	6216	4.798	6279	4.810	7349	4003	191
Thick	45	8	9877	4.533	9952	4.545	11645	7414	875
Thick	90	1	1917	4.282	2324	4.644	975	2853	1179
Thick	90	4	7143	4.705	8957	5.115	5669	9745	5778
Thick	90	8	11289	4.637	15669	5.147	10025	16629	7480
Thick	Off	1	984	3.031	1716	3.583	1459	1159	353
Thick	Off	4	6750	4.440	7276	4.524	6647	6469	465
Thick	Off	8	13243	4.672	13349	4.686	12436	9192	735
Thin	0	1	973	3.308	1138	3.621	1013	869	265
Thin	0	4	5048	4.578	5173	4.566	5096	4694	514
Thin	0	8	9386	4.523	9446	4.519	10149	7441	40
Thin	45	1	977	3.559	1100	3.915	1034	940	76
Thin	45	4	4750	4.508	7380	5.194	5151	8651	1731
Thin	45	8	7708	5.053	12948	5.825	8820	14225	1879
Thin	90	1	2268	4.683	2278	4.700	1148	2543	118
Thin	90	4	7523	5.137	8729	5.370	5499	9003	1802
Thin	90	8	9140	4.650	16649	5.367	13525	16744	7900
Thin	Off	1	807	3.707	837	4.039	755	1033	126
Thin	Off	4	4788	4.487	4916	4.519	4658	3700	175
Thin	Off	8	8868	4.454	9000	4.468	8394	6490	768

Notes:

- The blunt-nose end conditions were fixed-fixed and clamps were used.
- ID denotes inner diameter, P denotes the type of penetrator, and Or denotes the orientation of the blunt nose.

5. COMPARISON OF STATIC RING TESTS TO FE SIMULATIONS.

5.1 OVERVIEW.

FE simulations of the off-axis static ring tests were conducted and the results were compared with the static experimental tests in this section. The multiple layers of fabric in the FE simulation were modeled with one layer of elements with the thickness of the multilayer of fabrics. In the following sections, the FE models used to generate the models had the following characteristics.

- The ABAQUS®/Standard FE program [6] was used on Windows® XP® computer platform. The FEA involved static loads (load control), nonlinear stress-strain material behavior with smooth, finite sliding between the various contact surfaces, and used large displacement theory.

- Linear solid elements (8-noded hexahedral and 4-noded tetrahedral elements) were used throughout the model. The use of ABAQUS/Standard [6] precluded the use of shell elements to model the fabrics. Contact definition between shell and solid elements is difficult to capture in ABAQUS/Standard.

Additional theoretical and modeling details are available in reference 1.

5.2 THE FE MODEL DESCRIPTION.

Different mesh densities were used for steel ring, fabric, and the blunt nose. Table 26 shows the model type and element length for each orientation of the model. The mesh only depends on the orientation, irrespective of the fabric and number of layers.

Table 26. Model Type and Typical Element Length

Model Orientation	Model Type	Steel Ring (in.)	Fabric (in.)	Blunt Nose (in.)
0-degree	Quarter model	0.075	0.1	0.05
45-degree	Full model	0.15	0.2 and 0.1 near blunt-nose contact	0.1
90-degree	Quarter model	0.075	0.1	0.05
Off-center	Half model	0.15	0.2	0.1

Figures 75-79 show the typical mesh for each blunt-nose orientation.

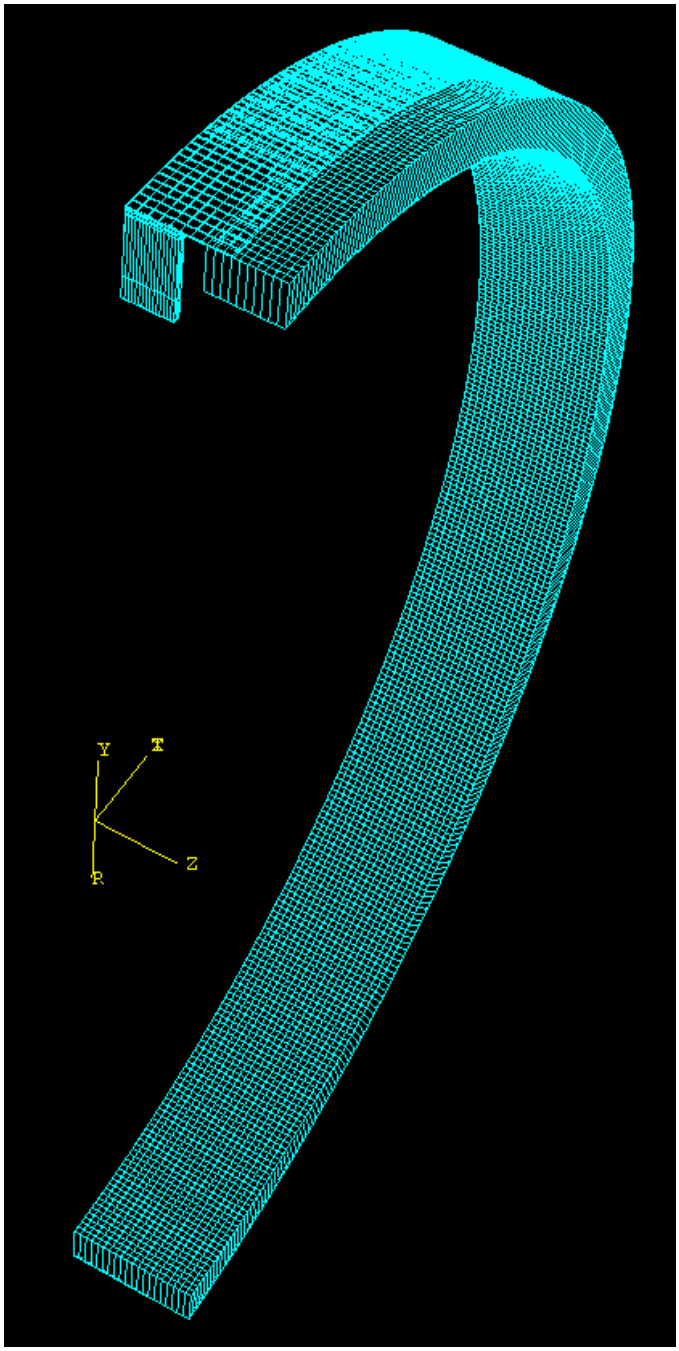

Figure 75. The FE Mesh for the 0-Degree Orientation Models

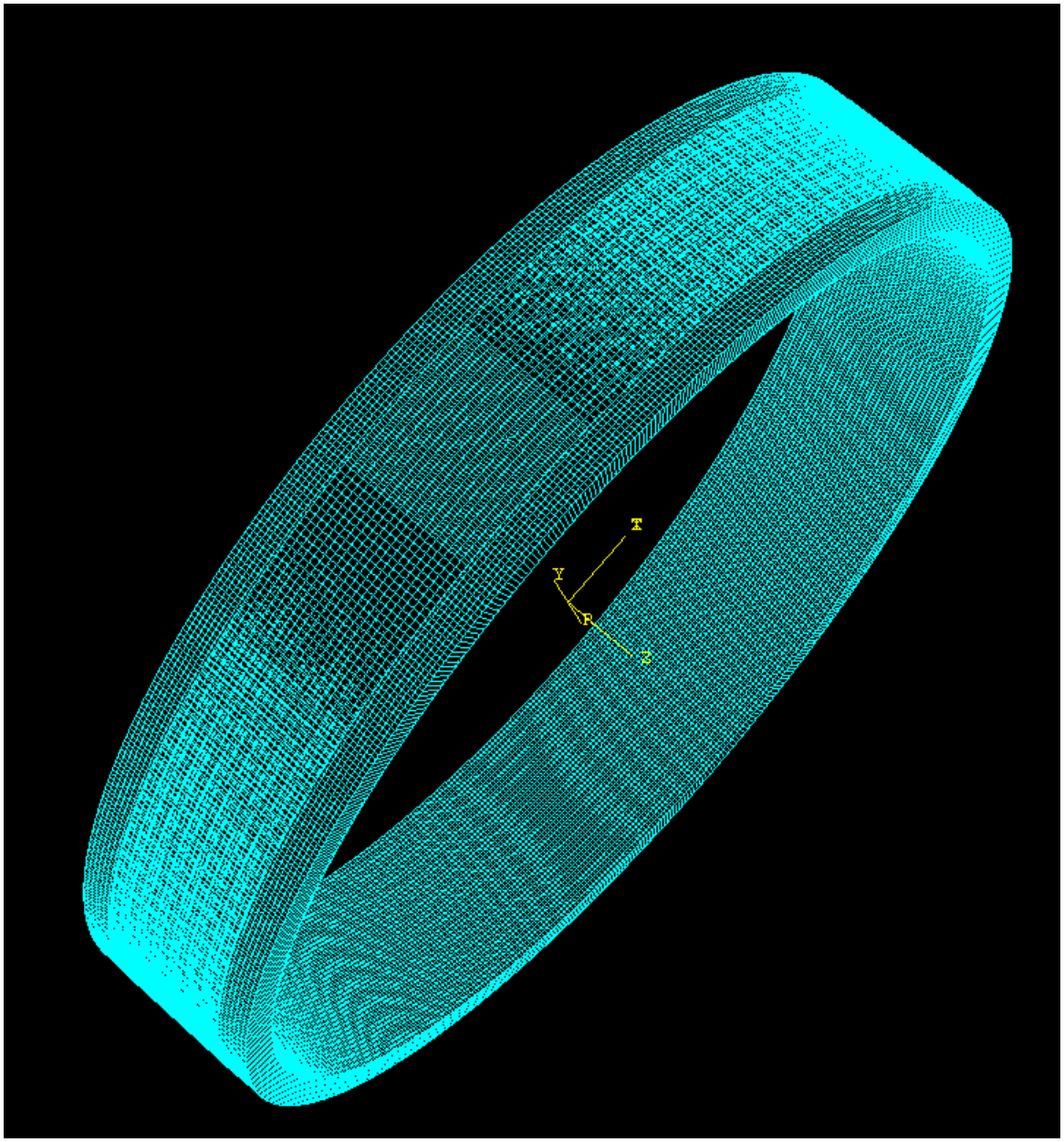

Figure 76. The FE Mesh for 45-Degree Orientation Models Showing the Outer Surface of the Ring

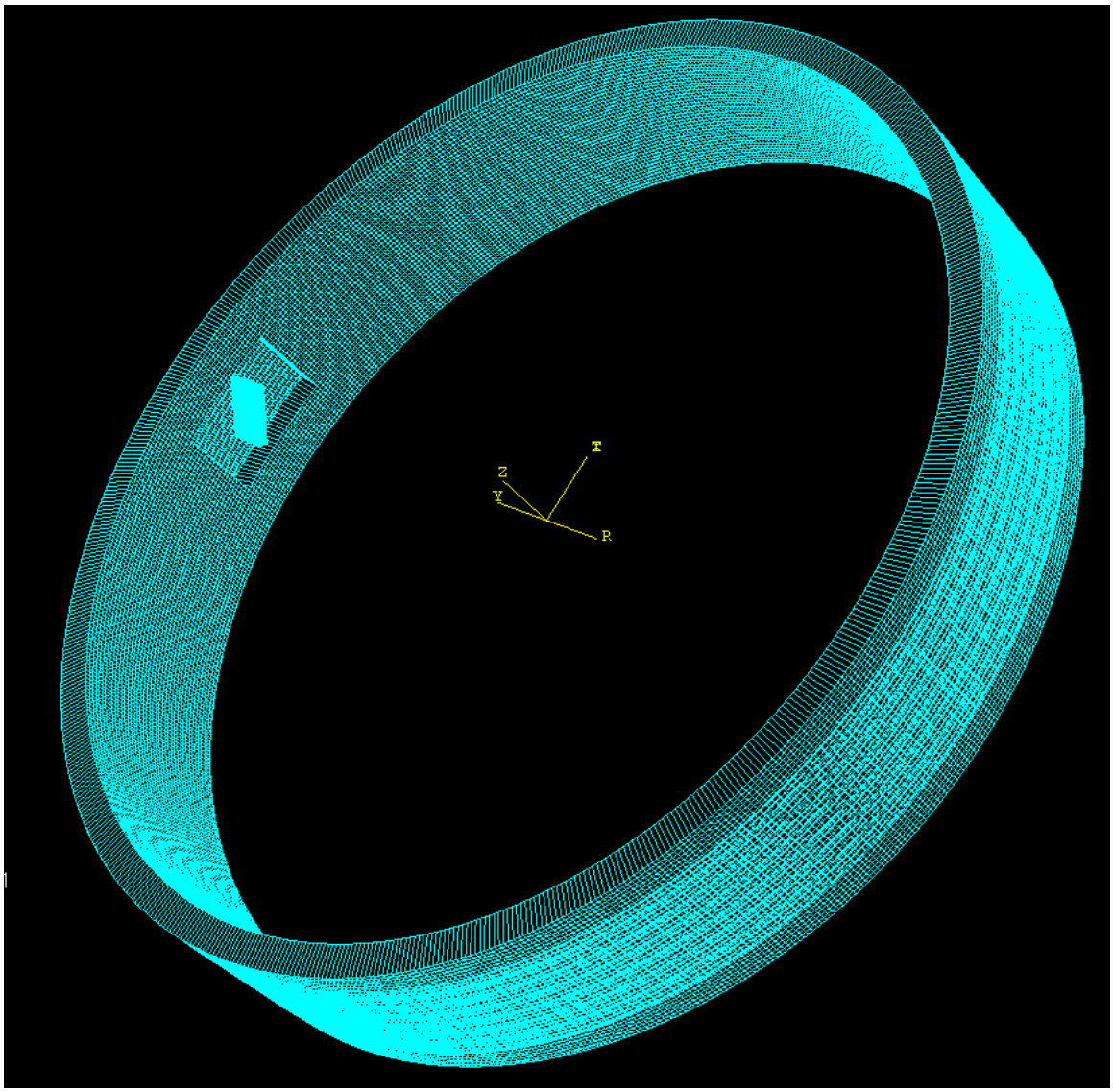

Figure 77. The FE Mesh for 45-Degree Orientation Models Showing the Inner Surface of the Ring

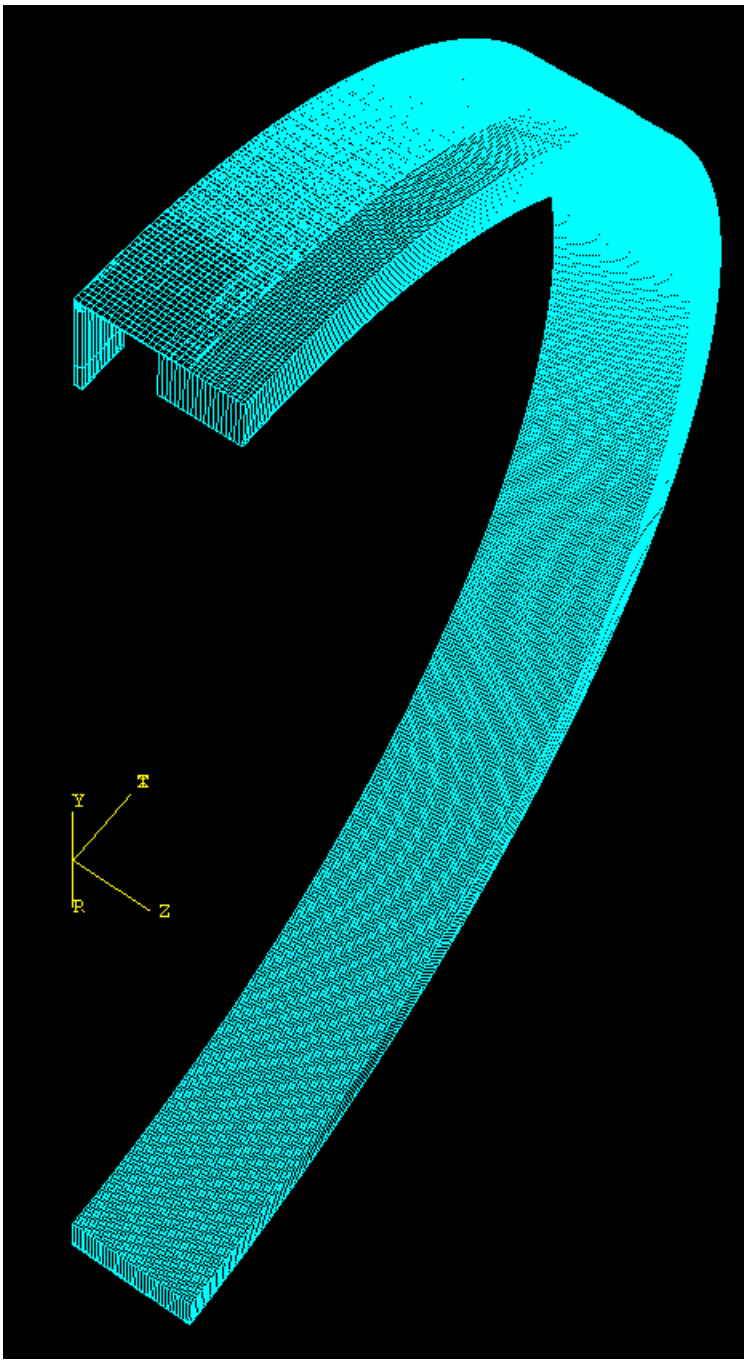

Figure 78. The FE Mesh for 90-Degree Orientation Models

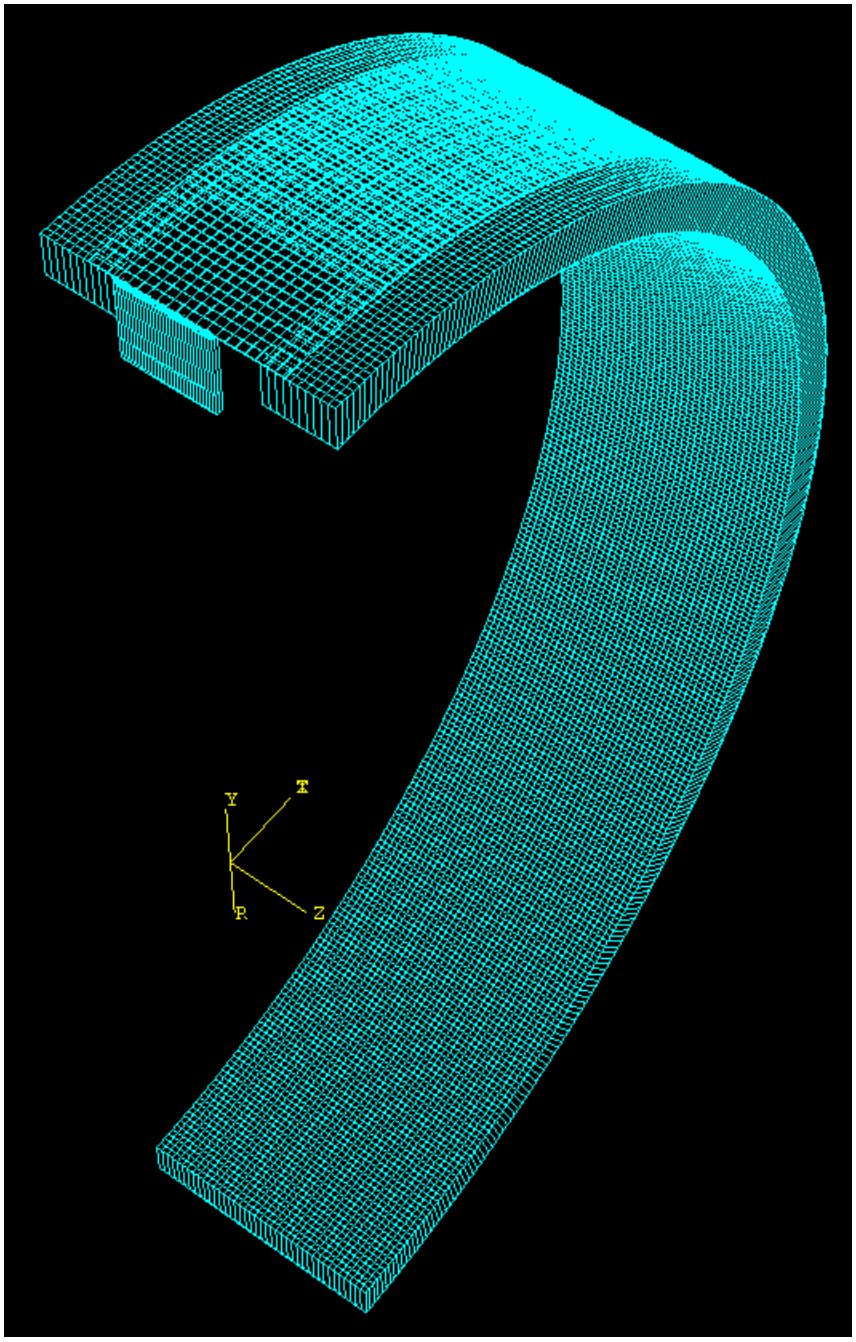

Figure 79. The FE Mesh for Off-Center Orientation Models

5.3 RESULTS.

5.3.1 Kevlar Results.

5.3.1.1 One Layer.

Figure 80a and table 27 compare the static test FE simulation to the experimental results for the one-layer Kevlar, 0-degree orientation, thinner blunt-nose test case. Figures 80b and 80c show the FE simulation deformation.

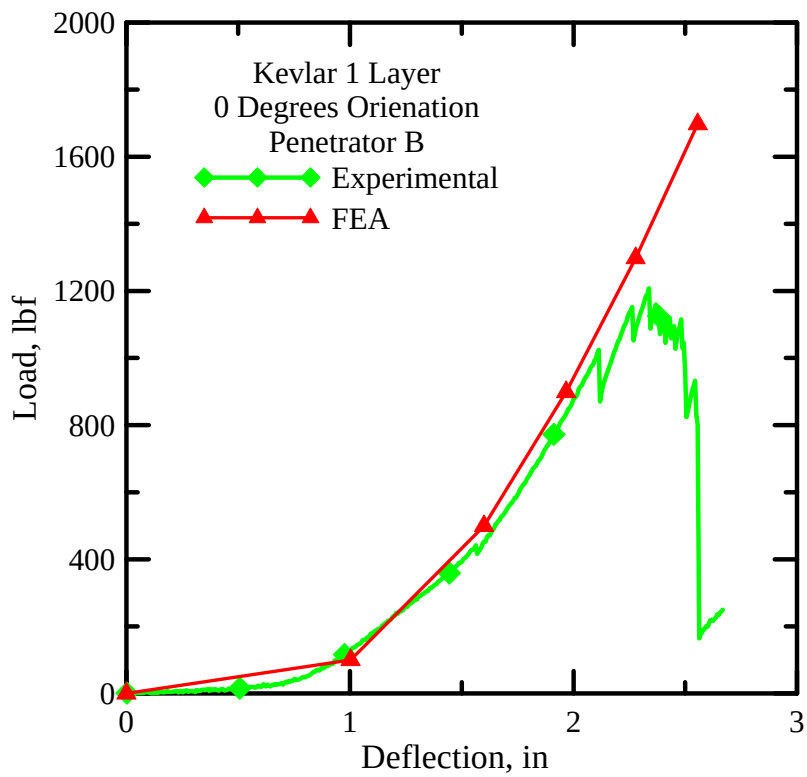

Figure 80a. Comparison of the Load-Displacement Graphs for the One-Layer Kevlar, 0-Degree Orientation, Thinner Blunt-Nose Test

Table 27. Static Test—FEA Comparison for the One-Layer Kevlar, 0-Degree Orientation, Thinner Blunt-Nose Test

	Static Test	FEA
Peak load (lb)	1211	1697
Displacement at peak load (in.)	2.638	2.556

The experimental curve was slack-shifted by 0.3 inch.

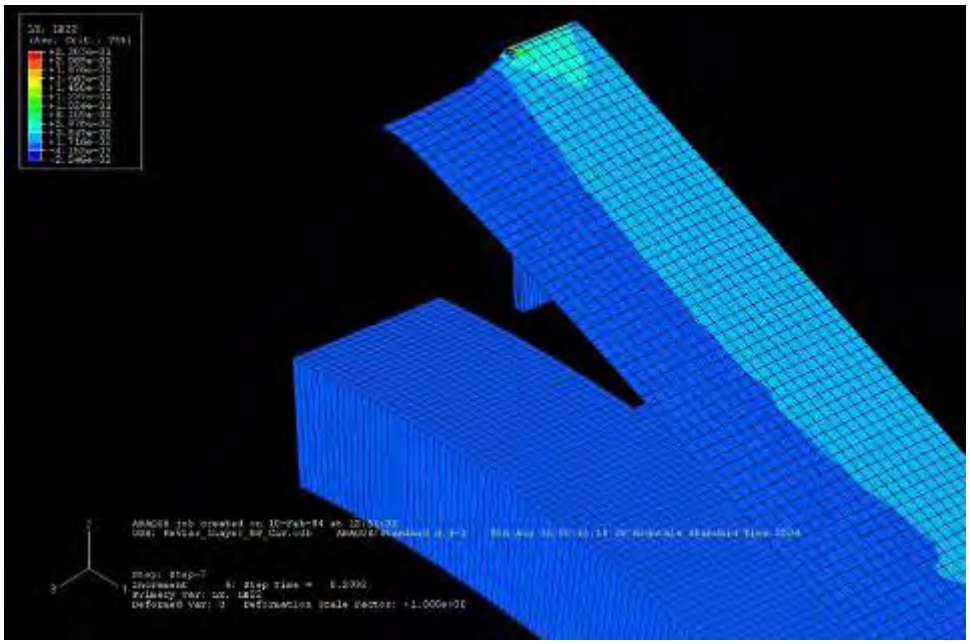

Figure 80b. One-Layer Kevlar—0-Degree Orientation (Thinner Blunt Nose)—Plot of In-Plane Strain ε_1 Superimposed on Deformation at the End of the Last Load Step

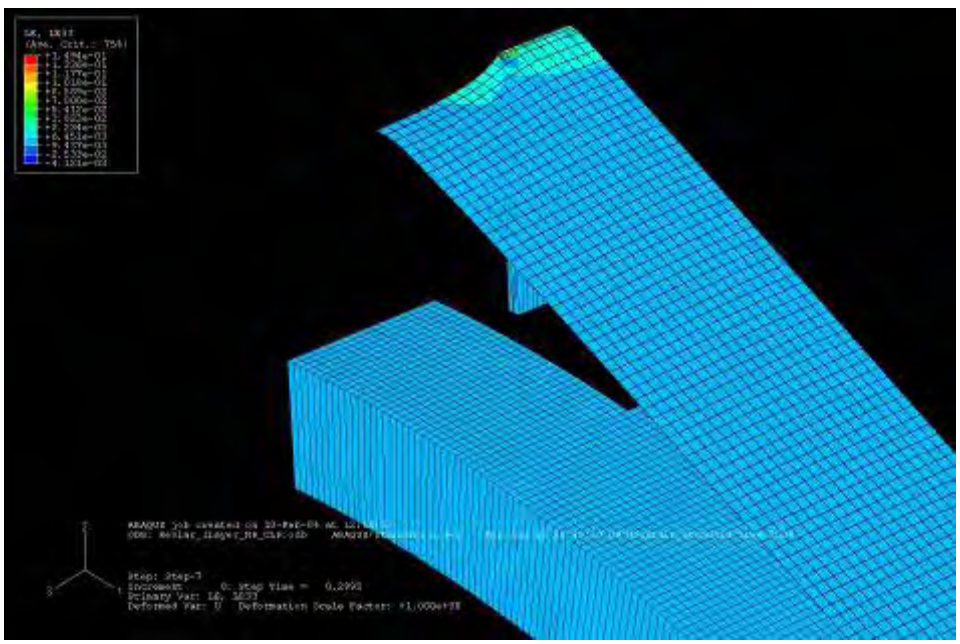

Figure 80c. One-Layer Kevlar—0-Degree Orientation (Thinner Blunt Nose)—Plot of In-Plane Strain ε_2 Superimposed on Deformation at the End of the Last Load Step

Figure 81a and table 28 compare the static test FE simulation to the experimental results for the one-layer Kevlar, 45-degree orientation, thinner blunt-nose test case. Figures 81b and 81c show the FE simulation deformation.

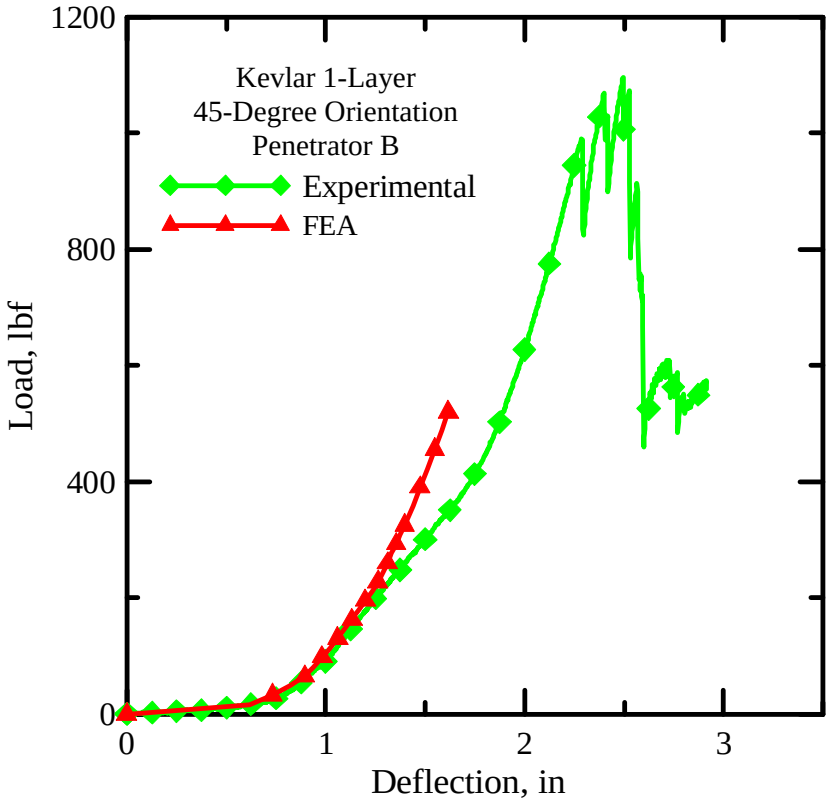

Figure 81a. Comparison of the Load-Displacement Graphs for the One-Layer Kevlar, 45-Degree Orientation, Thinner Blunt-Nose Test

Table 28. Static Test—FEA Comparison for the One-Layer Kevlar, 45-Degree Orientation, Thinner Blunt-Nose Test

	Static Test	FEA
Peak load (lb)	1104	577
Displacement at peak load (in.)	2.491	1.502

The experimental curve was slack-shifted by 0.23 inch.

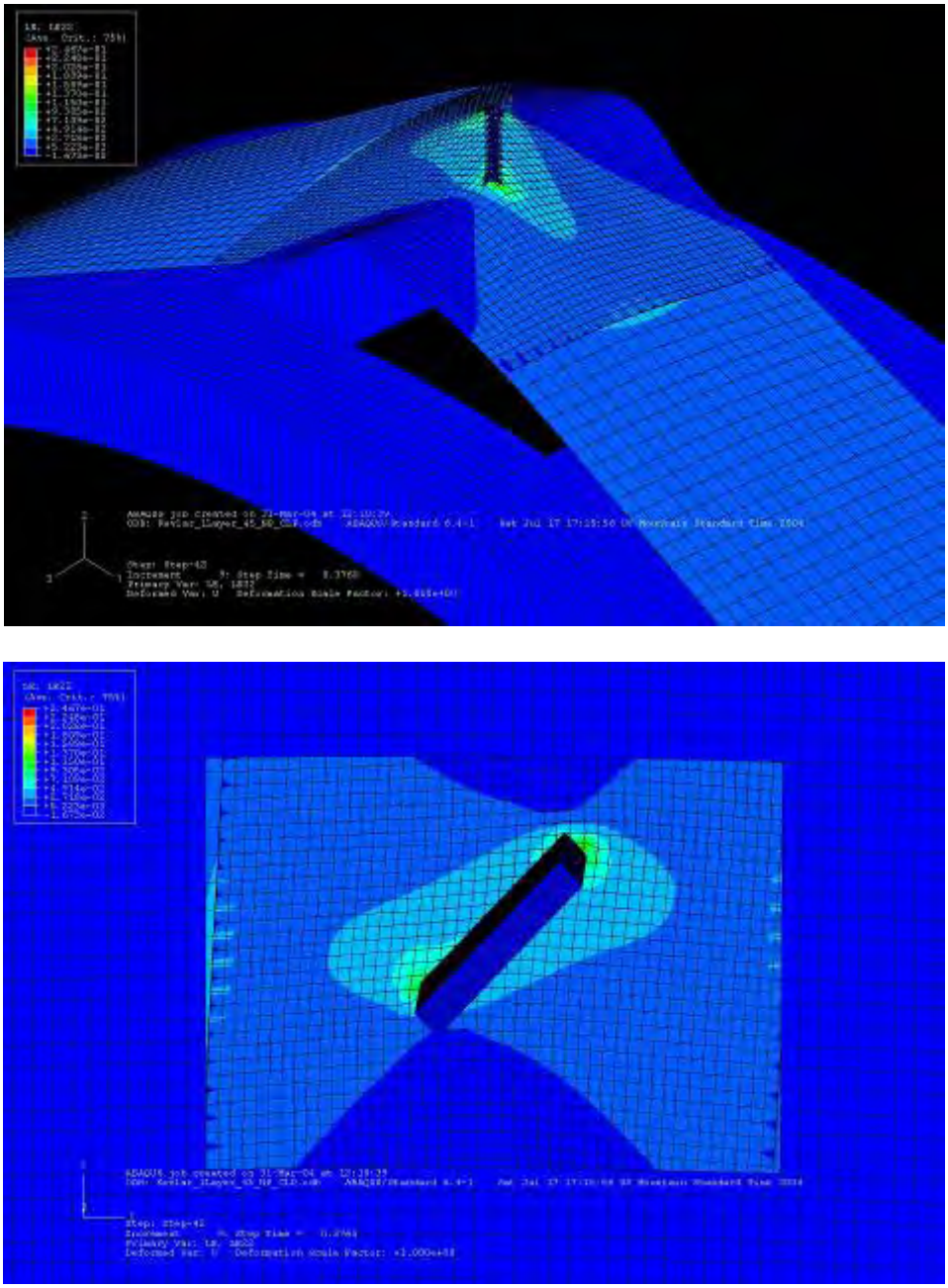

Figure 81b. One-Layer Kevlar—45-Degree Orientation (Thinner Blunt Nose)—Plot of In-Plane Strain ε_1 Superimposed on Deformation at the End of the Last Load Step

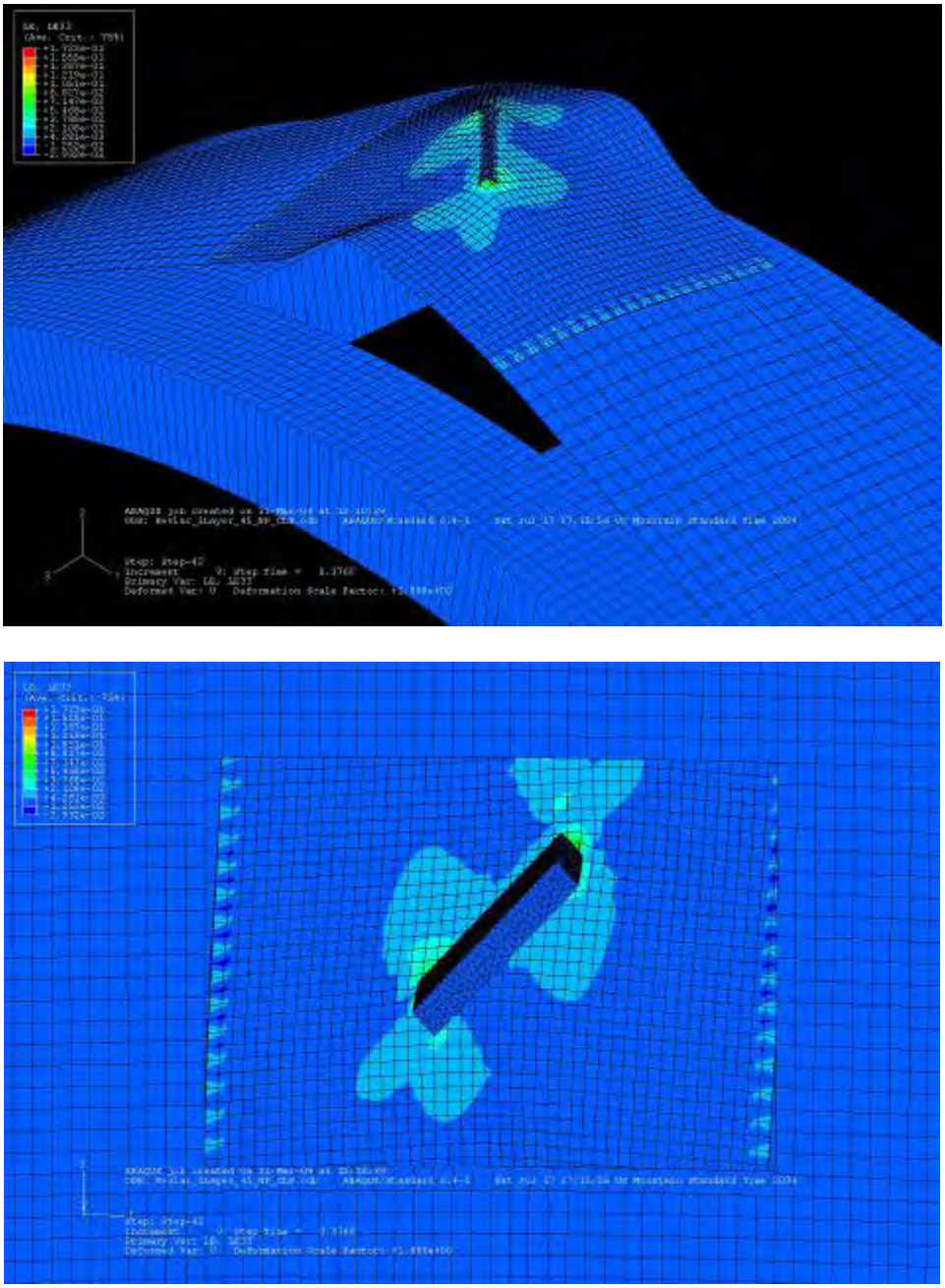

Figure 81c. One-Layer Kevlar—45-Degree Orientation (Thinner Blunt Nose)—Plot of In-Plane Strain ε_2 Superimposed on Deformation at the End of the Last Load Step

Figure 82a and table 29 compare the static test FE simulation to the experimental results for the one-layer Kevlar, 90-degree orientation, thinner blunt-nose test case. Figures 82b and 82c show the FE simulation deformation.

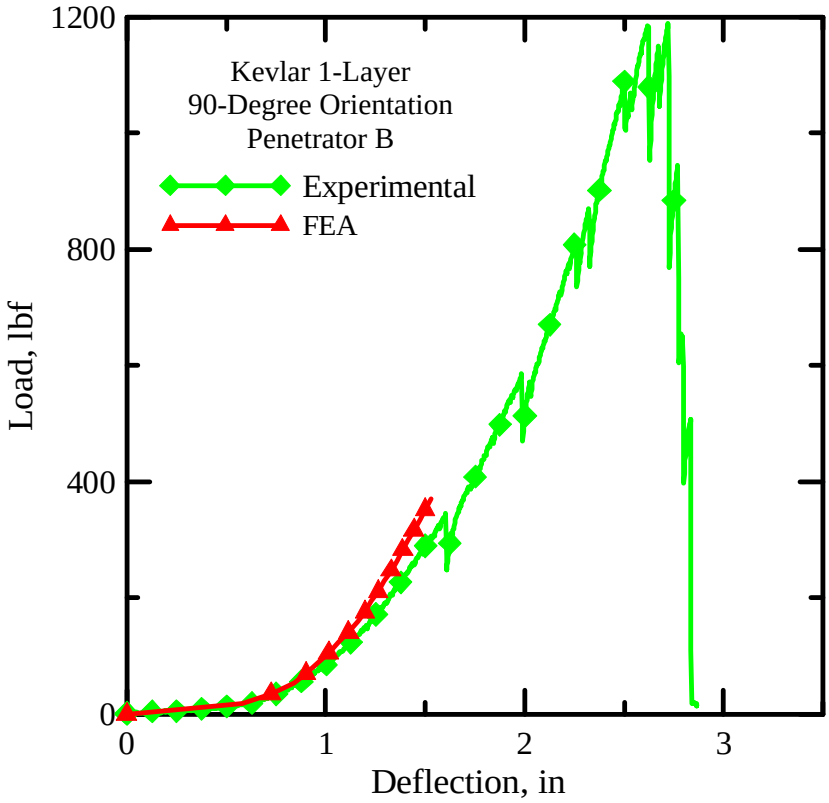

Figure 82a. Comparison of the Load-Displacement Graphs for the One-Layer Kevlar, 90-Degree Orientation, Thinner Blunt-Nose Test

Table 29. Static Test—FEA Comparison for the One-Layer Kevlar, 90-Degree Orientation, Thinner Blunt-Nose Test

	Static Test	FEA
Peak load (lb)	1198	370
Displacement at peak load (in.)	2.720	1.514

The experimental curve was slack-shifted by 0.28 inch.

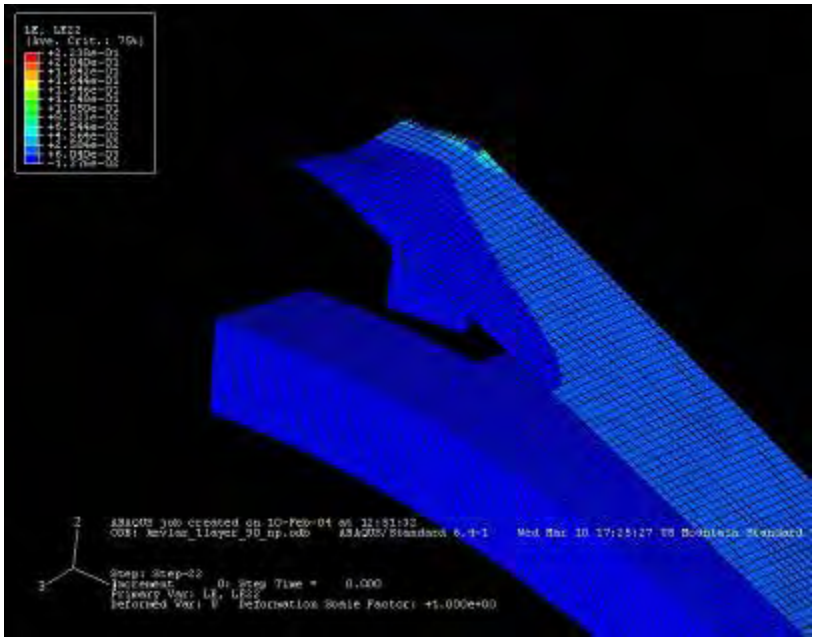

Figure 82b. One-Layer Kevlar—90-Degree Orientation (Thinner Blunt Nose)—Plot of In-Plane Strain ε_1 Superimposed on Deformation at the End of the Last Load Step

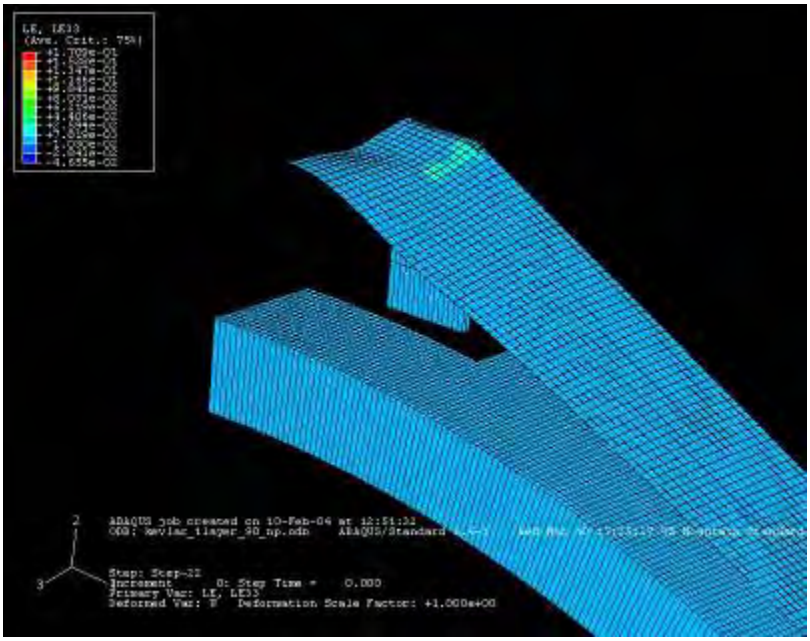

Figure 82c. One-Layer Kevlar—90-Degree Orientation (Thinner Blunt Nose)—Plot of In-Plane Strain ε_2 Superimposed on Deformation at the End of the Last Load Step

Figure 83a and table 30 compare the static test FE simulation to the experimental results for the one-layer Kevlar, 0-degree off-center orientation, thinner blunt-nose test case. Figures 83b and 83c show the FE simulation deformation.

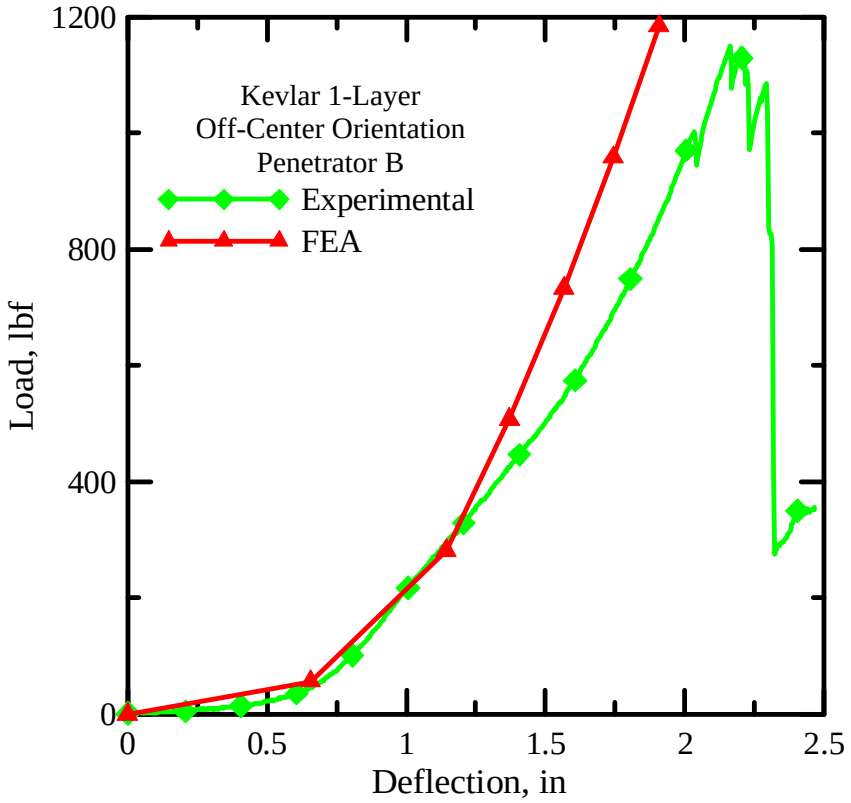

Figure 83a. Comparison of the Load-Displacement Graphs for the One-Layer Kevlar, Off-Center Orientation, Thinner Blunt-Nose Test

Table 30. Static Test—FEA Comparison for the One-Layer Kevlar, Off-Center Orientation, Thinner Blunt-Nose Test

	Static Test	FEA
Peak load (lb)	1154	1184
Displacement at peak load (in.)	2.221	1.907

The experimental curve was slack-shifted by 0.13 inch.

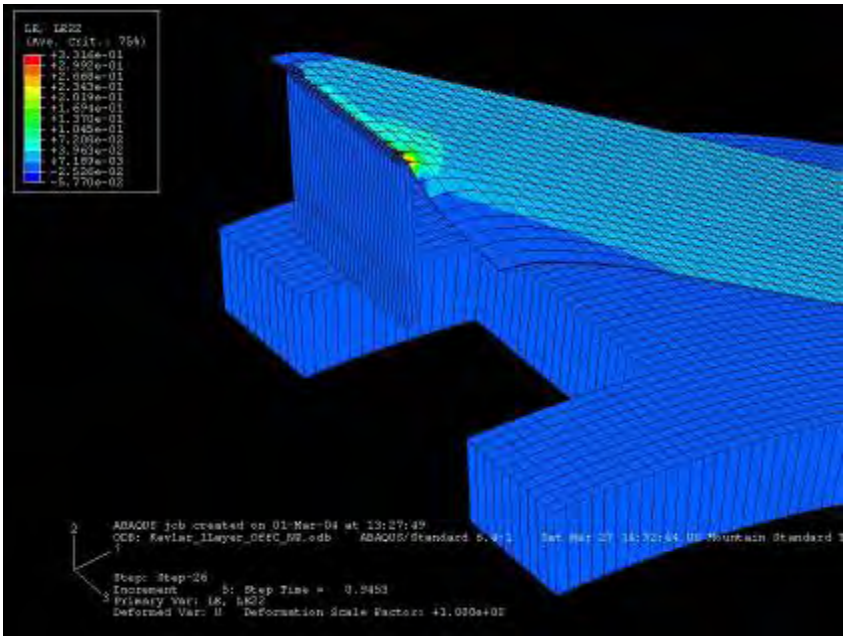

Figure 83b. One-Layer Kevlar—Off-Center Orientation (Thinner Blunt Nose)—Plot of In-Plane Strain ε_1 Superimposed on Deformation at the End of the Last Load Step

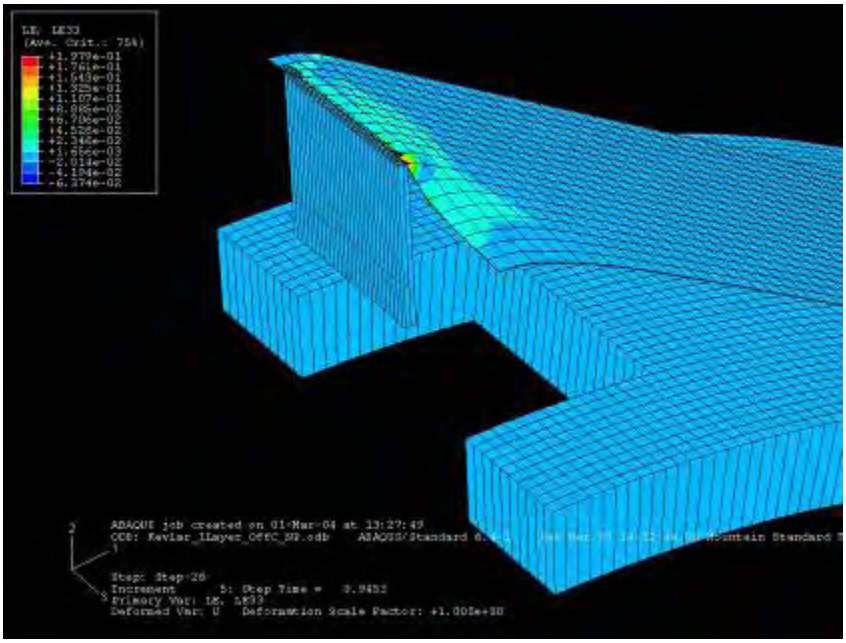

Figure 83c. One-Layer Kevlar—Off-Center Orientation (Thinner Blunt Nose)—Plot of In-Plane Strain ε_2 Superimposed on Deformation at the End of the Last Load Step

Figure 84a and table 31 compare the static test FE simulation to the experimental results for the one-layer Kevlar, 45-degree orientation, thicker blunt-nose test case. Figures 84b and 84c show the FE simulation deformation.

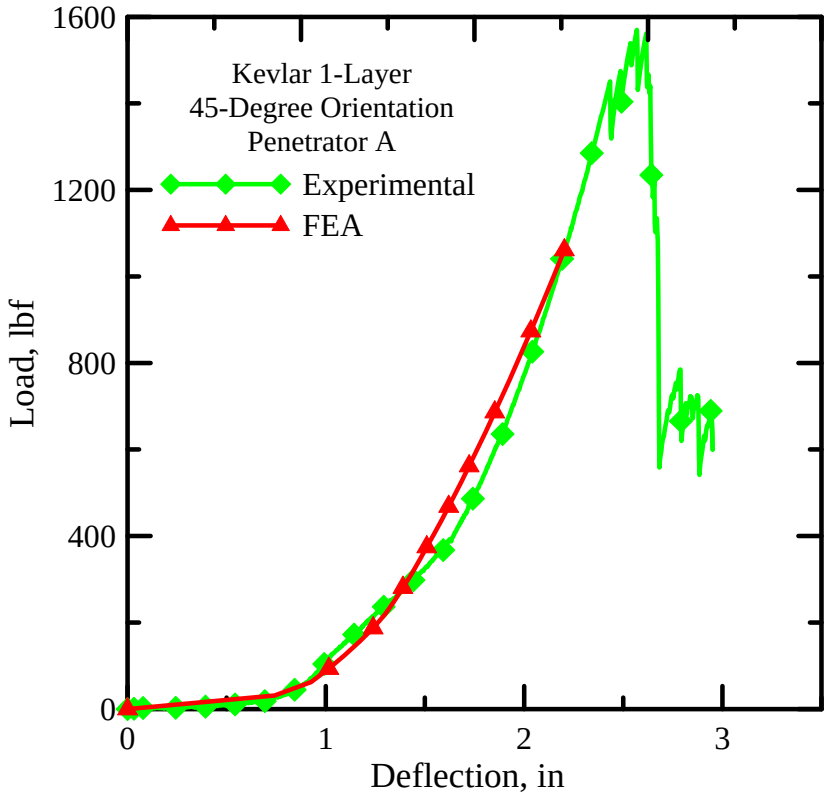

Figure 84a. Comparison of the Load-Displacement Graphs for the One-Layer Kevlar, 45-Degree Orientation, Thicker Blunt-Nose Test

Table 31. Static Test—FEA Comparison for the One-Layer Kevlar, 45-Degree Orientation, Thicker Blunt-Nose Test

	Static Test	FEA
Peak load (lb)	1573	1061
Displacement at peak load (in.)	2.571	2.161

The experimental curve was slack-shifted by 0.19 inch.

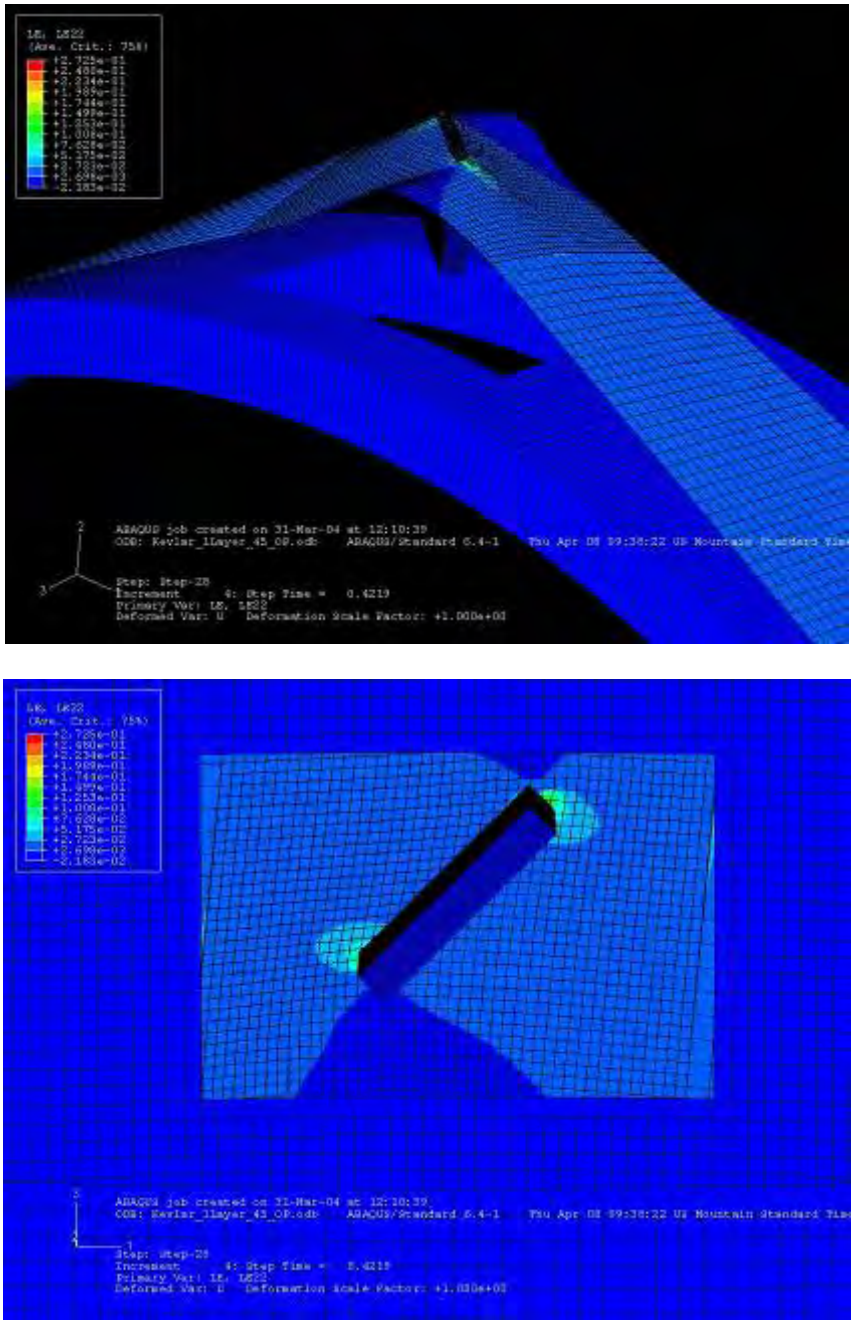

Figure 84b. One-Layer Kevlar—45-Degree Orientation (Thicker Blunt Nose)—Plot of In-Plane Strain ε_1 Superimposed on Deformation at the End of the Last Load Step

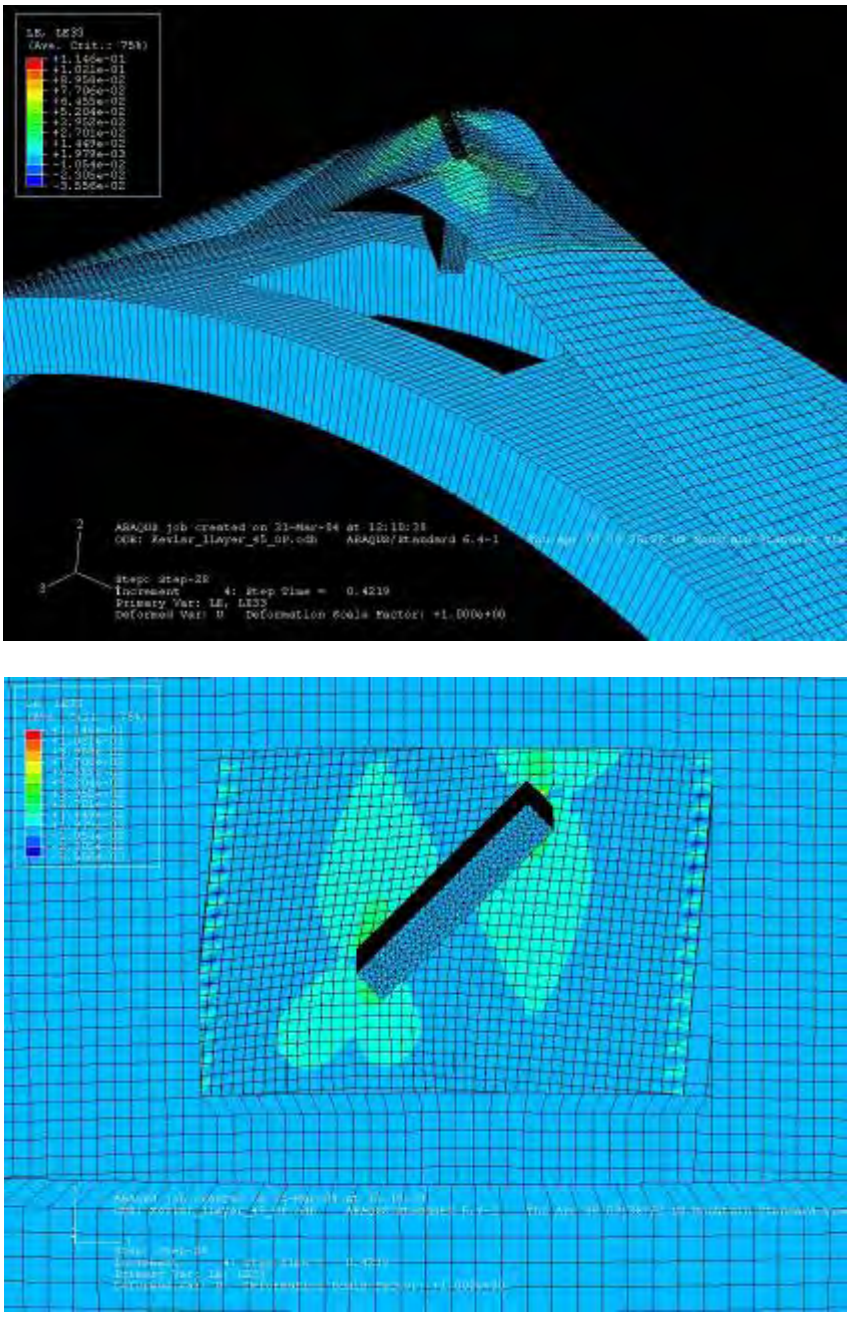

Figure 84c. One-Layer Kevlar—45-Degree Orientation (Thicker Blunt Nose)—Plot of In-Plane Strain ε_2 Superimposed on Deformation at the End of the Last Load Step

Figure 85a and table 32 compare the static test FE simulation to the experimental results for the one-layer Kevlar, 90-degree orientation, thicker blunt-nose test case. Figures 85b and 85c show the FE simulation deformation.

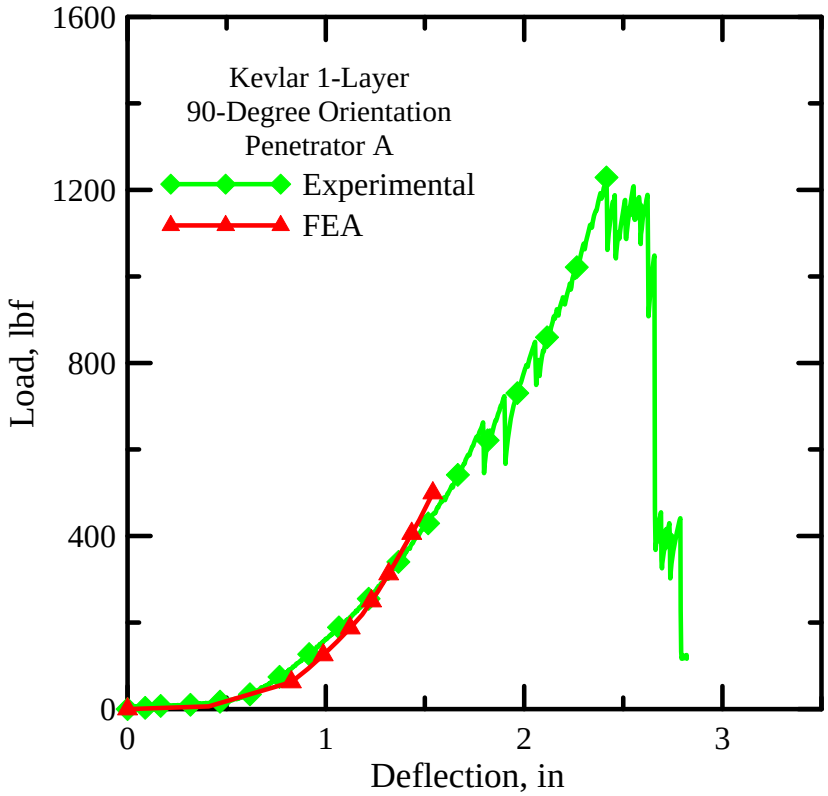

Figure 85a. Comparison of the Load-Displacement Graphs for the One-Layer Kevlar, 90-Degree Orientation, Thicker Blunt-Nose Test

Table 32. Static Test—FEA Comparison for the One-Layer Kevlar, 90-Degree Orientation, Thicker Blunt-Nose Test

	Static Test	FEA
Peak load (lb)	1228	543
Displacement at peak load (in.)	2.416	1.571

The experimental curve was slack-shifted by 0.31 inch.

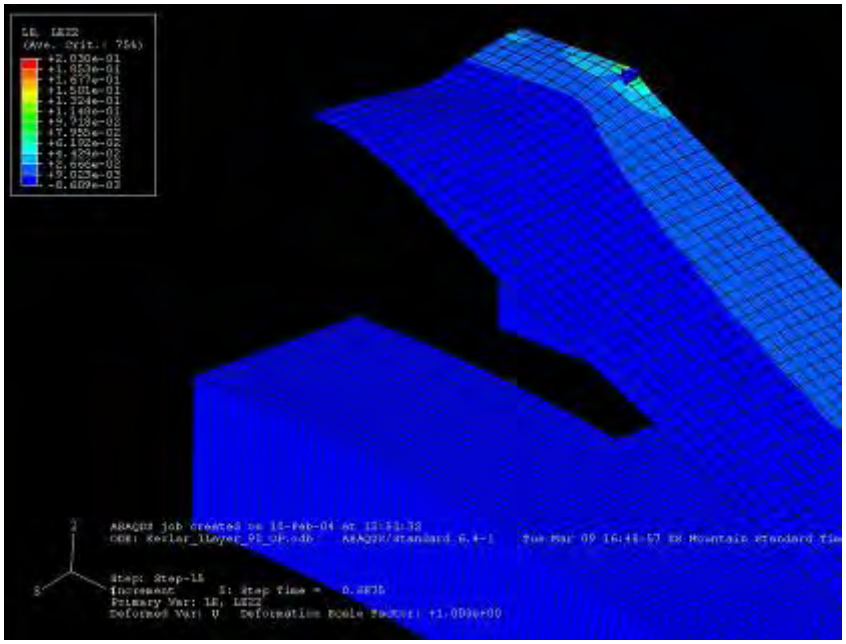

Figure 85b. One-Layer Kevlar—90-Degree Orientation (Thicker Blunt Nose)—Plot of In-Plane Strain ε_1 Superimposed on Deformation at the End of the Last Load Step

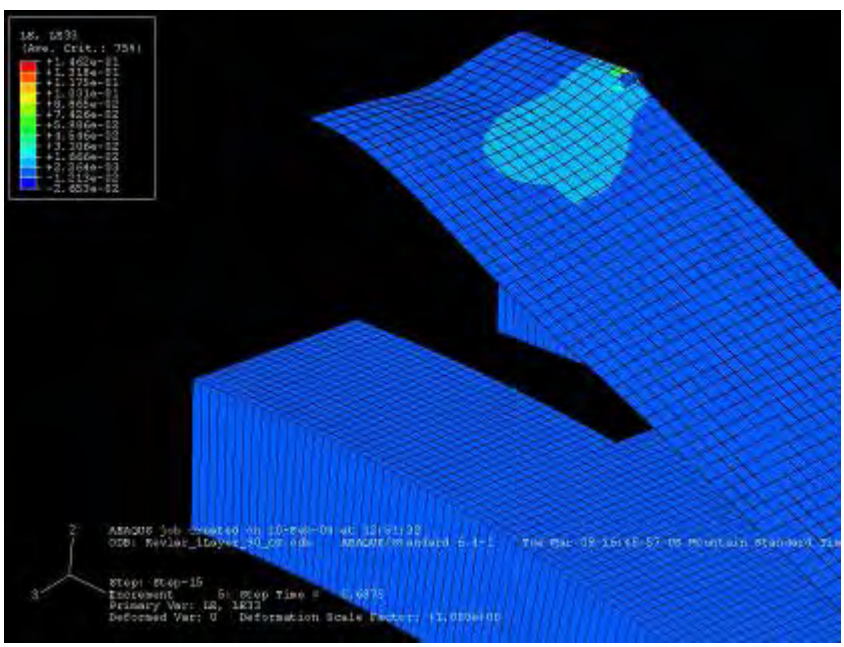

Figure 85c. One-Layer Kevlar—90-Degree Orientation (Thicker Blunt Nose)—Plot of In-Plane Strain ε_2 Superimposed on Deformation at the End of the Last Load Step

Figure 86a and table 33 compare the static test FE simulation to the experimental results for the one-layer Kevlar, off-center 0-degree orientation, thicker blunt-nose test case. Figures 86b and 86c show the FE simulation deformation.

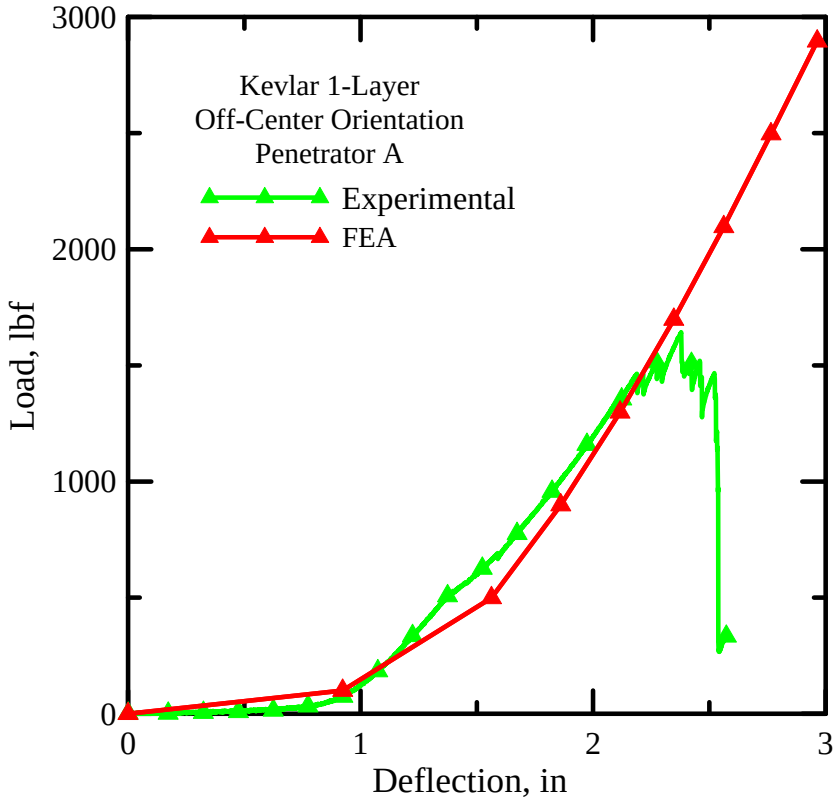

Figure 86a. Comparison of the Load-Displacement Graphs for the One-Layer Kevlar, Off-Center Orientation, Thicker Blunt-Nose Test

Table 33. Static Test—FEA Comparison for the One-Layer Kevlar, Off-Center Orientation, Thicker Blunt-Nose Test

	Static Test	FEA
Peak load (lb)	1642	2987
Displacement at peak load (in.)	2.329	2.954

The experimental curve was slack-shifted by 0.05 inch.

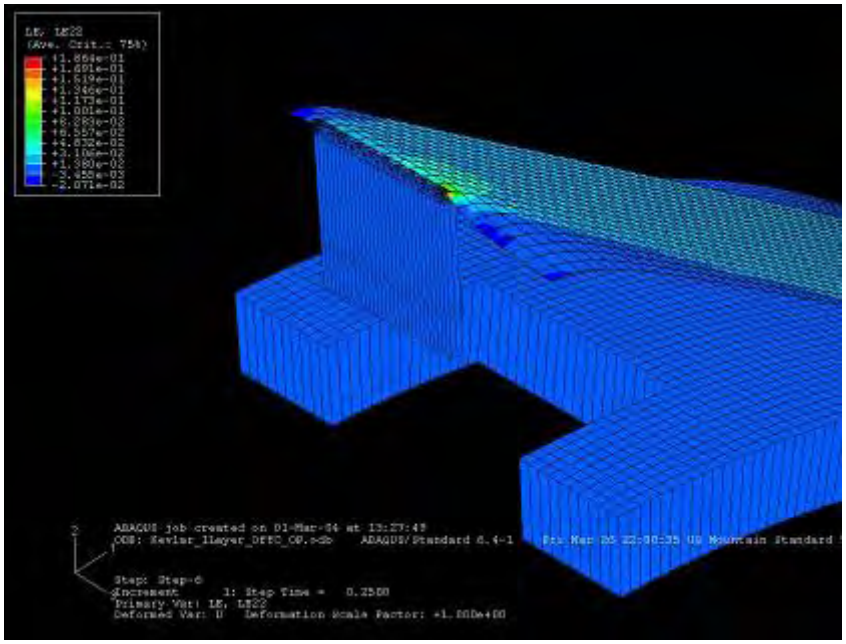

Figure 86b. One-Layer Kevlar—Off-Center Orientation (Thicker Blunt Nose)—Plot of In-Plane Strain ε_1 Superimposed on Deformation at the End of the Last Load Step

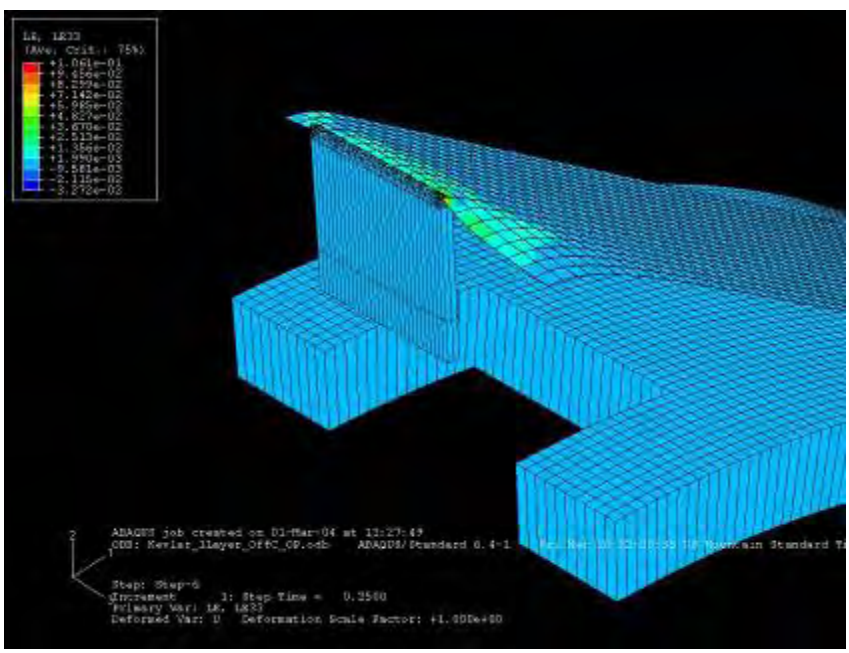

Figure 86c. One-Layer Kevlar—Off-Center Orientation (Thicker Blunt Nose)—Plot of In-Plane Strain ε_2 Superimposed on Deformation at the End of the Last Load Step

5.3.1.2 Four Layer.

Figure 87a and table 34 compare the static test FE simulation to the experimental results for the four-layer Kevlar, 0-degree orientation, thinner blunt-nose test case. Figures 87b and 87c show the FE simulation deformation.

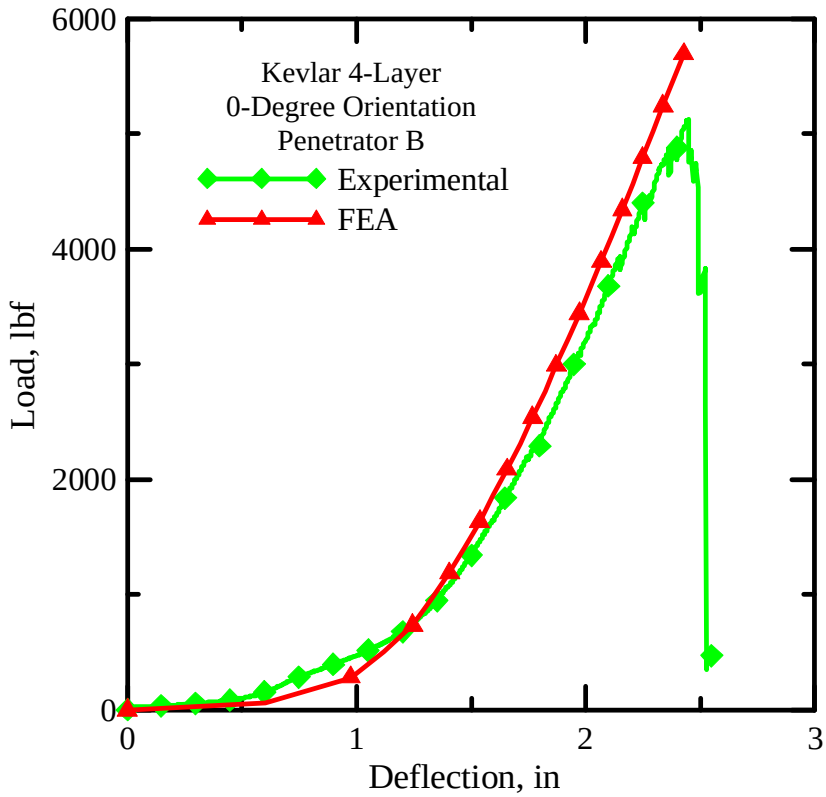

Figure 87a. Comparison of the Load-Displacement Graphs for the Four-Layer Kevlar, 0-Degree Orientation, Thinner Blunt-Nose Test

Table 34. Static Test—FEA Comparison for the Four-Layer Kevlar, 0-Degree Orientation, Thinner Blunt-Nose Test

	Static Test	FEA
Peak load (lb)	5169	5745
Displacement at peak load (in.)	2.451	2.45

The experimental curve was slack-shifted by 0.47 inch.

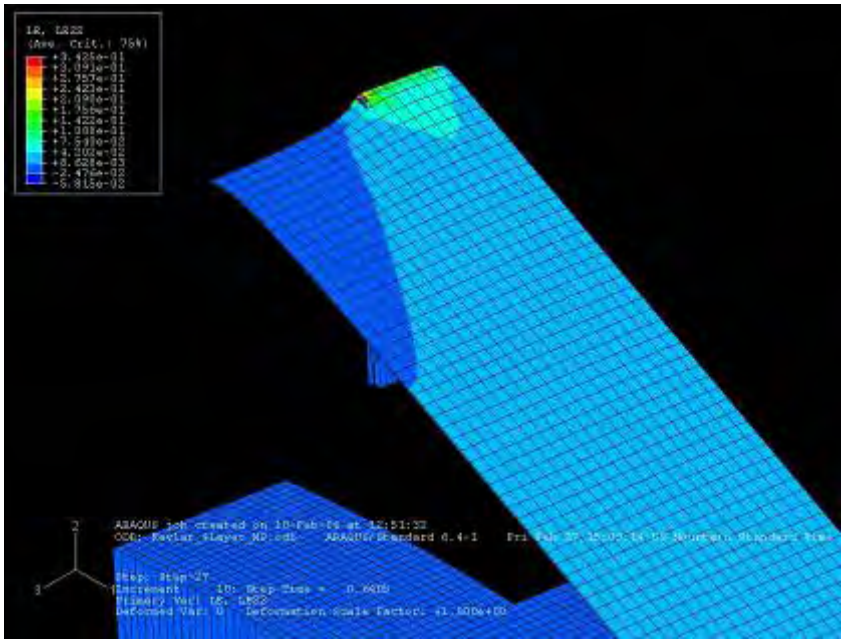

Figure 87b. Four-Layer Kevlar—0-Degree Orientation (Thinner Blunt Nose)—Plot of In-Plane Strain ε_1 Superimposed on Deformation at the End of the Last Load Step

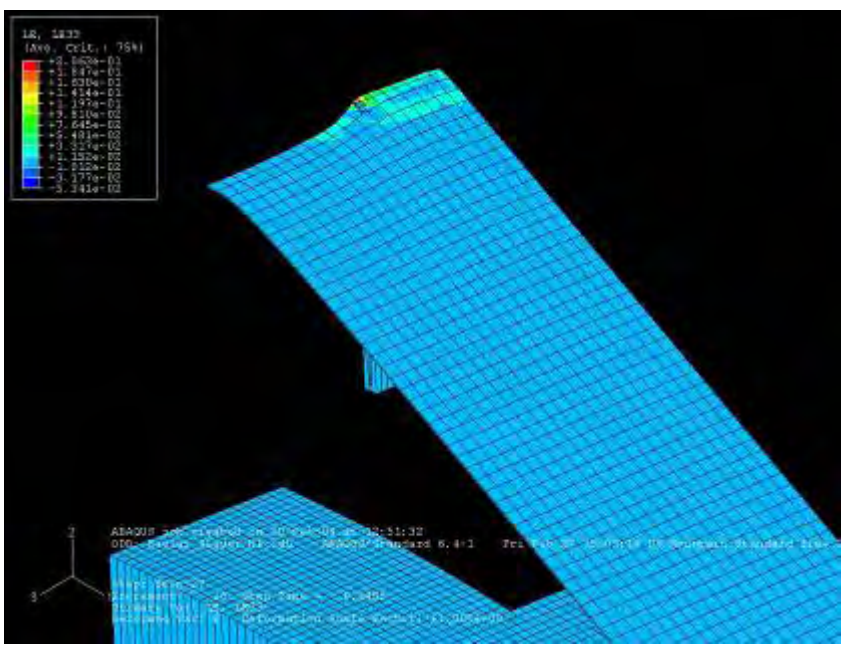

Figure 87c. Four-Layer Kevlar—0-Degree Orientation (Thinner Blunt Nose)—Plot of In-Plane Strain ε_2 Superimposed on Deformation at the End of the Last Load Step

Figure 88a and table 35 compare the static test FE simulation to the experimental results for the four-layer Kevlar, 45-degree orientation, thinner blunt-nose test case. Figures 88b and 88c show the FE simulation deformation.

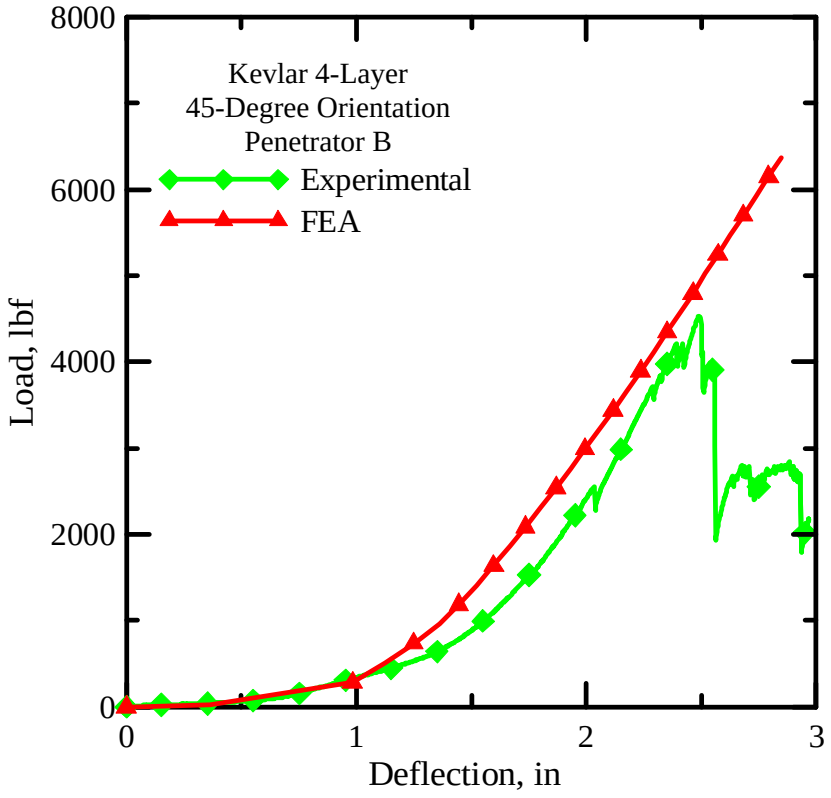

Figure 88a. Comparison of the Load-Displacement Graphs for the Four-Layer Kevlar, 45-Degree Orientation, Thinner Blunt-Nose Test

Table 35. Static Test—FEA Comparison for the Four-Layer Kevlar, 45-Degree Orientation, Thinner Blunt-Nose Test

	Static Test	FEA
Peak load (lb)	4552	6373
Displacement at peak load (in.)	2.491	2.85

The experimental curve was slack-shifted by 0.48 inch.

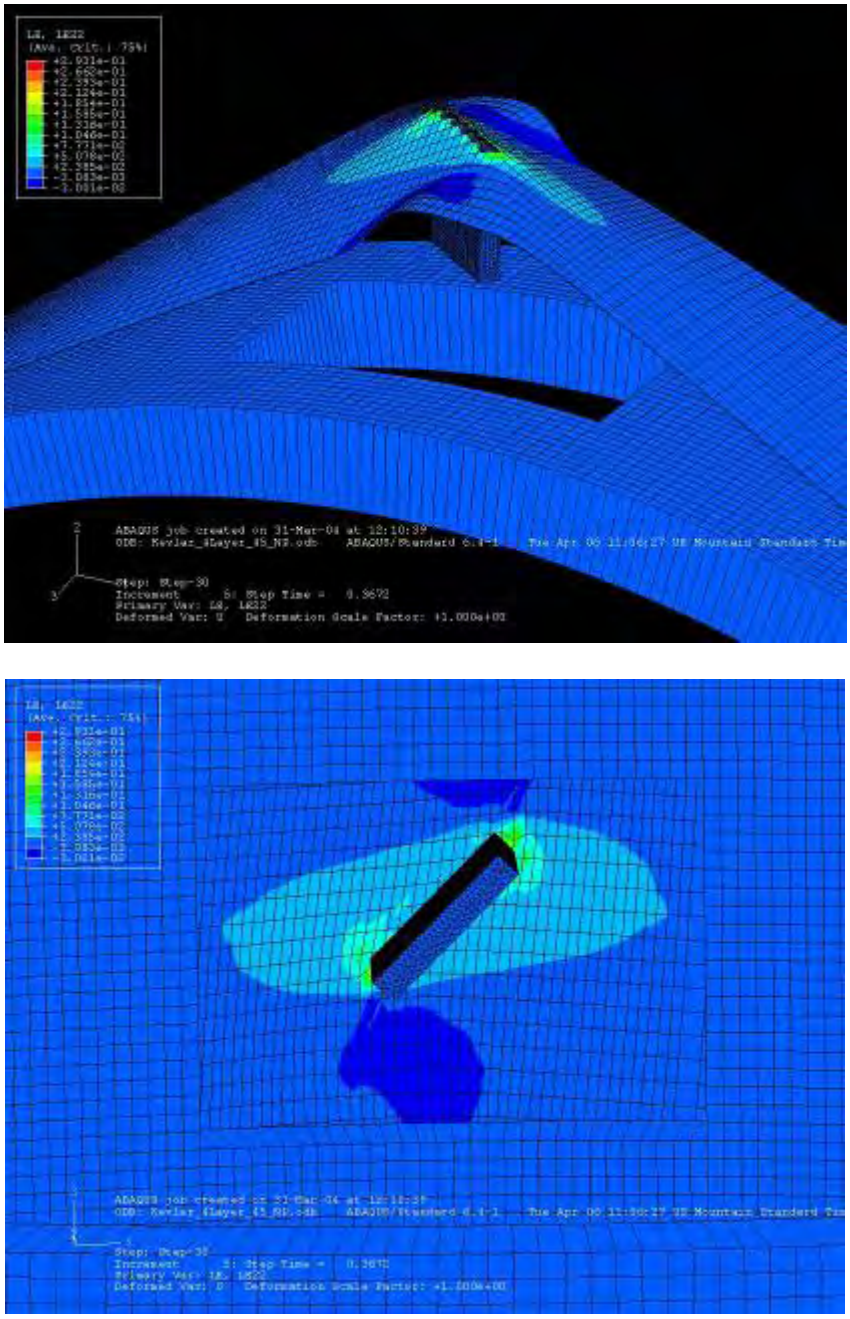

Figure 88b. Four-Layer Kevlar—45-Degree Orientation (Thinner Blunt Nose)—Plot of In-Plane Strain ε_1 Superimposed on Deformation at the End of the Last Load Step

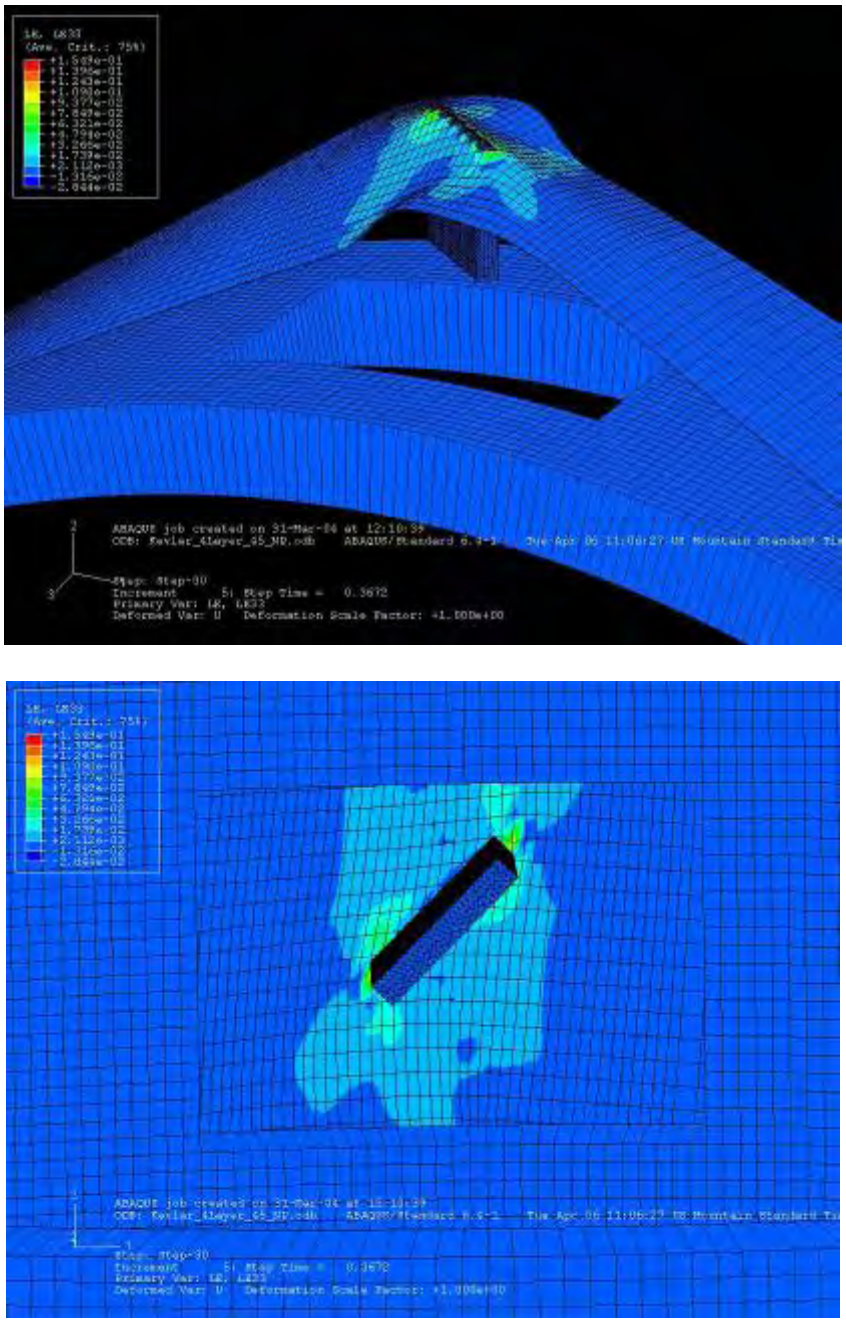

Figure 88c. Four-Layer Kevlar—45-Degree Orientation (Thinner Blunt Nose)—Plot of In-Plane Strain ε_2 Superimposed on Deformation at the End of the Last Load Step

Figure 89a and table 36 compare the static test FE simulation to the experimental results for the four-layer Kevlar, 90-degree orientation, thinner blunt-nose test case. Figures 89b and 89c show the FE simulation deformation.

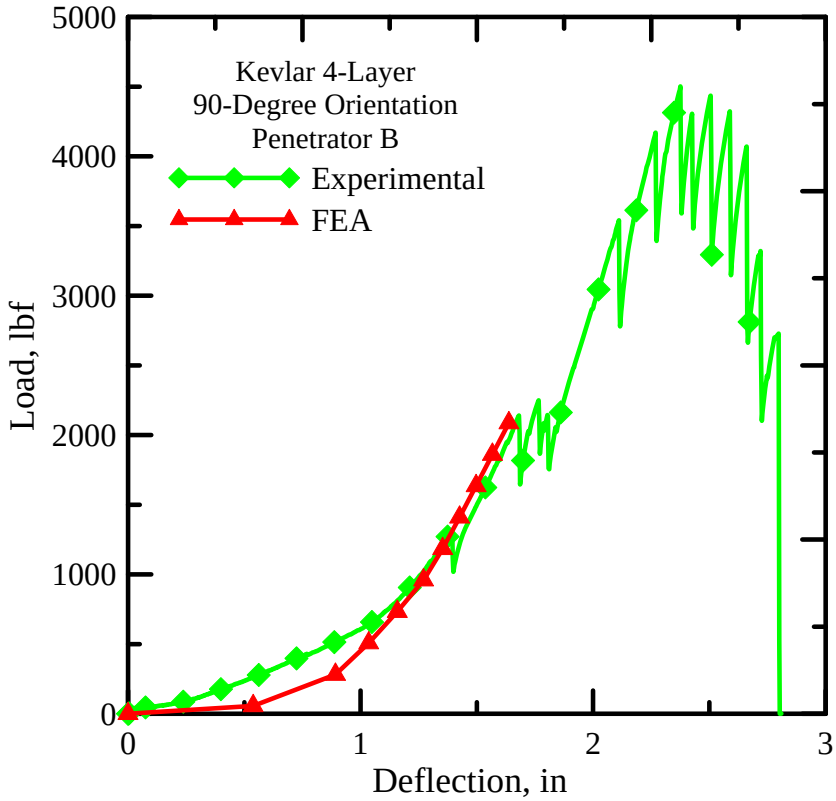

Figure 89a. Comparison of the Load-Displacement Graphs for the Four-Layer Kevlar, 90-Degree Orientation, Thinner Blunt-Nose Test

Table 36. Static Test—FEA Comparison for the Four-Layer Kevlar, 90-Degree Orientation, Thinner Blunt-Nose Test

	Static Test	FEA
Peak load (lb)	4511	2087
Displacement at peak load (in.)	2.379	1.638

The experimental curve was slack-shifted by 0.63 inch.

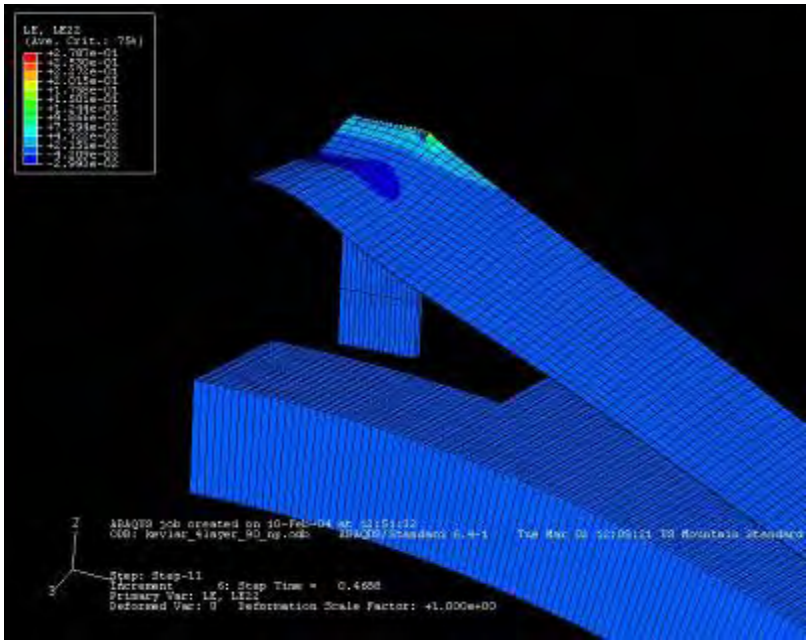

Figure 89b. Four-Layer Kevlar—90-Degree Orientation (Thinner Blunt Nose)—Plot of In-Plane Strain ε_1 Superimposed on Deformation at the End of the Last Load Step

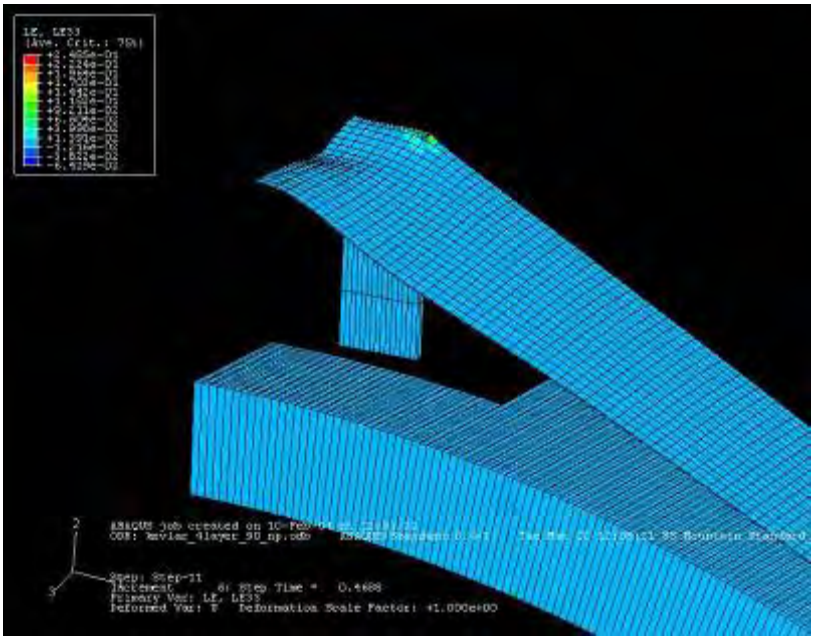

Figure 89c. Four-Layer Kevlar—90-Degree Orientation (Thinner Blunt Nose)—Plot of In-Plane Strain ε_2 Superimposed on Deformation at the End of the Last Load Step

Figure 90a and table 37 compare the static test FE simulation to the experimental results for the four-layer Kevlar, off-center 0-degree orientation, thinner blunt-nose test case. Figures 90b and 90c show the FE simulation deformation.

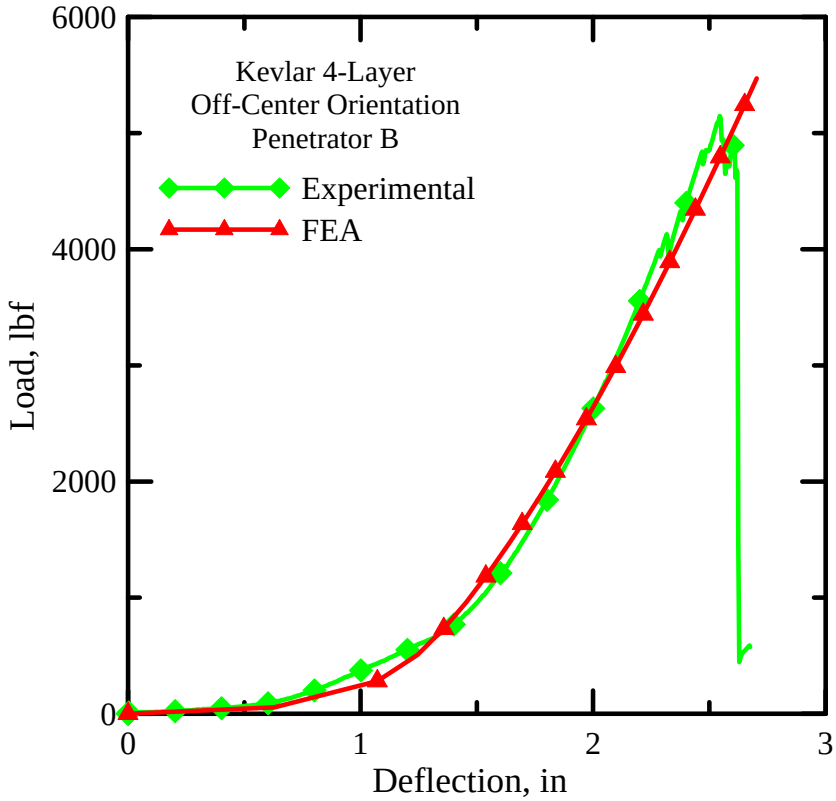

Figure 90a. Comparison of the Load-Displacement Graphs for the Four-Layer Kevlar, Off-Center Orientation, Thinner Blunt-Nose Test

Table 37. Static Test—FEA Comparison for the Four-Layer Kevlar, Off-Center Orientation, Thinner Blunt-Nose Test

	Static Test	FEA
Peak load (lb)	5181	5471
Displacement at peak load (in.)	2.352	2.62

The experimental curve was slack-shifted by 0.31 inch.

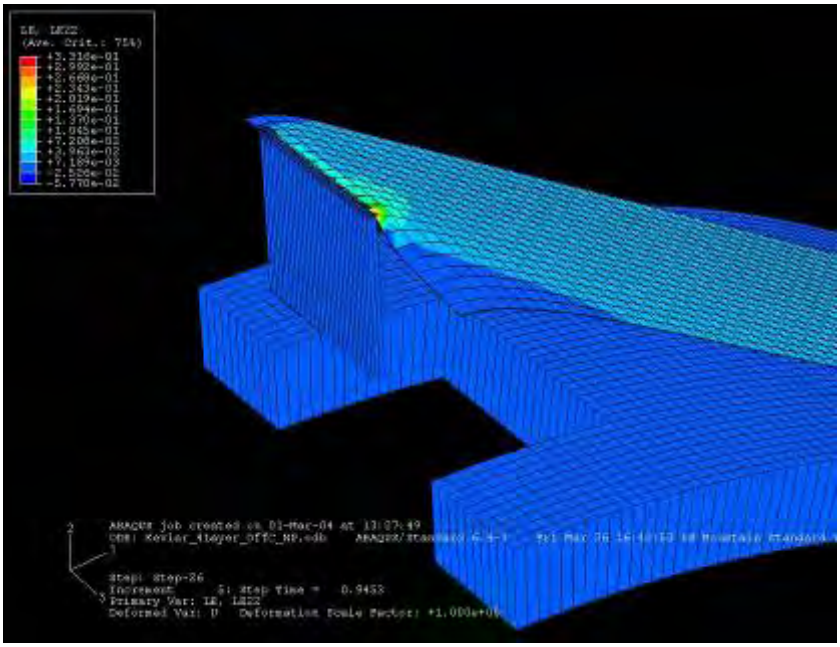

Figure 90b. Four-Layer Kevlar—Off-Center Orientation (Thinner Blunt Nose)—Plot of In-Plane Strain ε_1 Superimposed on Deformation at the End of the Last Load Step

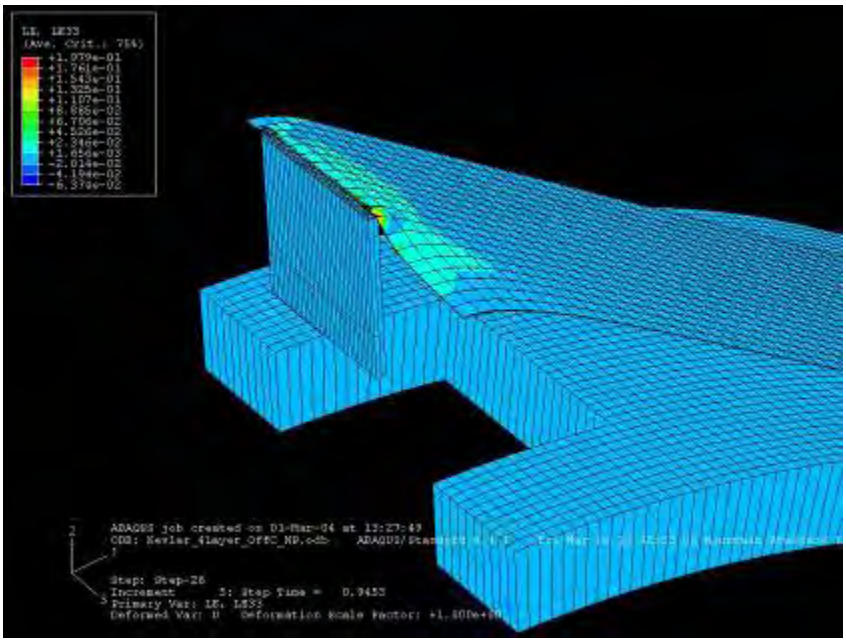

Figure 90c. Four-Layer Kevlar—Off-Center Orientation (Thinner Blunt Nose)—Plot of In-Plane Strain ε_2 Superimposed on Deformation at the End of the Last Load Step

Figure 91a and table 38 compare the static test FE simulation to the experimental results for the four-layer Kevlar, 45-degree orientation, thicker blunt-nose test case. Figures 91b and 91c show the FE simulation deformation.

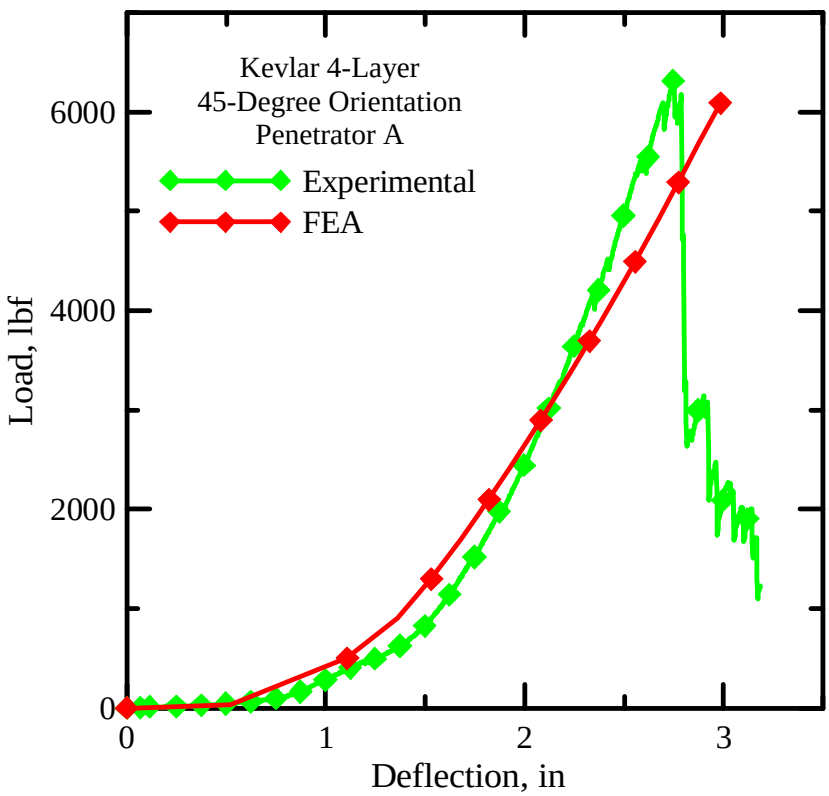

Figure 91a. Comparison of the Load-Displacement Graphs for the Four-Layer Kevlar, 45-Degree Orientation, Thicker Blunt-Nose Test

Table 38. Static Test—FEA Comparison for the Four-Layer Kevlar, 45-Degree Orientation, Thicker Blunt-Nose Test

	Static Test	FEA
Peak load (lb)	6363	5691
Displacement at peak load (in.)	2.751	1.933

The experimental curve was slack-shifted by 0.24 inch.

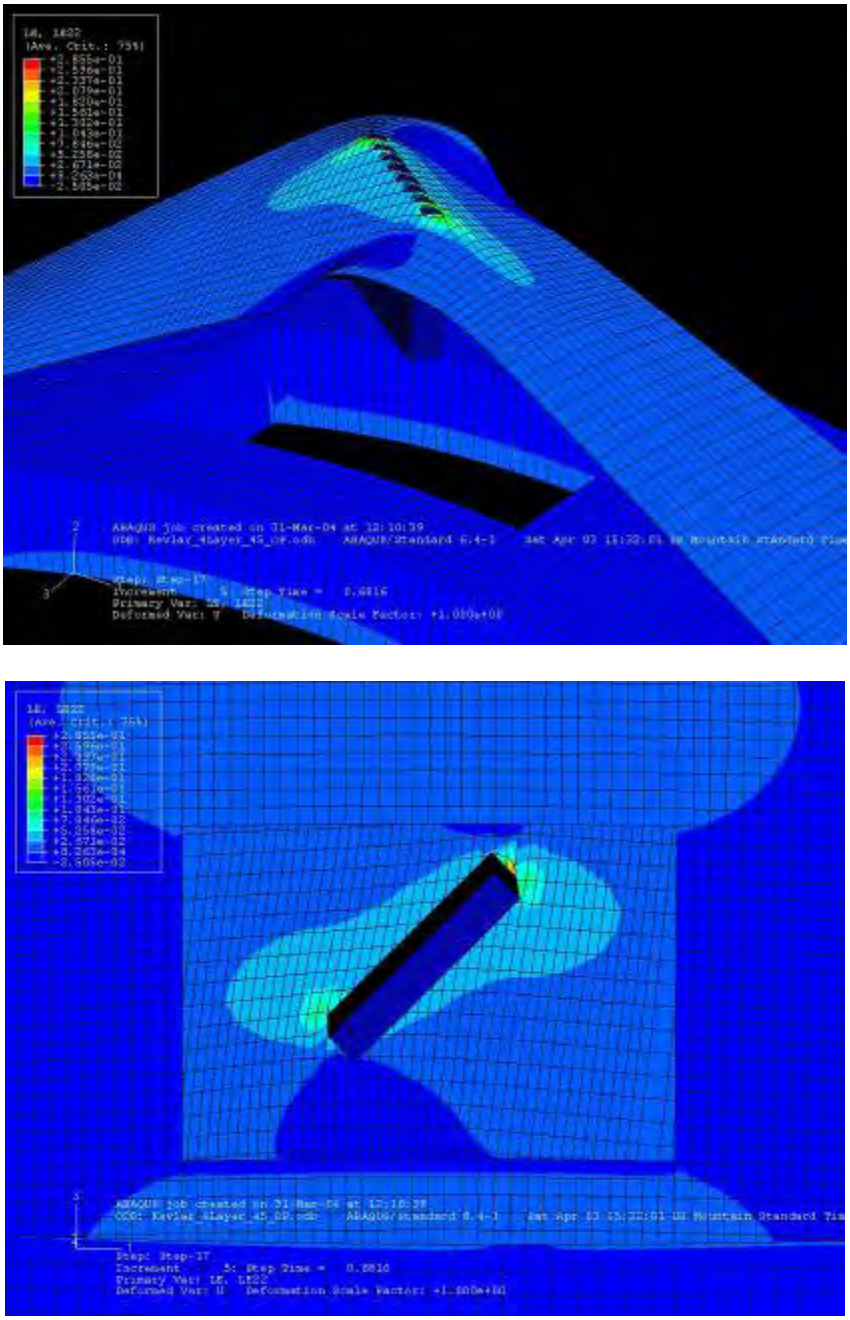

Figure 91b. Four-Layer Kevlar—45-Degree Orientation (Thicker Blunt Nose)—Plot of In-Plane Strain ε_1 Superimposed on Deformation at the End of the Last Load Step

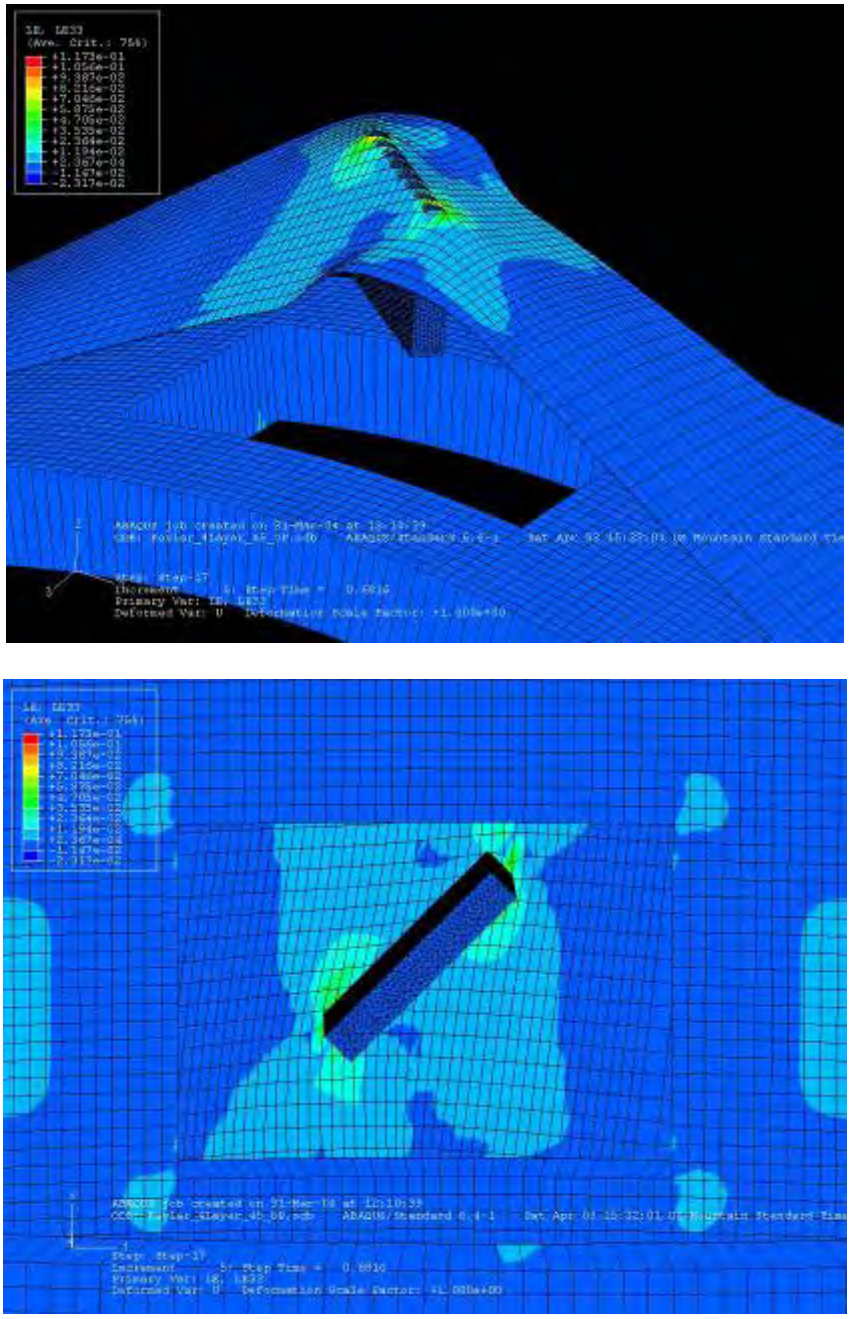

Figure 91c. Four-Layer Kevlar—45-Degree Orientation (Thicker Blunt Nose)—Plot of In-Plane Strain ε_2 Superimposed on Deformation at the End of the Last Load Step

Figure 92a and table 39 compare the static test FE simulation to the experimental results for the four-layer Kevlar, 90-degree orientation, thicker blunt-nose test case. Figures 92b and 92c show the FE simulation deformation.

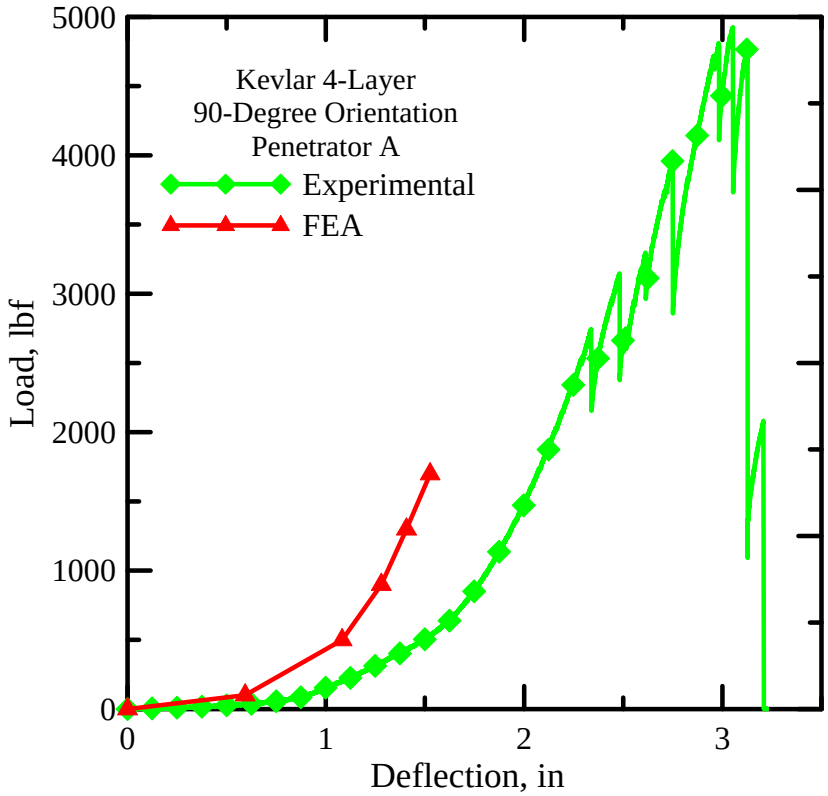

Figure 92a. Comparison of the Load-Displacement Graphs for the Four-Layer Kevlar, 90-Degree Orientation, Thicker Blunt-Nose Test

Table 39. Static Test—FEA Comparison for the Four-Layer Kevlar, 90-Degree Orientation, Thicker Blunt-Nose Test

	Static Test	FEA
Peak load (lb)	4925	1697
Displacement at peak load (in.)	2.866	1.494

The experimental curve was slack-shifted by 0.48 inch.

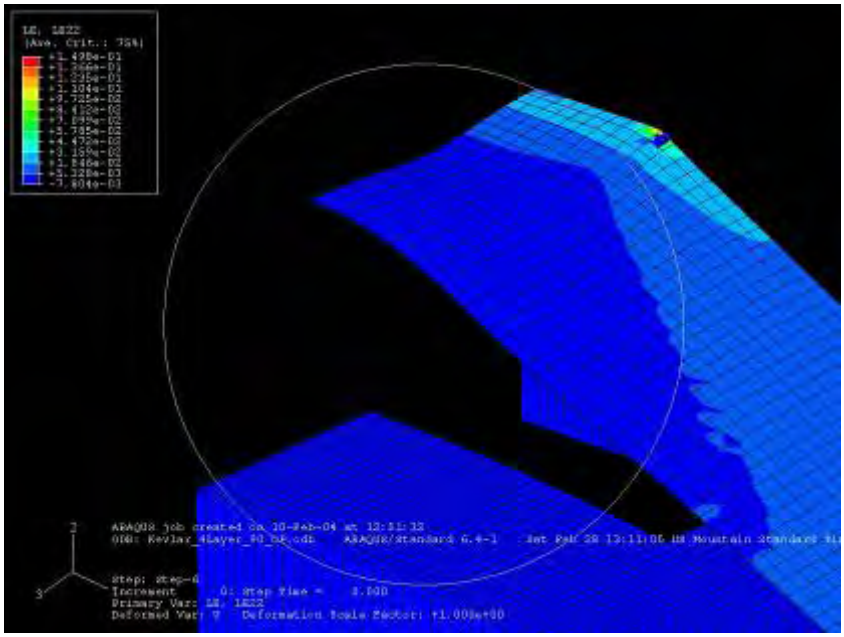

Figure 92b. Four-Layer Kevlar—90-Degree Orientation (Thicker Blunt Nose)—Plot of In-Plane Strain ε_1 Superimposed on Deformation at the End of the Last Load Step

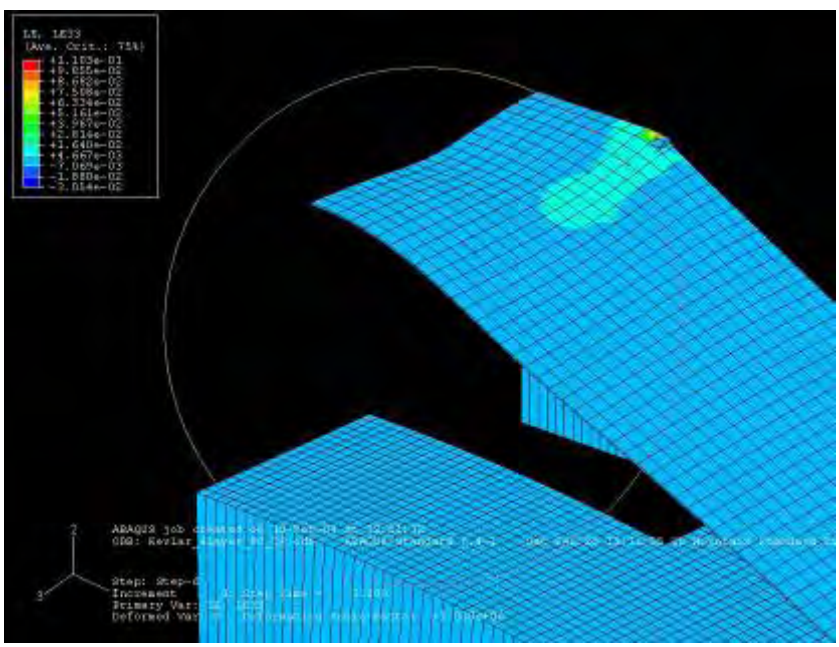

Figure 92c. Four-Layer Kevlar—90-Degree Orientation (Thicker Blunt Nose)—Plot of In-Plane Strain ε_2 Superimposed on Deformation at the End of the Last Load Step

Figure 93a and table 40 compare the static test FE simulation to the experimental results for the four-layer Kevlar, 0-degree off-center orientation, thicker blunt-nose test case. Figures 93b and 93c show the FE simulation deformation.

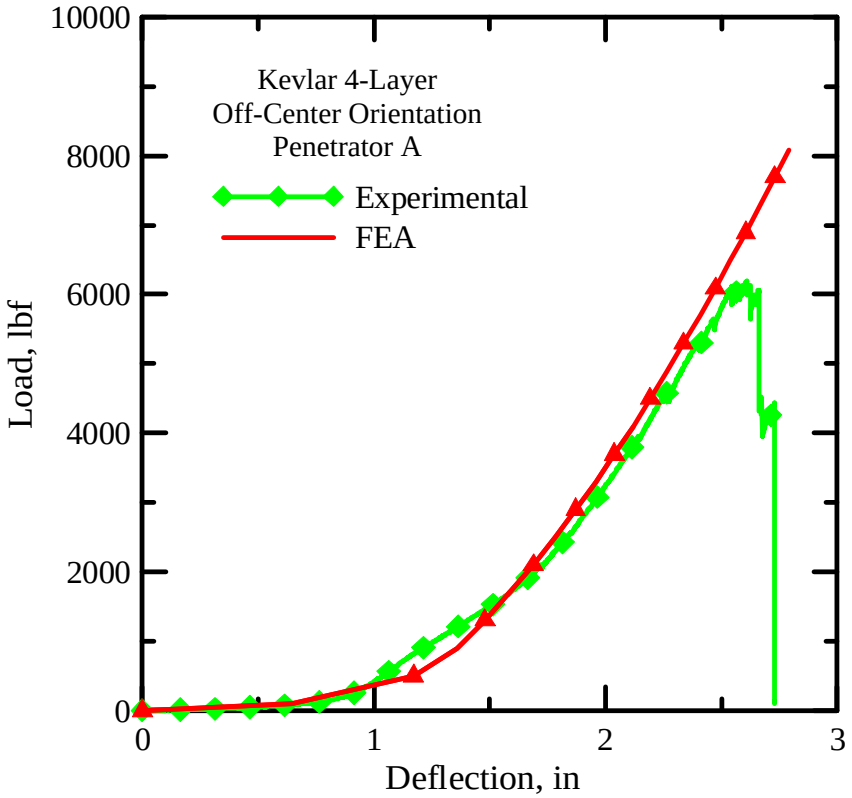

Figure 93a. Comparison of the Load-Displacement Graphs for the Four-Layer Kevlar, Off-Center Orientation, Thicker Blunt-Nose Test

Table 40. Static Test—FEA Comparison for the Four-Layer Kevlar, Off-Center Orientation, Thicker Blunt-Nose Test

	Static Test	FEA
Peak load (lb)	6202	8087
Displacement at peak load (in.)	2.611	2.754

The experimental curve was not slack-shifted.

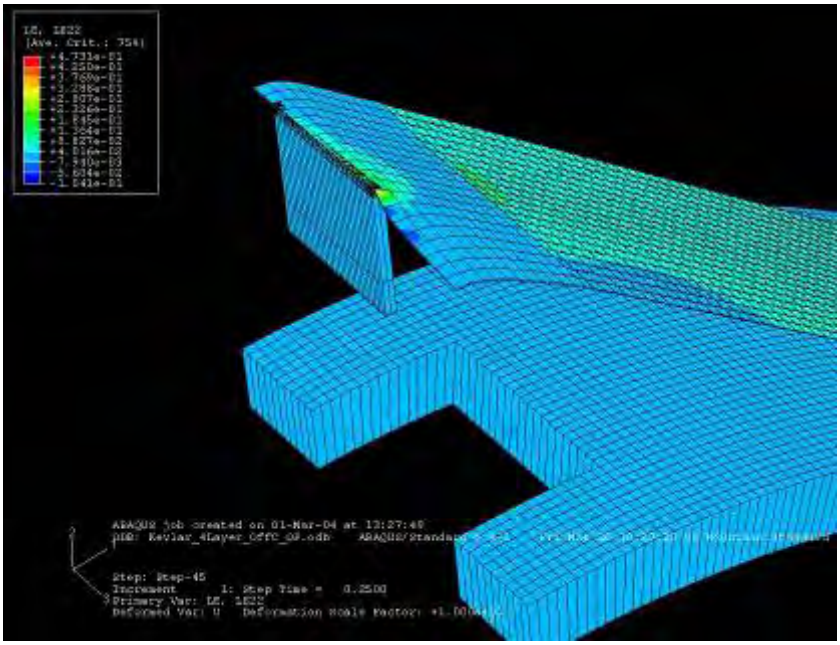

Figure 93b. Four-Layer Kevlar—Off-Center Orientation (Thicker Blunt Nose)—Plot of In-Plane Strain ε_1 Superimposed on Deformation at the End of the Last Load Step

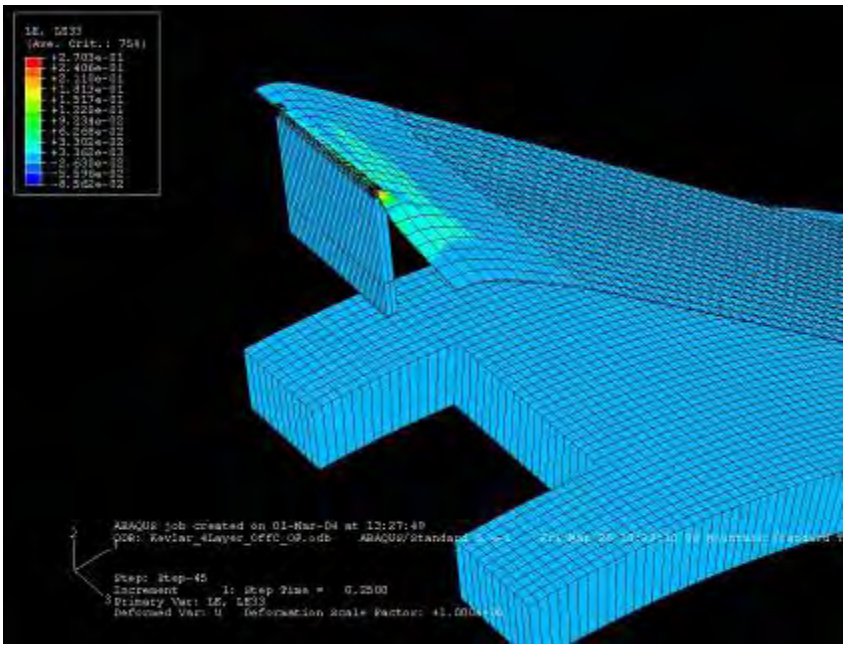

Figure 93c. Four-Layer Kevlar—Off-Center Orientation (Thicker Blunt Nose)—Plot of In-Plane Strain ε_2 Superimposed on Deformation at the End of the Last Load Step

5.3.1.3 Eight Layer.

Figure 94a and table 41 compare the static test FE simulation to the experimental results for the eight-layer Kevlar, 0-degree orientation, thinner blunt-nose test case. Figures 94b and 94c show the FE simulation deformation.

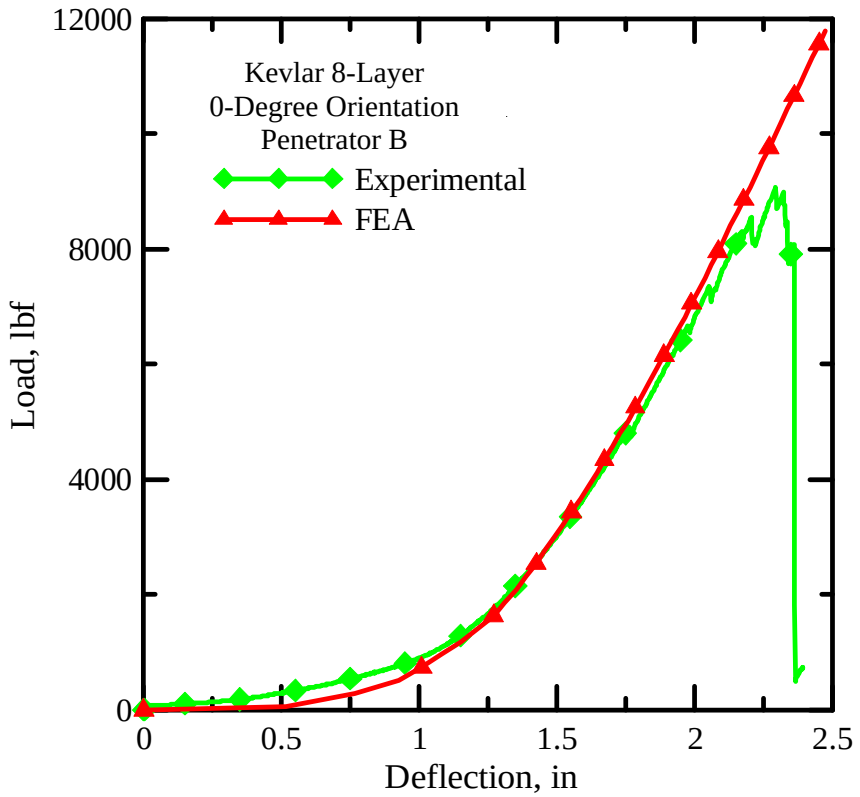

Figure 94a. Comparison of the Load-Displacement Graphs for the Eight-Layer Kevlar, 0-Degree Orientation, Thinner Blunt-Nose Test

Table 41. Static Test—FEA Comparison for the Eight-Layer Kevlar, 0-Degree Orientation, Thinner Blunt-Nose Test

	Static Test	FEA
Peak load (lb)	9095	11788
Displacement at peak load (in.)	2.295	2.473

The experimental curve was slack-shifted by 0.6 inch.

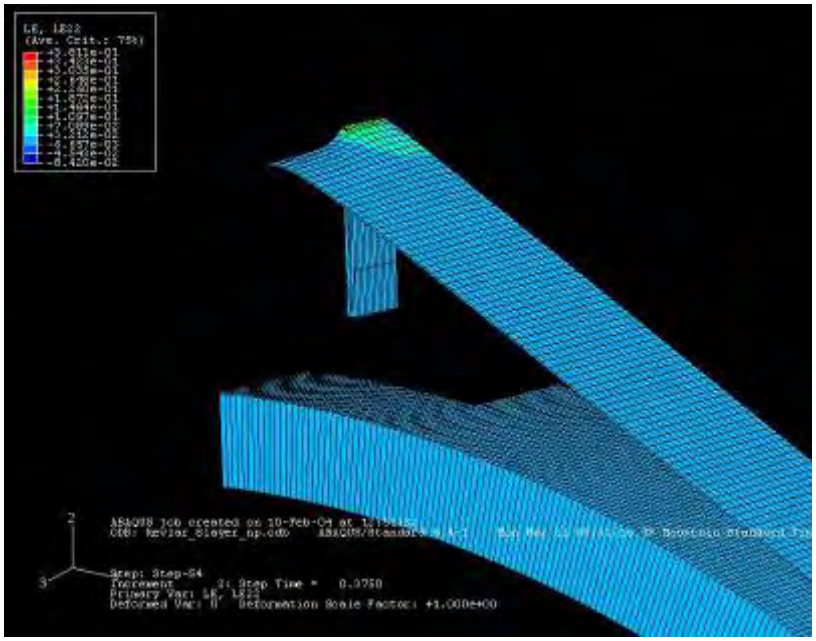

Figure 94b. Eight-Layer Kevlar—0-Degree Orientation (Thinner Blunt Nose)—Plot of In-Plane Strain ε_1 Superimposed on Deformation at the End of the Last Load Step

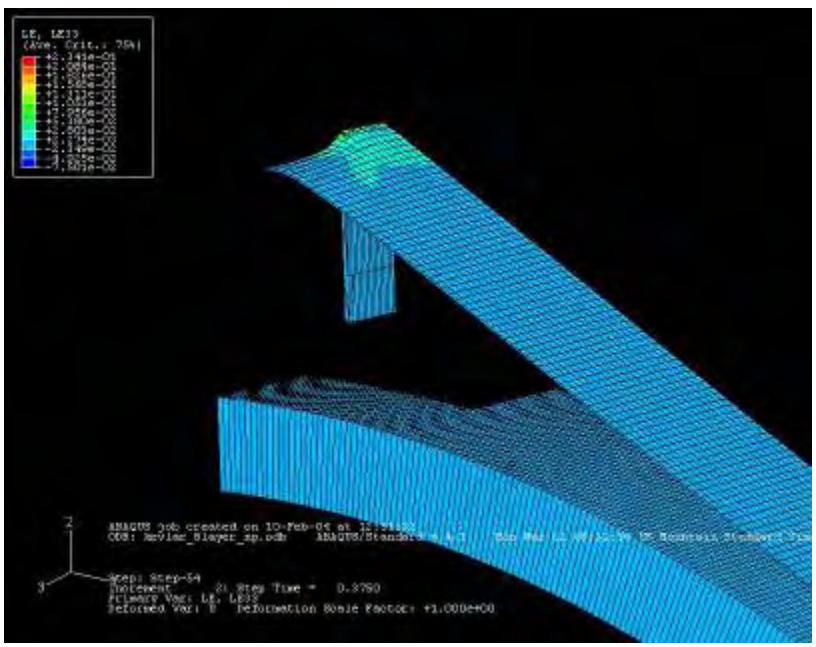

Figure 94c. Eight-Layer Kevlar—0-Degree Orientation (Thinner Blunt Nose)—Plot of In-Plane Strain ε_2 Superimposed on Deformation at the End of the Last Load Step

Figure 95a and table 42 compare the static test FE simulation to the experimental results for the eight-layer Kevlar, 45-degree orientation, thinner blunt-nose test case. Figures 95b and 95c show the FE simulation deformation.

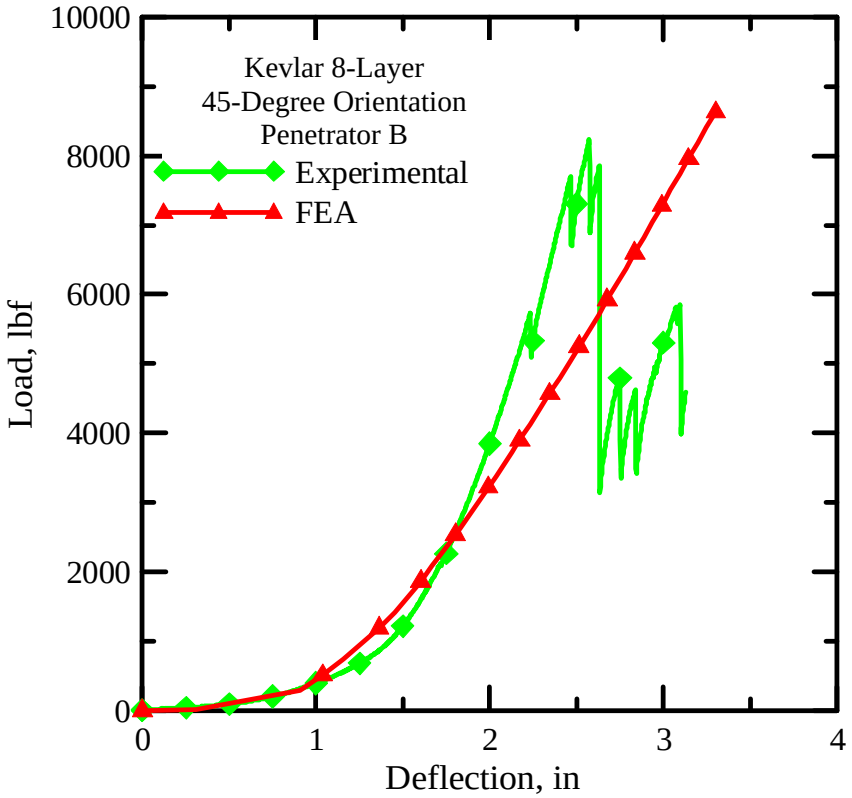

Figure 95a. Comparison of the Load-Displacement Graphs for the Eight-Layer Kevlar, 45-Degree Orientation, Thinner Blunt-Nose Test

Table 42. Static Test—FEA Comparison for the Eight-Layer Kevlar, 45-Degree Orientation, Thinner Blunt-Nose Test

	Static Test	FEA
Peak load (lb)	8257	8629
Displacement at peak load (in.)	2.577	3.301

The experimental curve was slack-shifted by 0.14 inch.

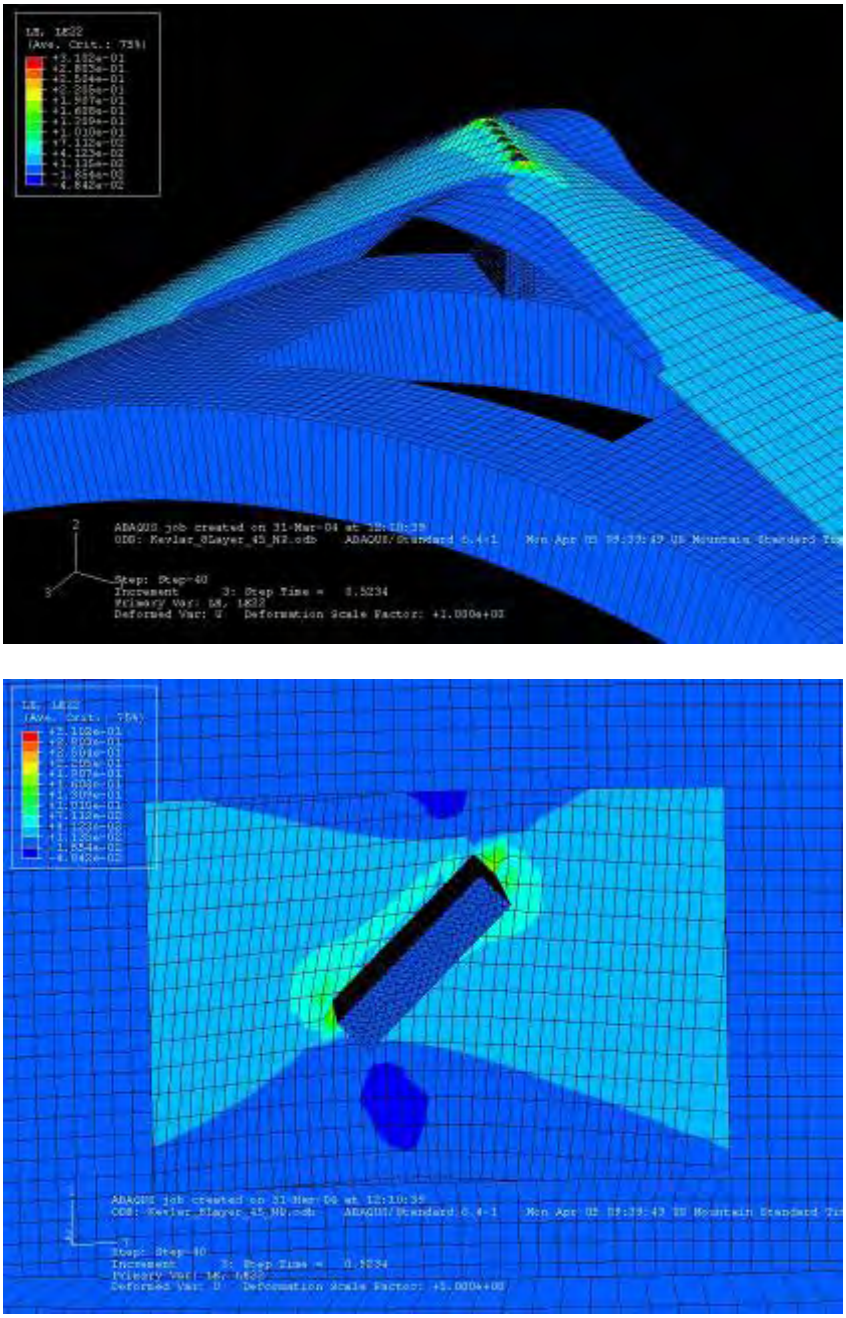

Figure 95b. Eight-Layer Kevlar—45-Degree Orientation (Thinner Blunt Nose)—Plot of In-Plane Strain ε_1 Superimposed on Deformation at the End of the Last Load Step

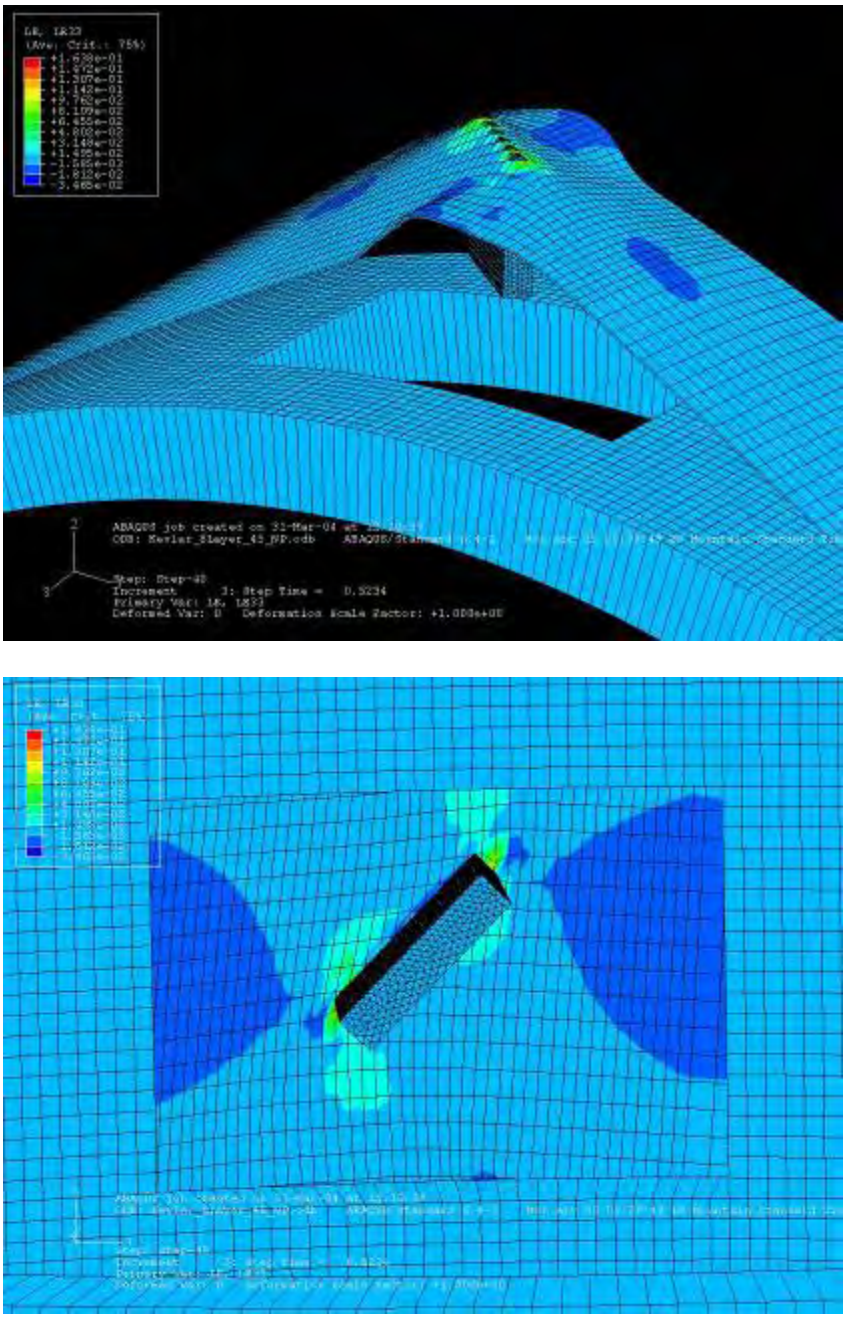

Figure 95c. Eight-Layer Kevlar—45-Degree Orientation (Thinner Blunt Nose)—Plot of In-Plane Strain ε_2 Superimposed on Deformation at the End of the Last Load Step

Figure 96a and table 43 compare the static test FE simulation to the experimental results for the eight-layer Kevlar, 90-degree orientation, thinner blunt-nose test case. Figures 96b and 96c show the FE simulation deformation.

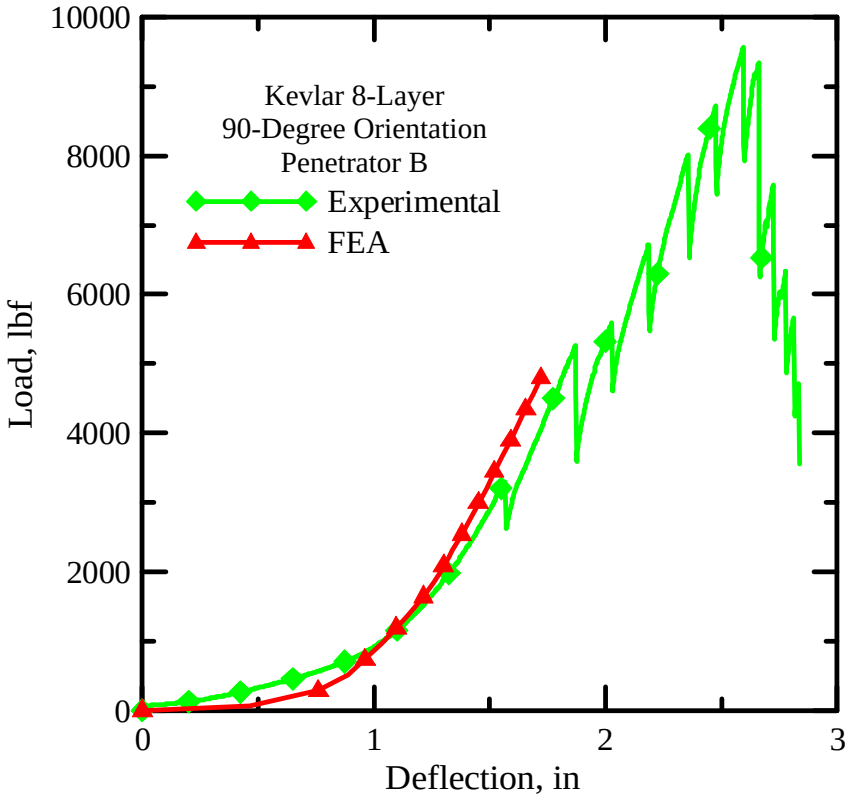

Figure 96a. Comparison of the Load-Displacement Graphs for the Eight-Layer Kevlar, 90-Degree Orientation, Thinner Blunt-Nose Test

Table 43. Static Test—FEA Comparison for the Eight-Layer Kevlar, 90-Degree Orientation, Thinner Blunt-Nose Test

	Static Test	FEA
Peak load (lb)	9575	4794
Displacement at peak load (in.)	2.597	1.72

The experimental curve was slack-shifted by 0.57 inch.

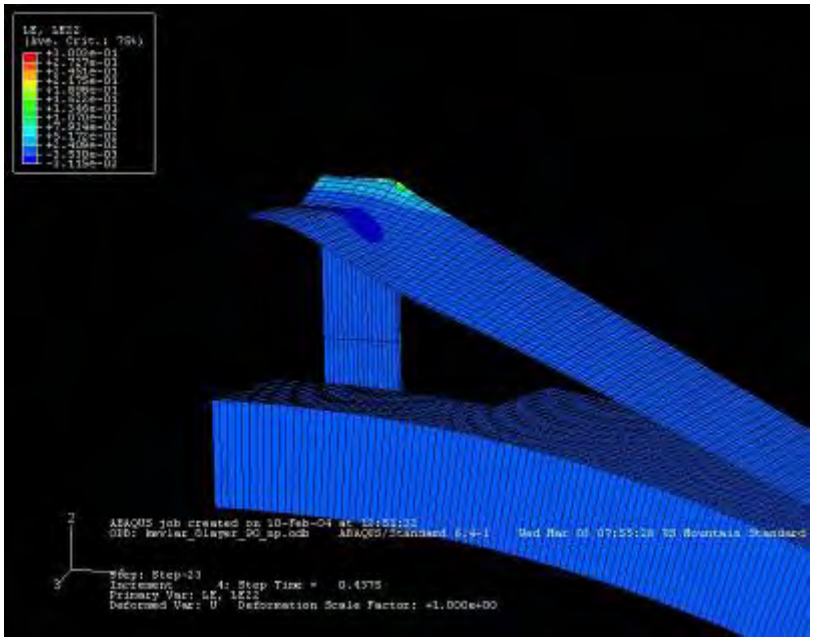

Figure 96b. Eight-Layer Kevlar—90-Degree Orientation (Thinner Blunt Nose)—Plot of In-Plane Strain ε_1 Superimposed on Deformation at the End of the Last Load Step

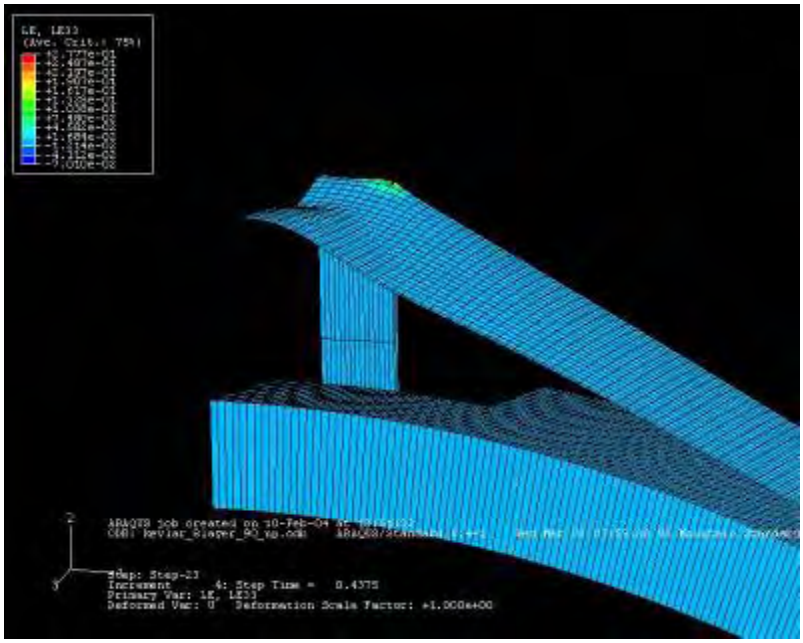

Figure 96c. Eight-Layer Kevlar—90-Degree Orientation (Thinner Blunt Nose)—Plot of In-Plane Strain ε_2 Superimposed on Deformation at the End of the Last Load Step

Figure 97a and table 44 compare the static test FE simulation to the experimental results for the eight-layer Kevlar, 0-degree off-center orientation, thinner blunt-nose test case. Figures 97b and 97c show the FE simulation deformation.

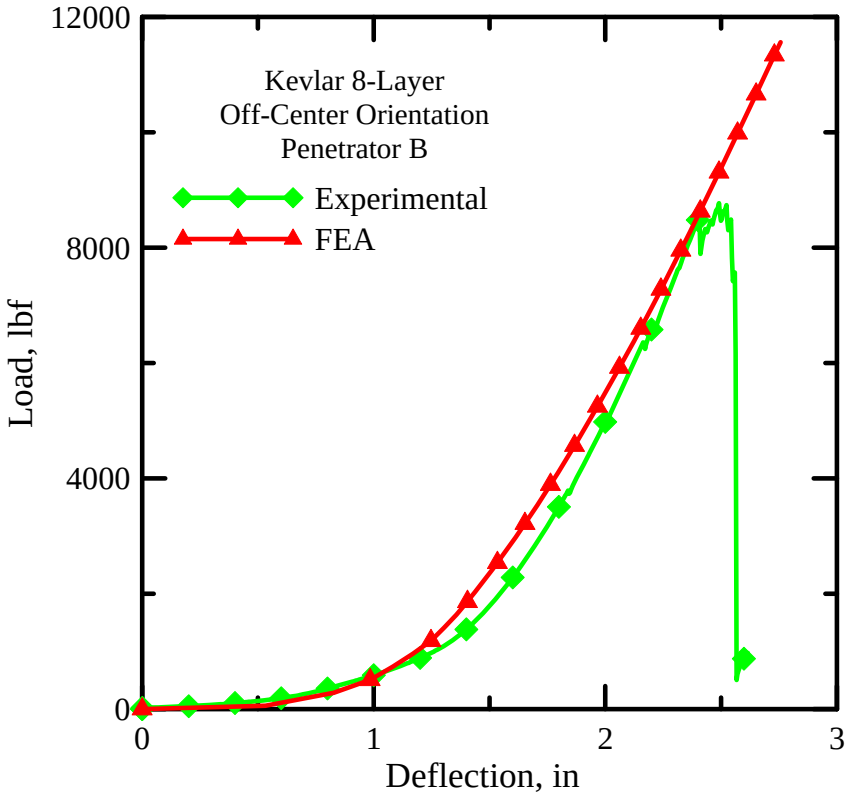

Figure 97a. Comparison of the Load-Displacement Graphs for the Eight-Layer Kevlar, Off-Center Orientation, Thinner Blunt-Nose Test

Table 44. Static Test—FEA Comparison for the Eight-Layer Kevlar, Off-Center Orientation, Thinner Blunt-Nose Test

	Static Test	FEA
Peak load (lb)	8796	11208
Displacement at peak load (in.)	2.493	2.70

The experimental curve was slack-shifted by 0.18 inch.

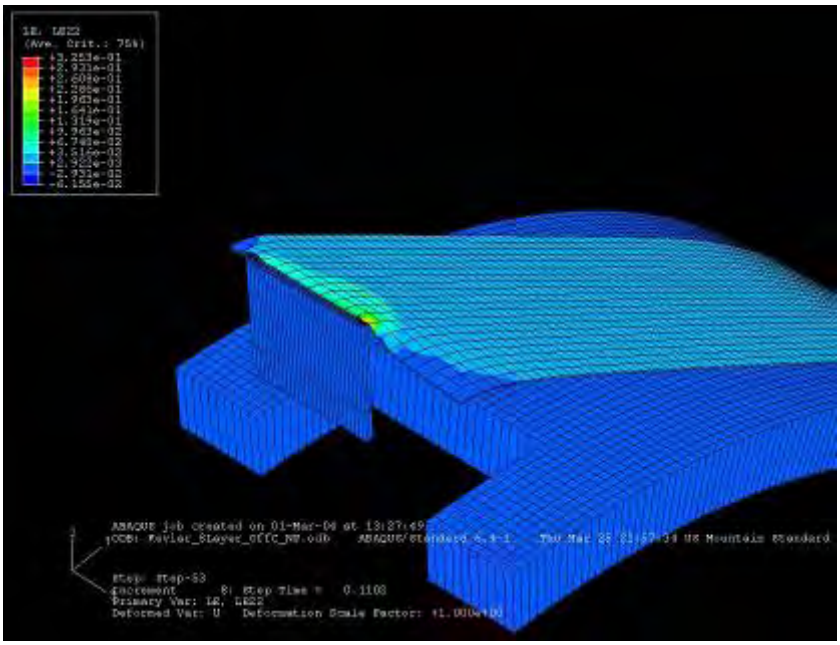

Figure 97b. Eight-Layer Kevlar—Off-Center Orientation (Thinner Blunt Nose)—Plot of In-Plane Strain ε_1 Superimposed on Deformation at the End of the Last Load Step

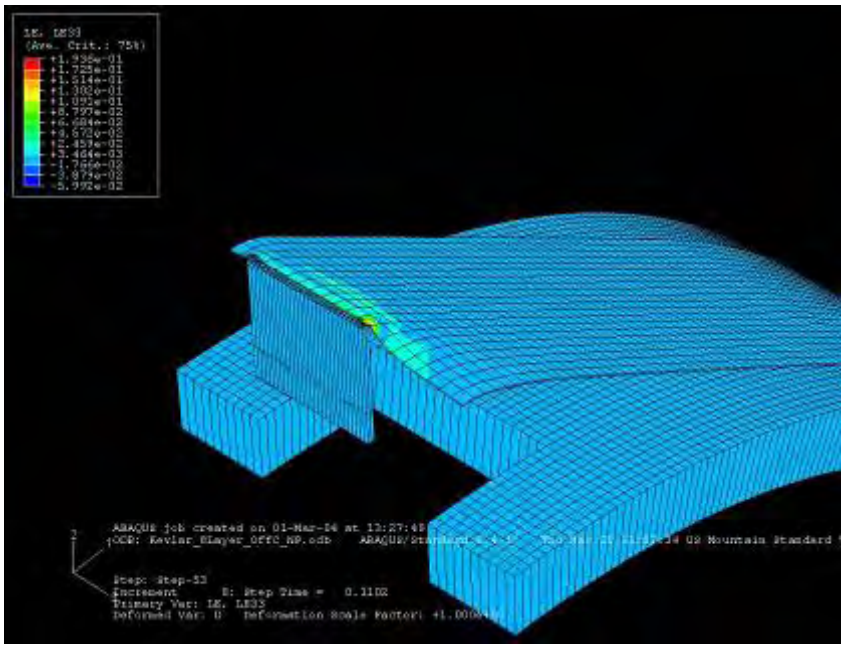

Figure 97c. Eight-Layer Kevlar—Off-Center Orientation (Thinner Blunt Nose)—Plot of In-Plane Strain ε_2 Superimposed on Deformation at the End of the Last Load Step

Figure 98a and table 45 compare the static test FE simulation to the experimental results for the eight-layer Kevlar, 45-degree orientation, thicker blunt-nose test case. Figures 98b and 98c show the FE simulation deformation.

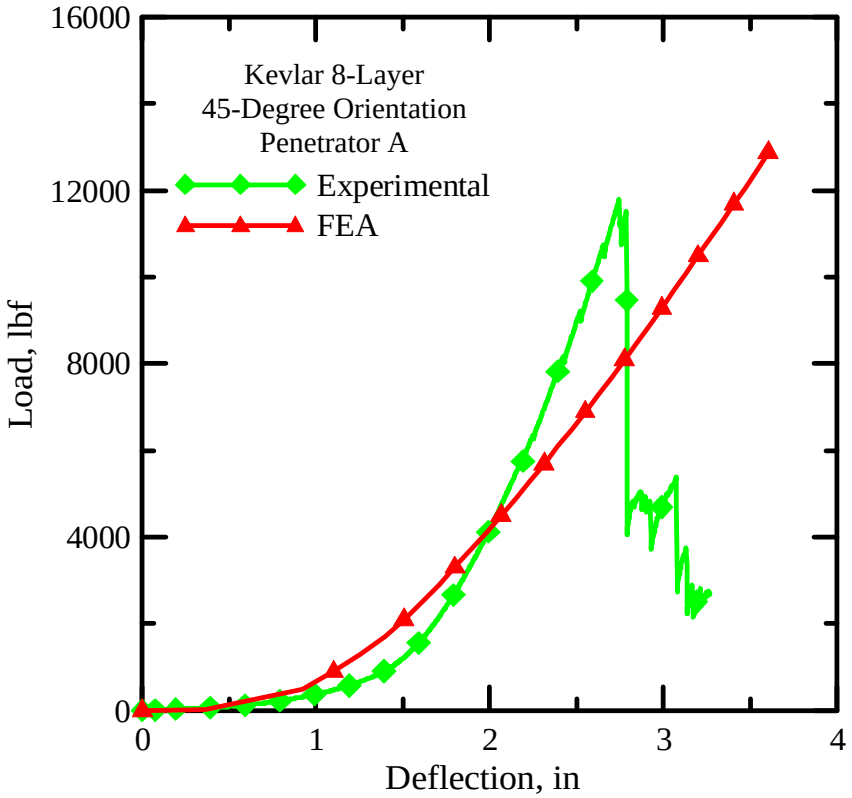

Figure 98a. Comparison of the Load-Displacement Graphs for the Eight-Layer Kevlar, 45-Degree Orientation, Thicker Blunt-Nose Test

Table 45. Static Test—FEA Comparison for the Eight-Layer Kevlar, 45-Degree Orientation, Thicker Blunt-Nose Test

	Static Test	FEA
Peak load (lb)	11796	12879
Displacement at peak load (in.)	2.745	3.604

The experimental curve was slack-shifted by 0.25 inch.

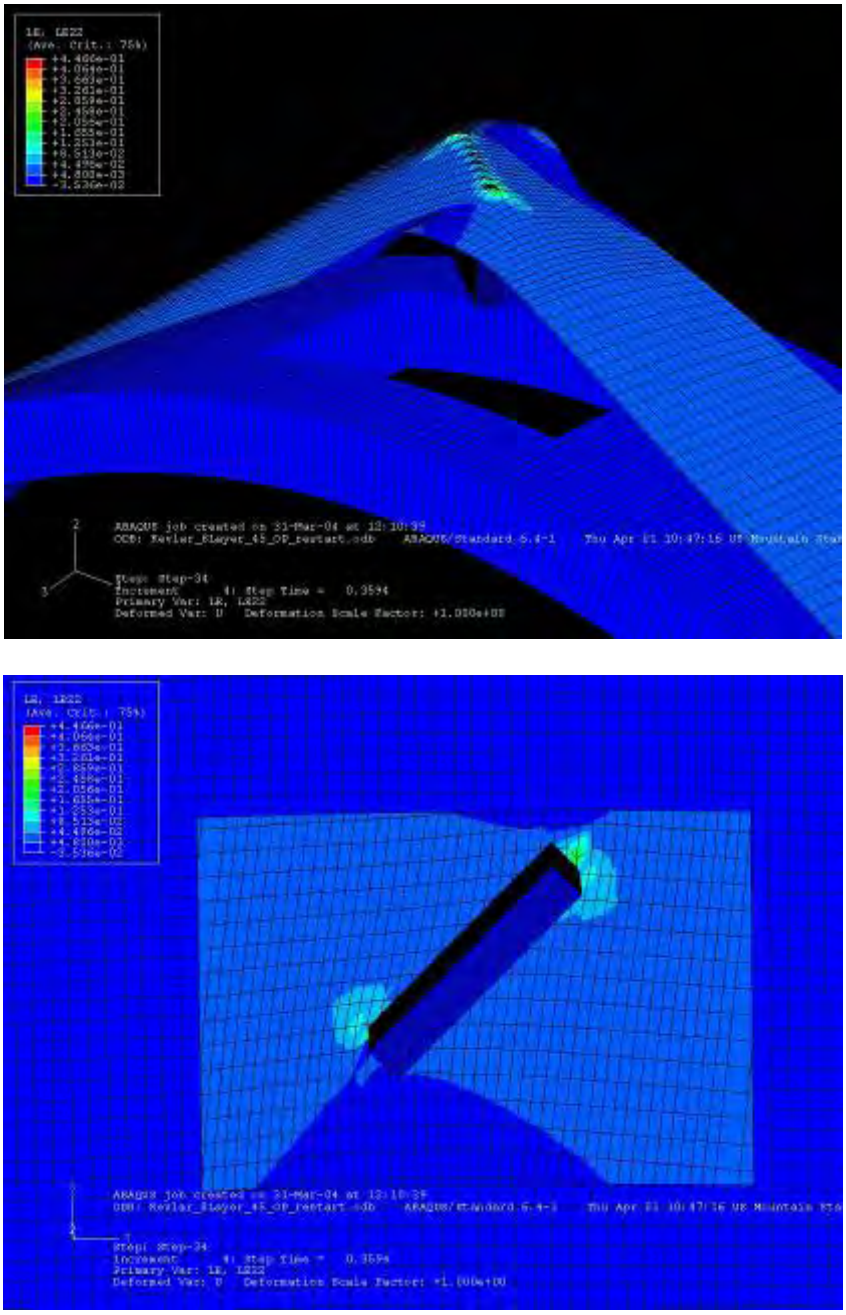

Figure 98b. Eight-Layer Kevlar—45-Degree Orientation (Thicker Blunt Nose)—Plot of In-Plane Strain ε_1 Superimposed on Deformation at the End of the Last Load Step

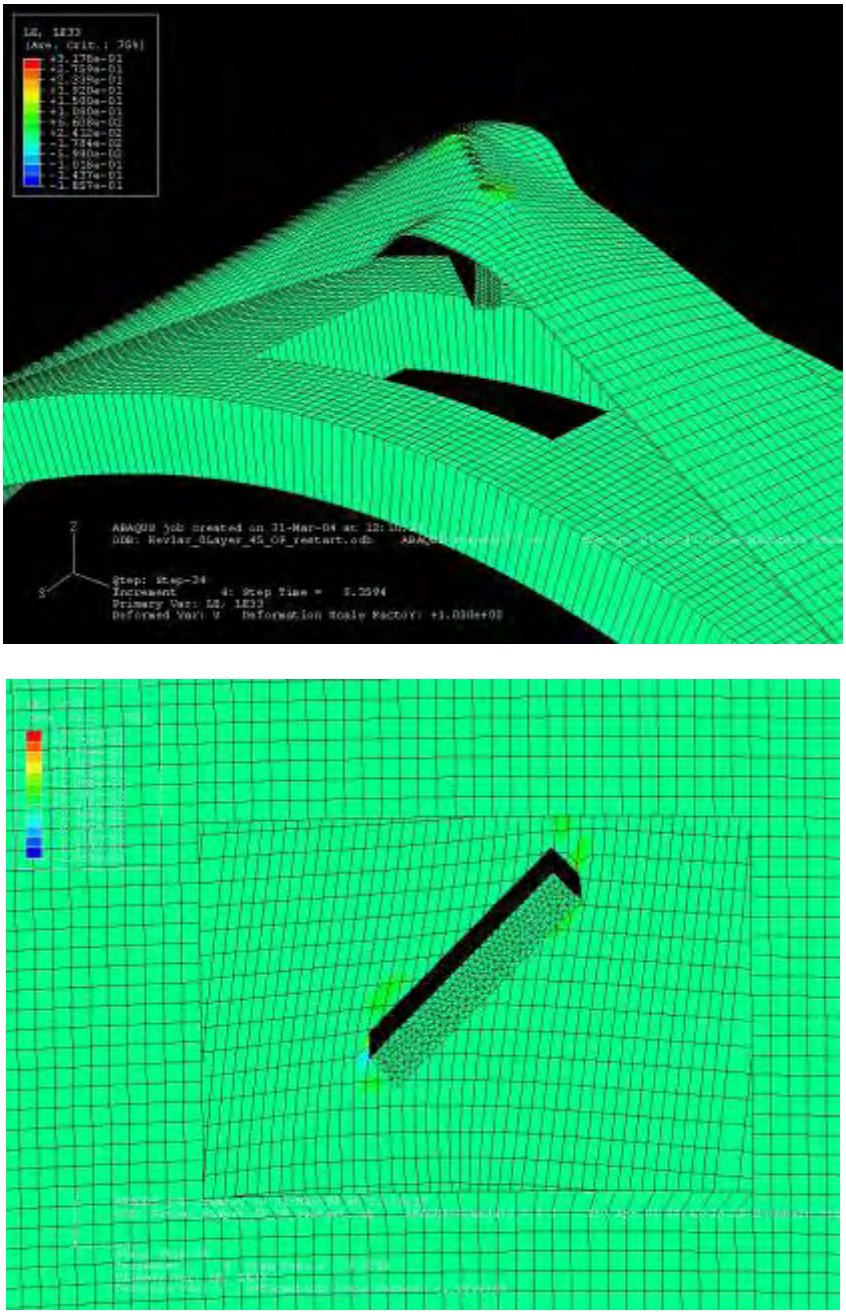

Figure 98c. Eight-Layer Kevlar—45-Degree Orientation (Thicker Blunt Nose)—Plot of In-Plane Strain ε_2 Superimposed on Deformation at the End of the Last Load Step

Figure 99a and table 46 compare the static test FE simulation to the experimental results for the eight-layer Kevlar, 90-degree orientation, thicker blunt-nose test case. Figures 99b and 99c show the FE simulation deformation.

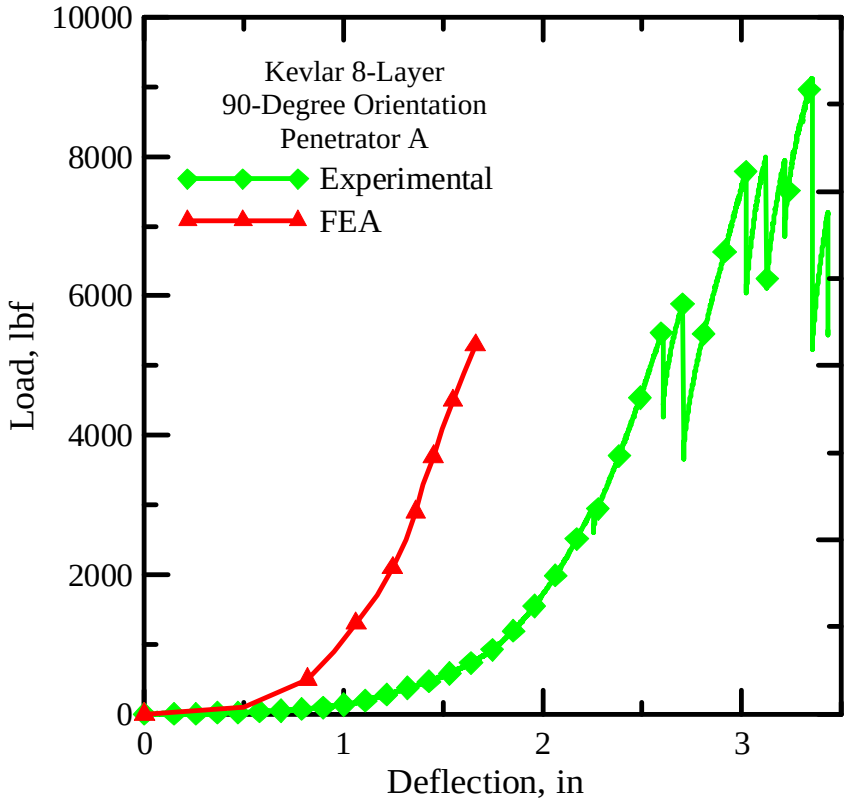

Figure 99a. Comparison of the Load-Displacement Graphs for the Eight-Layer Kevlar, 90-Degree Orientation, Thicker Blunt-Nose Test

Table 46. Static Test—FEA Comparison for the Eight-Layer Kevlar, 90-Degree Orientation, Thicker Blunt-Nose Test

	Static Test	FEA
Peak load (lb)	9110	5292
Displacement at peak load (in.)	3.369	1.587

The experimental curve was slack-shifted by 0.78 inch.

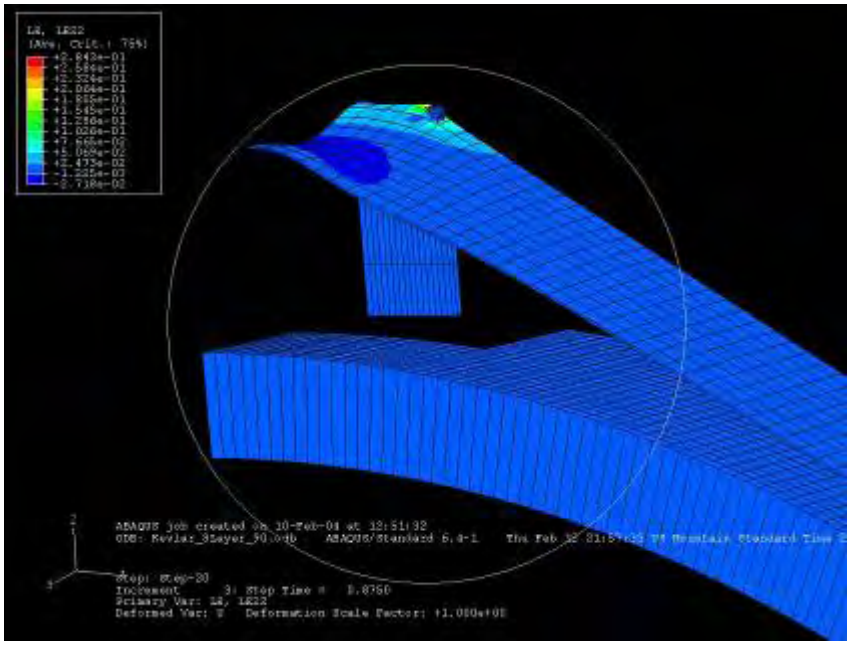

Figure 99b. Eight-Layer Kevlar—90-Degree Orientation (Thicker Blunt Nose)—Plot of In-Plane Strain ε_1 Superimposed on Deformation at the End of the Last Load Step

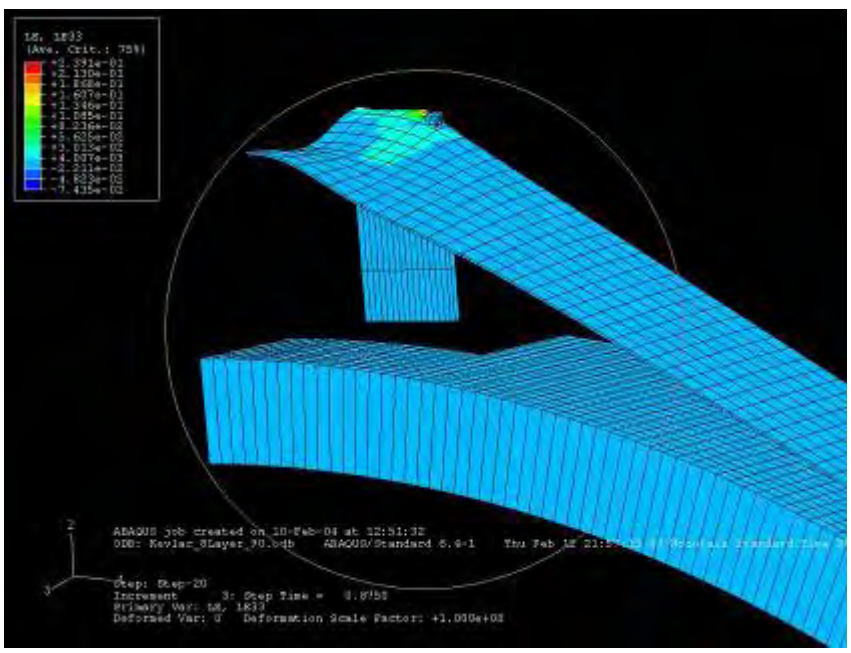

Figure 99c. Eight-Layer Kevlar—90-Degree Orientation (Thicker Blunt Nose)—Plot of In-Plane Strain ε_2 Superimposed on Deformation at the End of the Last Load Step

Figure 100a and table 47 compare the static test FE simulation to the experimental results for the eight-layer Kevlar, 0-degree off-center orientation, thicker blunt-nose test case. Figures 100b and 100c show the FE simulation deformation.

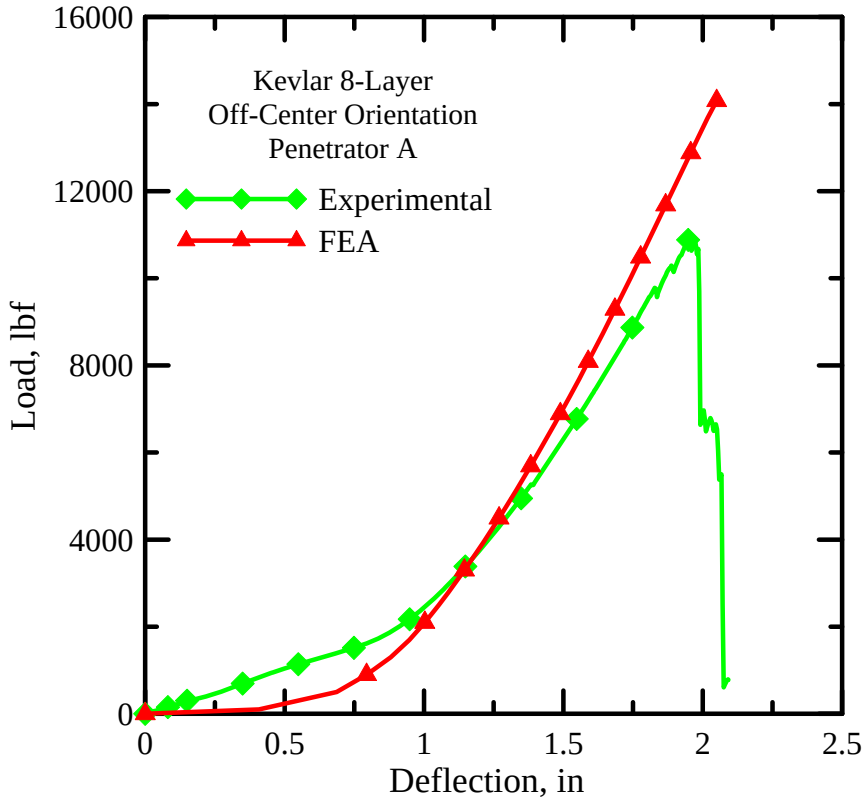

Figure 100a. Comparison of the Load-Displacement Graphs for the Eight-Layer Kevlar, Off-Center Orientation, Thicker Blunt-Nose Test

Table 47. Static Test—FEA Comparison for the Eight-Layer Kevlar, Off-Center Orientation, Thicker Blunt-Nose Test

	Static Test	FEA
Peak load (lb)	10967	14077
Displacement at peak load (in.)	1.955	2.05

The experimental curve was slack-shifted by 0.73 inch.

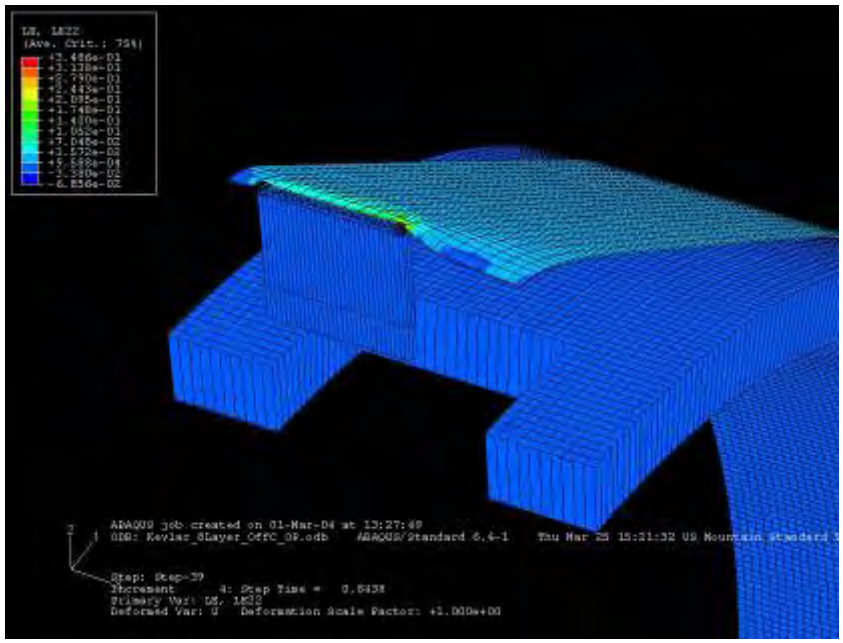

Figure 100b. Eight-Layer Kevlar—Off-Center Orientation (Thicker Blunt Nose)—Plot of In-Plane Strain ε_1 Superimposed on Deformation at the End of the Last Load Step

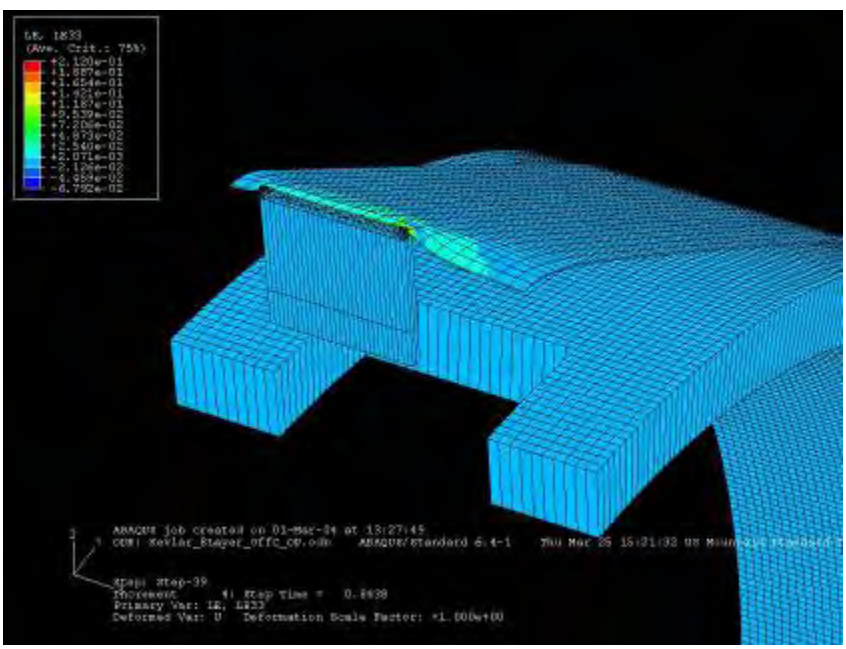

Figure 100c. Eight-Layer Kevlar—Off-Center Orientation (Thicker Blunt Nose)—Plot of In-Plane Strain ε_2 Superimposed on Deformation at the End of the Last Load Step

5.3.2 Zylon AS-500 Results.

5.3.2.1 One Layer.

Figure 101 and table 38 show the static test experimental results for the one-layer Zylon, 0-degree orientation, thinner blunt-nose test case. The FEA failed to converge.

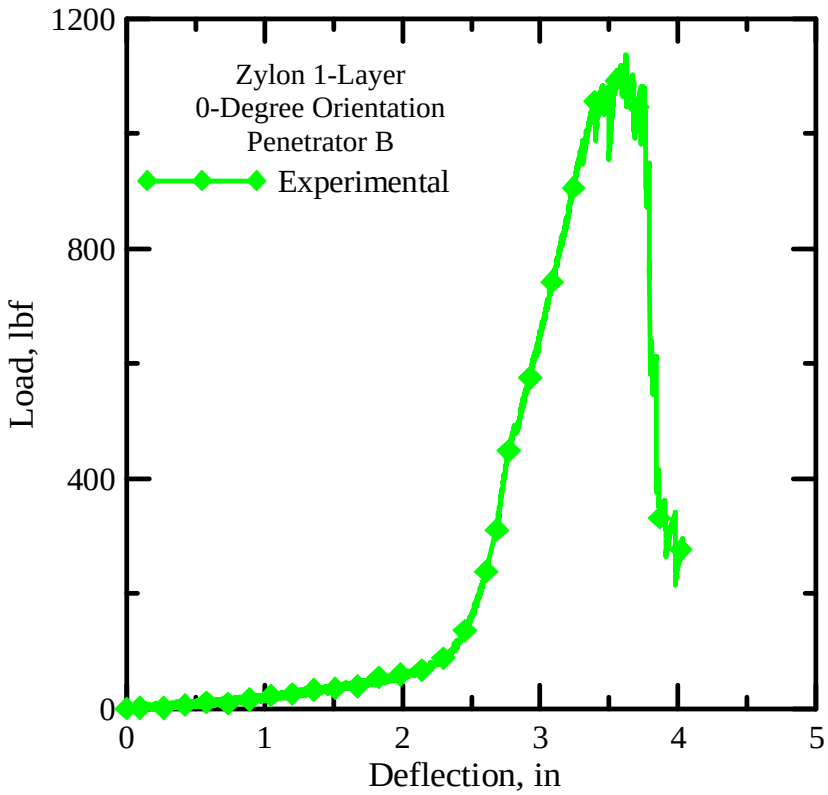

Figure 101. Comparison of the Load-Displacement Graphs for the One-Layer Zylon, 0-Degree Orientation, Thinner Blunt-Nose Test

Table 48. Static Test—FEA Comparison for the One-Layer Zylon, 0-Degree Orientation, Thinner Blunt-Nose Test

	Static Test	FEA
Peak load (lb)	1138	-
Displacement at peak load (in.)	3.621	-

The experimental curve was not slack-shifted.

Figure 102a and table 49 compare the static test FE simulation to the experimental results for the one-layer Zylon, 90-degree orientation, thinner blunt-nose test case. Figures 102b and 102c show the FE simulation deformation.

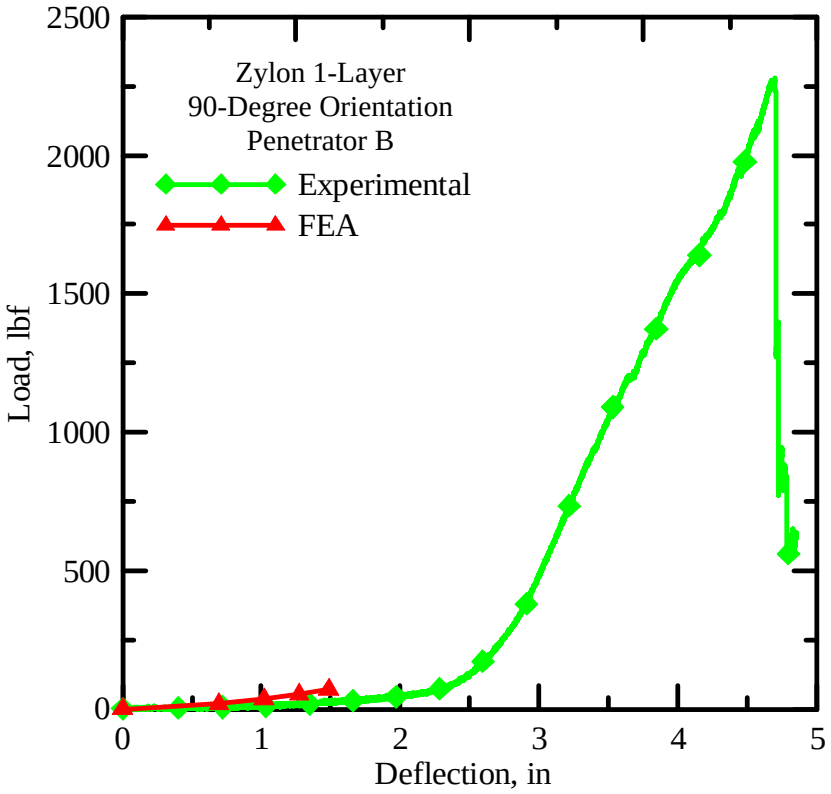

Figure 102a. Comparison of the Load-Displacement Graphs for the One-Layer Zylon, 90-Degree Orientation, Thinner Blunt-Nose Test

Table 49. Static Test—FEA Comparison for the One-Layer Zylon, 90-Degree Orientation, Thinner Blunt-Nose Test

	Static Test	FEA
Peak load (lb)	2278	53
Displacement at peak load (in.)	4.7	1.61

The experimental curve was not slack-shifted.

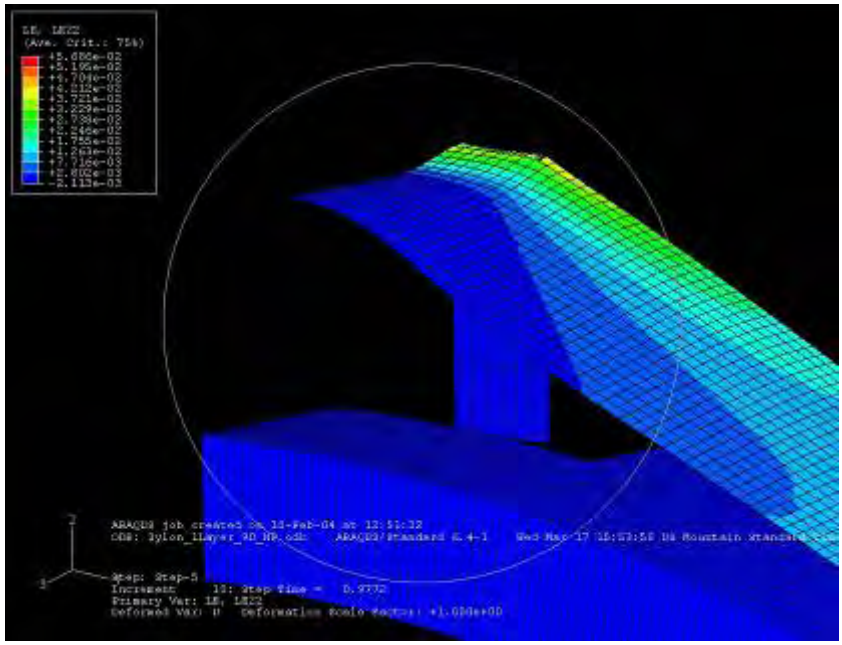

Figure 102b. One-Layer Zylon—90-Degree Orientation (Thinner Blunt Nose)—Plot of In-Plane Strain ε_1 Superimposed on Deformation at the End of the Last Load Step

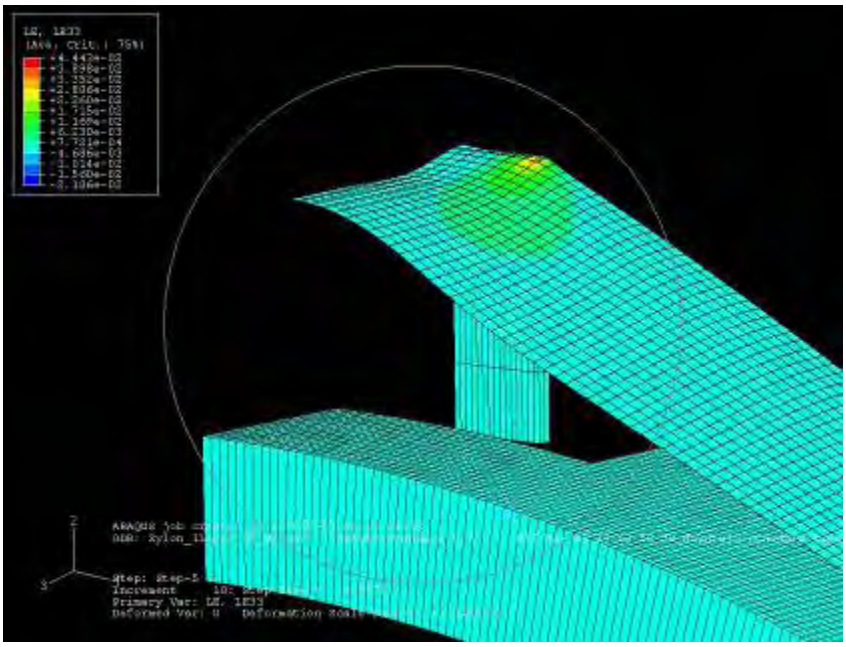

Figure 102c. One-Layer Zylon—90-Degree Orientation (Thinner Blunt Nose)—Plot of In-Plane Strain ε_2 Superimposed on Deformation at the End of the Last Load Step

Figure 103a and table 50 compare the static test FE simulation to the experimental results for the one-layer Zylon, 0-degree off-center orientation, thinner blunt-nose test case. Figures 103b and 103c show the FE simulation deformation.

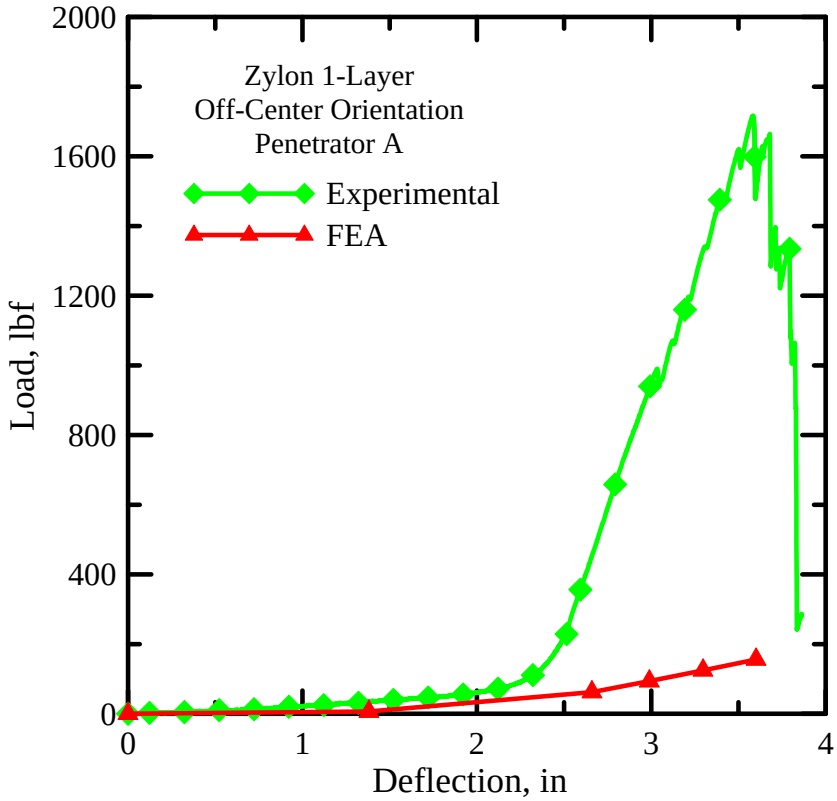

Figure 103a. Comparison of the Load-Displacement Graphs for the One-Layer Zylon, Off-Center Orientation, Thinner Blunt-Nose Test

Table 50. Static Test—FEA Comparison for the One-Layer Zylon, Off-Center Orientation, Thinner Blunt-Nose Test

	Static Test	FEA
Peak load (lb)	837	106
Displacement at peak load (in.)	4.039	4.62

The experimental curve was not slack-shifted.

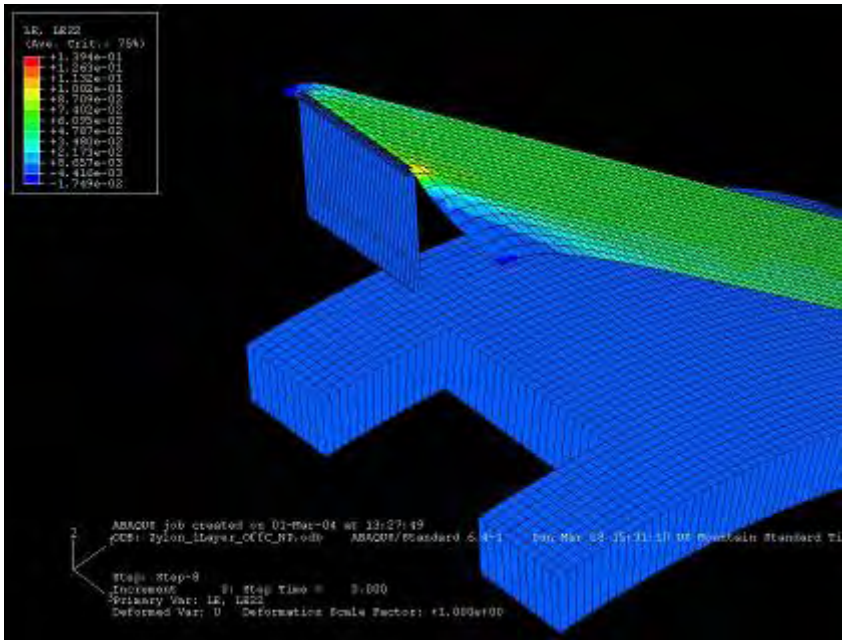

Figure 103b. One-Layer Zylon—Off-Center Orientation (Thinner Blunt Nose)—Plot of In-Plane Strain ε_1 Superimposed on Deformation at the End of the Last Load Step

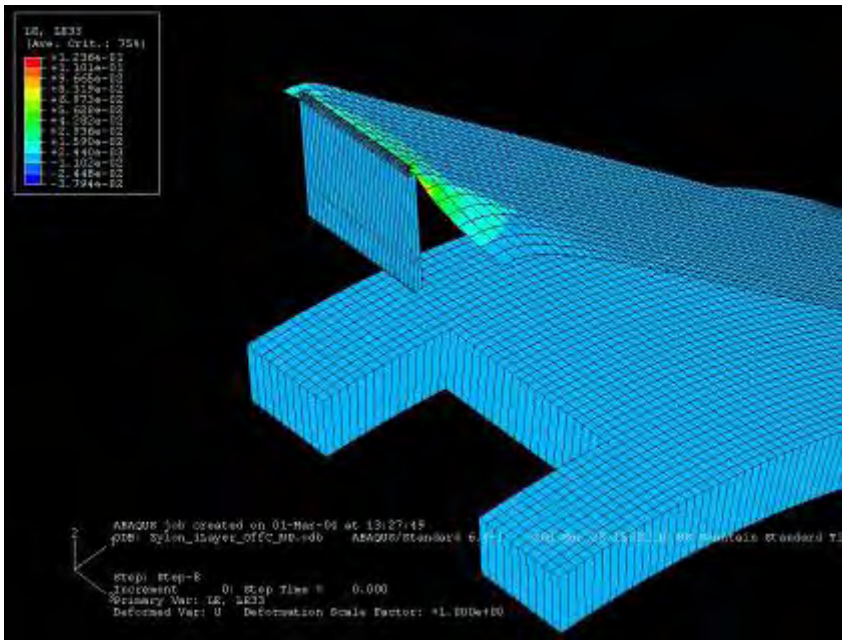

Figure 103c. One-Layer Zylon—Off-Center Orientation (Thinner Blunt Nose)—Plot of In-Plane Strain ε_2 Superimposed on Deformation at the End of the Last Load Step

Figure 104a and table 51 compare the static test FE simulation to the experimental results for the one-layer Zylon, 45-degree orientation, thicker blunt-nose test case. Figures 104b and 104c show the FE simulation deformation.

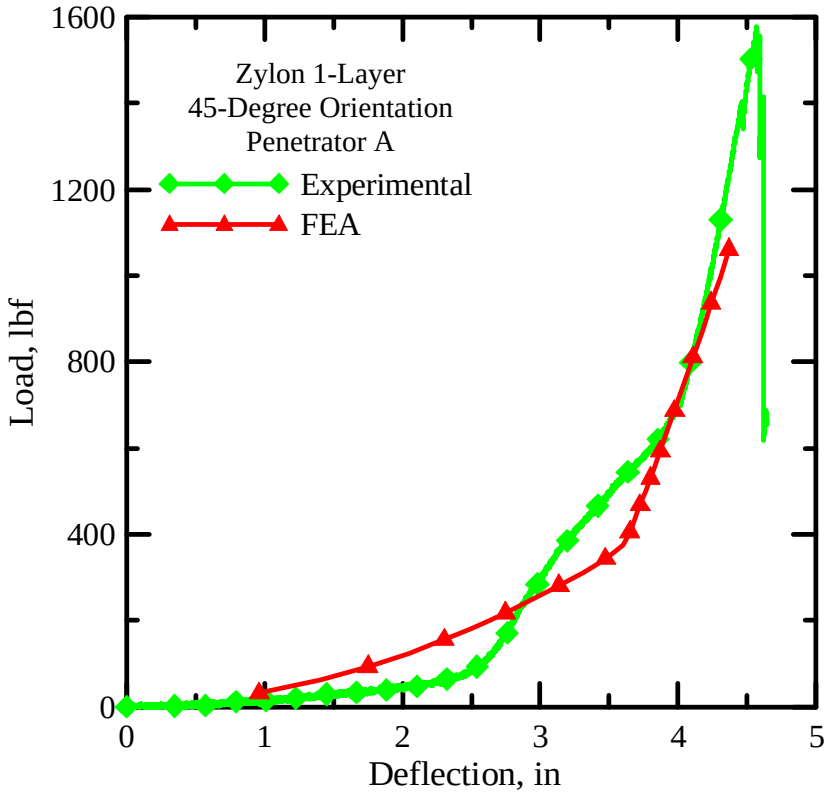

Figure 104a. Comparison of the Load-Displacement Graphs for the One-Layer Zylon, 45-Degree Orientation, Thicker Blunt-Nose Test

Table 51. Static Test—FEA Comparison for the One-Layer Zylon, 45-Degree Orientation, Thicker Blunt-Nose Test

	Static Test	FEA
Peak load (lb)	1577	1061
Displacement at peak load (in.)	4.57	4.368

The experimental curve was not slack-shifted.

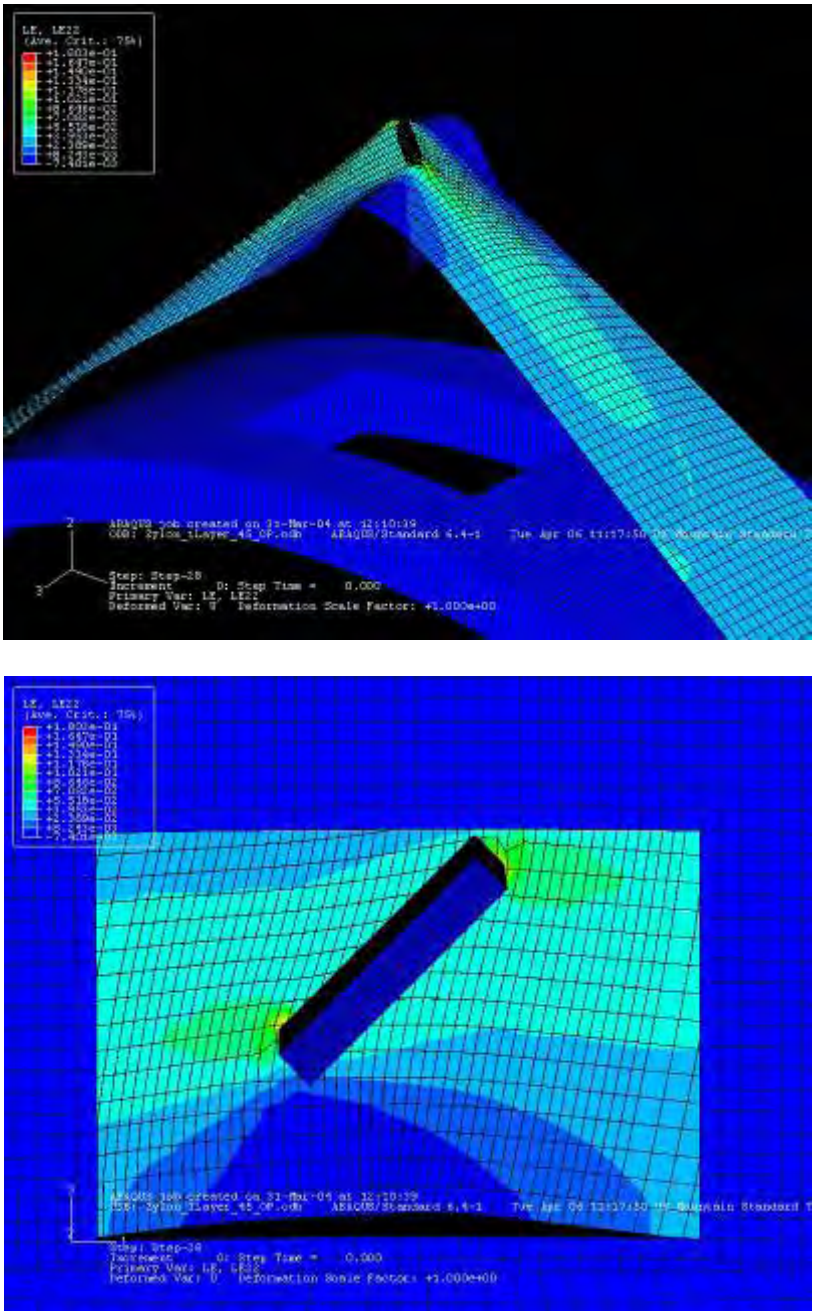

Figure 104b. One-Layer Zylon—45-Degree Orientation (Thicker Blunt Nose)—Plot of In-Plane Strain ε_1 Superimposed on Deformation at the End of the Last Load Step

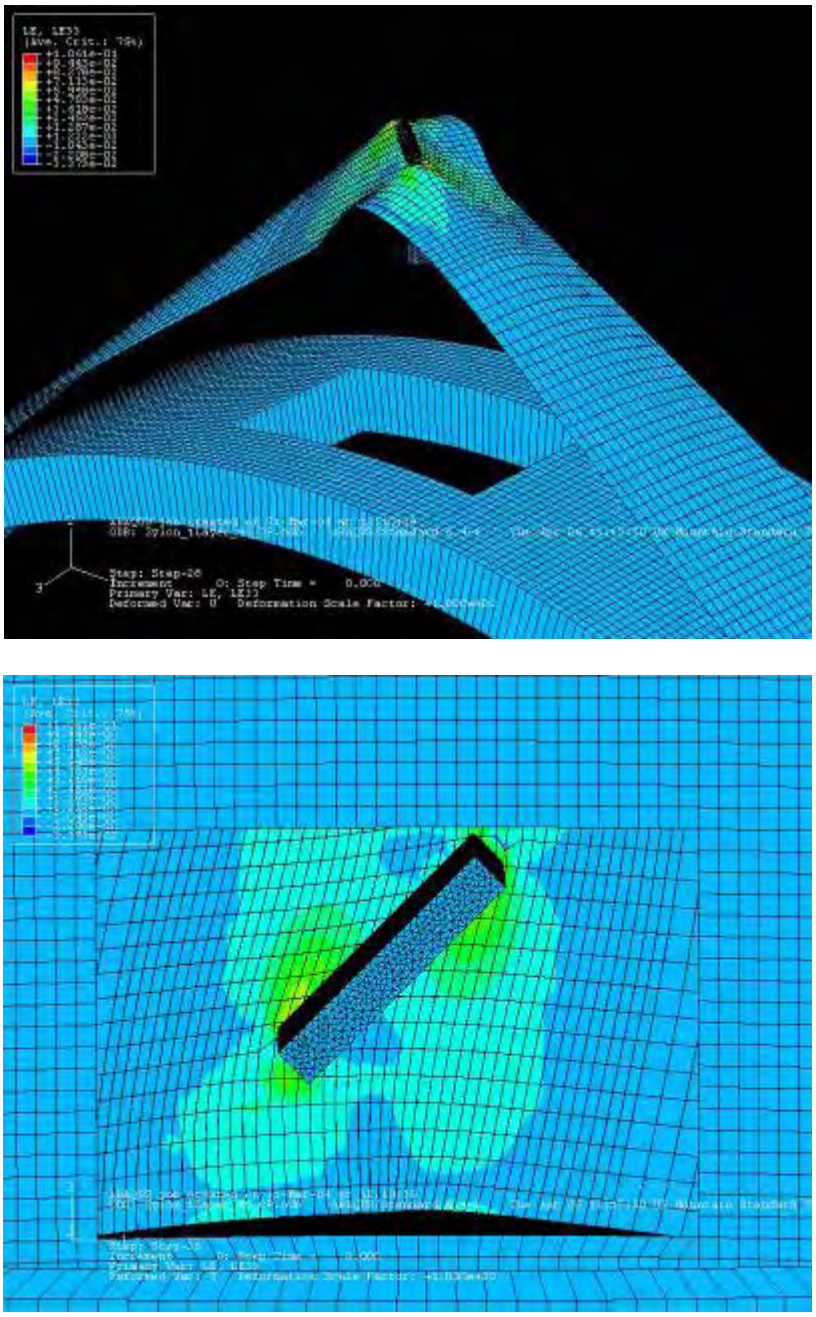

Figure 104c. One-Layer Zylon—45-Degree Orientation (Thicker Blunt Nose)—Plot of In-Plane Strain ε_2 Superimposed on Deformation at the End of the Last Load Step

Figure 105a and table 52 compare the static test FE simulation to the experimental results for the one-layer Zylon, 90-degree orientation, thicker Blunt-Nose Test case. Figures 105b and 105c show the FE simulation deformation.

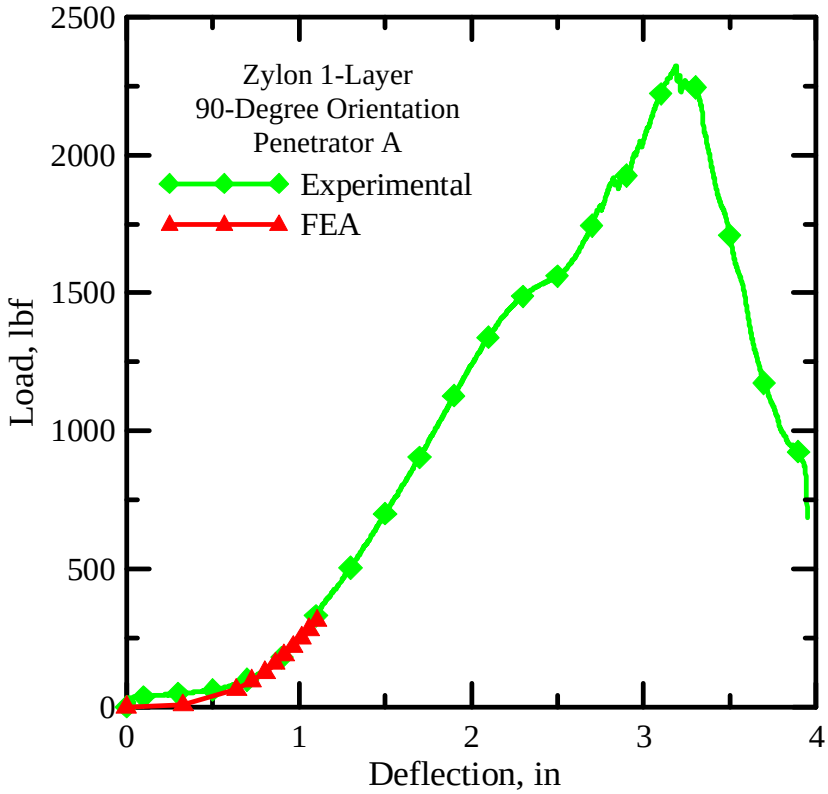

Figure 105a. Comparison of the Load-Displacement Graphs for the One-Layer Zylon, 90-Degree Orientation, Thicker Blunt-Nose Test

Table 52. Static Test—FEA Comparison for the One-Layer Zylon, 90-Degree Orientation, Thicker Blunt-Nose Test

	Static Test	FEA
Peak load (lb)	2324	312
Displacement at peak load (in.)	3.188	1.106

The experimental curve was slack-shifted by 1.46 inches.

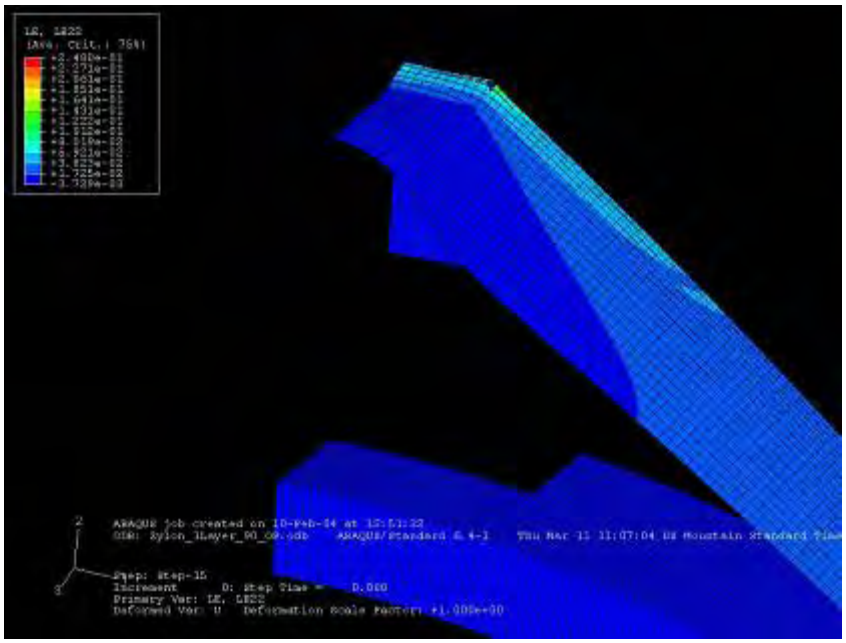

Figure 105b. One-Layer Zylon—90-Degree Orientation (Thicker Blunt Nose)—Plot of In-Plane Strain ε_1 Superimposed on Deformation at the End of the Last Load Step

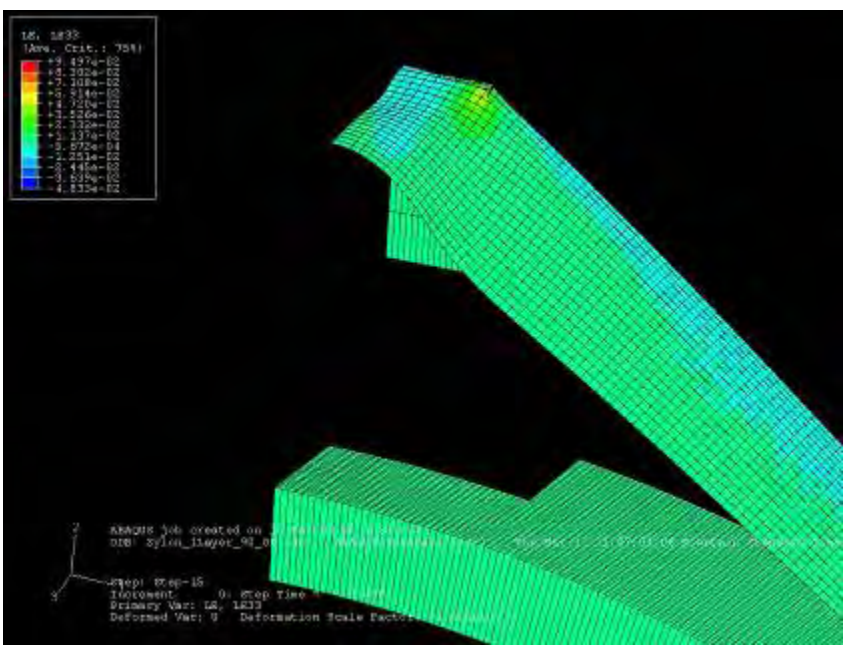

Figure 105c. One-Layer Zylon—90-Degree Orientation (Thicker Blunt Nose)—Plot of In-Plane Strain ε_2 Superimposed on Deformation at the End of the Last Load Step

Figure 106a and table 53 compare the static test FE simulation to the experimental results for the one-layer Zylon, 0-degree off-center orientation, thicker blunt-nose test case. Figures 106b and 106c show the FE simulation deformation.

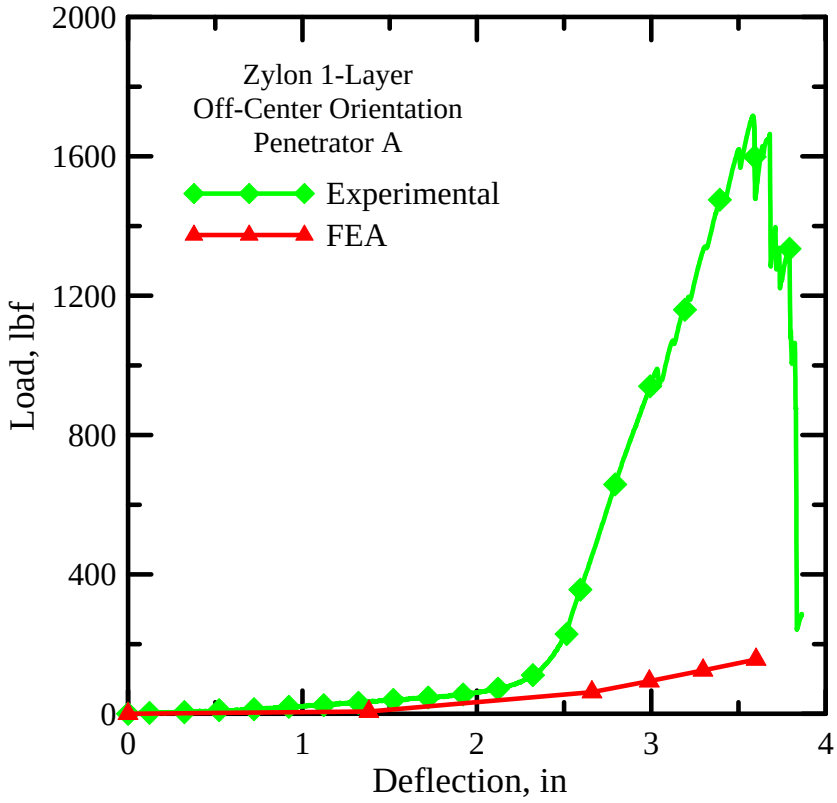

Figure 106a. Comparison of the Load-Displacement Graphs for the One-Layer Zylon, Off-Center Orientation, Thicker Blunt-Nose Test

Table 53. Static Test—FEA Comparison for the One-Layer Zylon, Off-Center Orientation, Thicker Blunt-Nose Test

	Static Test	FEA
Peak load (lb)	1716	156
Displacement at peak load (in.)	3.583	3.601

The experimental curve was been slack-shifted.

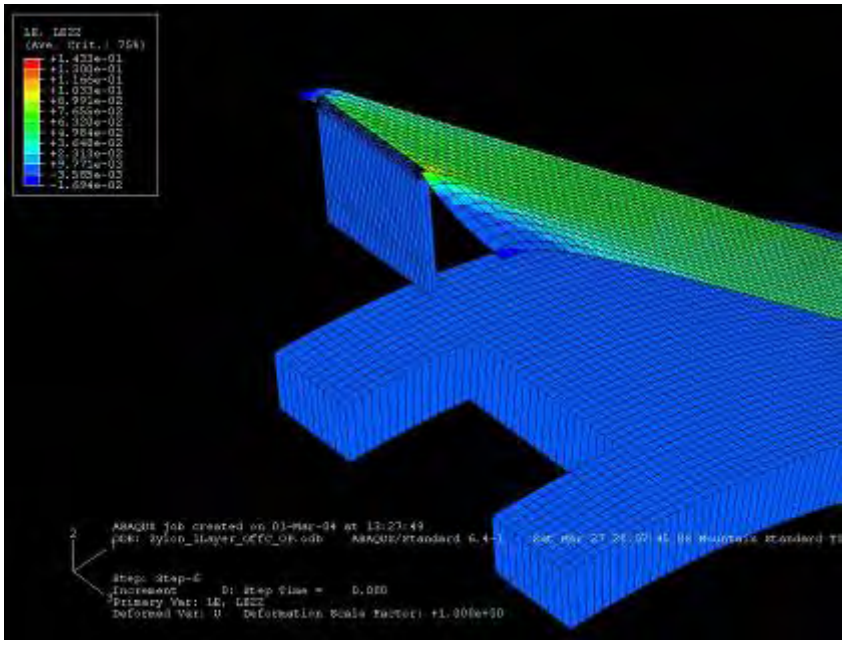

Figure 106b. One-Layer Zylon—Off-Center Orientation (Thicker Blunt Nose)—Plot of In-Plane Strain ε_1 Superimposed on Deformation at the End of the Last Load Step

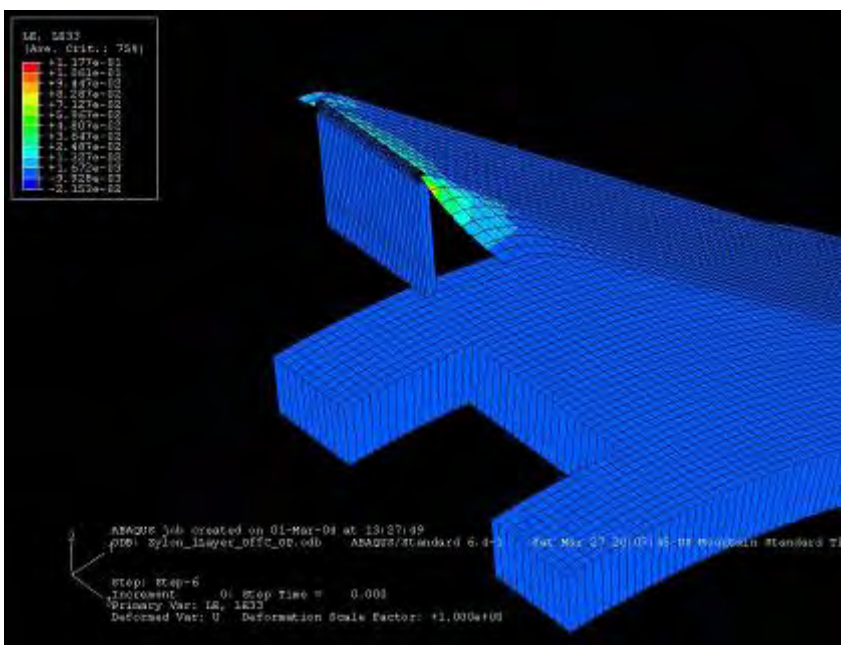

Figure 106c. One-Layer Zylon—Off-Center Orientation (Thicker Blunt Nose)—Plot of In-Plane Strain ε_2 Superimposed on Deformation at the End of the Last Load Step

5.3.2.2 Four Layer.

Figure 107a and table 54 compare the static test FE simulation to the experimental results for the four-layer Zylon, 0-degree orientation, thinner blunt-nose test case. Figures 107b and 107c show the FE simulation deformation.

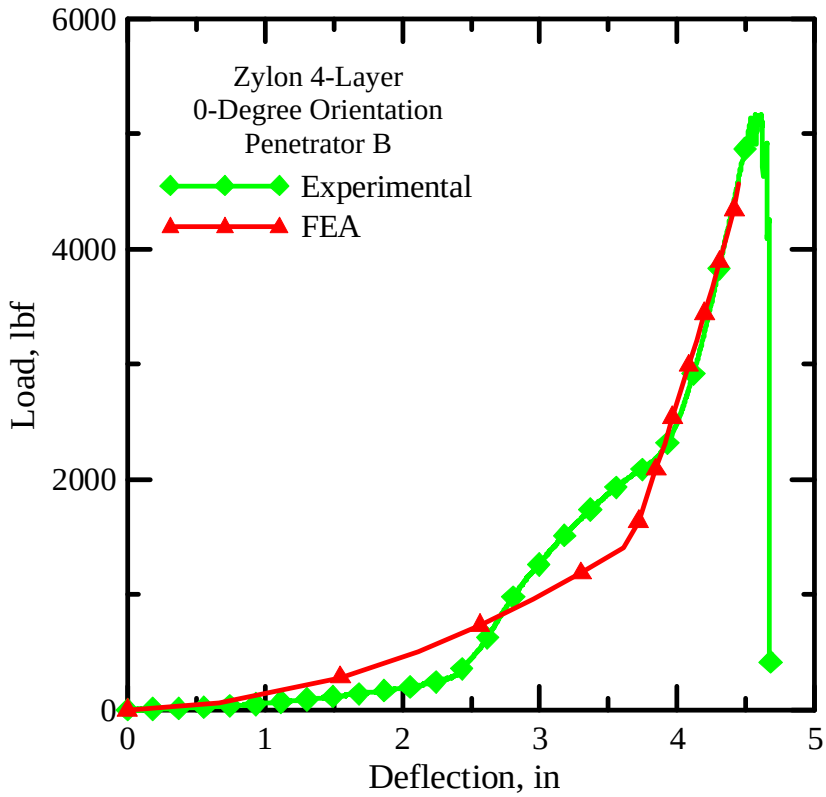

Figure 107a. Comparison of the Load-Displacement Graphs for the Four-Layer Zylon, 0-Degree Orientation, Thinner Blunt-Nose Test

Table 54. Static Test—FEA Comparison for the Four-Layer Zylon, 0-Degree Orientation, Thinner Blunt-Nose Test

	Static Test	FEA
Peak load (lb)	5173	4685
Displacement at peak load (in.)	4.566	4.341

The experimental curve was not slack-shifted.

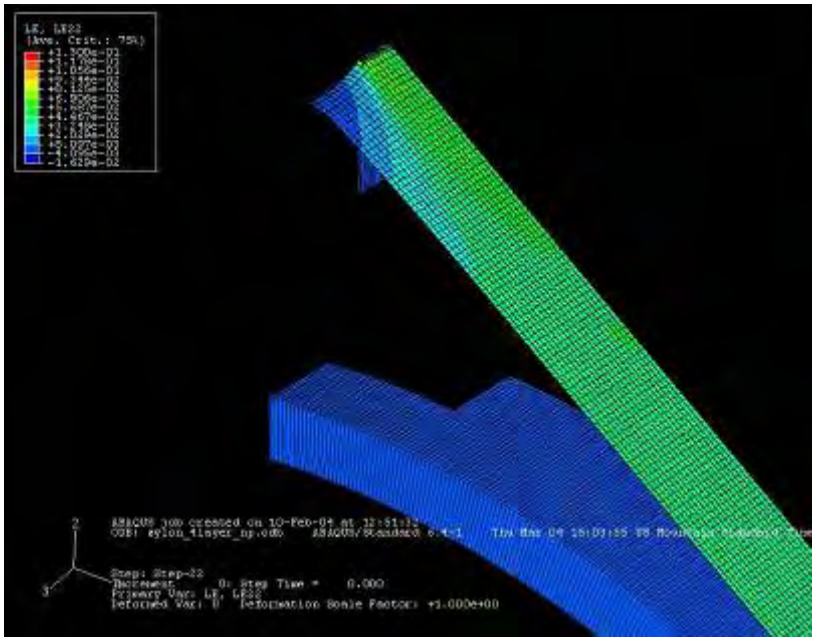

Figure 107b. Four-Layer Zylon—0-Degree Orientation (Thinner Blunt Nose)—Plot of In-Plane Strain ε_1 Superimposed on Deformation at the End of the Last Load Step

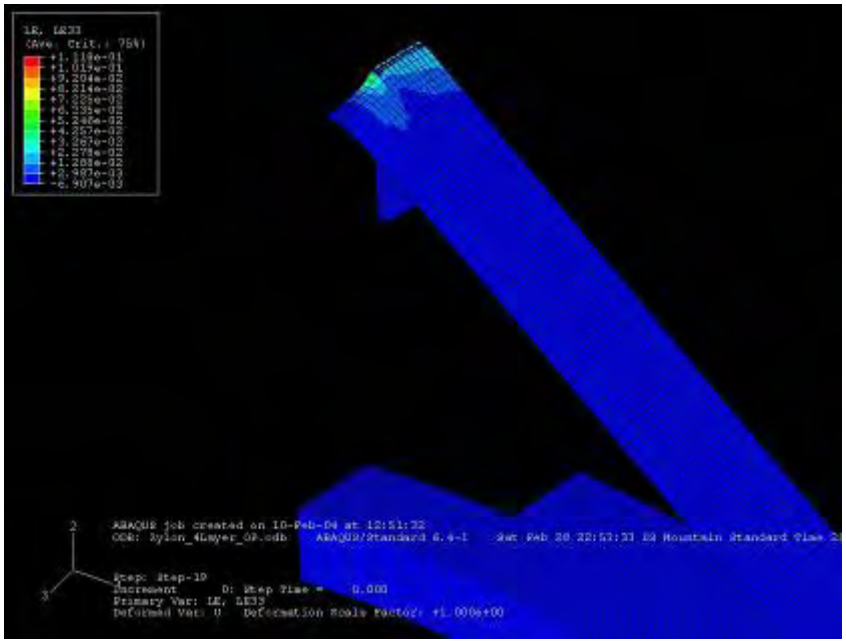

Figure 107c. Four-Layer Zylon—0-Degree Orientation (Thinner Blunt Nose)—Plot of In-Plane Strain ε_2 Superimposed on Deformation at the End of the Last Load Step

Figure 108a and table 55 compare the static test FE simulation to the experimental results for the four-layer Zylon, 45-degree orientation, thinner blunt-nose test case. Figures 108b and 108c show the FE simulation deformation.

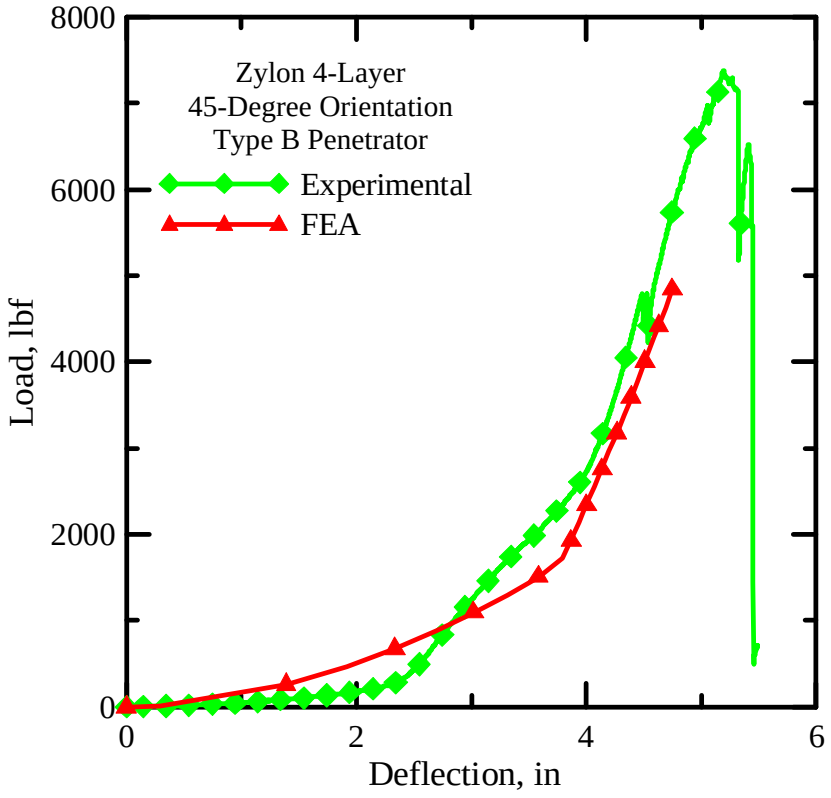

Figure 108a. Comparison of the Load-Displacement Graphs for the Four-Layer Zylon, 45-Degree Orientation, Thinner Blunt-Nose Test

Table 55. Static Test—FEA Comparison for the Four-Layer Zylon, 45-Degree Orientation, Thinner Blunt-Nose Test

	Static Test	FEA
Peak load (lb)	7380	4839
Displacement at peak load (in.)	5.194	4.749

The experimental curve was not slack-shifted.

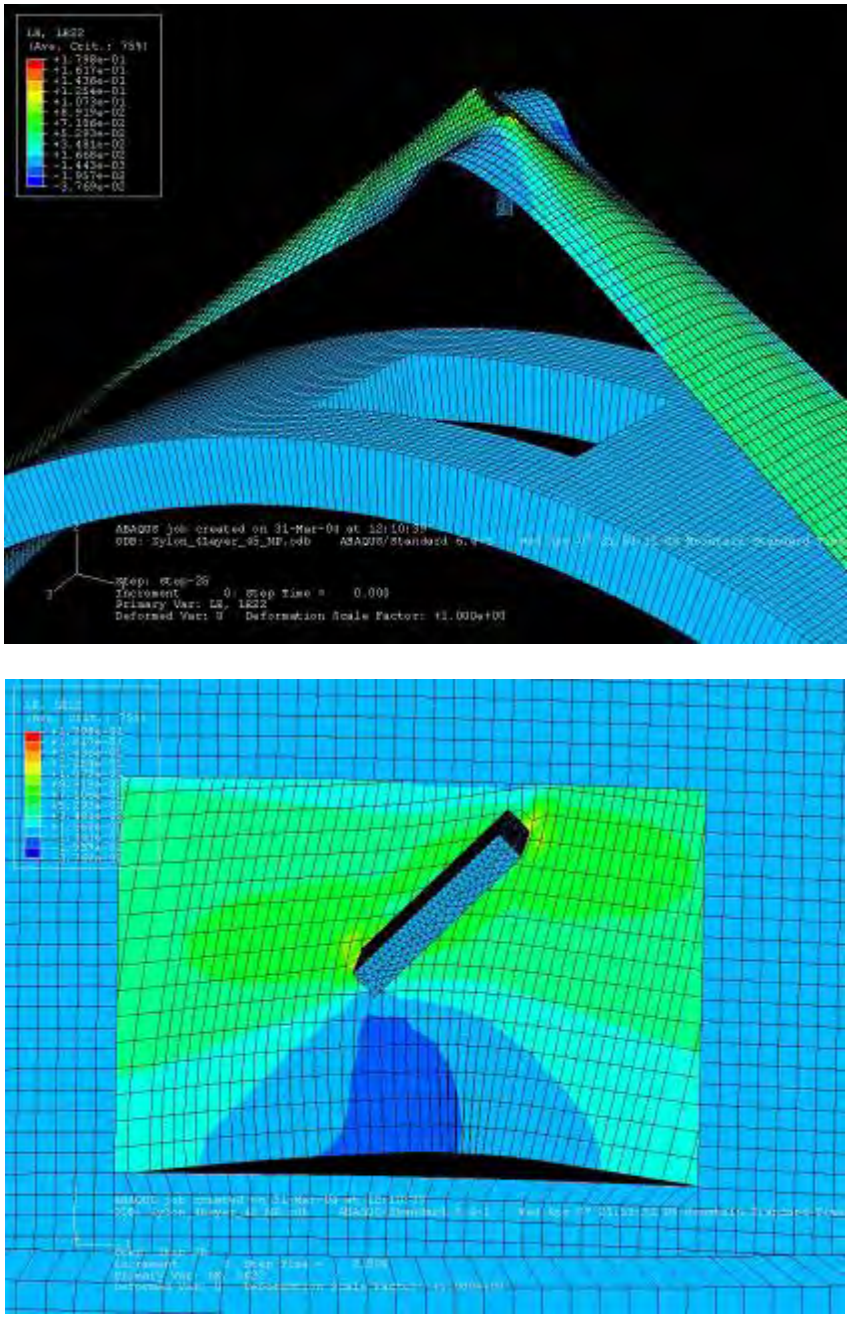

Figure 108b. Four-Layer Zylon—45-Degree Orientation (Thinner Blunt Nose)—Plot of In-Plane Strain ε_1 Superimposed on Deformation at the End of the Last Load Step

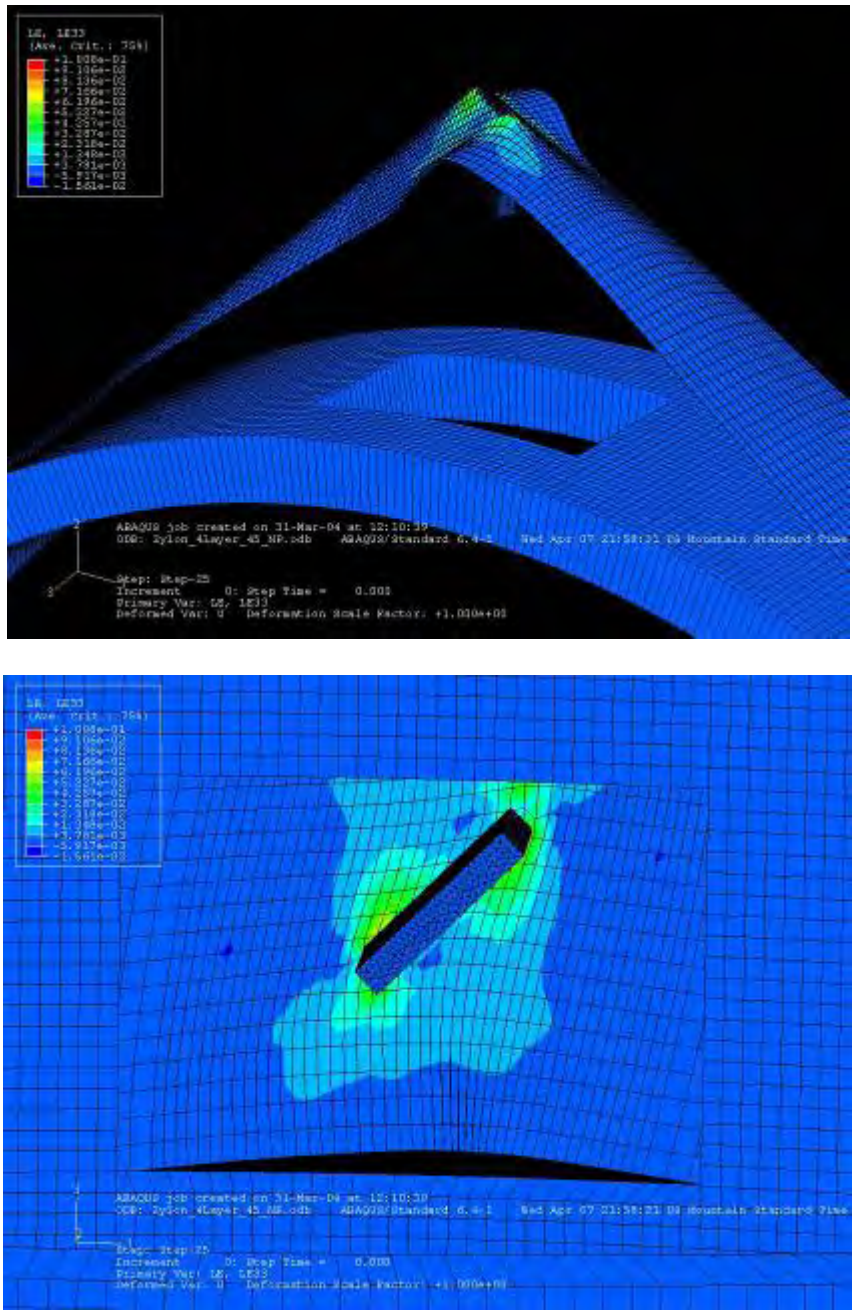

Figure 108c. Four-Layer Zylon—45-Degree Orientation (Thinner Blunt Nose)—Plot of In-Plane Strain ε_2 Superimposed on Deformation at the End of the Last Load Step

Figure 109a and table 56 compare the static test FE simulation to the experimental results for the four-layer Zylon, 90-degree orientation, thinner Blunt-Nose Test case. Figures 109b and 109c show the FE simulation deformation.

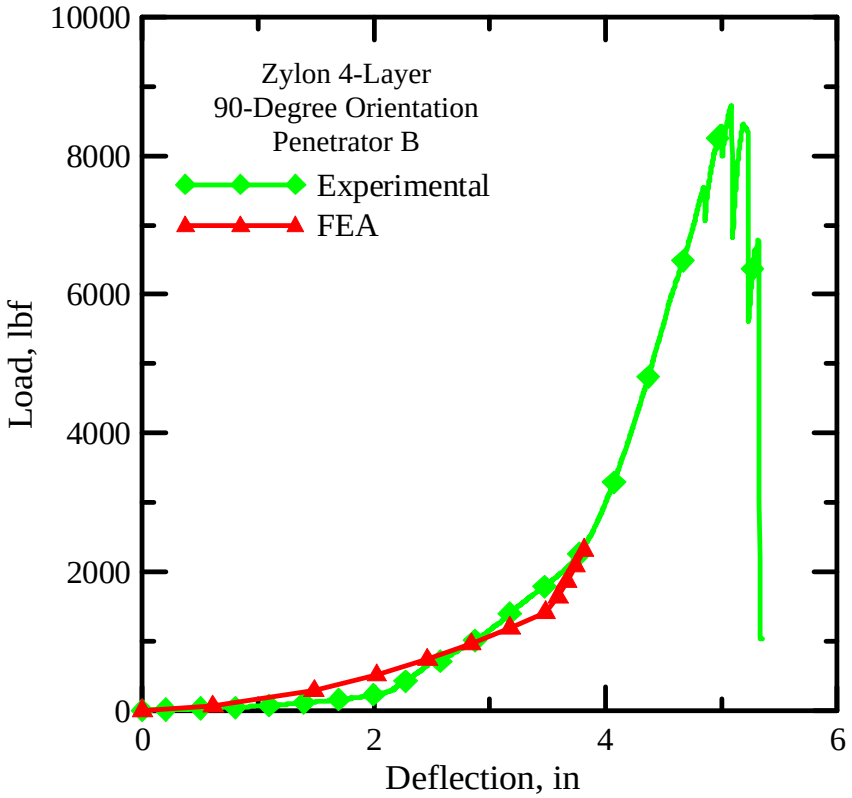

Figure 109a. Comparison of the Load-Displacement Graphs for the Four-Layer Zylon, 90-Degree Orientation, Thinner Blunt-Nose Test

Table 56. Static Test—FEA Comparison for the Four-Layer Zylon, 90-Degree Orientation, Thinner Blunt-Nose Test

	Static Test	FEA
Peak load (lb)	8729	2194
Displacement at peak load (in.)	5.087	3.85

The experimental curve was slack-shifted by 0.28 inch.

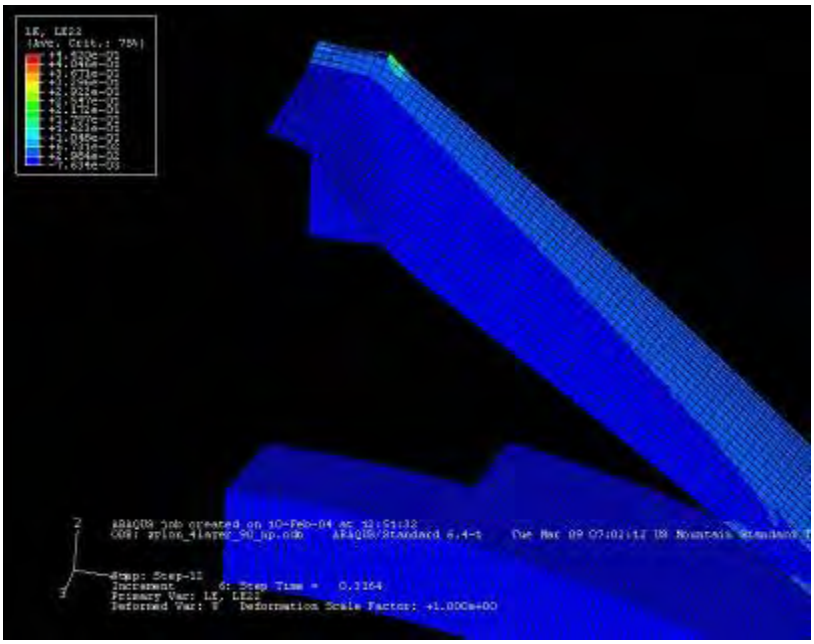

Figure 109b. Four-Layer Zylon—90-Degree Orientation (Thinner Blunt Nose)—Plot of In-Plane Strain ε_1 Superimposed on Deformation at the End of the Last Load Step

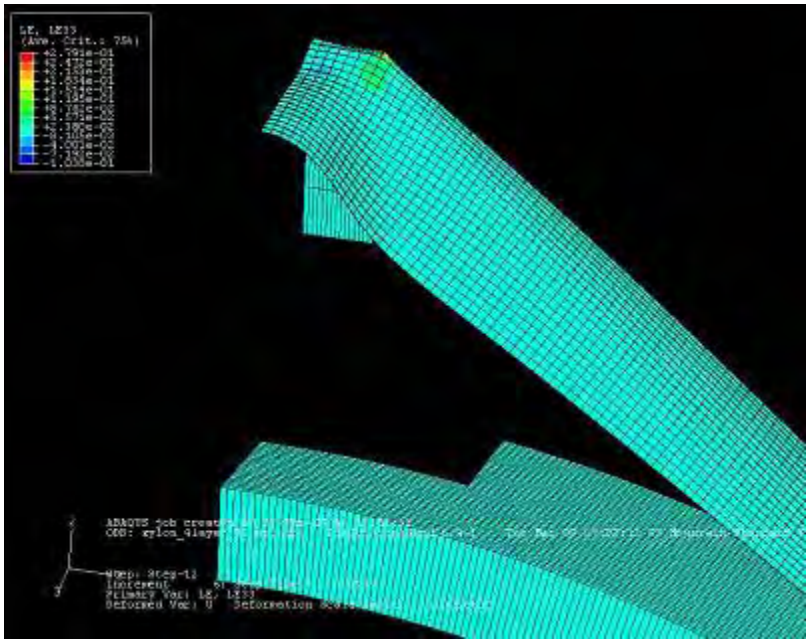

Figure 109c. Four-Layer Zylon—90-Degree Orientation (Thinner Blunt Nose)—Plot of In-Plane Strain ε_2 Superimposed on Deformation at the End of the Last Load Step

Figure 110a and table 57 compare the static test FE simulation to the experimental results for the four-layer Zylon, 0-degree off-center orientation, thinner blunt-nose test case. Figures 110b and 110c show the FE simulation deformation.

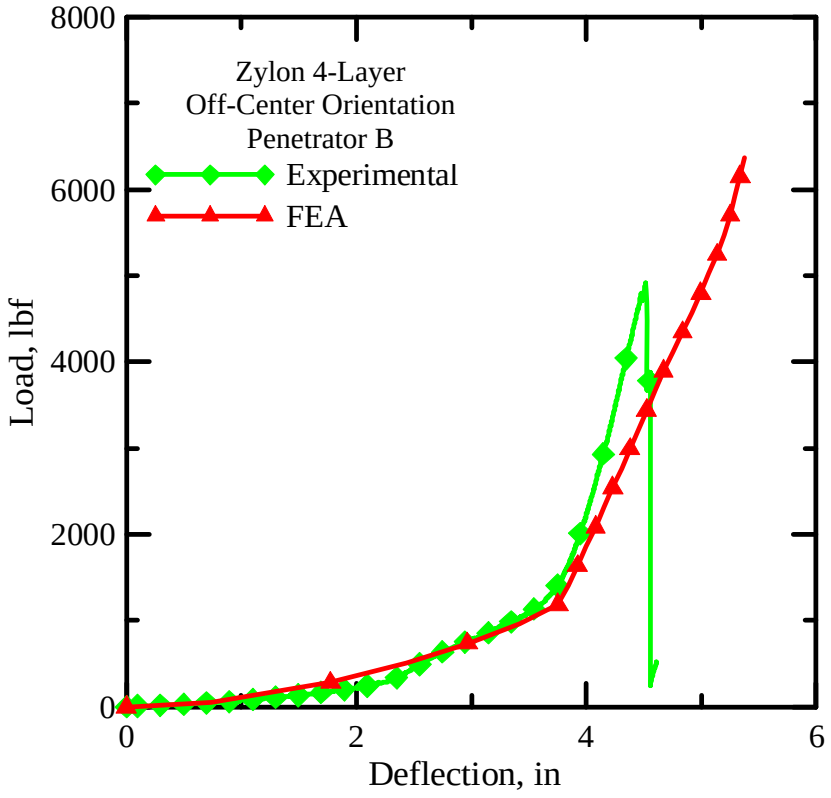

Figure 110a. Comparison of the Load-Displacement Graphs for the Four-Layer Zylon, Off-Center Orientation, Thinner Blunt-Nose Test

Table 57. Static Test—FEA Comparison for the Four-Layer Zylon, Off-Center Orientation, Thinner Blunt-Nose Test

	Static Test	FEA
Peak load (lb)	4916	6206
Displacement at peak load (in.)	4.519	5.512

The experimental curve was not slack-shifted.

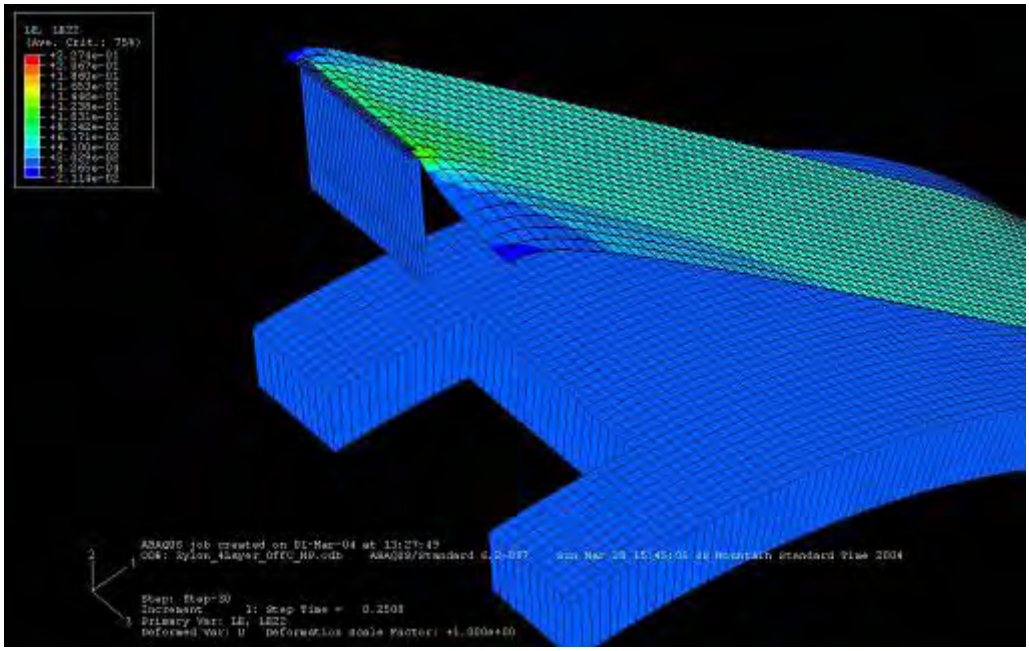

Figure 110b. Four-Layer Zylon—Off-Center Orientation (Thinner Blunt Nose)—Plot of In-Plane Strain ε_1 Superimposed on Deformation at the End of the Last Load Step

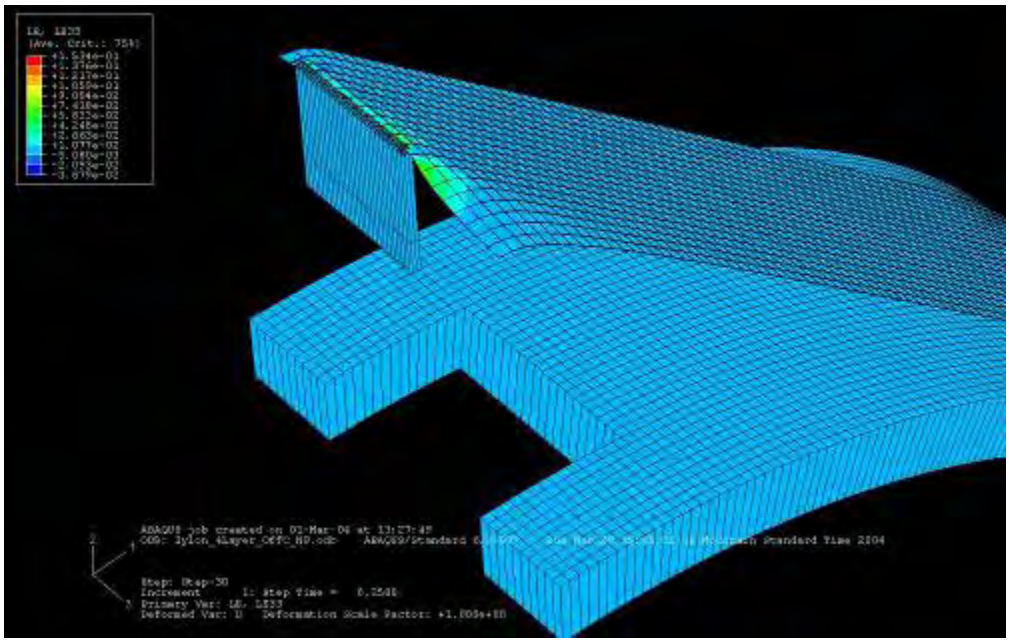

Figure 110c. Four-Layer Zylon—Off-Center Orientation (Thinner Blunt Nose)—Plot of In-Plane Strain ε_2 Superimposed on Deformation at the End of the Last Load Step

Figure 111a and table 58 compare the static test FE simulation to the experimental results for the four-layer Zylon, 45-degree orientation, thicker blunt-nose test case. Figures 111b and 111c show the FE simulation deformation.

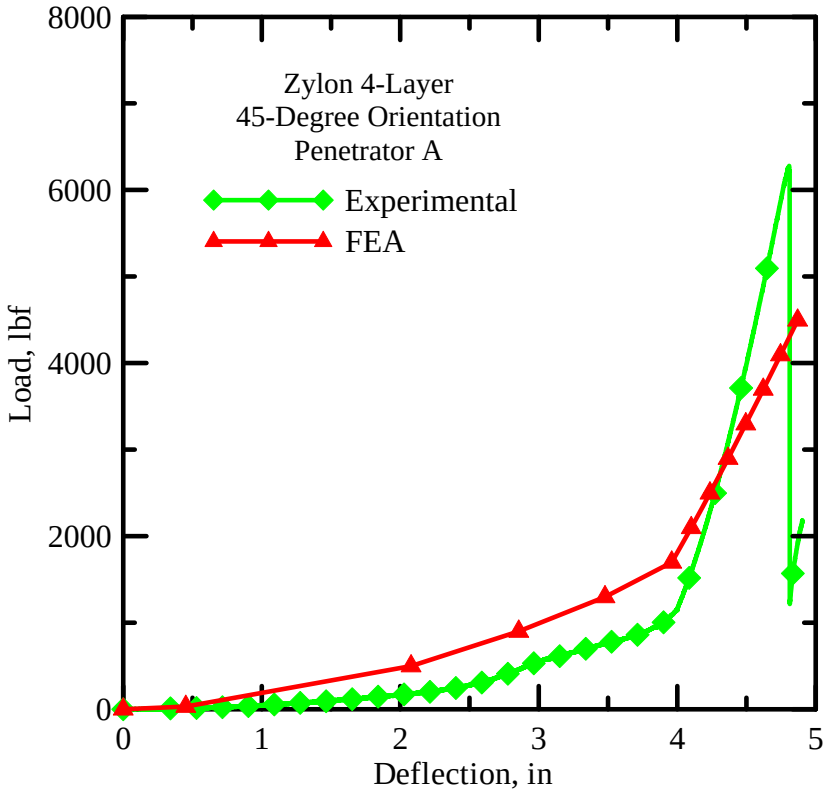

Figure 111a. Comparison of the Load-Displacement Graphs for the Four-Layer Zylon, 45-Degree Orientation, Thicker Blunt-Nose Test

Table 58. Static Test—FEA Comparison for the Four-Layer Zylon, 45-Degree Orientation, Thicker Blunt-Nose Test

	Static Test	FEA
Peak load (lb)	6279	4892
Displacement at peak load (in.)	4.81	4.92

The experimental curve was not slack-shifted.

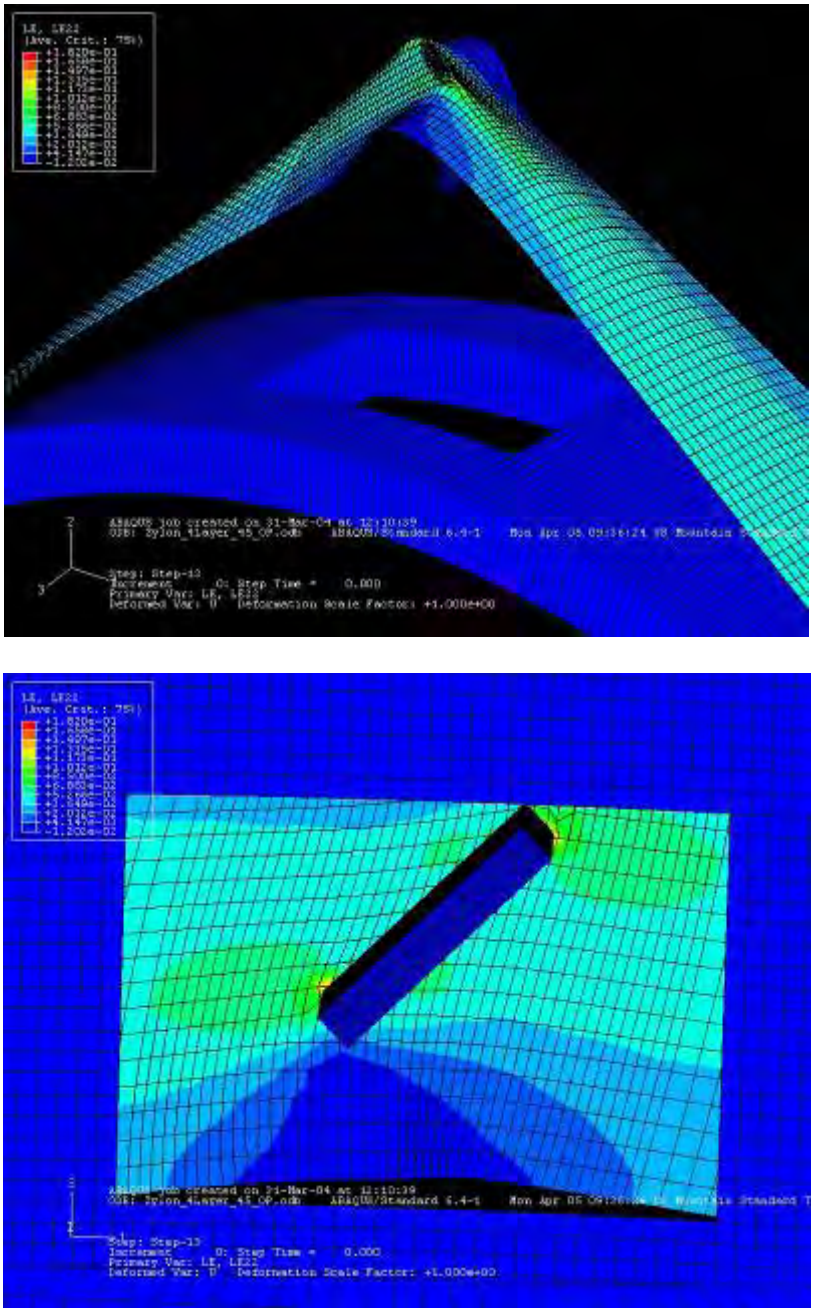

Figure 111b. Four-Layer Zylon—45-Degree Orientation (Thicker Blunt Nose)—Plot of In-Plane Strain ε_1 Superimposed on Deformation at the End of the Last Load Step

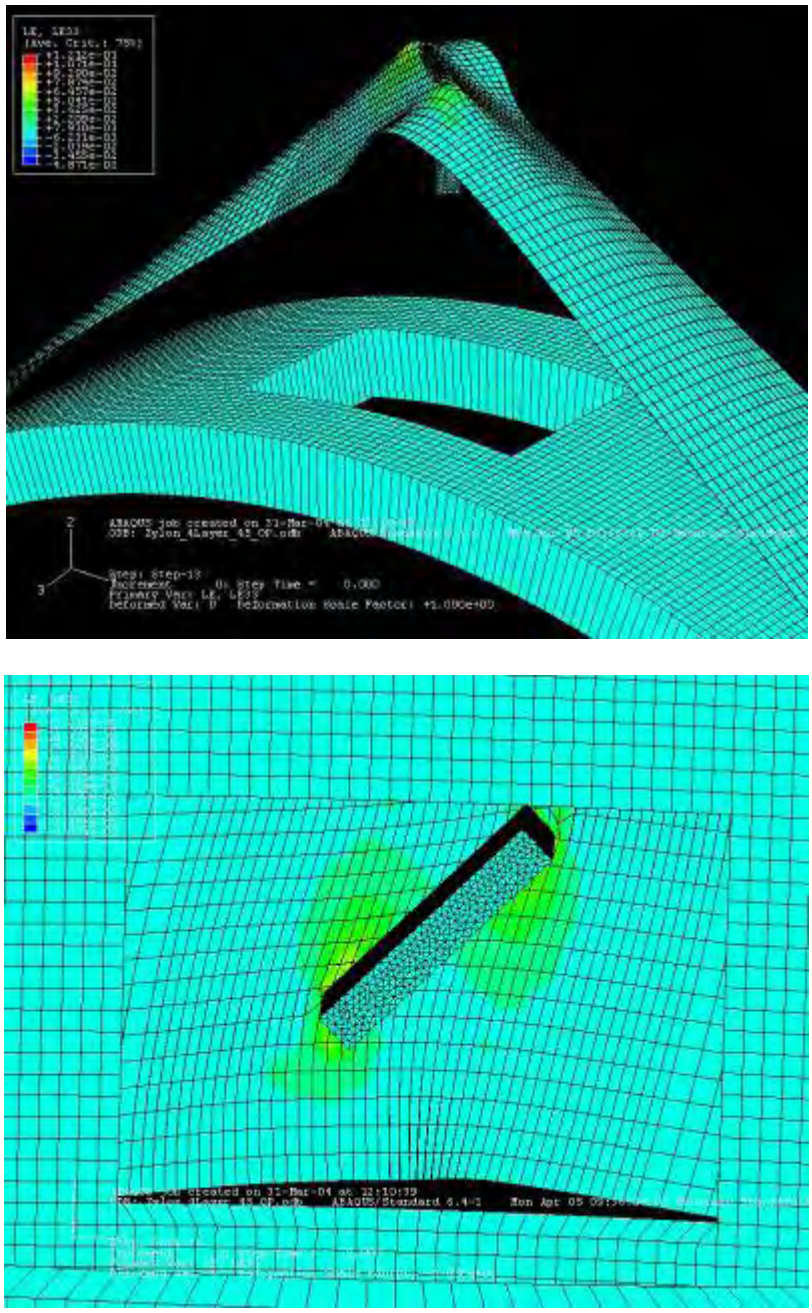

Figure 111c. Four-Layer Zylon—45-Degree Orientation (Thicker Blunt Nose)—Plot of In-Plane Strain ε_2 Superimposed on Deformation at the End of the Last Load Step

Figure 112a and table 59 compare the static test FE simulation to the experimental results for the four-layer Zylon, 90-degree orientation, thicker blunt-nose test case. Figures 112b and 112c show the FE simulation deformation.

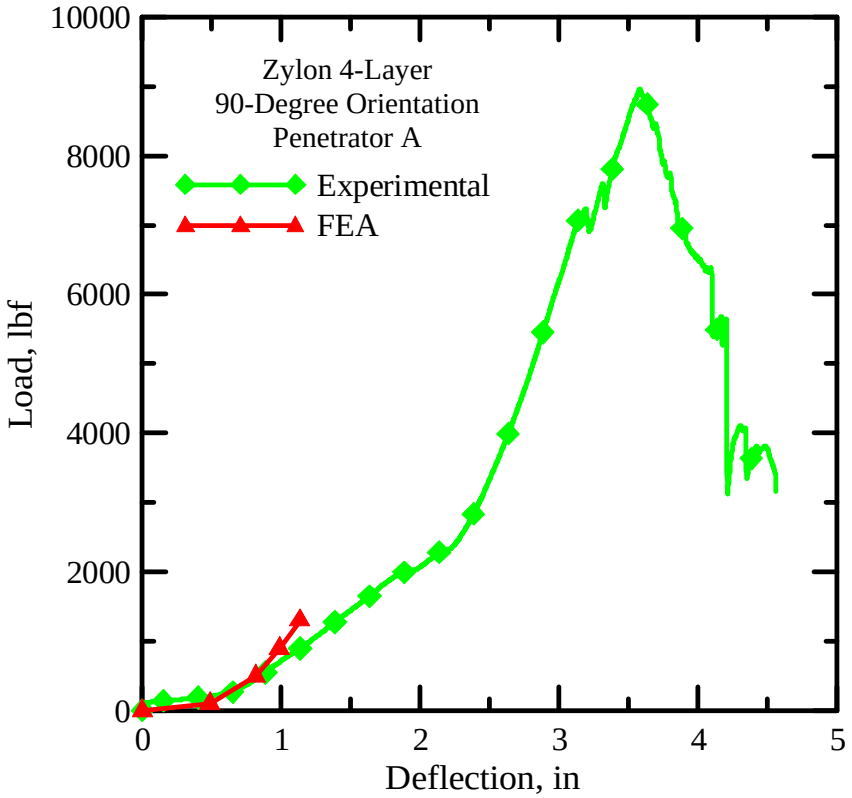

Figure 112a. Comparison of the Load-Displacement Graphs for the Four-Layer Zylon, 90-Degree Orientation, Thicker Blunt-Nose Test

Table 59. Static Test—FEA Comparison for the Four-Layer Zylon, 90-Degree Orientation, Thicker Blunt-Nose Test

	Static Test	FEA
Peak load (lb)	8957	1298
Displacement at peak load (in.)	3.58	1.132

The experimental curve was slack-shifted by 1.54 inches.

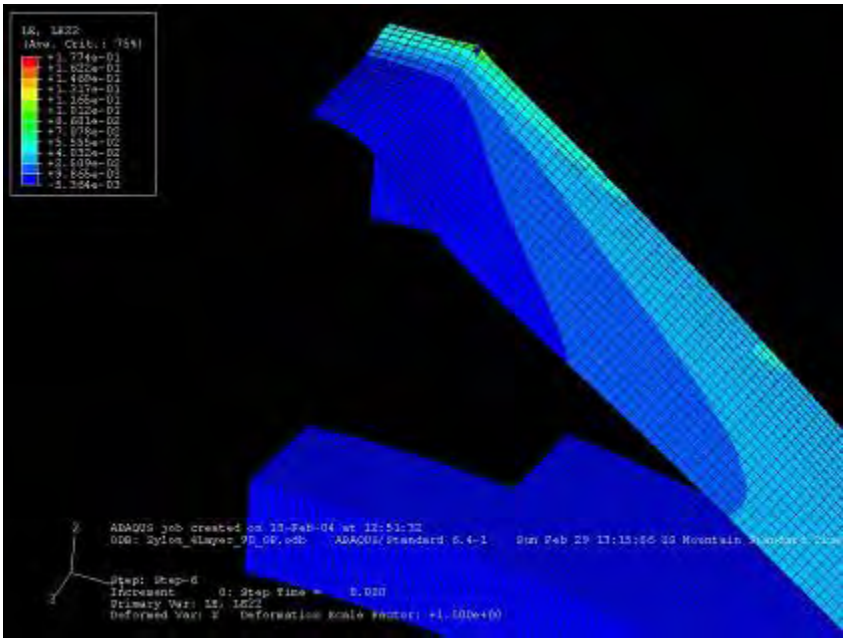

Figure 112b. Four-Layer Zylon—90-Degree Orientation (Thicker Blunt Nose)—Plot of In-Plane Strain ε_1 Superimposed on Deformation at the End of the Last Load Step

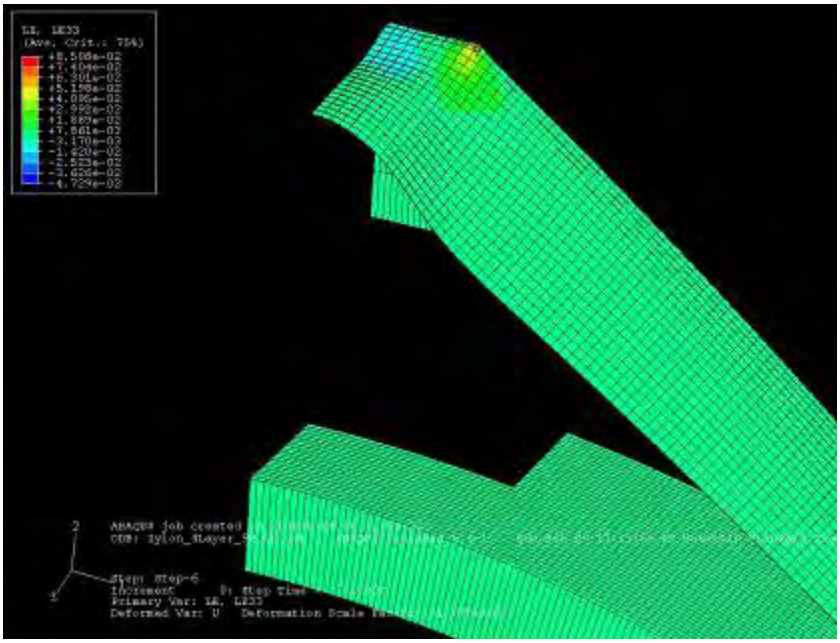

Figure 112c. Four-Layer Zylon—90-Degree Orientation (Thicker Blunt Nose)—Plot of In-Plane Strain ε_2 Superimposed on Deformation at the End of the Last Load Step

Figure 113a and table 60 compare the static test FE simulation to the experimental results for the four-layer Zylon, 0-degree off-center orientation, thicker blunt-nose test case. Figures 113b and 113c show the FE simulation deformation.

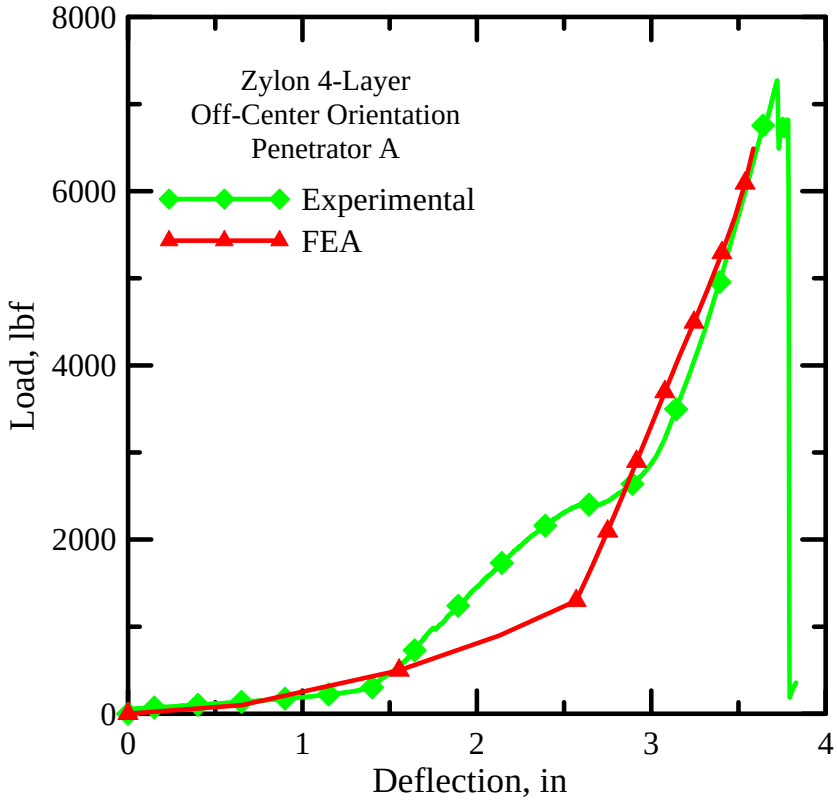

Figure 113a. Comparison of the Load-Displacement Graphs for the Four-Layer Zylon, Off-Center Orientation, Thicker Blunt-Nose Test

Table 60. Static Test—FEA Comparison for the Four-Layer Zylon, Off-Center Orientation, Thicker Blunt-Nose Test

	Static Test	FEA
Peak load (lb)	7276	6490
Displacement at peak load (in.)	3.586	3.49

The experimental curve was slack-shifted by 1.24 inches.

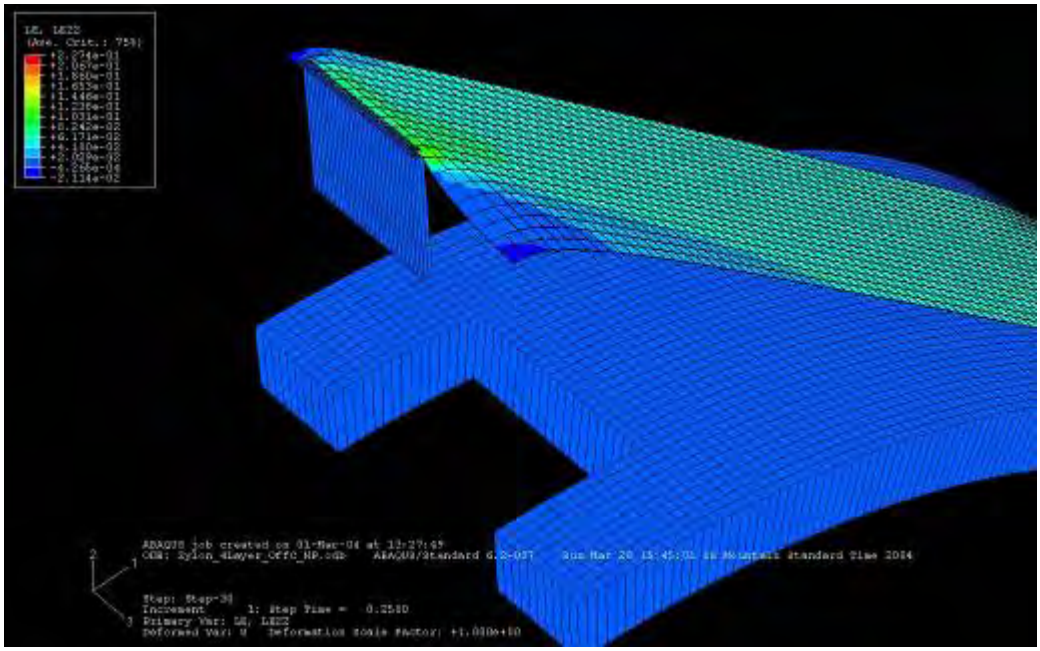

Figure 113b. Four-Layer Zylon—Off-Center Orientation (Thicker Blunt Nose)—Plot of In-Plane Strain ε_1 Superimposed on Deformation at the End of the Last Load Step

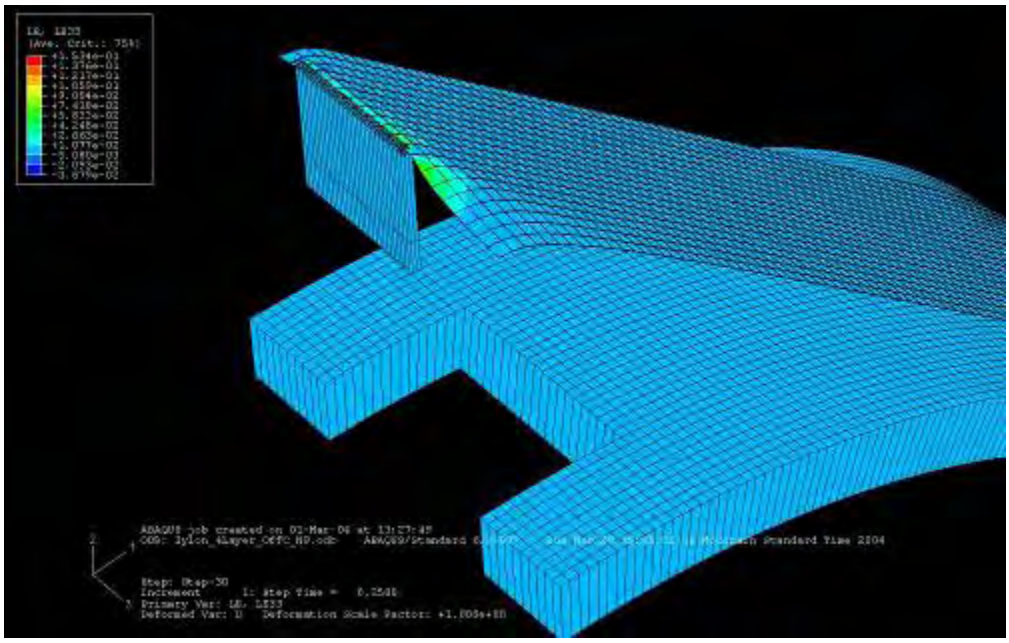

Figure 113c. Four-Layer Zylon—Off-Center Orientation (Thicker Blunt Nose)—Plot of In-Plane Strain ε_2 Superimposed on Deformation at the End of the Last Load Step

5.3.2.3 Eight Layer.

Figure 114a and table 61 compare the static test FE simulation to the experimental results for the eight-layer Zylon, 0-degree orientation, thinner blunt-nose Test case. Figures 114b and 114c show the FE simulation deformation.

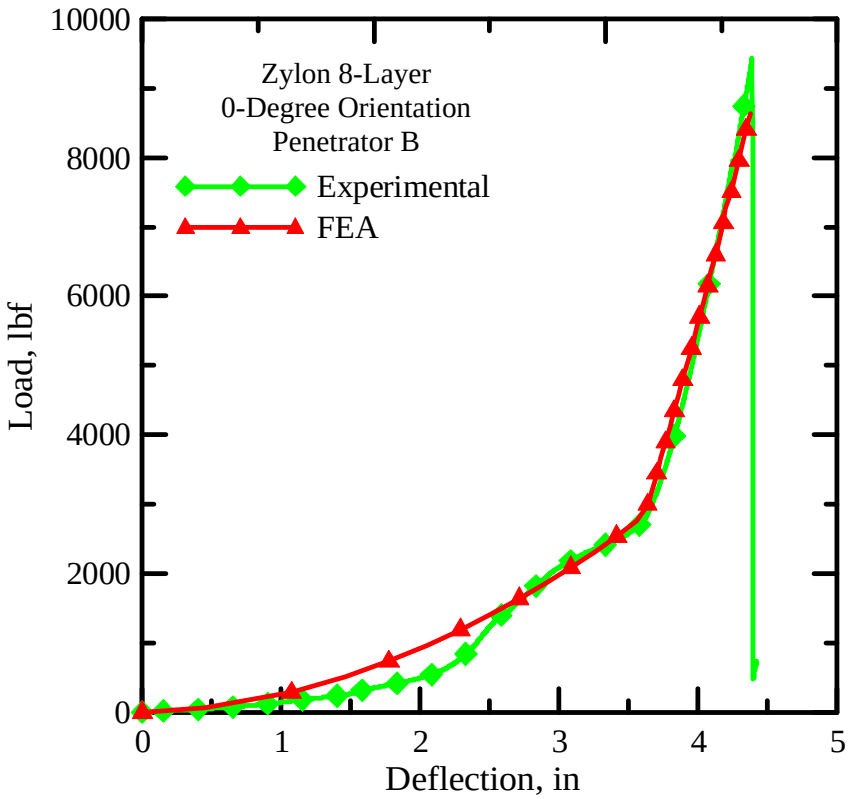

Figure 114a. Comparison of the Load-Displacement Graphs for the Eight-Layer Zylon, 0-Degree Orientation, Thinner Blunt-Nose Test

Table 61. Static Test—FEA Comparison for the Eight-Layer Zylon, 0-Degree Orientation, Thinner Blunt-Nose Test

	Static Test	FEA
Peak load (lb)	9446	8629
Displacement at peak load (in.)	4.391	4.374

The experimental curve was slack-shifted by 0.13 inch.

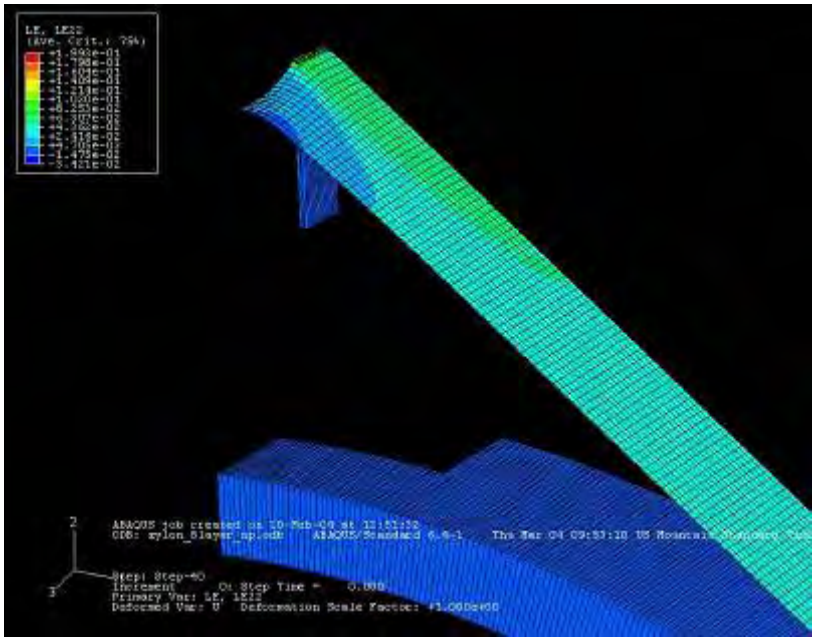

Figure 114b. Eight-Layer Zylon—0-Degree Orientation (Thinner Blunt Nose)—Plot of In-Plane Strain ε_1 Superimposed on Deformation at the End of the Last Load Step

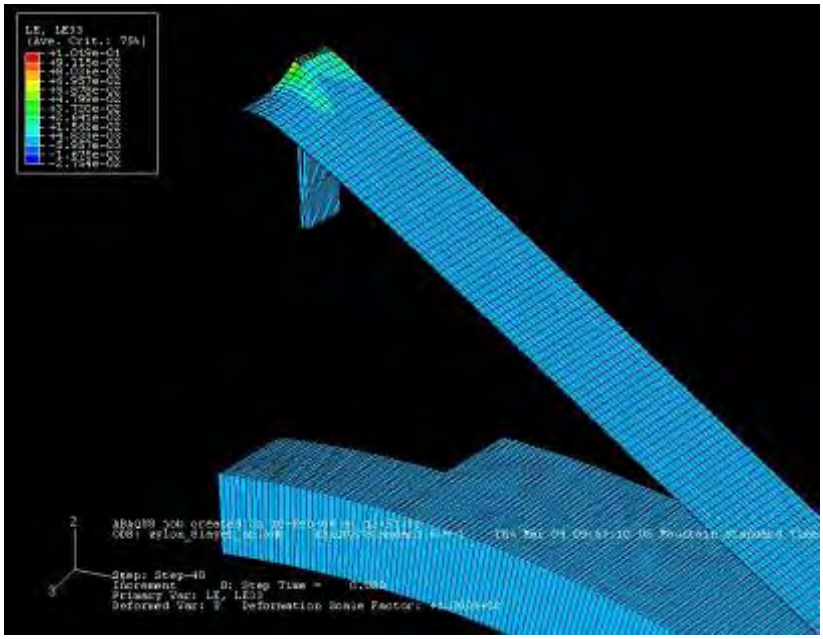

Figure 114c. Eight-Layer Zylon—0-Degree Orientation (Thinner Blunt Nose)—Plot of In-Plane Strain ε_2 Superimposed on Deformation at the End of the Last Load Step

Figure 115a and table 62 compare the static test FE simulation to the experimental results for the eight-layer Zylon, 45-degree orientation, thinner blunt-nose test case. Figures 115b and 115c show the FE simulation deformation.

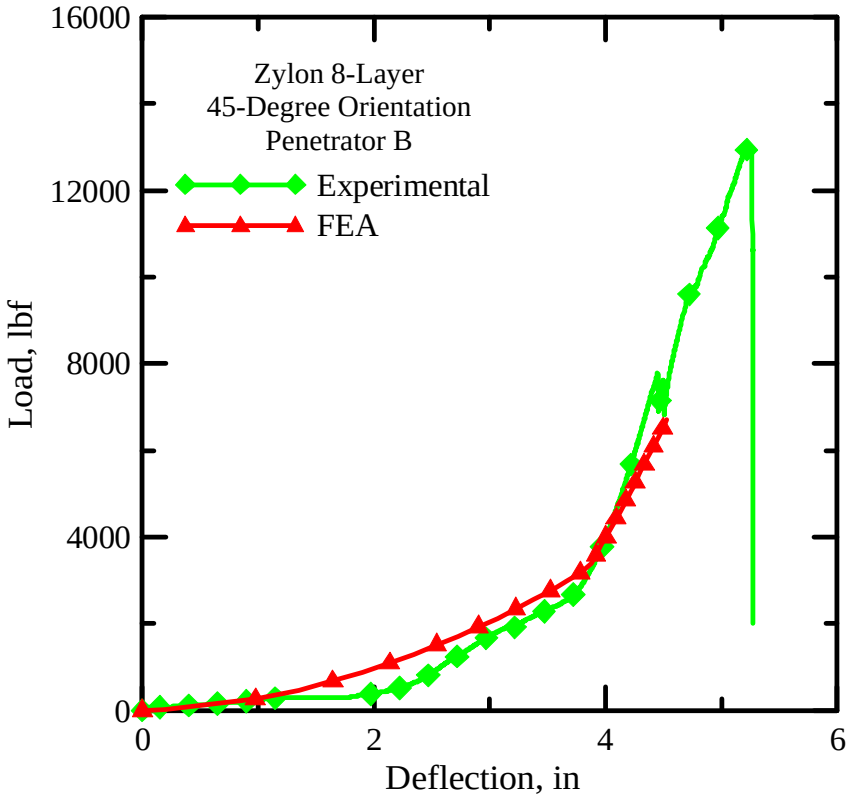

Figure 115a. Comparison of the Load-Displacement Graphs for the Eight-Layer Zylon, 45-Degree Orientation, Thinner Blunt-Nose Test

Table 62. Static Test—FEA Comparison for the Eight-Layer Zylon, 45-Degree Orientation, Thinner Blunt-Nose Test

	Static Test	FEA
Peak load (lb)	12948	6712
Displacement at peak load (in.)	5.219	4.532

The experimental curve was slack-shifted by 0.6 inch.

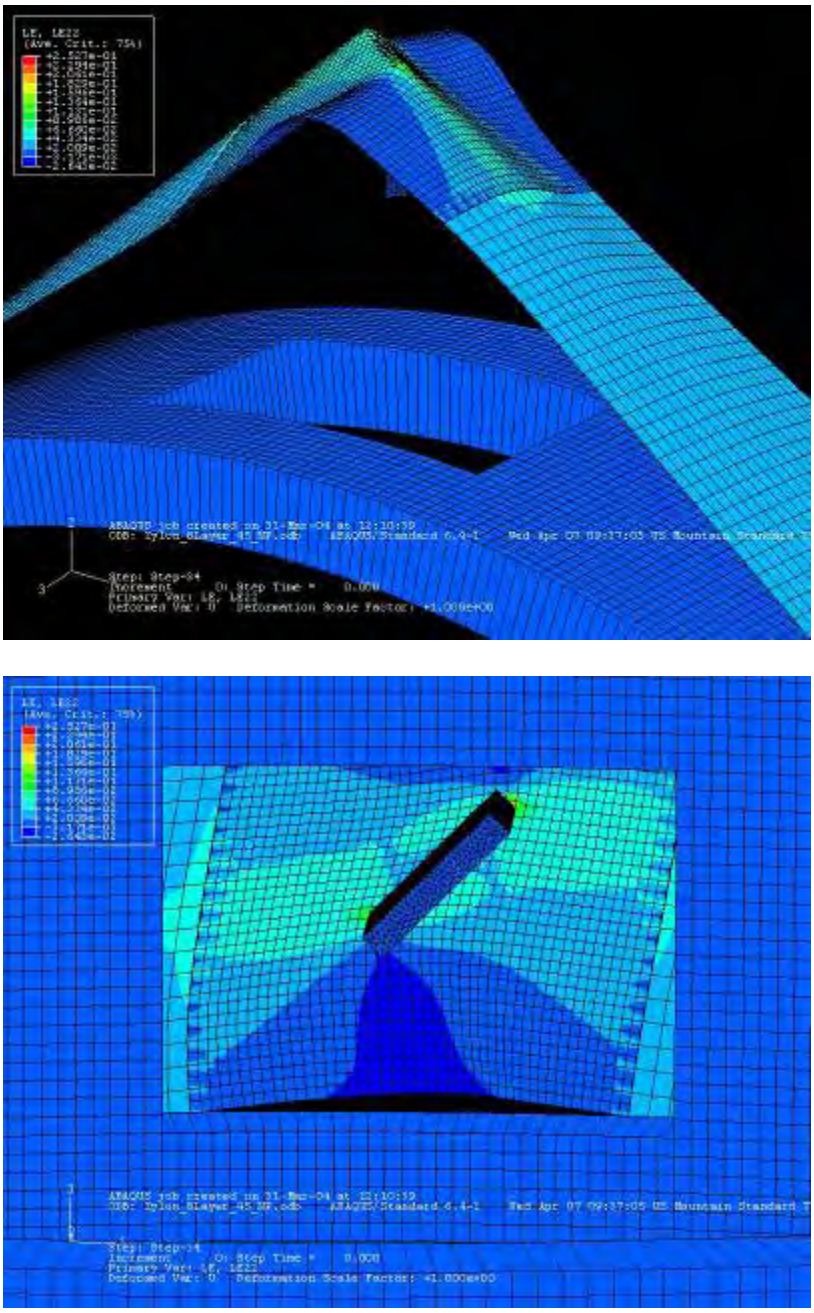

Figure 115b. Eight-Layer Zylon—45-Degree Orientation (Thinner Blunt Nose)—Plot of In-Plane Strain ε_1 Superimposed on Deformation at the End of the Last Load Step

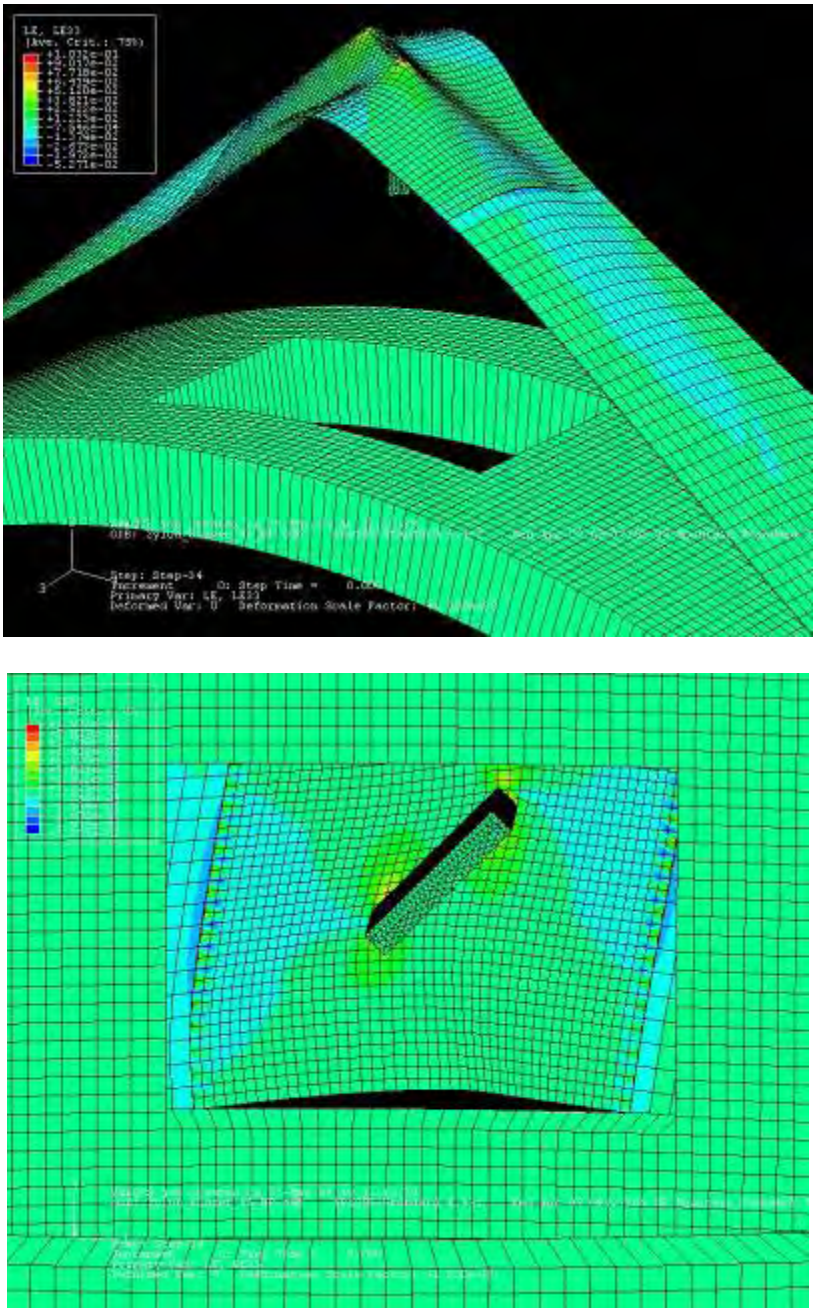

Figure 115c. Eight-Layer Zylon—45-Degree Orientation (Thinner Blunt Nose)—Plot of In-Plane Strain ε_2 Superimposed on Deformation at the End of the Last Load Step

Figure 116a and table 63 compare the static test FE simulation to the experimental results for the eight-layer Kevlar, 90-degree orientation, thinner blunt-nose test case. Figures 116b and 116c show the FE simulation deformation.

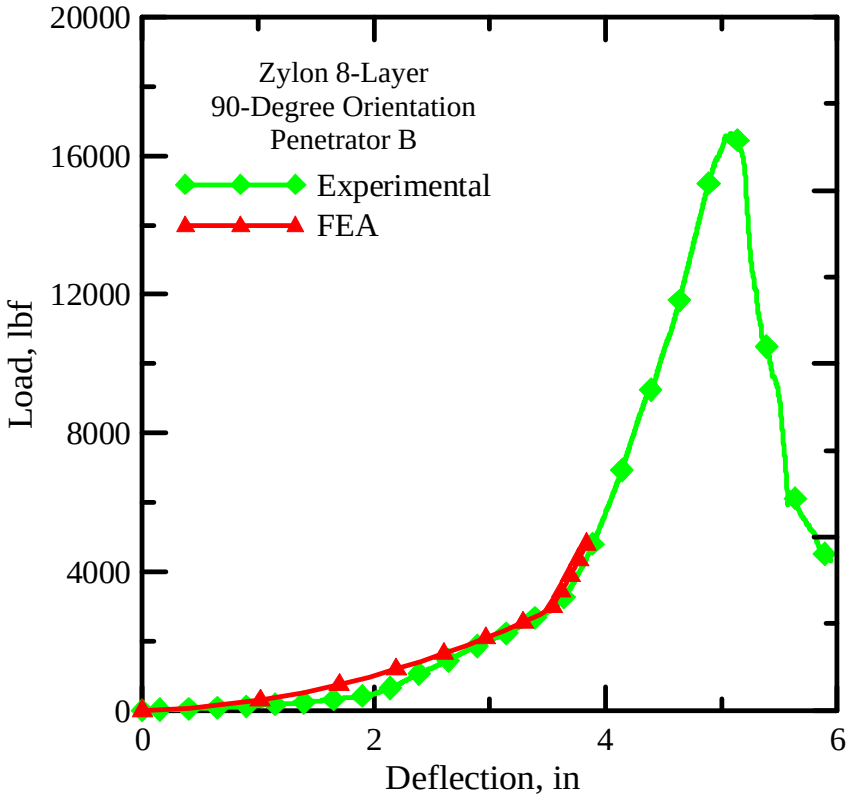

Figure 116a. Comparison of the Load-Displacement Graphs for the Eight-Layer Zylon, 90-Degree Orientation, Thinner Blunt-Nose Test

Table 63. Static Test—FEA Comparison for the Eight-Layer Zylon, 90-Degree Orientation, Thinner Blunt-Nose Test

	Static Test	FEA
Peak load (lb)	16649	4343
Displacement at peak load (in.)	5.08	3.854

The experimental curve was slack-shifted by 0.29 inch.

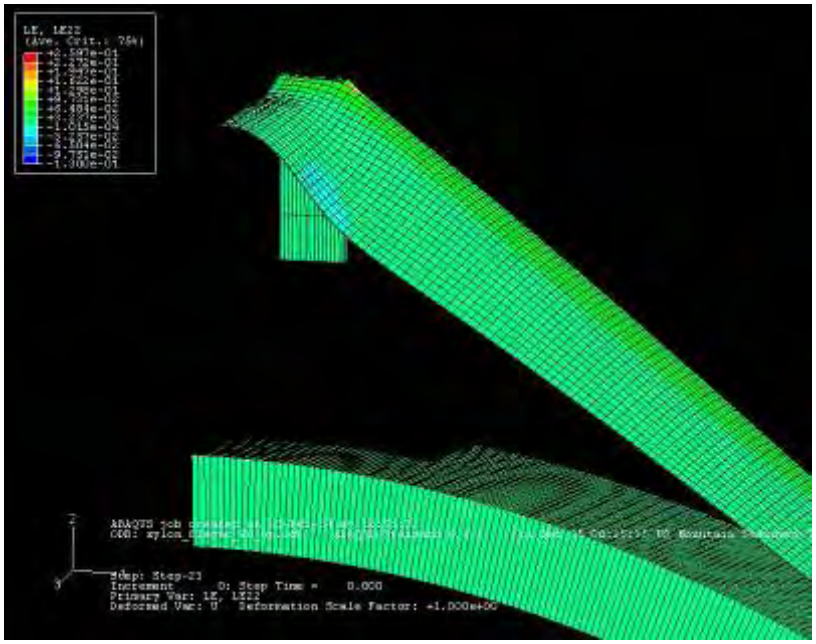

Figure 116b. Eight-Layer Zylon—90-Degree Orientation (Thinner Blunt Nose)—Plot of In-Plane Strain ε_1 Superimposed on Deformation at the End of the Last Load Step

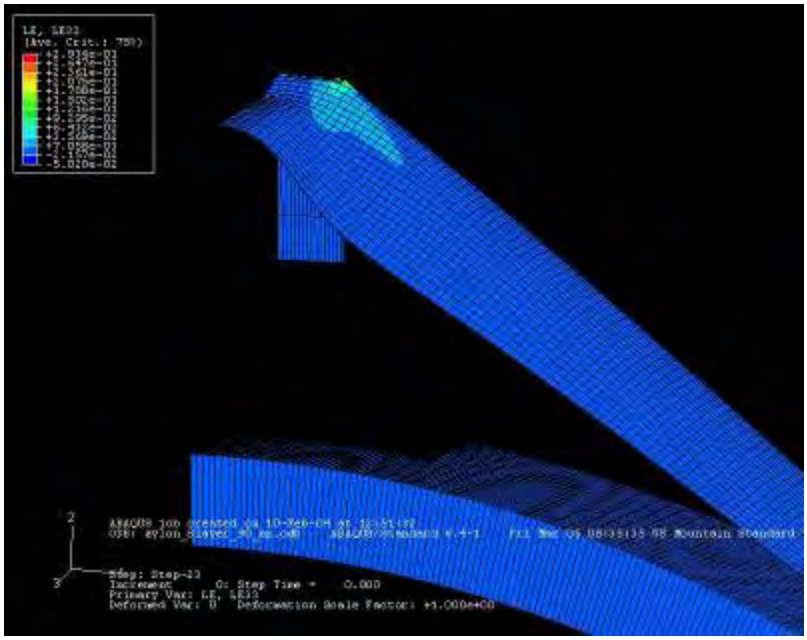

Figure 116c. Eight-Layer Zylon—90-Degree Orientation (Thinner Blunt Nose)—Plot of In-Plane Strain ε_2 Superimposed on Deformation at the End of the Last Load Step

Figure 117a and table 64 compare the static test FE simulation to the experimental results for the eight-layer Zylon, 45-degree orientation, thicker blunt-nose test case. Figures 117b and 117c show the FE simulation deformation.

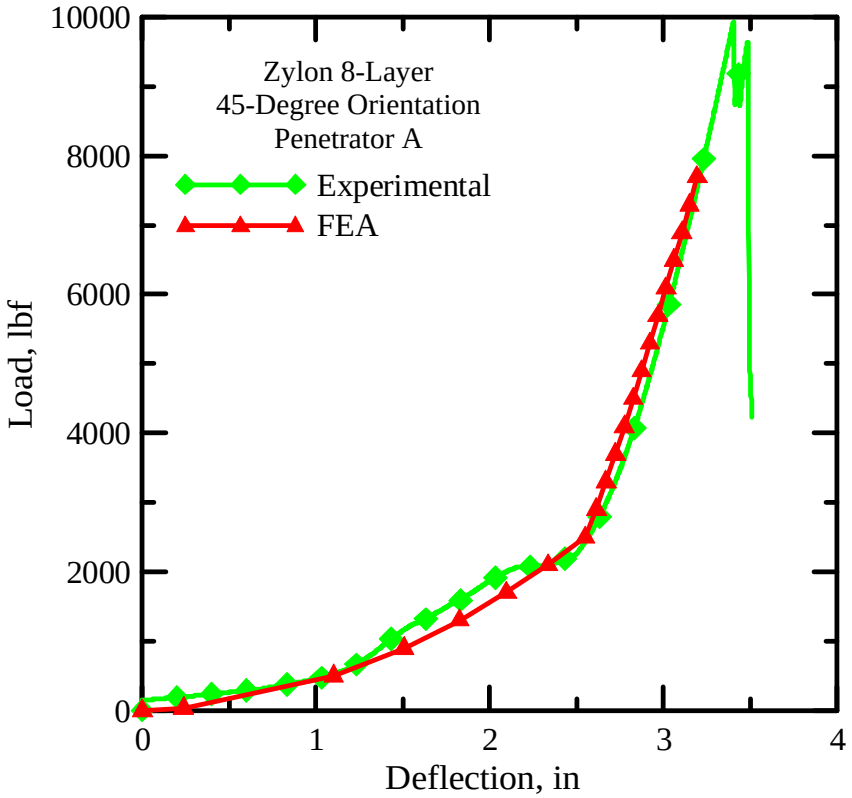

Figure 117a. Comparison of the Load-Displacement Graphs for the Eight-Layer Zylon, 45-Degree Orientation, Thicker Blunt-Nose Test

Table 64. Static Test—FEA Comparison for the Eight-Layer Zylon, 45-Degree Orientation, Thicker Blunt-Nose Test

	Static Test	FEA
Peak load (lb)	9952	7688
Displacement at peak load (in.)	3.405	3.194

The experimental curve was slack-shifted by 1.14 inches.

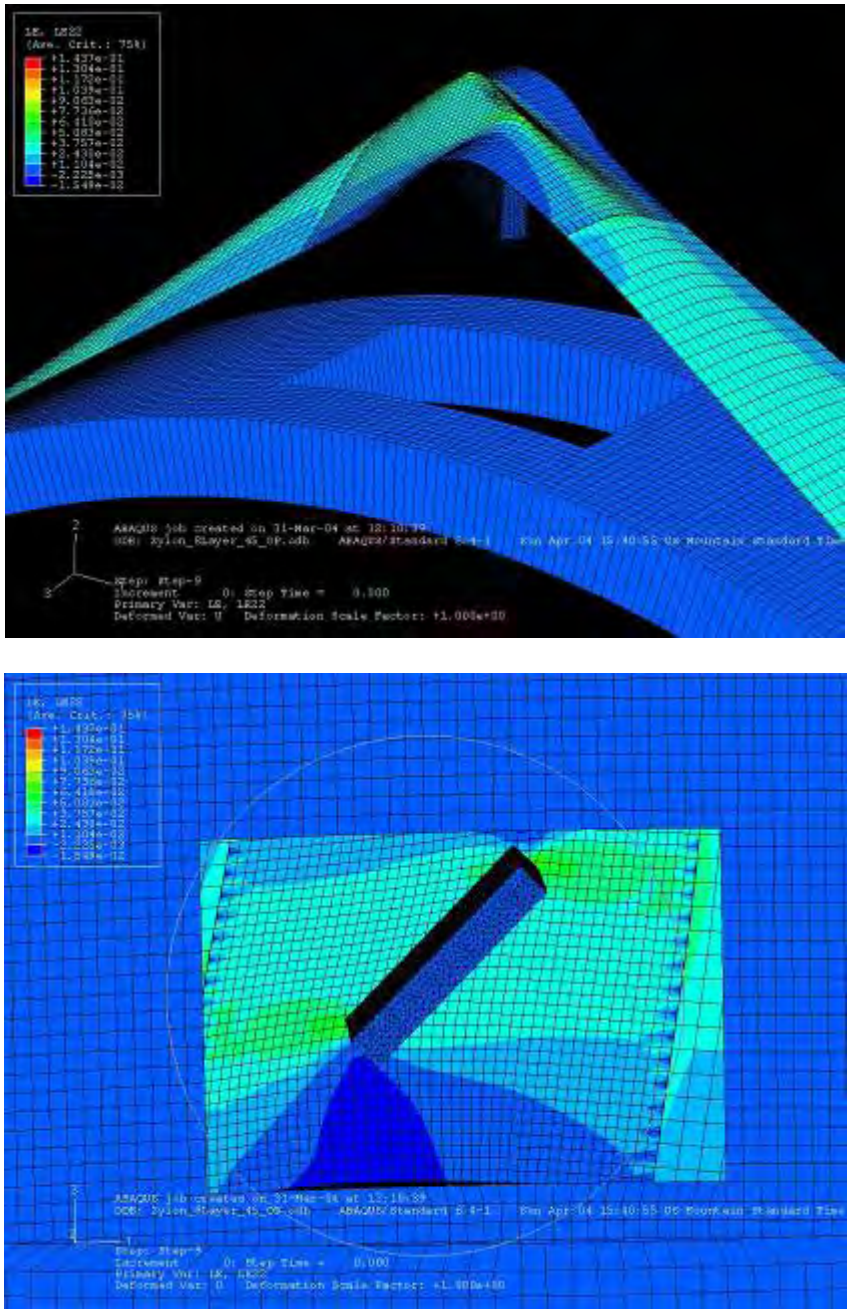

Figure 117b. Eight-Layer Zylon—45-Degree Orientation (Thicker Blunt Nose)—Plot of In-Plane Strain ε_1 Superimposed on Deformation at the End of the Last Load Step

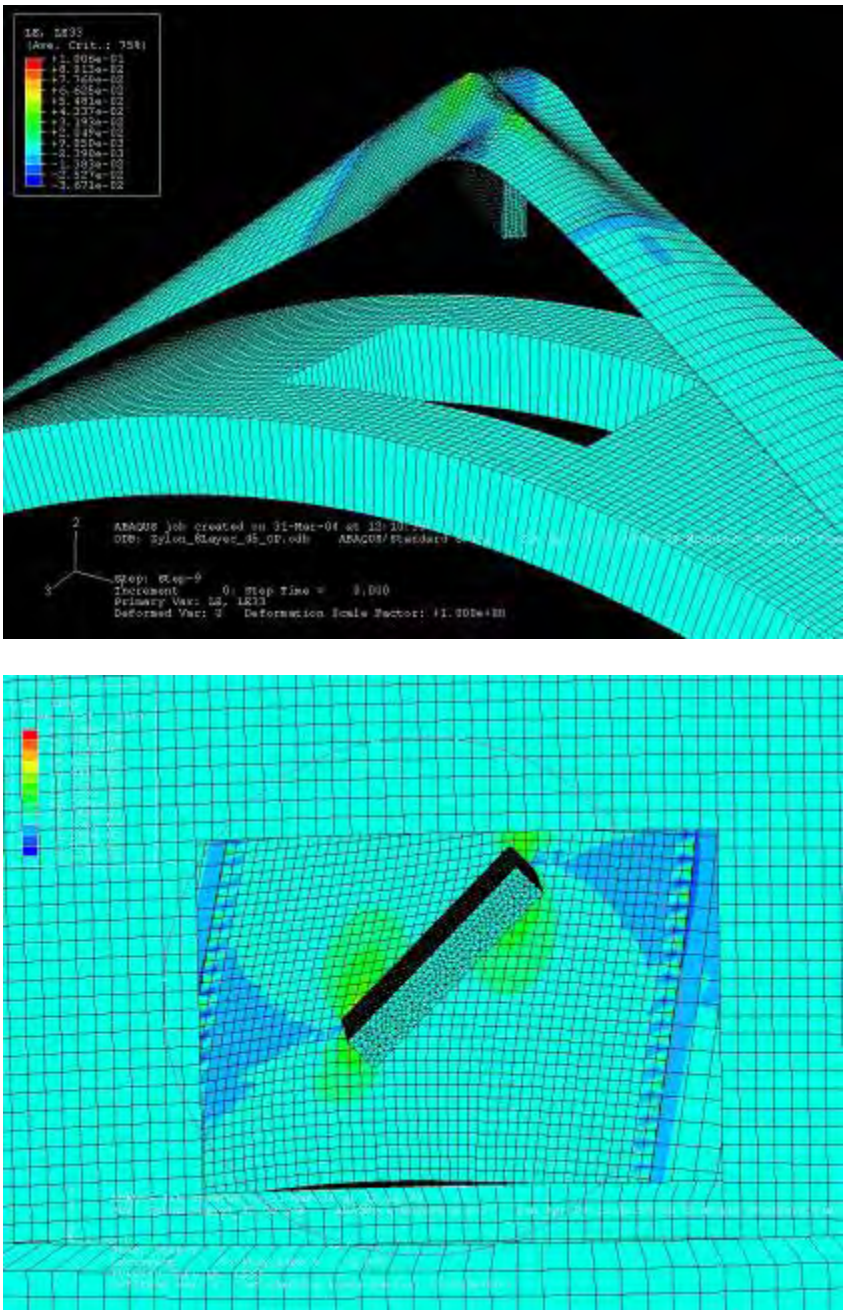

Figure 117c. Eight-Layer Zylon—45-Degree Orientation (Thicker Blunt Nose)—Plot of In-Plane Strain ε_2 Superimposed on Deformation at the End of the Last Load Step

Figure 118a and table 65 compare the static test FE simulation to the experimental results for the eight-layer Zylon, 90-degree thicker orientation, blunt-nose test case. Figures 118b and 118c show the FE simulation deformation.

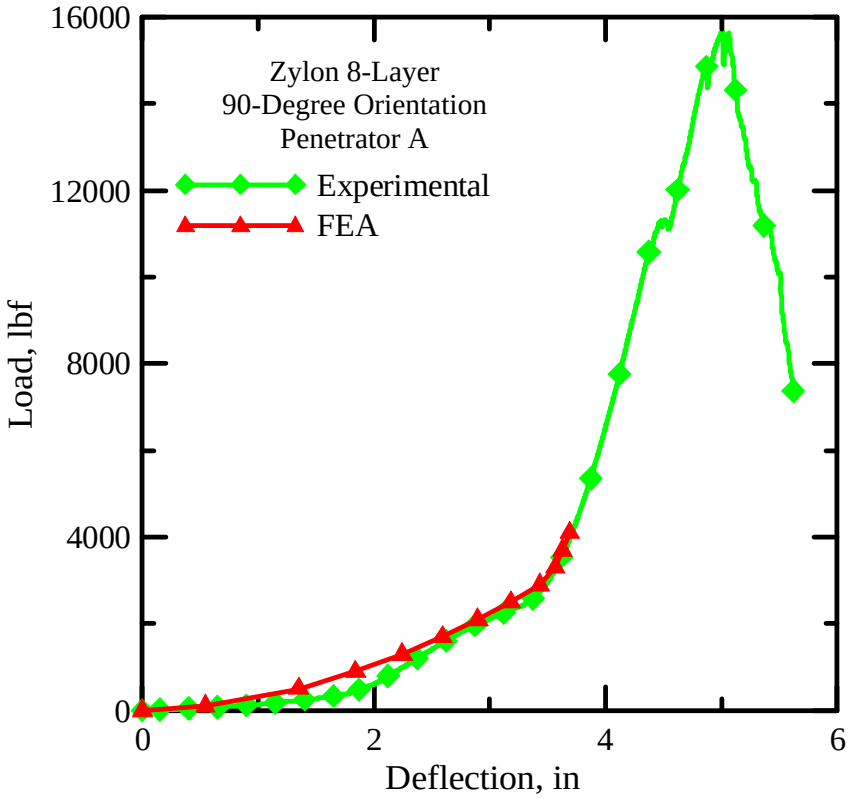

Figure 118a. Comparison of the Load-Displacement Graphs for the Eight-Layer Zylon, 90-Degree Orientation, Thicker Blunt-Nose Test

Table 65. Static Test—FEA Comparison for the Eight-Layer Zylon, 90-Degree Orientation, Thicker Blunt-Nose Test

	Static Test	FEA
Peak load (lb)	15669	4093
Displacement at peak load (in.)	5.009	3.691

The experimental curve was slack-shifted by 0.14 inch.

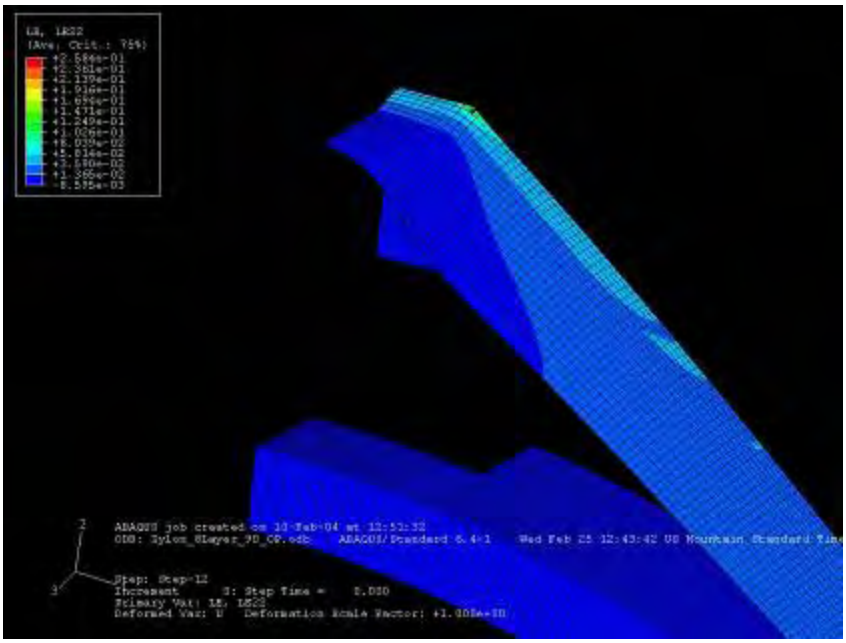

Figure 118b. Eight-Layer Zylon—90-Degree Orientation (Thicker Blunt Nose)—Plot of In-Plane Strain ε_1 Superimposed on Deformation at the End of the Last Load Step

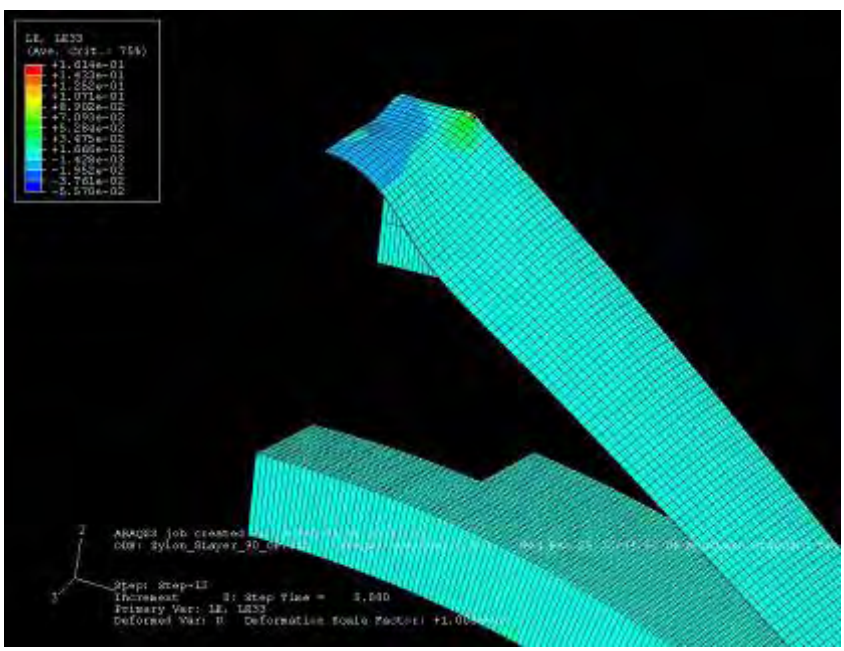

Figure 118c. Eight-Layer Zylon—90-Degree Orientation (Thicker Blunt Nose)—Plot of In-Plane Strain ε_2 Superimposed on Deformation at the End of the Last Load Step

Figure 119a and table 66 compare the static test FE simulation to the experimental results for the eight-layer Zylon, off-center orientation, thicker blunt-nose test case. Figures 119b and 119c show the FE simulation deformation.

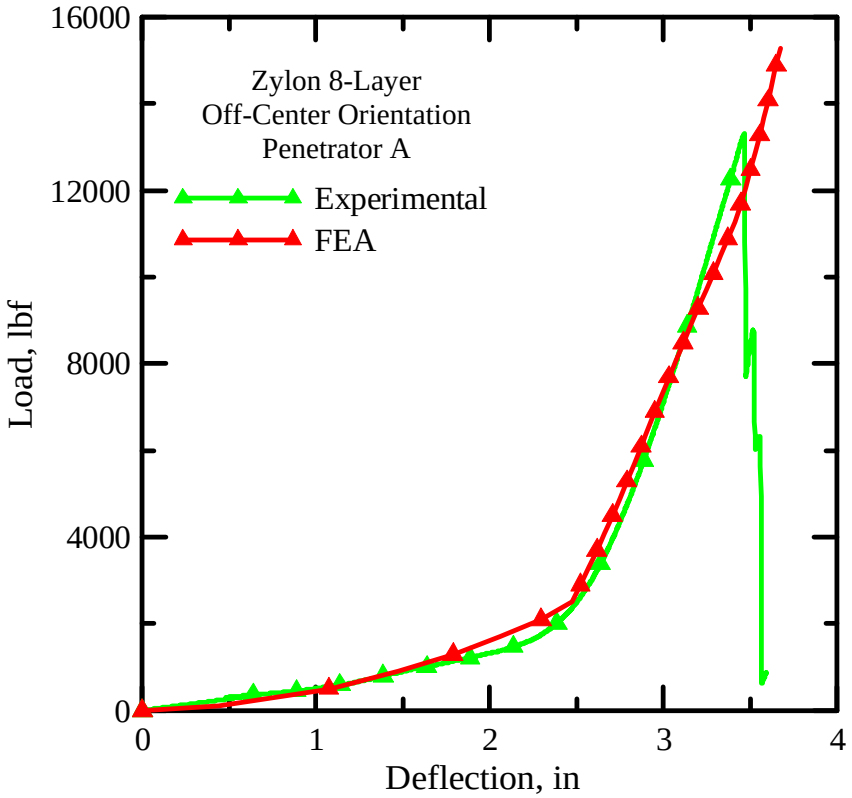

Figure 119a. Comparison of the Load-Displacement Graphs for the Eight-Layer Zylon, Off-Center Orientation, Thicker Blunt-Nose Test

Table 66. Static Test—FEA Comparison for the Eight-Layer Zylon, Off-Center Orientation, Thicker Blunt-Nose Test

	Static Test	FEA
Peak load (lb)	13349	15276
Displacement at peak load (in.)	3.468	3.672

The experimental curve was slack-shifted by 1.22 inches.

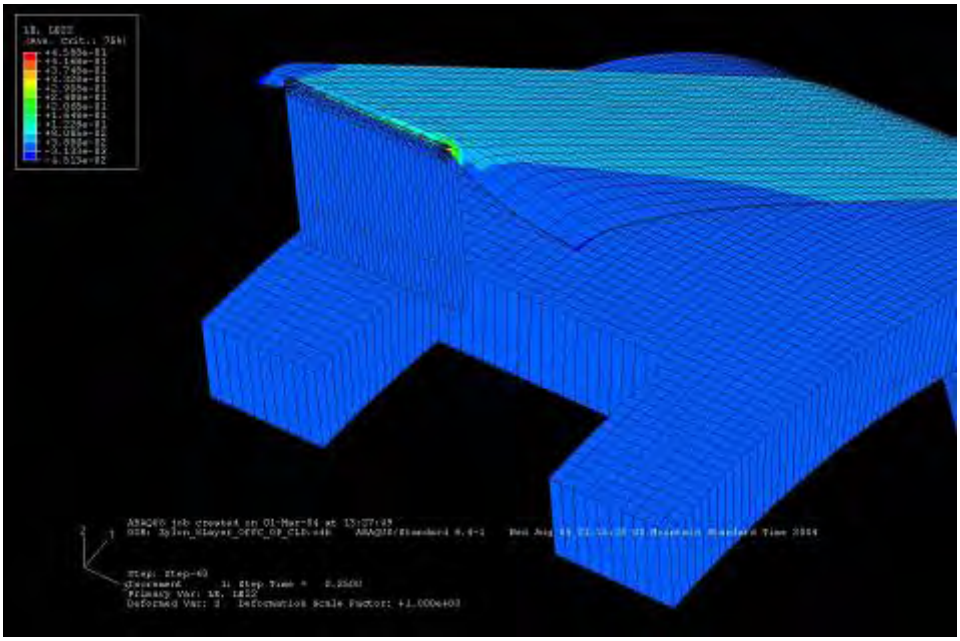

Figure 119b. Eight-Layer Zylon—Off-Center Orientation (Thicker Blunt Nose)—Plot of In-Plane Strain ε_1 Superimposed on Deformation at the End of the Last Load Step

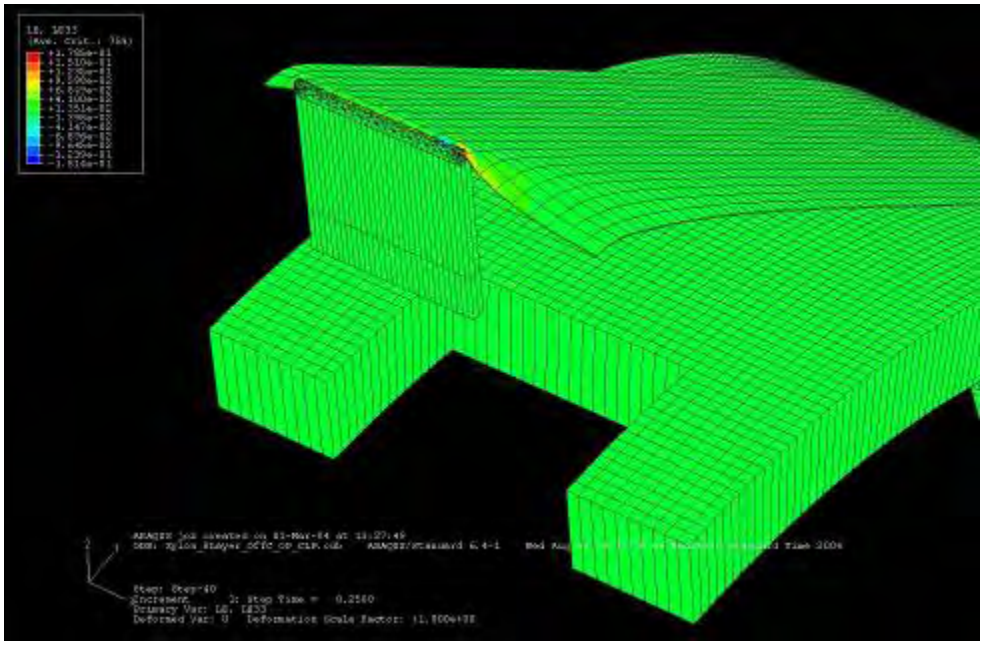

Figure 119c. Eight-Layer Zylon—Off-Center Orientation (Thicker Blunt Nose)—Plot of In-Plane Strain ε_2 Superimposed on Deformation at the End of the Last Load Step

For all the Kevlar and Zylon simulations, the following observations were made.

- The maximum tensile strain in the fabric occurs at the area in contact with the edge of the blunt nose. This was consistent with the failure mode that was observed, during the static tests, to initiate at and around the blunt-nose contact region. The strain gradient was high near the edges of the blunt nose and decreased rapidly away from the blunt nose. Strain values greater than the ultimate strain value are found in all FE simulations. This is because FEs are not deleted when the ultimate strain values are exceeded. However, this high-strain zone is very localized.

- The highest compressive strains occurred in the fabric at the end diametrically opposite the blunt nose and at the edge of the fabric near the blunt nose. These compressive strains were prominent only after the postpeak stiffness value was reached. The fabric-draping effect shown in the deformation plot was more prominent with Zylon specimens than with Kevlar specimens.

- The average relative error (prediction of the peak load) for the 21 Kevlar simulations was 7.54% and for the 19 Zylon simulations was 45.5%. For the Kevlar simulations, the largest error in underpredicting the peak load was 69% and the largest error in overpredicting the peak load was 82%. The corresponding values for the Zylon simulations were 98% and 26%, respectively.

- Typical implicit FEA simulations terminated when the solution started diverging due to the presence of negative eigenvalues in the system stiffness matrix (matrix was not positive definite) or when the contact surface between the fabric and the blunt nose could not be resolved at large displacement values. The contact issue affects the Zylon models more than the Kevlar models. It was assumed this was due to the extremely small Zylon fabric thickness (compared to Kevlar fabric thickness). Of the 19 Zylon simulations, one simulation (one layer) failed to produce any result, and 9 simulations terminated prematurely (error was more than 50%).

- FE simulations of 0-degree-oriented blunt-nose configurations were the closest to experimental results. The worst results were from the 90-degree-oriented blunt-nose configurations. Interestingly, all the Kevlar off-center models overpredicted the peak load, while two off-center Zylon models overpredicted the peak load.

- When the multiple-layer results are compared to the FE-obtained curves, the FE results indicated a stiffer model or behavior. One of the reasons was because in the FEAs only one equivalent fabric layer was modeled (or represented multiple-fabric layers).

6. CONCLUDING REMARKS.

The tasks specified in the statement of work for this research project have been met. To summarize, the following is the list of tasks discussed in this report.

- Experimental Tests
  - Simple tension tests
  - Fabric-on-fabric friction tests
  - Static ring tests
- Finite Element Analysis (FEA)
  - Generation and analysis of the finite element (FE) models for the static ring tests
- Comparison of experimental and FE results
  - Comparison of the FE results with respect to experimentally obtained results

The simple tension tests were performed on a number of Kevlar and Zylon fabrics to determine the stress-strain relationship in the principal material direction. Response of fabrics to adhesion was determined in the splice tests. It was found that adhesion was a problem, especially for Zylon. Hence, it was decided to clamp the fabric specimens to the steel ring in the static ring tests. These tests facilitated an understanding of the performance in terms of strength, stiffness, and energy-absorption capacity for Kevlar and Zylon in terms of single- and multiple-layer fabrics. User-defined, materially nonlinear, large displacement, multiple-contact surface FEAs were carried out to compare the FE simulation results with those obtained experimentally.

The FE modeling and the results are extremely encouraging for a number of reasons. First, the FEAs verified the constitutive model developed from a number of experiments using fabric swatches—tension tests and friction tests. Second, it showed that development of a damage evolution model was necessary to capture the yarn breakages that took place before the peak load was reached. (It is much more difficult to handle this phenomenon if an implicit FEA were used.) Third, the developed basic constitutive model can be adapted for use in an explicit FEA where damage evolution, element deletion, or material erosion can be more readily programmed and executed. The results also show that issues such as yarn reorientation (affecting shear modulus values), contact formulation (contact between blunt nose and fabric), and contact between fabric layers (which is not included in the implicit analysis) are important issues that need to be addressed.

7. REFERENCES.

1. Rajan, S.D., Mobasher, B., Sharda, J., Yanna, V., Deenadaylu, C., Lau, D., and Shah, D., "Explicit FEA Modeling of Multilayer Composite Fabric for Gas Turbine Engines Containment Systems, Part 1: Static Tests and Modeling," FAA report DOT/FAA/AR-04/40,P1, November 2004.

2. Pereira, J.M. and Revilock, D.M., "Explicit FEA Modeling of Multilayer Composite Fabric for Gas Turbine Engines Containment Systems, Part 2: Ballistic Impact Testing," FAA report DOT/FAA/AR-04/40,P2, November 2004.

3. Simmons, J., Erlich, D., and Shockey, D., "Explicit FEA Modeling of Multilayer Composite Fabric for Gas Turbine Engines Containment Systems, Part 3: Model Development and Simulation of Experiments," FAA report DOT/FAA/AR-04/40,P3, November 2004.

4. Gomuc, Reha, "Explicit FEA Modeling of Multilayer Composite Fabric for Gas Turbine Engines Containment Systems, Part 4: Model Simulation for Ballistic Tests, Engine Fan Blade-Out, and Generic Engine," FAA report DOT/FAA/AR-04/40,P4, November 2004.

5. Chen, J., Lussier, D.S., Cao, J., and Peng, X.Q., "Materials Characterization Methods and Material Models for Stamping of Plain Woven Composites," *Intl. Journal of Forming Processes*, 4-3:4, 2004.

6. Dassault Systèmes Simulia Corporation, ABAQUS Suite, Version 6.4, Providence, RI, 2005.

APPENDIX A—DIFFERENCES BETWEEN HONEYWELL AND SRI LS-DYNA MODELS

A.1 INTRODUCTION.

The purpose of this document is to specify the differences between the finite element (FE) models and input files developed by SRI International (SRI) and Honeywell Engines, Systems & Services that simulate the National Aeronautics and Space Administration (NASA) ballistic tests. Both parties developed their respective input files for use with the LS-DYNA FE program. A specific case, LG610, will be used as a means for comparison.

A.2 FABRIC AND RING MODEL.

Both Honeywell and SRI models use a 0.25 in. mesh size for the ring and the fabric; however, Honeywell uses a uniform mesh for both the ring and the fabric, while SRI uses a nonuniform mesh for the ring and a uniform mesh for the fabric. An example of each mesh is shown in figures A-1 and A-2.

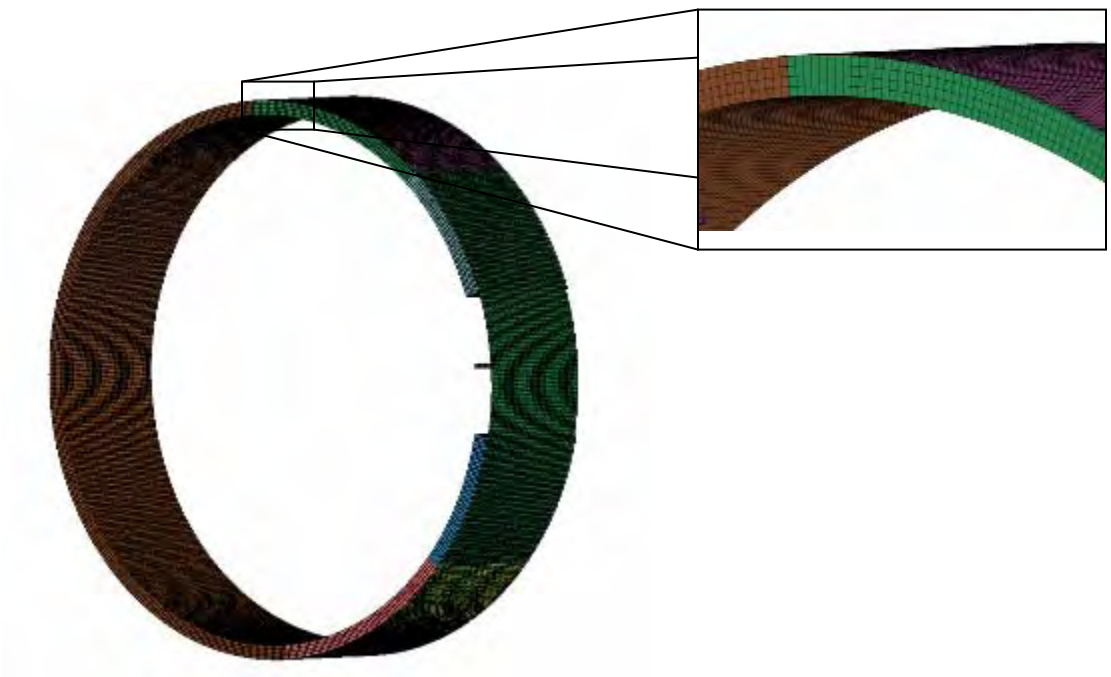

Figure A-1. Honeywell Ring and Fabric Mesh

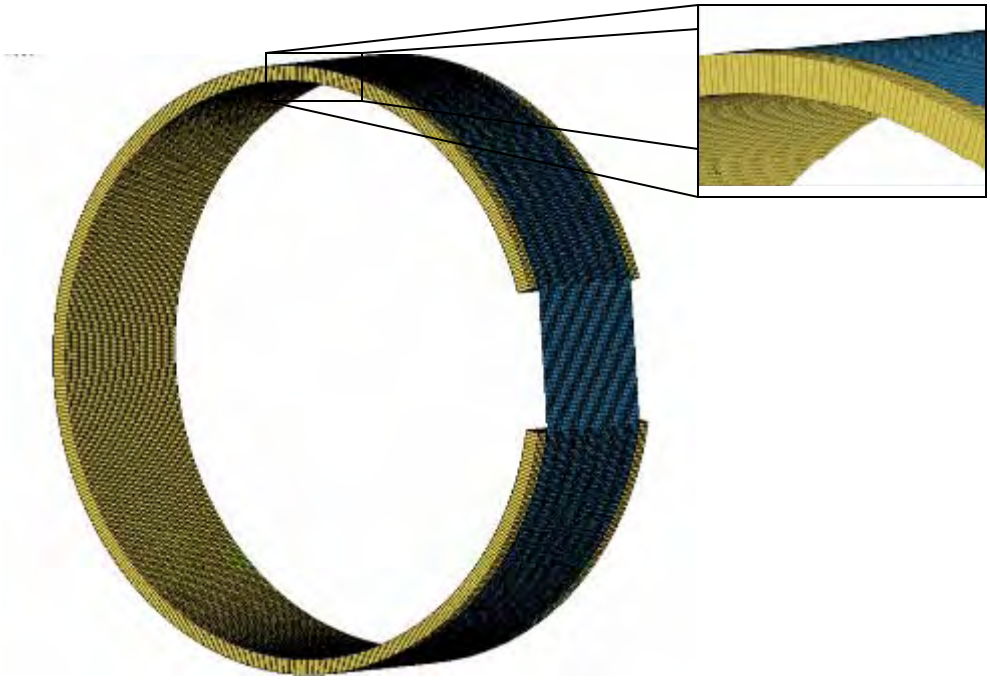

Figure A-2. SRI Ring and Fabric Mesh

Each model has different fabric geometry at the opening of the ring. Honeywell assumes that the fabric at the opening continues its arc, while SRI assumes that the fabric is pulled tight or that the plane of the fabric is straight (See figures A-3 and A-4). Also, in the Honeywell model, the ring opening is at 30°, while in the SRI model the ring opening is at 27.5°.

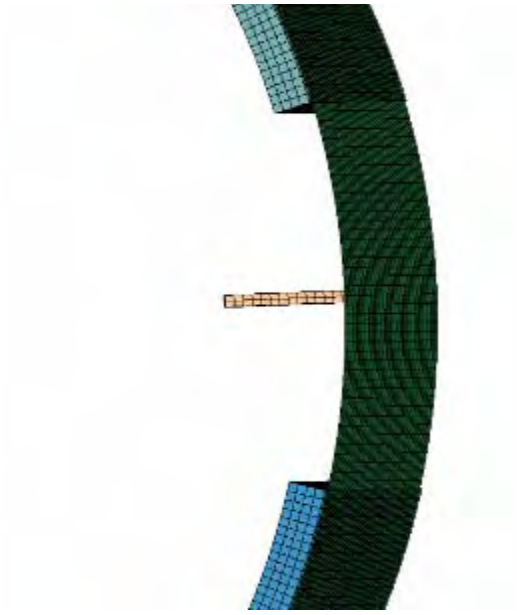

Figure A-3. Honeywell Model at Ring Opening

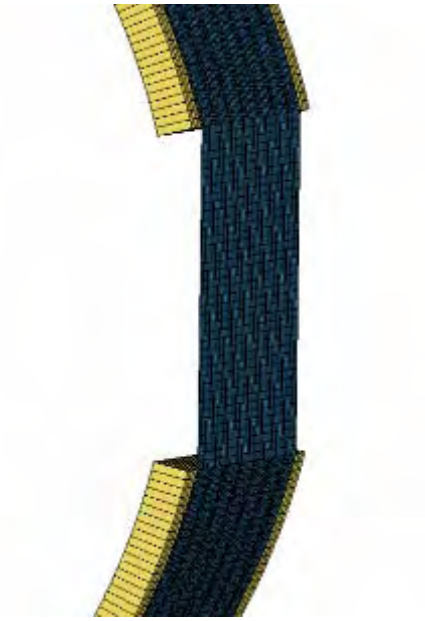

Figure A-4. SRI Model at Ring Opening

A.3 MODEL ORIENTATION.

Both models use a different methodology to simulate the 15° tilt in the ring. SRI tilts the ring 15° about the global coordinate system and gives the penetrator a velocity along one of the appropriate global coordinate axes, i.e., x or y. Honeywell does not tilt the ring about the global coordinate system, but rather, tilts the penetrator 15° with respect to the ring and gives the penetrator an initial velocity that has components along two global coordinate axes, i.e., x and y.

A.4 PENETRATOR MODEL.

Each model has a different mesh for the penetrator tip. The Honeywell model uses a squared tip with an approximate mesh size of 0.2 in., as shown in figure A-5. The SRI model uses a rounded tip with an approximate mesh size of 0.15 in., as shown in figure A-6. Both models use hexagonal elements. Also, the Honeywell model uses a total penetrator length of 7.25 in. with a thickness of 0.235 in., while the SRI model uses a total penetrator length of 7.0 in. with a thickness of 0.255 in. (LG610 represents a test using the "new" penetrator).

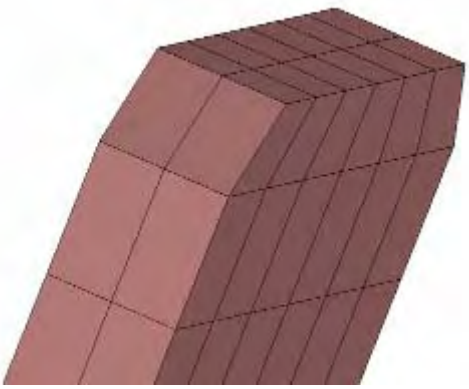

Figure A-5. Honeywell Model of Penetrator Tip

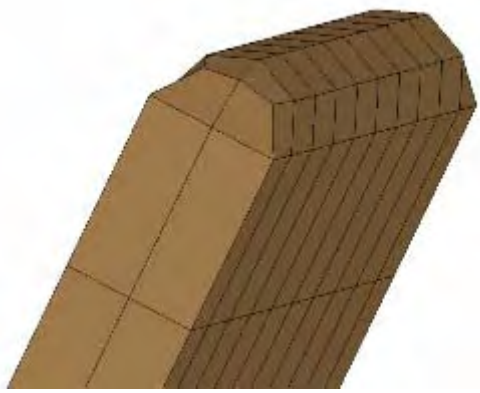

Figure A-6. SRI Model of Penetrator Tip

A.5 PENETRATOR ORIENTATION.

Both SRI and Honeywell rotate the penetrator to its pitch, roll, and yaw angles separately by defining a new local coordinate system with each rotation. Positive angles are defined using the right hand rule, as shown in figure A-7.

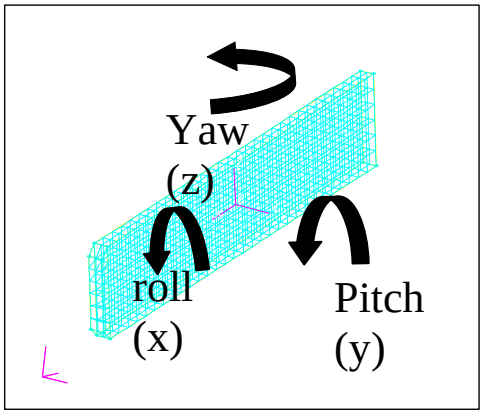

Figure A-7. Definition of Penetrator Orientation

A.6 INPUT FILE.

The general differences between the two models' input files are associated with the contact definition. Honeywell uses the *CONTACT_AUTOMATIC_SURFACE_TO_SURFACE feature in LS-DYNA while SRI uses the *CONTACT_ERODING_SINGLE_SURFACE feature. Tables A-1 and A-2 show the differences in the HOURGLASS values used, as well as the differences in the contact definition values for the both the Honeywell and SRI input files. Table A-3 shows a comparison of other analysis variables used by both parties.

Table A-1. Comparison of Honeywell and SRI HOURGLASS Values

Variable	Description	Default	SRI	HON
Fabric				
			HOURGLASS	
IHQ	Hourglass control type	1	4 (stiffness form hourglass control)	4 (stiffness form hourglass control)
QM	Hourglass coefficient	0.1	0.15	0.1
QB, QW	Hourglass coefficient for shell warping	0.1	0.0	0.1
Steel				
			HOURGLASS	
IHQ	Hourglass control type	1	2 (viscous form hourglass control)	4 (stiffness form hourglass control)
QM	Hourglass coefficient	0.1	0.0	0.1
IBQ	Bulk viscosity type		0	1
QB, QW	Hourglass coefficient for shell warping	0.1	0.0	0.1

Table A-2. Comparison of Honeywell and SRI Contact Definition

Variable	Description	Default	SRI	HON
			CONTACT_ERODING_SINGLE_SURFACE_ID	CONTACT_AUTOMATIC_SURFACE_TO_SURFACE
Card 1				
SSTYP	Corresponding ID		5 (include all)	3 (Part Id)
Card 2				
FS	Static friction coefficient	0.0	0.2	0.0
FD	Dynamic friction coefficient	0.0	0.2	0.0
VCD	Viscous damping coefficient (%)	0.0	2.0	0.0
DT	Death time	1.0E+20	0.0	1.0E+20
Card 3				
SFS	Scale factor on slave penalty stiffness	1.0	1.0	0.1
SFM	Scale factor on master penalty stiffness	1.0	1.0	0.1
SST	True thickness override	elm thk	0.0	elm thk
SFST	Scale true thickness	1.0	1.0	1.0
SFMT	Scale true thickness	1.0	1.0	1.0
Card 4				
EROSOP	Erosion/interior node option	0	1	NA
Card A				
SOFT	Soft constraint option	0	2	2
SOFSCL	Scale factor for constraint forces	0.1	0.0	0.1
BSORT	Number of cycles between bucket sorts		10	
IGAP	Flag to improve implicit convergence	1	1 (improve convergence)	2 (do not)

Table A-3. Comparison of Other Honeywell and SRI Analysis Variables

Variable	Description	Default	SRI	HON
			DAMPING_PART_STIFFNESS	
COEF	Rayleigh damping coefficient	0.0	0.25	not used
			CONTROL_ENERGY	
HGEN	Hourglass energy calculation	1.0	1 (hourglass energy not computed)	2 (hourglass energy is computed)
			CONTROL_ACCURACY	
OSU	2nd order objective stress updates	0	1 (on)	not used